Pontificia Universidad Católica de Chile
Facultad de Física
Instituto de Astrofísica

Supersoft X-Ray Nebulae in the Large Magellanic Cloud

by

Diego Andrés Farías Hinojosa

Thesis report presented to the Physics Faculty
of Pontificia Universidad Católica de Chile,
as one of the requirements for the
Master degree in Astronomy.

Supervisor : Dr. Alejandro Clocchiatti (PUC, Chile)
Correctors : Dr. Franz Bauer (PUC, Chile)
Dr. Márcio Catelan (PUC, Chile)

August, 2019

Santiago, Chile

Acknowledgements

“No toda recaída va de arriba abajo, porque arriba y abajo no quieren decir gran cosa cuando ya no se sabe donde se está.”

Extracto de “Me caigo y me levanto”, Julio Cortázar.

Contents

List of Figures

List of Tables

Abstract

Supersoft X-rays binaries sources (SSSs) are said to be potential SN Ia progenitors. Surrounding these sources, due to X-rays emission of a steady-state accreting white dwarf (WD), there should be an associated [O III]λ5007 nebulae. If a SN Ia occurs at this SSS phase, these nebulae should be present in early images surrounding supernova remnants (SNRs). The aim of this work is to find these expected nebulae surrounding four SSSs, CAL 83, CAL 87, RX J0513.9-6751 and RX J0550.0-7151, and three SNRs, SNR 0509-67.5, SNR 0519.69.0 and SNR N103B, in the Large Magellanic Cloud (LMC). In order to do this, we obtain images from the Inamori Magellan Areal Camera and Spectrograph (IMACS) using a broadband Bessell V filter, and a narrowband [O III] filter, centered at $\approx$ 5007 Å. The images were processed by the pipeline PHOTPIPE, which does the astrometry, stacking and differencing of the images, the last step using the well-known HOTPANTS code. By measuring the flux around the coordinates of the source, we study the surface brightness profiles up to 25 pc of the diffuse nebula, to later compare them to the theoretical profiles made by the photoionization code CLOUDY.

Our [O III] flux measurements for CAL 83 are consistent within 2σ with previous results (Remillard et al., 1995), probably due to systematic effects in our calibration technique. In spite of this quantitative difference we confirm that CAL 83 is the only SSS with an associated [O III] ionized region of the seven candidates. The [O III] luminosity for the other objects at 7.5 pc from the central source, are $\lesssim 15\%$ of that of CAL 83. CLOUDY models of the nebulae allow us to constrain physical conditions, such as the ISM density of the source. For typical SSS parameters e.g., luminosity between $10^{37} - 10^{37.5}$ erg/s and effective temperature of the order of 5×10^5 K, the density of the CAL 83 nebula at 7.5 pc is suspected to be slightly lower than, but still consistent with, the range of $4 - 10$ cm^{-3} found by Remillard et al. (1995). For all the other regions, CLOUDY models indicate ISM densities unrealistically low to be consistent with the observed luminosity upper limits.

Chapter 1

Introduction

When a carbon-oxygen white dwarf reaches the Chandrasekhar limit due to mass transfer from a donor or a merger, it leads to a thermonuclear explosion called a Supernova Type Ia (Wang et al., 2007), hereafter SN Ia. This kind of event differs from the other major class of supernovae, core-collapse type (CC), mostly because they are the brightest class of SN, they lack of hydrogen and helium in their early spectra.[1] Also they display predominantly lines of intermediate-mass elements such as calcium, silicon, oxygen and magnesium near maximum light, and iron-peak elements, predominantly Fe II, starting three weeks after optical maximum (Wheeler & Benetti, 2002).

These objects have been extensively studied because of their usage as standard candles (e.g. Schmidt et al., 1998) which has been crucial to determine basic cosmological parameters namely, Ω_m and Ω_Λ, the density of mass and cosmological constant, respectively, in the ΛCDM paradigm. There are two main scenarios for producing SN Ia that have been proposed: the single degenerate (SD) channel, in which the progenitor is an interacting binary -star- system. The more massive -the primary- evolves faster to a white dwarf and the donor -the secondary-, transfers mass to it during its subsequent stellar evolution. This would typically occur when the secondary is a main sequence (MS), subgiant (SGB) or red giant star (RG). The mass transfer would be enough to reach the Chandrasekhar mass ($M_{\rm ch}$) limit $\approx 1.4 M_\odot$ where the $\odot$ symbol refers to the solar value. The other scenario is the

[1] Not entirely true as Hamuy et al. (2003) found Hα and Hβ emission lines in the spectra of SN 2002ic, but the feature ascribed to the interaction of the SN event with the circumstellar material (CSM), enriched by the mass loss of an Asymptotic Giant Branch (AGB) star.

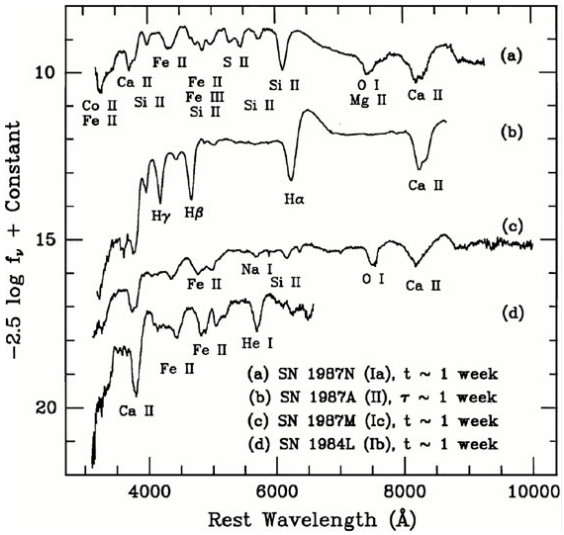

Figure 1.1: Spectra of SNe; we clearly see that in SN Ia dominate the intermediate-mass elements, while hydrogen and helium are lacking. From Filippenko (1997).

double degenerate (DD) channel, where we have a merger of two white dwarfs due to angular momentum and energy loss caused by the emission of gravitational radiation (Gilfanov & Bogdán, 2010) during, probably, the expulsion of a common envelope (hereafter CE). Both channels have received observational support and discouragement: no observations of companion stars after the SN Ia, i.e. near the location of the supernova remnant (hereafter SNR) and, in general, the lack of hydrogen in the spectra does not support the SD channel, while the expected outputs of the merger of two white dwarfs are O+Ne+Mg by off-center carbon ignition and neutron star via accretion-induced collapse (AIC), and the symmetry of SN Ia explosion do not support the DD channel (see Livio & Mazzali, 2018, for a complete review of SN Ia progenitors). A diagram that represents globally the supernovae classification is shown in Figure 1.2.

So it seems, in principle, that the study of binary systems with a white dwarf (WD) as the primary component plus a MS (which usually leads to cataclysmic variables such as recurrent novae, dwarf novae) or RG (the case known as symbiotic) star and accretion onto the WD are necessary in order to understand the SD channel. Accreting binary systems have been an outstanding source of studies, starting in the 70's with the pioneer (computationally-wise) works such as Paczyński (1970),

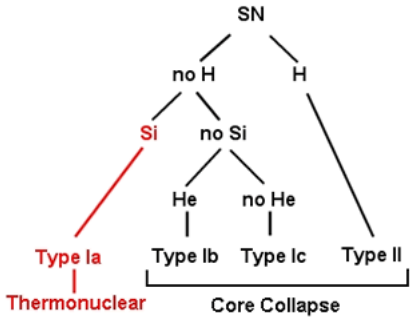

Figure 1.2: Scheme of types of SNe: SN Type Ia contains no hydrogen but silicon lines; it is thought to be the product of thermonuclear explosions of white dwarfs. Core-collapse SNe are the result of explosions of massive stars; in general, there are different types of these events depending on the absence of the certain elements on the spectra: Type Ib contains no hydrogen, no silicon but helium lines, while Type Ic lacks the same elements as Type Ib plus helium; if SNe contains hydrogen it is catalogued as Type II (even though there are differences depending on their light curves). From COSMOS webpage.[2]

which describes the evolutionary processes in close binary systems: it is expected that, given a range of values of periods, initial masses and distances among the stars (which are not independent but related by the third Kepler law), mass transfer (hereafter MT) naturally arises, for example, whenever the stellar radius of the donor exceeds a critical radius, defined approximately as the radius of its Roche lobe, through the inner Lagrangian point L_1, which is commonly called Roche Lobe Overflow (RLOF) (Figure 1.3), and -probably- regulated by the action of (optically thick) stellar winds from the WD (Hachisu et al., 1999a).

In this scenario, for example, during the transition from the main sequence to the red giant branch where the radius of a 1 $M_\odot$ grows to ~ 100 $R_\odot$, it is not hard to visualize how a WD + MS/RG system may be formed if the primary, the more massive star initially, fills several times its Roche lobe and MTs occur during its evolution to a WD,[3] accreting matter to the -eventual more massive- secondary star, which ends up filling its own Roche lobe and transfering mass to the WD, allowing the possibility of a SN Ia event.

[2]http://astronomy.swin.edu.au/cosmos/S/Supernova+Classification

[3]Among other interactions, e.g., Hachisu et al. (1999b) proposed that to form a close symbiotic binary system from wide binaries it was necessary that when the primary is in the AGB, a superwind leads to a CE evolution, that as a consequence, shrinks the distance between the stars.

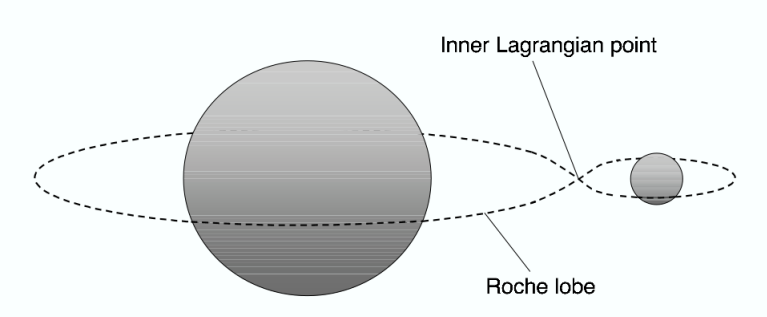

Figure 1.3: Scheme of a binary stars system with their respective Roche Lobes (equipotential surface surrounding each star), and the inner Lagrangian point L_1 (the intersection of the Roche Lobes in the equatorial plane). From Iliadis (2007).

Traditionally (e.g. Han & Podsiadlowski, 2004; Langer et al., 2000; Hachisu et al., 1999a,b), the first approach to study the binary stellar evolution of a WD + (non-degenerated) star system was to set up an already-evolved WD + donor at the onset of MT using a grid of three-parameters ($M_{\rm wd}$, $M_{\rm donor}$ and $P_{\rm orb}$) showed in Figure 1.4, following a detailed stellar structure time evolution of the binary, including the model of accretion, and discriminating as a progenitor those systems where the WD reaches $M_{\rm ch}$. Then rapid binary population synthesis (BPS) calculations were done in order to obtain, for example, the number CO WD + MS systems at a certain star formation rate (SFR) or single outburst. Recently, more BPS codes have been developed to follow the binary evolution from ZAMS (Toonen et al., 2014, to see the differences among them), with modifications of the assumptions of the CE-prescription, mass retention efficiencies, angular momentum losses by RLOF, etc. (e.g. Meng & Podsiadlowski, 2017; Chen et al., 2014).

In the case of Meng & Podsiadlowski (2017), the minimum initial mass found for a successful progenitor WD of a SN Ia is $0.65M_{\odot}$ (for $Z = 0.02$) and the typical maximum initial WD mass is assumed $\approx 1.2M_{\odot}$; therefore, in the SD channel, the WD needs to accrete at least $\approx 0.2M_{\odot}$ in order to ignite. We know mechanisms, such as rotation, that enlarge the WD mass at ignition,[4] which can explain over-luminous SN Ia events such as SNLS-03D3B (Howell et al., 2006). The luminosity

[4]For example, the WD ignition occurs at $\approx 1.5M_{\odot}$ for a solid rigid rotation (Uenishi et al., 2003), and at $\approx 2M_{\odot}$ for differential rotation (Yoon & Langer., 2005).

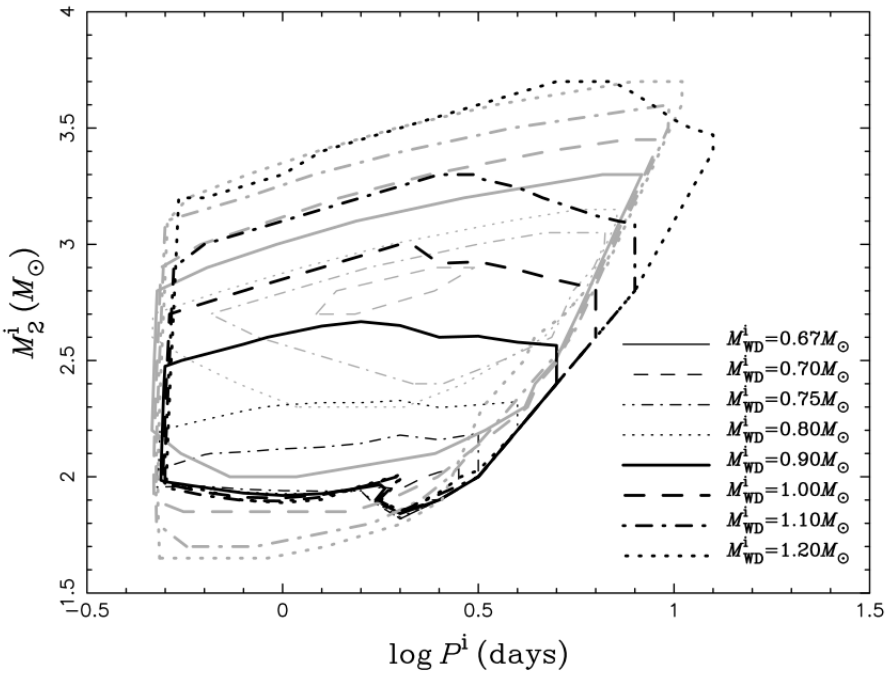

Figure 1.4: Initial parameters in the $M_{\rm donor} - P_{\rm orb}$ for different WD masses (0.7 to $1.2 M_\odot$ (inner to outer region) of all progenitors of SN Ia. From Han & Podsiadlowski (2004).

($2.2 \times L_{\rm SNIa}$) and kinetic energy derived from spectral lines of this SN, implied a WD mass at explosion that was larger than $M_{\rm ch}$. Once the WD achieves this mass limit, explosion models (delayed detonation, carbon deflagration, off-center carbon ignition) agree in general with the luminosity, color and spectral feature evolution of "normal" SN Ia.

Nuclear detonations that might start below the Chandrasekhar mass limit have also been proposed. These so-called sub-Chandrasekhar (sub-Ch) models assume that a helium detonation of the accreted helium layer triggers a carbon ignition near the center of the WD (e.g. Woosley & Weaver, 1994; Livne & Arnett, 1995). In principle, sub-Ch models would expand the initial parameters of binary systems and thus increase the expected SN Ia rate, better matching the observational rate. Unfortunately, these models have failed to reproduce the UV deficit observed in sub-luminous/normal SN Ia (Nugent et al., 1995) as we can see in Figure 1.5, where the sub-luminous normal-like SN Ia 1991bg (Turatto et al., 1996) is compared with two sub-Ch models; WW2 ($0.7 M_\odot$ CO WD + 0.2 accreted He layer) and LA4 ($0.7 M_\odot$ CO WD + 0.17 accreted He layer).

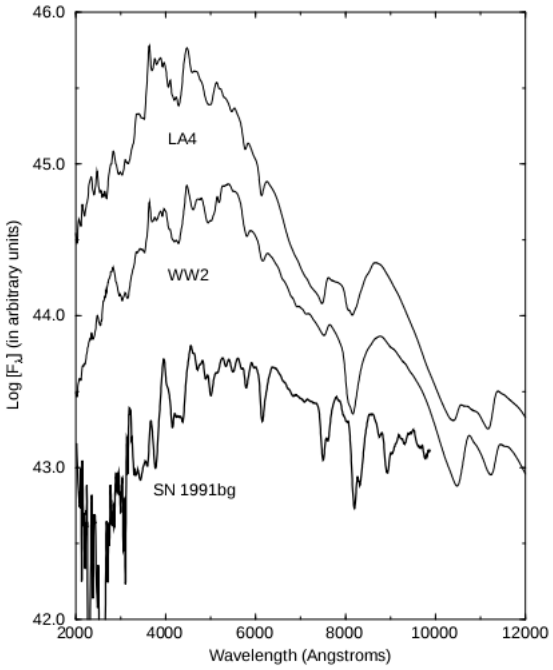

Figure 1.5: Synthetic spectra of WW2 (Woosley & Weaver, 1994) and LA4 (Livne & Arnett, 1995) at 20 days compared with the spectrum of sub-luminous SN 1991bg (Nugent et al., 1995) at maximum light. From Nugent et al. (1995).

Observationally, it is difficult to confirm the nature of the progenitor of a SN Ia: we do not expect any surviving remnant for the DD channel, while in the SD scenario the companion should remain close to the explosion location. Only one SN Ia (SN 1572) has shown a possible companion. Ruiz-Lapuente et al. (2004) uses kinematics (position with respect to the SNR and expected kick velocity), magnitude, and stellar atmosphere model arguments to propose that Tycho G, a star within the remnant, is the long sought after donor star of the SN. But it is a controversial case due to the subsequent parameters determinated such as radial velocity. (Kerzendorf et al., 2009). So, in order to constrain the donor type in the SD channel, we need precise measurements of the distance to the SNR and time of the explosion or, as shown recently (Woods et al., 2017, 2018), constraints provided by the medium surrounding the SNR. For this reason, SNRs of the LMC seem perfect to search the progenitors

of SN Ia due to the well-known distance to the LMC ≈ 50 Kpc (see Walker, 2012, and references therein), and the precise determination of the explosion time of some of them using light echoes (Rest et al., 2005).

Until this point, we have assumed that accreting WDs are responsible for the thermonuclear explosion of a SN Ia, mainly because the energetics and spectra match with the models (say, for example, the amount of nickel mass is the defining quantity for the luminosity of a SN Ia). But, how are we sure, empirically, that a WD is the source of the explosion of SN Ia? The answer may be found in one of the most well-recorded SN Ia in the recent times, SN 2011fe in M101, which has given key clues about its progenitors: the exploding star must be a compact star with upper limit $R_0 < 0.1R_\odot$, namely a WD (Nugent et al., 2011). The strong conclusion is based on the availability of spectra and photometry at very early epochs which made it possible to exclude a large number of possible progenitor systems such as helium and symbiotic stars. The only possible options remaining are the WD + MS/SGB channel with a strict upper limit to the luminosity of the progenitor (Graur et al., 2014), and DD systems (Li et al., 2011). The configuration of a WD and a not-so-evolved companion star is called the **supersoft channel** towards a SN Ia event.

In the early 90's, an important class of intrinsically bright X-rays sources was found and characterized in the Large Magellanic Cloud. These objects have extremely soft X-ray spectra, much softer than the classical X-rays binaries which contain neutron stars or blackholes[5] and luminosities of the order of the Eddington limit (Kahabka & van den Heuvel, 1997). For this reason, they were called **supersoft X-ray binary sources (SSSs)**. To explain their unique spectra, van den Heuvel et al. (1992) were the first to propose that SSSs should be compact objects accreting hydrogen or helium rich material from a companion star at the same rate that it burns close to the surface; this regime is usually called steady stable-burning-state. When hydrogen is accreted (at a specific rate $\dot{M} \sim 10^{-7} M_\odot \mathrm{yr}^{-1}$) onto the envelope of the WD ($M_{\mathrm{WD}} \approx 0.7 - 1.2 M_\odot$), it burns at steady rate and emits a large quantity of photons in the X-rays band as a blackbody (Figure 1.6) with the following approximated effective temperature

[5]The major contribution to the luminosity of the classical X-rays binaries is accretion onto the denser component, while nuclear-burning in its surface is considerably smaller.

$$T_{\rm eff} \approx 5 \times 10^5 \left(\frac{\dot{M}}{10^{-7} M_\odot \ {\rm yr}^{-1}} \right)^{1/4} \left(\frac{R_{\rm WD}}{10^{-2} R_\odot} \right)^{-1/2} \ {\rm K}, \tag{1.1}$$

where $\dot{M}$ is the mass accretion rate and $R_{\rm WD}$ is the white dwarf radius (typical values $\sim 10^{-2} R_\odot$) (Gilfanov & Bogdán, 2010); the typical wavelength of the peak (in energy) is ≈ 200 eV, which lays in the supersoft band. Therefore, the classical assumption that is made about SSSs is that their spectra is close to a blackbody in order to obtain ranges of effective temperature[6].

It did not take long to realize that these newly-discovered sources could contribute as a SD progenitor (Kahabka et al., 1994) based on the previous works of stability of mass transfer onto WDs such as Nomoto (1982) (for helium accretion) and Sienkiewicz (1980) (for hydrogen accretion).[7] The main result they obtained is that steady-stable states were found for an extremely narrow range for mass transfer $\dot{M} \approx 1 - 4 \times 10^{-7} M_\odot \ {\rm yr}^{-1}$, fixed by the **thermal timescale of the donor** (Nomoto et al., 2007), which should be a **not-so-evolved star**[8] able to fill its RLOF. When the mass transfer is above the stated range, the WD should form a RG-like envelope, possibly filling its own Roche lobe and sharing a common envelope with the donor. On the contrary, if accretion rate is lower than the stable-burning range, it is expected to be a recurrent nova event (due to the degenerated hydrogen layer), ejecting more mass than accreted due to the mixing of the accreted matter with that of the WD (Maoz et al., 2014).

How many of these objects should we encounter in the Milky Way and nearby galaxies? Di Stefano & Rappaport (1994) calculated the population of SSSs by seeding the M31, the Milky Way (MW) and the Magellanic Clouds (LMC and SMC) using a BPS-like study. The results from their theoretical study gives likely $\approx 2500, 1000, 30$ and 20 for M31, MW, LMC and SMC, respectively. A more recent

[6] Although Heise, van Teeseling & Kahabka (1994) showed with Local Thermodynamic Equilibrium (LTE) models of WD atmospheres, that, for example, due to the photo-absorption by highly ionized metals in the atmosphere, there are edges in the X-rays spectrum that do not appear in a simple blackbody model.

[7] If the hydrogen and helium mass retentions are not sufficiently low in order to avoid losing large portions of the envelope mass by flashes.

[8] Thus, the nexus with the supersoft channel.

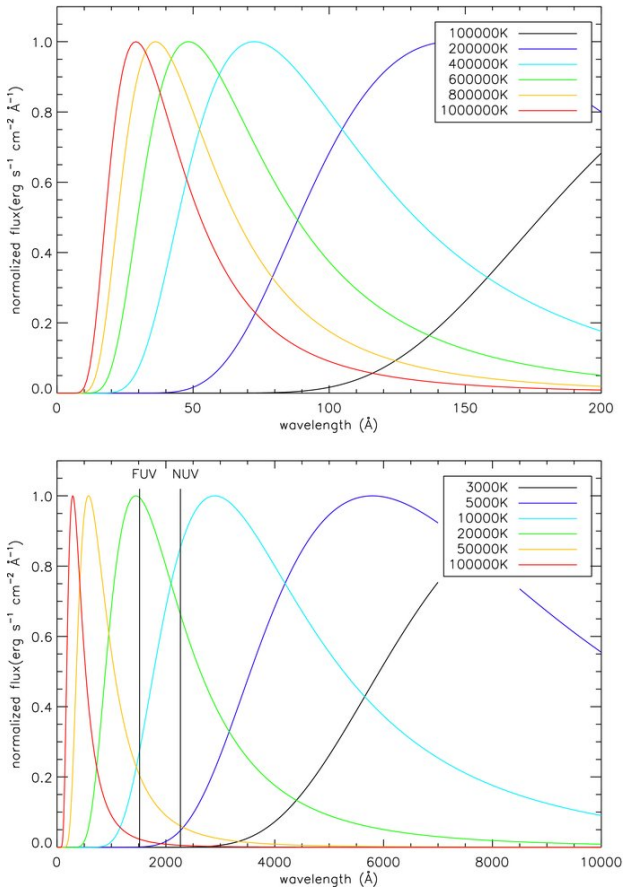

Figure 1.6: Normalized blackbody spectrum at different temperatures in the range corresponding to SSS. From Orio et al. (2010).

BPS-work done by Chen, Woods, Yungelson, Gilfanov & Han (2015) predicted that, for a $10^{11} M_{\odot}$ galaxy with a constant star formation rate (accounting for spiral galaxies), the number of observed SSSs should be $\sim 40 - 130$, while for a starburst galaxy (early-type like) with the same mass, the number would be much lower, $10 - 20$. These objects should be associated with a nebula because the large flux of X-ray radiation from the source (a few times 10^{37} erg s^{-1}) can ionize the interstellar medium (ISM) to distances of dozens of parsecs. These putative nebulae are called **"supersoft nebulae"** (Kahabka & van den Heuvel, 1997).

What is the importance of finding supersoft nebulae surrounding supersoft X-rays sources? By doing so, we can understand better the properties of the interstellar medium (ISM) and the luminosity of the source. Why? Using photoionization models such as CLOUDY (Ferland et al., 2013), we can constrain the temperature and

luminosity of the source (Rappaport et al., 1994). This is usually done by assuming the spectra of the central source and the density of the medium and obtaining radial profiles of strong (pseudo) forbidden lines such as [O III]λ5007 Å (Osterbrock & Ferland, 2006). Studying the supersoft nebulae is better than most of the supersoft X-rays surveys because most of the radiation in the soft X-rays is absorbed by the ISM and, few instruments cover with high efficiency the maximum of a SSS spectra. Figure 1.7 shows that using ROSAT energy bands, we would only measure the high energy tail photons from a SSS and the same happens for newer instruments such as Chandra and XMM-Newton.

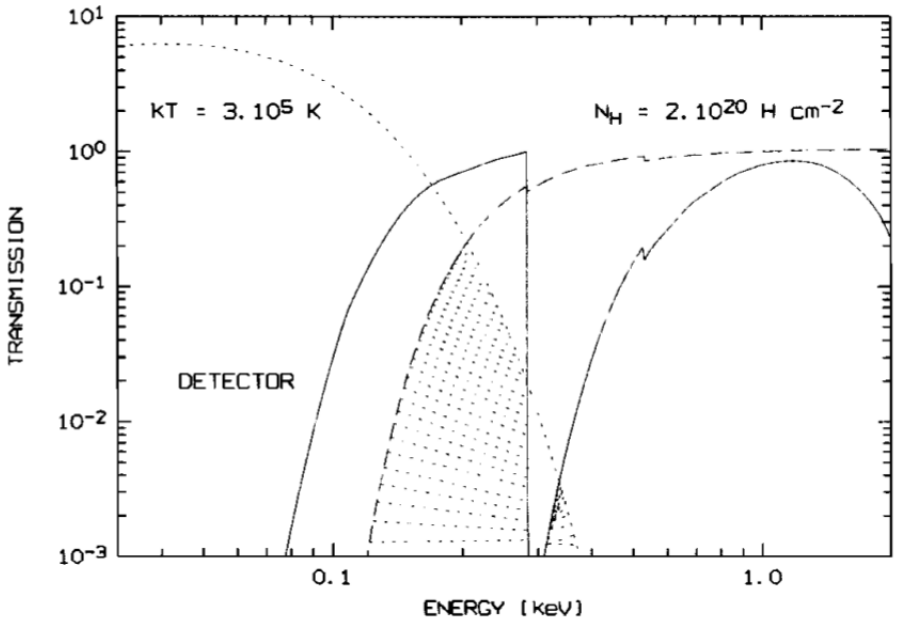

Figure 1.7: ROSAT efficiency (solid curve), transmission of ISM for $N_{\rm H} = 2 \times 10^{20}$ cm^{-2} (dashed line), distribution of a typical blackbody spectrum ($T_{\rm eff} = 3 \times 10^5$ K) representing a SSS (dotted line) and observed distribution (hatch markers). From Kahabka & van den Heuvel (1997).

Therefore, in principle, this could be an efficient way of finding more supersoft X-rays sources. Also, by finding these nebulae, we can study their nature: are they the product of an overdense ISM surrounding the SSS or due to the material expelled by the binary system during common envelope phases?

Previous searches of supersoft nebulae have found only one nebula associated with a SSS (CAL 83) out of nine supersoft sources in the Magellanic Clouds (Remillard et

al., 1995). Two main hypotheses were proposed to explain this: the time-averaged luminosity of the SSSs is lower than the luminosity inferred from current X-rays observations, or the supersoft nebulae surface brightness could be very low because the ISM has a very low density around the sources (Di Stefano et al., 1995). Both works tentatively conclude that roughly 10% of supersoft sources are associated with ionization nebulae, and that supersoft sources that are steady nuclear burners (on) likely have a nebula. Woods & Gilfanov (2016) demonstrated that most of the SSS nebulae in the LMC must lie in a much less dense ISM than CAL 83 based on the probability that a SSS lies sufficiently near to a dense cloud assuming a power-law distribution of the sizes of the clouds, a filling factor of 0.05 and that the minimum size to detect a nebula like the one of CAL 83 is $\approx$ 3 pc. As an alternative to the above hypothesis, it is also speculated that no true steady-burning state (but eruptive cycles) is occuring in these accreting WDs: Idan, Shaviv & Shaviv (2013), following high (hydrogen) accretion rates onto a $1.25 M_{\odot}$ WD, found that the eruption recurrence time is 16 yrs and the residual mass after the eruption is about 20% of the accreted mass, avoiding a significant WD mass growth and thus discarding these systems as SN Ia progenitors.

Our aim is to find nebulae surrounding SSSs in the LMC. We have two main motivations. One is to repeat the work of Remillard et al. (1995) with more modern instrumentation. Woods & Gilfanov (2016) suggested that with the availability of larger telescopes, e.g. Magellan telescope, with 6.5 meters of aperture, we may observe nebulae at densities of $n \approx 0.1$ cm^{-3} at typical SSS temperatures and luminosities, as opposed to ~ 0.4 cm^{-3} for Remillard et al. (1995) using the same exposure times approximately. This translates to stricter upper limits on the [O III]λ5007 Å surface brightness of a nebulae and therefore the ambient density of the SSSs could be established. The other motivation is to go further and try to find nebulae surrounding supernovae remnants. It is natural to think that if a supersoft nebula existed before the explosion, chances are we can find it after the explosion. In fact, this surviving time should be about the recombination time of a ionized nebula,

$$\tau_{\rm rec} \approx 10^5 \left(\frac{n_{\rm ISM}}{1{\rm cm}^{-3}}\right)^{-1} \ {\rm yr}.$$

Young SNe remnants such as those found in the LMC with ages $\sim$ 500 yrs (Rest

et al., 2005) would display these associated nebulae long after the explosion (Woods & Gilfanov, 2016). If found, the supersoft nebulae would support the idea that the SSSs are progenitors of SN Ia. How are we sure that the ionization of the nebulae associated with a supernovae remnant is due to the past emission of a SSS? Cumming et al. (1996) described the main sources of ionizing photons after a supernovae type Ia explosion; first, they claim that the quantity of ionizing photons produced at supernova shock breakout (see Maoz et al., 2014, for details) is probably small, capable of ionize only $\sim 1.3 \times 10^{-9} M_{\odot}$ of hydrogen; second, the radiation from the ^{56}Ni-decay is too hard, and third, the UV flux ($\lambda < 1000$Å) from the SN Ia explosion should be small (Woods & Gilfanov, 2016). Therefore, the SN explosion should neither contribute or change the ionization structure of the putative supersoft nebula **ahead of the forward shock** [9]. If the SSSs are not truly steady-state sources, the upper limits will depend on the recurrency of the "on" -state, i.e., the time-averaged luminosity (Chiang & Rappaport, 1996).

This thesis is divided in six chapters: Chapter 2 is a quantum physics reminder to clarify the concepts of forbidden lines, mainly from Fitzpatrick (2015) webpage version,[10] followed by Chapter 3 that contains the information of [O III]λ5007 Å and the photoionization code CLOUDY to model the expected behaviour of an ionized nebula. Chapter 4 aims to refresh the basis of the physical mechanisms governing the stellar evolution, focused mainly in core, shell burning and energy transport, using Iliadis (2007) and electron degeneracy (Section 4.1), based in several lectures from universities courses: white dwarfs introduction and physics popurri are given by Chapter 1-6 from Pols (2012a),[11] Collins (1989),[12] and the classical astronomy book Carroll & Ostlie (2007). Chapter 5 is focused entirely to understand the stability of mass transfer in binaries, mostly the supersoft channel and how SSSs may lead to a SN Ia, based on a very completed review from Chapters 6-8 of Pols (2012b),[13] Ivanova (2015) and several references therein. Chapter 6 is the description of the instrument, the fields in the LMC and the data that has been used in the present thesis. The required tools to obtain radial profiles of [O III]λ5007 from our measurements and compare them with photoionization models are contained in Chapter 7. Chapter 8 is

[9] Not too close because of the interaction of the shock and the ISM.
[10] https://farside.ph.utexas.edu/teaching/qm/Quantum/Quantumhtml.html
[11] https://www.astro.ru.nl/~onnop/education/stev_utrecht_notes/
[12] http://ads.harvard.edu/books/1989fsa..book/
[13] https://www.astro.ru.nl/~onnop/education/binaries_utrecht_notes/

the presentation and analysis of the results and Chapter 9 presents the conclusions of this work.

Chapter 2

Quantum Physics

One of the most important processes explained by the physics is the transition of an electron over different quantum states. Before introducing the probability of an electron to do this "jump", it is necessary a refresh of some quantum mechanical concepts.

2.1 Formalism

Let $|A\rangle$ be a vector which describes a particular state of a microscopic system[1] belonging to some vector space called -by Dirac- ket space, which has all of the properties of a Hilbert space. One of the well-known properties of this type of space is that the superposition principle holds: any state $|A\rangle$ is the superposition of two or more other states, in other words, it can be written in terms of the normalized basis $|i\rangle..|N\rangle$ of the ket space

$$|A\rangle = \sum_{i..N} \alpha_i |i\rangle \tag{2.1}$$

where α_i are an arbitrary set of complex numbers.[2] For each ket, its corresponding bra $\langle A|$, can be thought as a specific case of a linear functional $\langle F|$ on $|A\rangle$[3]

[1] Any system composed by interacting particles according to specific laws of force, such as an atom.

[2] α_i^* would be the conjugate of α_i and $\alpha_i^* \alpha_i = |\alpha_i|^2$ its norm.

[3] By dual correspondence (DC), with normalized basis $\langle i|..\langle N|$.

$$
\begin{aligned}
\langle F| &= \sum_{j..N} \beta_j^* \langle i| \\
\rightarrow \langle F|A\rangle &= \sum_{i..N}\sum_{j..N} \beta_j^* \alpha_i \underbrace{\langle j|i\rangle}_{\delta_{ij}} \\
&= \sum_{i..N} \beta_i^* \alpha_i \\
&= \sum_{i..N} (\beta_i \alpha_i^*)^* = \left(\sum_{i..N} \beta_i \alpha_i^*\right)^* \\
&= \langle A|F\rangle^*
\end{aligned}
$$

with δ_{ij} is the Kronecker delta; if $i = j$, $\delta_{ij} = 1$, otherwise is zero. The last equation is the definition of inner product, which gives as a result, in principle, a complex number. It is evident that if $\langle F| \rightarrow \langle A|$, the inner product is always real and equal to the norm of $|A\rangle$. Due to its importance, it is worth mentioning that the outer product of $\langle B|$ and $|A\rangle$, $|A\rangle\langle B|$, corresponds to a linear operator.

Now we introduce the concept of a linear operator $\hat{X}$ acting in kets $|A\rangle$, $|B\rangle$, producing another set of kets. Some properties of $\hat{X}$ are that it is associative on the kets[4] and does not (necessarily) commute with another operator $\hat{Y}$ ($\hat{X}\hat{Y} \neq \hat{Y}\hat{X}$). It is readily the existence of the null operator $\hat{X}|A\rangle = |0\rangle$ and the identity $\hat{X}|A\rangle = |A\rangle$. Also, it should be evident the existence of an operator $\hat{X}^\dagger$ due to DC such that $\hat{X}|A\rangle \leftrightarrow \langle A|\hat{X}^\dagger$ and

$$\langle B|\hat{X}^\dagger|A\rangle = \langle A|\hat{X}|B\rangle^*$$

could be easily verified. $\hat{X}^\dagger$ is usually called the adjoint operator of $\hat{X}$. If $\hat{\eta}$ is an operator equals to its adjoint $\hat{\eta}^\dagger$, we say that $\hat{\eta}$ is an Hermitian operator. If $\hat{\eta}$ acts on some special kets called eigenkets $|\eta'\rangle$, it follows that

$$\hat{\eta}|\eta'\rangle = \eta'|\eta'\rangle \tag{2.2}$$

[4]Given a, b constants, $\hat{X}(a|A\rangle + b|B\rangle) = a\hat{X}|A\rangle + b\hat{X}|B\rangle$.

with $\eta^{'}$ being a real number called **eigenvalue**. For an Hermitian operator, the eigenvalues are always real[5] and the eigenkets (i.e. **eigenstates**) are orthogonals (after normalizing, orthonormals).

Any Hermitian operator $\hat{\eta}$ can be thought as an **observable** of the system in a state $|\eta^{'}\rangle$ through a measurement $\eta^{'}$. Then, given an initial state $|A\rangle$ of the system, what is the probability $P(\eta^{'})$ to make a transition to a state $|\eta^{'}\rangle$?. Using that $|A\rangle$ is a linear combination of the elements of the basis and these satisfy $\sum |\eta^{'}\rangle\langle\eta^{'}| = 1$ (sum over all states $\eta^{'}$), this probability is intrinsically related to $|\langle A|\eta^{'}\rangle|^2$ given that $P(\eta^{'})$ is a positive number. In fact

$$P(\eta^{'}) = \frac{|\langle A|\eta^{'}\rangle|^2}{\sum\limits_{\eta^{'}} |\langle A|\eta^{'}\rangle|^2}. \tag{2.3}$$

As the probability of the system to "jump" from an initial state to a final state is already defined, we quickly move on to show a list of (easily) demonstrable quantum physics world:

S.1 For any any observable $\hat{\eta}$, its expectation value is $\langle\hat{\eta}\rangle = \langle A|\hat{\eta}|A\rangle$ given an ensemble of systems in a initial (normalized) state $|A\rangle$.

S.2 Generalization to a continuous spectra of the former definitions e.g. $\int d\eta^{'}|\eta^{'}\rangle\langle\eta^{'}| = 1$, $\langle\eta^{'}|\eta^{''}\rangle = \delta(\eta^{'} - \eta^{''})$ (with $\delta \equiv$ Dirac delta).

S.3 Commutation of two operators is written $[\hat{X}, \hat{Y}] = \hat{X}\hat{Y} - \hat{Y}\hat{X}$. If two operators commute, then they are simultaneously measurable.

S.4 Analogous to Hamiltonian mechanics, if a system can be describe by the (generalized) coordinates $x_1..x_i, x_j$ (position) and $p_1..p_i, p_j$ (momentum), the relations of commutation of their corresponding operators $\hat{x_1}, .., \hat{x_i}, \hat{x_j}$ and $\hat{p_1}, .., \hat{p_i}, \hat{p_j}$ are written as $\boldsymbol{[\hat{x}_i, \hat{x}_j] = 0}$, $\boldsymbol{[\hat{p}_i, \hat{p}_j] = 0}$ and $\boldsymbol{[\hat{x}_i, \hat{p}_j] = i\hbar\delta_{ij}}$ (unlike the classical result $\equiv 0$), with $\mathrm{i} = \sqrt{-1}$ and the reduced Planck constant $\hbar$.

S.5 In continous formalism, given position operator $\hat{x}$ with eigenvalues $x^{'}$ and eigenkets $|x^{'}\rangle$, and a general state $|A\rangle$, the quantity $\boldsymbol{\langle x^{'}|A\rangle}$ is a function of the

[5] Although not necessarily uniques, leading to the so-called degenerated states.

position $x^{'}$ and it is called (position-space) **wave function** $\Psi_A(x^{'})$. The same applies to the $\hat{p}$ operator. With this, the position-space and momentum-space wavefunctions are established as the Fourier transforms of each other.

S.6 With little effort, it can be shown that in the continuous-functional paradigm, the operators $\hat{x}$ and $\hat{p}_x$ ca be written as the derivative of the each other, $\boldsymbol{\hat{x} = \mathrm{i}\hbar\frac{d}{dp_x}}$ and $\boldsymbol{\hat{p}_x = -\mathrm{i}\hbar\frac{d}{dx}}$. This thesis will use the position-space representation (i.e, projection onto x space), usually called the **Schrödinger representation**.

S.7 Heisenberg Uncertainty Principle can be derived: $\Delta x \Delta p_x \sim \hbar$.

2.1.1 Schrödinger Equation

The system has been written in terms of the position and momentum at an instant (fixed) time t_0, which is the moment of the measurement that determines the probability at any time $t > t_0$ if the system remains unperturbed in the time interval $\Delta t = t - t_0$. Even if the probability to "jump" to a certain state does not change with time, the state itself might do. To see this, consider a system in an initial state at t_0 that evolves a certain time t, $|A_{t_0}\rangle$ and $|A_t\rangle$ respectively. The time evolution of this state is described by the (time evolution) operator T

$$T \rightarrow |A_t\rangle = T|A_{t_0}\rangle \tag{2.4}$$

that satisfies

$$\mathrm{i}\hbar\frac{dT}{dt} = \hat{H}(t)T \tag{2.5}$$

where $\hat{H}(t)$ is the Hamiltonian operator of the system, whose eigenvalues are the observables of the total energy of the system. The differential equation 2.5 has a solution of the form

$$T(t, t_0) = \exp\left(\frac{-\mathrm{i}}{\hbar}\int_{t_0}^{t}\hat{H}(t^{'})dt^{'}\right). \tag{2.6}$$

Equation 2.5 is the general form of the well-known **Schrödinger equation**.

Imagine an one dimensional particle of mass m described by its position x and momentum p_x ($\hat{x}$ and $\hat{p}_x$ operators, respectively) under the potential $V(x,t)$. The Hamiltonian operator can be written as $\hat{H} = \frac{\hat{p_x}^2}{2m} + V(x,t)$, therefore

$$\begin{aligned} \mathrm{i}\hbar\frac{dT}{dt} &= \hat{H}(t)T \\ \rightarrow \mathrm{i}\hbar\frac{dT|A_{t_0}\rangle}{dt} &= \hat{H}(t)T|A_{t_0}\rangle. \end{aligned}$$

Taking the definition of operator T (Equation 2.4), the last equation leads to

$$\rightarrow \mathrm{i}\hbar\frac{d|A_t\rangle}{dt} = \hat{H}(t)|A_t\rangle.$$

Written in terms of position space (Schrödinger representation)

$$\rightarrow \mathrm{i}\hbar\frac{\partial\langle x|A_t\rangle}{\partial t} = \hat{H}(t)\langle x|A_t\rangle$$

and by definition of $\Psi_A(x) \equiv \Psi(x,t)$

$$\Rightarrow \mathrm{i}\hbar\frac{\partial\Psi(x,t)}{\partial t} = \hat{H}(t)\Psi(x,t). \tag{2.7}$$

Using $\hat{H}(t)$, it can be shown that generalizing to three dimension space, Equation 2.7 is written as

$$\Rightarrow \mathrm{i}\hbar\frac{\partial\Psi(\mathbf{x},t)}{\partial t} = \left(\frac{-\hbar^2}{2m}\right)\boldsymbol{\nabla}^2\Psi(\mathbf{x},t) + V(\mathbf{x},t)\Psi(\mathbf{x},t) \tag{2.8}$$

with e.g. $\mathbf{x} = (x,y,z)$ and $\boldsymbol{\nabla} = (\frac{\partial}{\partial x}, \frac{\partial}{\partial y}, \frac{\partial}{\partial z})$. Equation 2.8 is called time-dependent Schrödinger equation, the governing quantum mechanics equation[6].

[6]It is worth noting that the time-independent version of this equation, $H\Phi = E\Phi$, arises when the total energy of the system E (eigenvalue of the operator H) is a constant of motion, i.e., $\hat{H}(\hat{p},x,t) = \hat{H}(\hat{p},x)$.

2.1.2 Orbital Angular Momentum

Analogous to classical mechanics, the orbital angular momentum operator $\hat{L} = (\hat{L}_x, \hat{L}_y, \hat{L}_z)$ in quantum mechanics can be written using the statement S.4 for position $\hat{\mathbf{x}} = (\hat{x}, \hat{y}, \hat{z})$ and momentum $\hat{\boldsymbol{p}} = (\hat{p}_x, \hat{p}_y, \hat{p}_z)$ operators and $\hat{\boldsymbol{L}} = \hat{\boldsymbol{x}} \times \hat{\boldsymbol{p}}$

$$\begin{aligned} \hat{L}_x &= \hat{y}\hat{p}_z - \hat{z}\hat{p}_y \\ \hat{L}_y &= \hat{z}\hat{p}_x - \hat{x}\hat{p}_z \\ \hat{L}_z &= \hat{x}\hat{p}_y - \hat{y}\hat{p}_x \\ \Rightarrow &\begin{cases} [\hat{L}_x, \hat{L}_y] = \mathrm{i}\hbar\hat{L}_z \\ [\hat{L}_y, \hat{L}_z] = \mathrm{i}\hbar\hat{L}_x \\ [\hat{L}_z, \hat{L}_y] = \mathrm{i}\hbar\hat{L}_y \\ \quad\vdots \end{cases} \end{aligned} \tag{2.9}$$

It is clear that $\hat{L}_x$, $\hat{L}_y$ and $\hat{L}_z$ do not commuted so they cannot be measurable at the same time. Choosing $\hat{L}_z$ as the observable and the definition of the operator $\hat{L}^2 = \hat{L}_x^2 + \hat{L}_y^2 + \hat{L}_z^2$, it is easy to see that

$$[\hat{L}^2, \hat{L}_z] = 0. \tag{2.10}$$

Thus, $\hat{L}^2$ commutes with $\hat{L}_z$. What are the corresponding eigenvalues for eigenkets $|l, m\rangle$ of $\hat{L}^2$ and $\hat{L}_z$ operators? Commonly, using the ladder operators of the orbital angular momentum $\hat{L}^{\pm} = \hat{L}_x \pm \mathrm{i}\hat{L}_y$, it can be shown that if m_l, the magnetic quantum number, is part of the eigenvalue of $\hat{L}_z$,

$$\hat{L}_z|l, m_l\rangle = m_l\hbar|l, m_l\rangle \tag{2.11}$$

for m_l integer and $-l \leq m_l \leq l$, with l called the azimuthal quantum number, it is necessary that l satisfies

$$\hat{L}^2|l, m_l\rangle = \hbar^2 l(l+1)|l, m_l\rangle \tag{2.12}$$

setting up the corresponding eigenvalues of $\hat{L}^2$.

What about the eigenkets? In order to show them, it is very useful to use the Schrödinger representation and move onto spherical coordinates $(x, y, z) \rightarrow (r\sin\theta\cos\phi, r\sin\theta\sin\phi, r\cos\theta)$, where the operators of Hamiltonian $\hat{H} = \frac{\hat{p_x}^2}{2\mathrm{m}} + V(x,t)$ end up forming

$$\begin{cases} L_z &= -\mathrm{i}\hbar\left(\sin\phi\frac{\partial}{\partial\phi}\right) \\ L_y &= -\mathrm{i}\hbar\left(\cos\phi\frac{\partial}{\partial\theta} - \cot\theta\sin\phi\frac{\partial}{\partial\phi}\right) \\ L_x &= \mathrm{i}\hbar\left(\sin\phi\frac{\partial}{\partial\theta} - \cot\theta\cos\phi\frac{\partial}{\partial\phi}\right) \\ &\vdots \end{cases} \tag{2.13}$$

$$\Rightarrow \begin{cases} L^2 &= -\hbar^2\left(\frac{1}{\sin\theta}\frac{\partial}{\partial\theta}\sin\theta\frac{\partial}{\partial\theta} + \frac{1}{\sin^2\theta}\frac{\partial^2}{\partial^2\phi}\right) \\ H &= \frac{\hbar^2}{2\mathrm{m}}\left(-\frac{1}{r^2}\frac{\partial}{\delta r}r^2\frac{\partial}{\partial r} + \frac{L^2}{\hbar^2 r^2}\right) + V(r,\theta,\phi) \\ &\vdots \end{cases} \tag{2.14}$$

and consequently, changing the form of the Schrödinger equation[7]. In this representation, it is more comfortable to write the the eigenfunctions $\psi(\theta,\phi)$ of L^2; the special set of functions called **spherical harmonics**

$$\psi_{lm}(\theta,\phi) = \sqrt{\frac{2l+1}{4\pi}\frac{(l-m)!}{(l+m)!}}P_{lm}(\cos\theta)e^{\mathrm{i}m\phi} \tag{2.15}$$

where P_{lm} is the associated Legendre function. These ψ_{lm}s have many interesting properties, but we focus on the restriction of the quantum numbers in Equations 2.11 and 2.12: $-l \leq m_l \leq l$ and l, m_l must be integers.

2.1.3 Example: Hydrogen Atom

The canonical example of the usage of the Schrödinger equation is by solving the wavefunctions of the Hydrogen atom, since hydrogen has only one proton (subscript p) and one electron (subscript e). As this thesis does not have as a goal to show

[7]Note that $[L^2, H] = 0$ and $[L_j, H] = 0$ for $j = \{x, y, z\}$.

how to solve these complex equations, we only write the important aspects of this example.

For instance, let us take Φ as the eigenfunction that satisfies the time-independent Schrödinger equation with the simple Coulomb potential for an electron of charge $-e$ (e for proton), written as $V(r) = -\frac{e^2}{4\pi\epsilon_0 r}$, with ϵ_0 the permittivity of vacuum. The mass of the system is strictly speaking μ, the reduced mass, but for simplicity, $\mu \approx m_e \equiv m$. In order to solve $H\Phi = E\Phi$, we assume that $\Phi(r, \theta, \phi)$ can be decomposed in radial and angular functions, $\rho(r)$ and $\psi(\theta, \phi)$, respectively. Replacing these expressions in the (spherical) Schrödinger equation,

$$\Phi(r, \theta, \phi) = \rho(r)\psi(\theta, \phi)$$

$$\rightarrow \frac{\hbar^2}{2m} + \left(\left[-\frac{1}{r^2}\frac{\partial}{\partial r} r^2 \frac{\partial \rho(r)}{\partial r} \right] \psi(\theta, \phi) + \left[\frac{\rho(r)}{\hbar^2 r^2} \right] \underbrace{L^2 \psi(\theta, \phi)}_{\hbar^2 l(l+1)\psi(\theta,\phi)} \right) - \left(\frac{e^2}{4\pi\epsilon_0 r} - E \right) \Phi = 0$$

$$\rightarrow \left[\frac{\hbar^2}{2m} \left(-\frac{1}{r^2}\frac{\partial}{\partial r} r^2 \frac{\partial}{\partial r} + \frac{l(l+1)}{r^2} \right) - \frac{e^2}{4\pi\epsilon_0 r} - E \right] \rho(r) = 0$$

we end up with the Sturm-Liouville equation for $\rho(r)$, whose solutions are well-studied mathematically. Given appropriate boundary conditions, the energy E can only take discrete values: $E = \frac{-13.6\text{eV}}{n^2}$, for $n > 1$ and $l = 0 \ldots n-1$.

2.1.4 Spin Angular Momentum

Finally, the basic notions of quantum mechanics end up with the introduction of an entirely pure quantum mechanical angular momentum called spin. The definition of the Hermitian operators $\mathbf{S} = (S_x, S_y, S_z)$ satisfy the commutation laws of operator $\hat{L}$. By S_z and S^2 as operators in the new basis $|s.m_s\rangle$, the corresponding eigenvalues are defined as

$$S^2|s, m_s\rangle = m_s\hbar|s, m_s\rangle \tag{2.16}$$

$$S_z|s, m_s\rangle = s(s+1)\hbar^2|s, m_s\rangle \tag{2.17}$$

where $m_s = \{-s, -s+1, \ldots, s-1, s\}$. Elemental particles such as electrons and protons have half-integer spin numbers ($s = \frac{1}{2}$), so they are classified as fermions and must obey the Pauli exclusion principle, while photons, whose spin number is integer ($s = 1$), are bosons.

2.2 Time-dependent perturbations

After setting up the basic formulation, we move on to the second goal of this chapter: finding how transitions occur between levels in order to understand the so-called **forbidden transitions**. To do this, we skip all the canonical examples of time-independent Hamiltonians and degenerate perturbation of states[8], but it is necessary to state that LS coupling, i.e. spin-orbit interaction ($\propto L \cdot S$) contribution to the Hamiltonian is treated as a perturbation, is going to be assumed from now. This means, basically, that $\hat{L}^2$ and $\hat{S}^2$ operators commutes with H, which implies that the **total angular momentum $\hat{\boldsymbol{J}}^{\mathbf{2}}$** and its projection in, e.g., $z-$axis $\hat{\boldsymbol{J}}_{\boldsymbol{z}}$ are also good operators, defined as[9]

$$\hat{J} \equiv \hat{L} + \hat{S} \tag{2.18}$$

$$\rightarrow \hat{J}^2|j, m_j\rangle = j(j+1)\hbar^2|j, m_j\rangle$$

$$\rightarrow \hat{J}_z|j, m_j\rangle = m_j\hbar|j, m_j\rangle. \tag{2.19}$$

Following the time-dependent perturbation theory, a small time-dependent perturbation (H_1) is added to the classical time-independent quantum Hamiltonian (H_0) that satisfies $H_0|i\rangle = E_i|i\rangle$,

$$H = H_0 + H_1(t).$$

For $H(t) = H$, the time operator 2.6 yields to

$$T(t, t_0) = \exp\left\{-\frac{\mathrm{i}H(t-t_0)}{\hbar}\right\}. \tag{2.20}$$

In the absence of perturbation, the time evolution of a general ket $|A\rangle$ (Equation

[8]When two states or more have the same energy, it is required a perturbation H_1 to lift the degeneracy through the generation of new eigenstates. This is seen in the Stark effect, Zeeman effect, among others.

[9]The correspondence between any state $|l, s, m_l, m_s\rangle$ with its $|l, s, j, m_j\rangle$ counterpart is given by the Clebsch-Gordon coefficients.

2.1), from $t = t_0$, and the probability $P_f(t)$ to "jump" to the state $|f\rangle$ are written as

$$
\begin{aligned}
&|A, t_0, t\rangle = \sum_i c_i T(t, t_0)|i\rangle \qquad (2.21)\\
&P_f(t) \equiv |\langle f|A, t, t_0\rangle|^2\\
&\rightarrow = \left| \sum_i c_i \exp\left\{ -\frac{\mathrm{i}E_i(t-t_0)}{\hbar} \right\} \underbrace{\langle f|i\rangle}_{\delta_{fi}} \right|^2\\
&\rightarrow = |c_f|^2\\
&\Rightarrow P_f(t) = P_f(t_0)
\end{aligned}
$$

meaning that P_f does not change over time. In the case of a time-dependent Hamiltonian, the coefficients c_i on Equation 2.21 vary with time

$$
|A, t_0, t\rangle = \sum_i c_i(t) \exp\left\{ -\frac{\mathrm{i}E_i(t-t_0)}{\hbar} \right\} |i\rangle. \qquad (2.22)
$$

Using the time-dependent Schrödinger equation (Equation 2.7) with $H = H_0 + H_1$ and equating **RHS = LHS**

$$
\begin{aligned}
&\textbf{RHS: } \langle f|(H_0 + H_1)|A, t_0, t\rangle = \langle f| \sum_i c_i(t) \exp\left\{ -\frac{E_i(t-t_0)}{\hbar} \right\} (E_i + H_1)|i\rangle\\
&\rightarrow = \underbrace{\sum_i c_i(t) \exp\left\{ -\frac{E_i(t-t_0)}{\hbar} \right\} \left(E_i \overbrace{\langle f|i\rangle}^{\delta_{fi}} + \langle f|H_1|i\rangle \right)}_{c_f(t) E_f \exp\left\{ \frac{-\mathrm{i}E_f(t-t_0)}{\hbar} \right\}}\\
&\textbf{LHS: } \langle f|\mathrm{i}\hbar\frac{\partial}{\partial t}\left(|A, t_0, t\rangle \right) = \sum_i \left[\mathrm{i}\hbar\frac{dc_i(t)}{dt} + c_i(t)E_i \right] \exp\left\{ -\frac{\mathrm{i}E_i(t-t_0)}{\hbar} \right\} \overbrace{\langle f|i\rangle}^{\delta_{fi}}\\
&\qquad\qquad \rightarrow = \left(\mathrm{i}\hbar\frac{dc_f(t)}{dt} + c_f(t)E_f \right) \exp\left\{ -\frac{\mathrm{i}E_f(t-t_0)}{\hbar} \right\}\\
&\Rightarrow \mathrm{i}\hbar\frac{dc_f(t)}{dt} = \sum_i H_{fi}(t) \exp\{\mathrm{i}\omega_{fi}(t-t_0)\} c_i(t) \qquad (2.23)
\end{aligned}
$$

with

$$H_{fi} = \langle f|H_1(t)|i\rangle \tag{2.24}$$

$$\omega_{fi} = \frac{E_f - E_i}{\hbar}. \tag{2.25}$$

Now it is clear that the transition probability between initial state i and final state f will change satisfying the equation for the time-varying coefficients $c_f(t)$.

2.2.1 Dyson Series

Retaking the analysis from Equation 2.22, what it is needed now is a solution to Equation 2.23. The simpler way to do this is defining a "new" time evolution operator of the form

$$T(t_0, t) = \exp\left\{\frac{-\mathrm{i}H_0(t - t_0)}{\hbar}\right\} T_I(t_0, t) \tag{2.26}$$

subject to condition $T(t_0, t_0) = 1$. Replacing in Equation 2.5 for $H = H_0 + H_1$, it is easy to see that $T_I(t, t_0)$ satisfies

$$\mathrm{i}\hbar\frac{\partial T_I(t_0, t)}{\partial t} = H_I(t_0, t)T_I(t_0, t) \tag{2.27}$$

with $H_I(t_0, t) = \exp\left\{\frac{\mathrm{i}H_0(t-t_0)}{\hbar}\right\} H_1 \exp\left\{\frac{-\mathrm{i}H_0(t-t_0)}{\hbar}\right\}$. H_I contains all the information about the transitions. If a system is defined by $|i\rangle$ at t_0 and jumps to state $|f\rangle$ at time t, then $c_f(t)$ and the probability $P_{i\to f} = |c_f(t)|^2$ can be written in terms of $T_I(t_0, t)$

$$\begin{cases} 2.22 & \to \langle f|i, t_0, t\rangle = c_f(t)\exp\cancel{\left\{\frac{-\mathrm{i}E_f(t-t_0)}{\hbar}\right\}} \\ 2.4 & \to \langle f|i, t_0, t\rangle = \cancel{\exp\left\{\frac{-\mathrm{i}E_f(t-t_0)}{\hbar}\right\}}\langle f|T_I(t_0, t)|i\rangle \end{cases} \tag{2.28}$$

$$\Rightarrow c_f(t) = \langle f|T_I(t_0, t)|i\rangle \tag{2.29}$$

$$\Rightarrow P_{i\to f}(t_0, t) = |\langle f|T_I(t_0, t)|i\rangle|^2 \tag{2.30}$$

In order to derive an explicit expression for Equations 2.29 and 2.30, operator $T_I(t_0, t)$ must be found. The approximated solution to this problem is expressed

with the Dyson series:

$$T_I(t_0,t) \simeq 1 + \left(\frac{-\mathrm{i}}{\hbar}\right)\int_{t_0}^{t} dt^{'} H_I(t_0,t^{'}) + \left(\frac{-\mathrm{i}}{\hbar}\right)^2 \int_{t_0}^{t} dt^{'} \int_{t_0}^{t^{'}} dt^{''} H_I(t_0,t^{'}) H_I(t_0,t^{''}) \ldots \tag{2.31}$$

If $c_f(t) = {c_f}^{(0)} + {c_f}^{(1)} + {c_f}^{(2)} \ldots$, then using Equations 2.24 and 2.25 for the first two coefficients, the probability is finally set up.

$$\begin{cases} {c_f}^{(0)} & = \delta_{if} \\ {c_f}^{(1)} & = \left(\frac{-\mathrm{i}}{\hbar}\right) \int_{t_0}^{t} dt' \exp\left\{\mathrm{i}\omega_{fi}\right\} H_{fi}(t') \\ & \vdots \end{cases} \tag{2.32}$$

$$\Rightarrow P_{i\to f}(t_0,t) = \left|{c_f}^{(0)} + {c_f}^{(1)} + {c_f}^{(2)} + \ldots\right|^2 \tag{2.33}$$

The next step is to figure out the transition rate given the initial and final states using the obtained probability of the transition.

2.2.2 Fermi's Golden Rule

What Fermi's golden rule tells is the exact transition rate among different states. The definition of transition rate is written as

$$w_{i\to[f]}(t) = \frac{dP_{i\to[f]}(t)}{dt} \tag{2.34}$$

In order to derive the rule, let us assume a sudden perturbation to H_0 of the form $H_1(t \geq t_0) = H_1$. Let H_1 be independent of time for simplicity[10]. In order to get $P_{i\to f}(t)$, we calculate the coefficients in 2.32 using the definitions from Equations 2.24 and 2.25, only taking ${c_f}^{(1)}(t)$ coefficient[11]. Therefore, the probability is written as $P_{i\to f}(t) = |{c_f}^{(1)}(t)|^2$ and

[10] Not necessary.

[11] Because $\delta_{fi} = 0$, meaning that in absence of a perturbation, we cannot have any transition $|i\rangle \to |f\rangle$.

$$
\begin{aligned}
{c_f}^{(1)}(t) &= \frac{H_{fi}}{E_f - E_i}\left[1 - \exp\left(\mathrm{i}\omega_{fi}t\right)\right] \\
P_{i\to[f]} &= \frac{4\left|H_{fi}\right|^2}{\left|E_f - E_i\right|^2}\sin^2\left\{\frac{(E_f - E_i)}{2\hbar}\right\}
\end{aligned}
\tag{2.35}
$$

The focus will be put in transitions that conserve energy, so $E_f = E_i$. One big caution is needed to notice: the transition from state $|i\rangle$ is over a density of states $\rho(E_f)$ because there is a group of (final) states that have nearly the same energy as E_i. To account for this, the total probability over this group of states is defined as

$$
P_{i\to[f]}(t) = \int_{-\infty}^{\infty} dE_f P_{i\to f}(t)\rho(E_f) \tag{2.36}
$$

Replacing 2.35 into the last equation and noticing that $P_{i\to t}$ is only non-zero at $E_f \approx E_i$, $\rho(E_f)$ and $|H_{fi}|^2$ are nearly constant, so by defining $\overline{|H_{fi}|^2}$ as the average over that range of energies, we have the real probability and thus the transition rate 2.34:

$$
P_{i\to[f]}(t) = \frac{2\pi}{\hbar}\overline{|H_{fi}|^2}\rho(E_f)t\Big|_{E_f\approx E_i} \tag{2.37}
$$

$$
\Rightarrow w_{i\to[f]} = \frac{2\pi}{\hbar}\overline{|H_{fi}|^2}\rho(E_f)\Big|_{E_f\approx E_i} \tag{2.38}
$$

$$
\equiv \frac{2\pi}{\hbar}\overline{|H_{fi}|^2}\delta(E_f - E_i) \tag{2.39}
$$

Equation 2.39 is better known as the Fermi's Golden Rule[12]. Applying the rule to a Hamiltonian $H_1(t)$ corresponding to **harmonic perturbations**,

$$
H_1(t) = V\exp(\mathrm{i}\omega t) + V^\dagger\exp(-\mathrm{i}\omega t) \tag{2.40}
$$

[12]Never forget that it should be thought as the integrand of $\int dE\ldots\rho(E)$, which gives the real transition rate.

the calculations of the coefficient ${c_f}^{(1)}(t)$ in Equation 2.32 follows as

$$ {c_f}^{(1)}(t) = \frac{1}{\hbar}\left(\frac{1-\exp\{i(\omega_{fi}+\omega)t\}}{\omega_{fi}+\omega}V_{fi} + \frac{1-\exp\{i(\omega_{fi}-\omega)t\}}{\omega_{fi}-\omega}{V_{fi}}^{\dagger}\right) \tag{2.41} $$

where $V_{fi} = \langle f|V|i\rangle$ and ${V_{fi}}^{\dagger} = \langle f|V^{\dagger}|i\rangle$. Looking at the exponentials, there are two distinct cases where $P(t) = \left|{c_f}^{(1)}(t)\right|^2$ does not vanish at $t \to \infty$:

$$ \omega_{fi} + \omega \simeq 0 \quad \text{or} \quad E_f \simeq E_i - \hbar\omega \tag{2.42} $$

$$ \omega_{fi} - \omega \simeq 0 \quad \text{or} \quad E_f \simeq E_i + \hbar\omega \tag{2.43} $$

Clearly, in case 2.42, E_f is going to be $\hbar\omega$ energy-wise lower than E_i, so energy is lost from the system to the perturbing field. In the second case 2.43, the opposite happens: the system gains energy. The former case is usually known as **stimulated emission** and the latter **absorption**. Their corresponding transition rates are written using Fermi's golden rule as

$$ w^{\text{stm}}_{i\to f} = \frac{2\pi}{\hbar}\left|V_{fi}\right|^2 \delta(E_f - E_i + \hbar\omega) \tag{2.44} $$

$$ w^{\text{abs}}_{i\to f} = \frac{2\pi}{\hbar}\left|{V_{fi}}^{\dagger}\right|^2 \delta(E_f - E_i + \hbar\omega) \tag{2.45} $$

The last derivation has led to the so-called Einstein coefficients.

2.2.3 Interaction e-EM Wave

From now and go on, it is a necessity to think in terms of **Local Thermodynamic Equilibrium (LTE)**: from Collins (1989) Chapter 1, LTE is defined as the (statistical) equilibrium of particles such as free electrons, following the Maxwell-Boltzmann statistics (or Fermi-Dirac in case of degeneracy) and photons, following the Planck distribution[13], both described by a single temperature T, as long the mean free path of the particles that transport heat (e.g. photons and electrons) is much smaller than the lenght scale over T changes.

[13] Although LTE admits departures from this distribution.

One of the most important principle in these thermodynamical systems is called **detailed balance**: all microscopic process must be balance by its inverse (Osterbrock & Ferland, 2006). Applied to this context, it means that **every absorption of a photon must be balanced by an emission**. From the last subsection, stimulated emission and absorption must be naturally considered by this principle given the interaction of the system with certain (external) perturbation. But this is not the whole story: in quantum mechanics, there is a non-zero probability that an electron "jumps" from a higher energy level E_i to a lower energy level by E_f by emiting a photon without an external driver, the so-called **spontaneous emission**.

Incorporating this emission to the detailed balance equation for the transition, the problem simplifies to find an explicit form of the absorption and emission coefficients using the Hamiltonian of the interaction between an electromagnetic (EM) wave and an electron. Classically, H is written in terms of the vector, $\vec{A}(\boldsymbol{x})$, and scalar, $\phi(\boldsymbol{x})$ potential, using the Coulomb potential $\nabla \cdot \vec{A} = 0$:

$$H = \frac{(\hat{p} + e\vec{A})^2}{2m_e} - e\phi + \underbrace{\Phi(x)}_{\boldsymbol{x}\to r} \tag{2.46}$$

$$\Rightarrow H = \underbrace{\frac{p^2}{2m_e} + \Phi(r)}_{H_0} + \underbrace{\frac{\vec{A}\cdot\hat{p}}{m_e} + \cancel{\frac{e^2A^2}{2m_e}} - e\phi}_{H_1} \tag{2.47}$$

with $\Phi(r)$ a central potential. The EM-e interaction is contained in the term $\propto A \cdot p$ while discarding $\propto A^2$ term. The simplest solution of the wave equation, a plane-wave of angular frequency ω, polarization direction $\vec{\epsilon}$, direction of propagation $\vec{n}$ (hence $\vec{\epsilon}\cdot\vec{n} = 0$) and c the speed of light,

$$\phi = 0 \tag{2.48}$$

$$\vec{A}(\boldsymbol{x}, t) = 2A_0 \cos\left\{\left(\frac{\omega}{c}\right)\vec{n}\cdot\boldsymbol{x} - \omega t\right\}\vec{\epsilon} \tag{2.49}$$

is a good example of incident radiation. Replacing the last equation into the time-dependent Hamiltonian in Equation 2.46 leads to

$$H_1 = \frac{eA_0}{m_e}\left[\exp\left\{\mathrm{i}\left(\frac{\omega}{c}\right)\vec{n}\cdot\boldsymbol{x} - i\omega t\right\} + \exp\left\{-\mathrm{i}\left(\frac{\omega}{c}\right)\vec{n}\cdot\boldsymbol{x} - i\omega t\right\}\right]\vec{\epsilon}\cdot\hat{p} \tag{2.50}$$

Looking at the Fermi's gold rule for harmonic oscillations (Equation 2.40), it is clear that if

$$V = \frac{eA_0}{m_e}\exp\left\{-\mathrm{i}\left(\frac{\omega}{c}\right)\vec{n}\cdot\boldsymbol{x}\right\}\vec{\epsilon}\cdot\hat{p} \tag{2.51}$$

the absorption and stimulated emission transition rates are obtained via Equations 2.44 and 2.45. To do this, first define $\mathbf{d_{fi}}$, which can be thought as the multipole moment of the transition, as

$$\mathbf{d_{fi}} = \frac{-\mathrm{i}}{m_e\omega_{if}}\left\langle i\middle|\exp\left\{\mathrm{i}\left(\frac{\omega}{c}\right)\vec{n}\cdot\boldsymbol{x}\right\}\hat{p}\middle|f\right\rangle \tag{2.52}$$

$$\vec{\epsilon}\cdot\mathbf{d_{fi}} = \frac{-\mathrm{i}}{eA_0\omega_{if}}\langle i|V^\dagger|f\rangle \tag{2.53}$$

and replacing these expressions in Equations 2.44 and 2.45

$$w_{i\to f}^{\mathrm{abs}} = 2\pi\frac{e^2{\omega_{fi}}^2}{\hbar^2}|A_0|^2|\vec{\epsilon}\cdot\mathbf{d_{fi}}|^2\delta(\omega-\omega_{fi}) \tag{2.54}$$

$$w_{i\to f}^{\mathrm{stm}} = 2\pi\frac{e^2{\omega_{if}}^2}{\hbar^2}|A_0|^2|\vec{\epsilon}\cdot\mathbf{d_{if}}|^2\delta(\omega-\omega_{if}) \tag{2.55}$$

In this form, the transition rates certainly do not resemble to B_{21} ($w_{i\to f}^{\mathrm{stm}}$) and B_{12} Einstein coefficients. Applying the relation of $\vec{A}$ and $\vec{E}$ into the definition of the energy density per ω, $u(\omega)$, the rates can be written as a function of $u(\omega)$

$$w_{i\to f}^{\mathrm{abs}} = 4\pi^2\alpha\frac{c}{\hbar}u(\omega_{fi})|\vec{\epsilon}\cdot\mathbf{d_{fi}}|^2 \tag{2.56}$$

$$w_{i\to f}^{\mathrm{stm}} = 4\pi^2\alpha\frac{c}{\hbar}u(\omega_{if})|\vec{\epsilon}\cdot\mathbf{d_{if}}|^2 \tag{2.57}$$

with α the so-called fine structure constant. The spontaneous emission (A_{21}) is easily found by invoking LTE: using the Planck law for $u(\omega)$ and the Boltzmann

distribution[14] for the ratio of the ocuppation levels, detailed balance equation leads to

$$w^{\text{abs}}_{i\to f} = w^{\text{stm}}_{i\to f} \qquad \text{and} \qquad w^{\text{spn}}_{i\to f} = \frac{\hbar\omega^3}{\pi^2 c^3} w^{\text{abs}}_{i\to f} \tag{2.58}$$

Typically, the spontaneous emission is integrated over all polarizations, which leads to[15]

$$\left\langle |\vec{\epsilon}\cdot \mathbf{d_{if}}| \right\rangle = \frac{|\mathrm{d}_{if}|^2}{3} \equiv \frac{\mathbf{d^*_{if}}\cdot \mathbf{d_{if}}}{3}$$

It is worth noticing that the quantity usually called as **lifetime** of the state $|i\rangle$, Γ_i , is defined as

$$\Gamma_i \equiv \frac{1}{\sum\limits_f w^{\text{spn}}_{i\to f}} \tag{2.59}$$

2.2.4 Electric and Magnetic Multipole transitions

The transitions $i \to f$ and $f \to i$ are induced by radiation with wavelength λ

$$\lambda = \frac{2\pi c}{\omega} \sim 10^3 \text{ Å} \sim 10^{-7} \text{ m}$$

If compared to the typical radius of a hydrogen atom, $\sim 10^{-11}$ m, they differ abour four orders of magnitude. So in principle, the exponential from Equation 2.49 can be approximated by

$$\exp\left\{\mathrm{i}\left(\frac{\omega}{c}\right)\vec{n}\cdot\boldsymbol{x}\right\} = 1 + \mathrm{i}\left(\frac{\omega}{c}\right)\vec{n}\cdot\boldsymbol{x} + \cdots \tag{2.60}$$

By taking the first term of the expression is what we call **electric dipole approximation**. Given that $[\boldsymbol{x}, H_0] = \frac{\mathrm{i}\hbar\hat{p}}{m_e}$ then the dipole matrix elements are obtained

[14] http://assets.cambridge.org/97805218/11194/excerpt/9780521811194_excerpt.pdf
[15] Easy to verify using spherical coordinates and chosing wisely the polarization vector.

by

$$\mathbf{d_{if}} = \langle i|\boldsymbol{x}|f\rangle \tag{2.61}$$

$$\rightarrow \langle i|z|f\rangle \neq 0 \qquad \text{only if} \qquad \Delta l = \pm 1,\ \Delta m = 0 \tag{2.62}$$

$$\rightarrow \langle i|y|f\rangle \neq 0 \qquad \text{only if} \qquad \Delta l = \pm 1,\ \Delta m \pm 1 \tag{2.63}$$

$$\rightarrow \langle i|x|f\rangle \neq 0 \qquad \text{only if} \qquad \Delta l = \pm 1,\ \Delta m \pm 1 \tag{2.64}$$

and

$$\Delta m_s = 0 \tag{2.65}$$

with the latter selection rule due to the independence of the dipole matrix to spin[16]. Written in terms of total angular momentum $j = |l-s| \cdots l+s$ and its corresponding magnetic quantum number, $m_j = -j, -j+1, ..., j-1, j$ (in LS coupling), the electric dipole selection rules are written as

$$\Delta j = 0, \pm 1 \tag{2.66}$$

$$\Delta m_j = 0, \pm 1 \tag{2.67}$$

where transitions to $j = 0 \rightarrow j = 0$ are strictly forbidden due to spherical symmetry.[17] All transitions which are ruled out by electric dipole selection are called forbidden. This does not mean that the transition is not strictly allowed, only the elements of the dipole matrix in Equation 2.61 turn out be zero.

Consider now the second order of the approximation in Equation 2.60, the **magnetic dipole approximation**, the probability of a forbidden line could be non-zero[18] and it is dictated by the interaction of the magnetic moment of the electron and the electromagnetic field (spin-orbit interaction), which ends up being proportional to

$$\mathbf{M_{if}} = \langle i|\boldsymbol{L} + \mathbf{2}\boldsymbol{S}|f\rangle \tag{2.68}$$

[16] Dommelen v5.63α (2018).
[17] In transitions with one photon emission.
[18] Although it takes a lot of more time to happen compared to electric dipole transitions.

where $\mathbf{M_{if}}$ contains the elements of the magnetic dipole matrix. It can be shown that for hydrogen-like atoms, the magnetic dipole transition rules may be found analytically using a good basis (j, m_j, see Zeeman effect in Fitzpatrick, 2015). The corresponding rules are written as

$$\langle i|L_z + 2S_z|f\rangle \neq 0 \rightarrow \Delta l = 0, \Delta m = 0, \Delta m_s = 0 \tag{2.69}$$
$$\langle i|L_y + 2S_y|f\rangle \neq 0 \rightarrow \Delta l = 0, \Delta m = \pm 1, \Delta m_s = \pm 1 \tag{2.70}$$
$$\langle i|L_x + 2S_x|f\rangle \neq 0 \rightarrow \Delta l = 0, \Delta m = \pm 1, \Delta m_s = \pm 1 \tag{2.71}$$
$$\Rightarrow \Delta j = 0, \pm 1 \tag{2.72}$$
$$\Rightarrow \Delta m_j = 0, \pm 1 \tag{2.73}$$

although $j = 0 \rightarrow 0$ is still forbidden. The next element of the expansion is called **electric quadrupole**, usually the last term used to constrain the transitions

$$\Delta l = 0, \pm 2 \tag{2.74}$$
$$\Delta m = 0, \pm 1, \pm 2 \tag{2.75}$$
$$\Delta m_s = 0 \tag{2.76}$$
$$\Rightarrow \Delta j = 0, \pm 1, \pm 2 \tag{2.77}$$
$$\Rightarrow \Delta m_j = 0, \pm 1, \pm 2 \tag{2.78}$$

with $j = 0 \rightarrow 0$, $j = \frac{1}{2} \rightarrow \frac{1}{2}$ or $j = 1 \rightarrow 0$ forbidden. So even if a transition is forbidden electric-wise, it may occur due to magnetic-dipole and electric-quadrupole radiation, therefore, in longer timescales. In fact, magnetic-dipole and electric-quadrupole transition probabilities are smaller by a factor of $\sim 10^{-4}$ and $\sim 10^{-6}$ respectively, in comparison to an allowed electric-dipole transition probability (Osterbrock & Ferland, 2006). In this way it is expected that, within each **electronic configuration** defined by nl quantum numbers, there are going to be multiple states given by the "new" multipole selection rules that were forbidden by the electric-wise rules such as $\Delta l = \pm 1$.

Before introducing the optical line of interest for this thesis, we need to do a caution: all this prelude of quantum physics was done for a single electron, meaning

that it can be applied only to any ion in the H-like sequence, but in principle, not in systems with more than one electron in completely-full orbitals, such as oxygen. For these complex systems, the simplest Hamiltonian must contain at least the electrostatic repulsion between the N-system of electrons. Taking Eissner et al. (1974) as an example, the time-independent Schrödinger equation in the non-relativistic limit is

$$\left[\sum_{i=1}^{N}\left\{-\frac{\hbar^2}{2m}\nabla^2{}_i-\frac{Ze}{r_i}+\sum_{j>i}\frac{e}{r_{ij}}\right\}\right]\Psi=E\Psi \tag{2.79}$$

with Z is the ion electric charge number. In practice, spin-orbit interaction, relativistic corrections, Darwin term, etc, are added to this Hamiltonian.[19] The eigenvalues of the Hamiltonian in Equation 2.79 are the good quantum numbers L, M_L, S, M_S, and with LS coupling, also J and M_J. These quantum numbers are the generalization to N-bodies of the quantum numbers of corresponding operators $\hat{L}$, $\hat{L}_z$, $\hat{S}$, $\hat{S}_z$, $\hat{J}$ and $\hat{J}_z$:

$$\begin{cases}\vec{L}=\sum_i^N\vec{l_i} & \vec{S}=\sum_i^N\vec{s_i}\\ M_L=\sum_i^N m_{li} & M_S=\sum_i^N m_{si}\end{cases}\Rightarrow\left\{\vec{J}=\vec{L}+\vec{S}\qquad M_J=\{J,J-1,\cdots,-J+1,-J\}\right. \tag{2.80}$$

An usual way to treat the states for multielectron systems is using the **spectroscopic notation**[20]:

$$n^{2S+1}L_J$$

with n is the principal quantum number and often omitted, S total spin quantum number, L is the total orbital angular momentum quantum number written as **S**, P, D, F, ... for $L=0,1,2,...$ and J is the total angular momentum quantum number,

[19] As it is now, the energy levels are no longer degenerate on l due to the breaking down of the (central) Coulomb potential.

[20] Brenson, Quantum Physics lecture notes, 2013.

all defined as vector sum in Equation 2.80. For each electron configuration nl, a term is defined as ${}^{2S+1}L$, a level as ${}^{2S+1}L_J$ and states are described with L, S, J, M_J quantum numbers.

Chapter 3

[O III]λ5007 Å forbidden line

This thesis revolves around measurements of [O III]λ5007Å surface brightness, flux and/or luminosity, in order to constrain physical conditions of the medium in which the sources are embeeded, i.e. a nebula. This line is created when an electron "jumps"[1] from $(1s^2 2s^2 2p^2)^1 D_2 \rightarrow {}^3P_2$ due to collision of thermal electrons and a double ionized oxygen (see Figure 3.1).

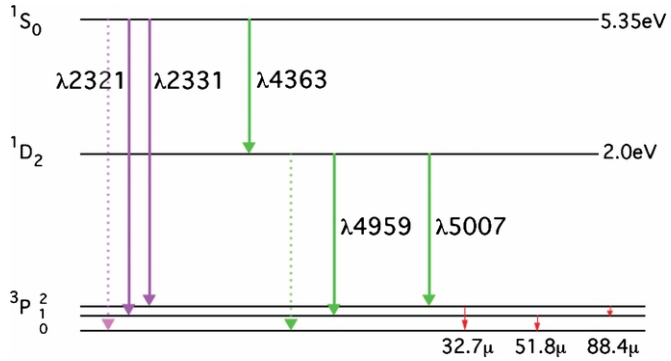

Figure 3.1: Grotrian diagram for double ionized oxygen, O III. This thesis is focused on [O III]λ5007 transition; an excited-level ($^1D_2$) electron jumps to a lower energy ($^3P_2$) level, in this case, the higher energy-wise level of the the ground state triplet (defined by the Hund's rules Osterbrock & Ferland, 2006). Originally from Nicholls et al. (2012).

It is necessary to explain in more detail the last statement: photoelectrons "created" by the strong radiation of a supersoft X-rays source tends to thermalize (follow a Maxwell-Boltzmann velocity distribution) quickly, with typical nebular temperatures of $\sim 10^4$ K (Osterbrock & Ferland, 2006). Whenever one of these electrons (of kinetic energy of order $\sim$ 1 eV) collisions with an ion, it "replaces" a low-energy

[1]Not strictly true, the electronic configuration, nl, does not change.

bounded electron (in this case, a $^3P_2$ ground state electron which becomes unbounded) but in an excited state ($^1D_2$), while the kinetic energy of the unbounded electron is lower than the incident one. This transitional mechanism is called **electron exchange**:

$$O^{+2}(2p^2\ ^3P) + kp \rightarrow O^{+2}(2p^2\ ^1D_2) + k^{'}p \tag{3.1}$$

with k, $k^{'}$ the kinetic energies of the unbounded electrons pre and post collision. By the selection rule for electric dipole radiation, the "jumping" electron must change its angular momentum $\Delta l = \pm 1$, which can be thought as a consequence of conservation of angular momentum if the emitted photon carries one unit of angular momentum ($l = 1$). [O III] λ5007Å transition line clearly does not satisfy this rule and also does not satisfy the spin-rule $\Delta S = 0$[2]. Now, considering the magnetic dipole selection rules $\Delta l = 0$ and $\Delta S = 1$, this forbidden transition is allowed, so the spin-orbit term has a big impact on the Hamiltonian.

For nebular forbidden lines, the density of electrons (n_e) in the medium plays an important role: if n_e is too large, the probability of -collisionally- deexcitating the ion, $^1D_2 \rightarrow {}^3P$ is high, therefore no collisional line is observed. This translates into a critical density that separates the observational availability of this line. By detailed balance, for a given level i, the transition rate between this population and others levels of a specific ion, including radiative and collisional excitation/deexcitation transitions is expressed as

$$\sum_{j \neq i} n_j n_e q_{ji} + \sum_{i>i} n_j A_{ji} = \sum_{j \neq i} n_i n_e q_{ij} + \sum_{j<i} n_i A_{ij} \tag{3.2}$$

with

$$\sum_j n_j = n$$

(Wei, 1988), where n_e is the electron density (all densities in cm^{-3}), n the total density of the ion, n_i the density of ions with an electron on level i, $n_e n q_{ji}$ is the rate of collisional excitation ($j < i$) or deexcitation ($j > i$) and $A_{ji} (j > i)$ is the spontaneous transition probability from level j to i (in s^{-1}) (Luridiana et al., 2015).

[2]Often called **parity**, $P = (-1)^{\sum l_i}$. In an allowed electric-dipole transition, parity must change.

The collisional excitation/deexcitation rates are usually written as

$$q_{ji} = \frac{8.629 \times 10^{-6}}{g_j} \frac{\Upsilon(T_e)_{ij}}{{T_e}^{1/2}} [\mathrm{cm}^{-3}\mathrm{s}^{-1}] \tag{3.3}$$

and

$$q_{ij} = \frac{g_j}{g_i} q_{ji} \exp\left(\frac{\Delta E_{ij}}{k_B T_e}\right) \tag{3.4}$$

where $j > i$, g_i and g_j are the statistical weights of levels i and j, respectively, ΔE_{ij} the energy difference between level j and i, k_B the Boltzmann constant, T_e the electron temperature and $\Upsilon(T_e)$ is the velocity-averaged collision strength, which is a function of T_e through the collision cross section $\Omega(E_{ij})$ using **Maxwell-Boltzmann velocity distribution** (MB) (Osterbrock & Ferland, 2006),

$$\Upsilon_{ij}(T_e) = \int_0^\infty \Omega(E) \exp(-E/k_B T_e) d\left(\frac{E}{k_B T_e}\right). \tag{3.5}$$

The critical density, at $n_e \to 0$, is expressed in terms of Equation 3.2 as

$$n_c(i) = \frac{\sum_{j<i} A_{ij}}{\sum_{j \neq i} q_{ij}} \tag{3.6}$$

If the density of the medium is lower than n_c (at a fixed $T_e \sim 10^4$ K), the (nebular) emitted spectrum is dominated by recombination lines of H (e.g Hα λ6564 Å) and He (e.g He II λ4686 Å), and forbidden lines of ions of abundant metals, such as nitrogen, oxygen and neon. [O III]λ5007 Å is expected in these physical conditions.

In practice, measurements of forbidden lines of [O III] are useful in the determination of the electron temperature of nebulae. First, it is worth noting that the ratio of transition probability A for ${}^1D_2 \to {}^3P_2$ and ${}^1D_2 \to {}^3P_1$ is given by

$$\frac{A({}^1D_2 \to {}^3P_2)}{A({}^1D_2 \to {}^3P_1)} = 3\frac{E({}^1D_2 \to {}^3P_2)}{E({}^1D_2 \to {}^3P_1)} \tag{3.7}$$

with E are the energy differences (Storey & Zeippen, 2000). The latter As ratios are usually ≈ 3 due to the small energy differences between the triplet levels. Using different Schrödinger equation solvers and corrections to the Hamiltonian; for example, Storey & Zeippen (2000) found a value of 3.01 using relativistic corrections to the magnetic dipole operator. So, the contribution of [O III]λ4969Å is overshadowed by [O III]λ5007 Å.

Second, to determine the electron temperature of a low electron density nebula, it is often used the fact that the ratio of the emission-line strenghts j between the singlet $^1S_0$ (e.g., [O III]λ4363Å) and $^1D_2$ levels depends strongly on the energy of both levels, thus the temperature of the medium. An analytical expression up to $n_e \approx 10^5$ cm^{-3} is found in Osterbrock & Ferland (2006)

$$\frac{j_{\lambda 4959} + j_{\lambda 5007}}{j_{\lambda 4363}} = \frac{7.9 \exp(3.29 \times 10^4 / T_e)}{1 + 4.5 \times 10^{-4} n_e {T_e}^{1/2}} \tag{3.8}$$

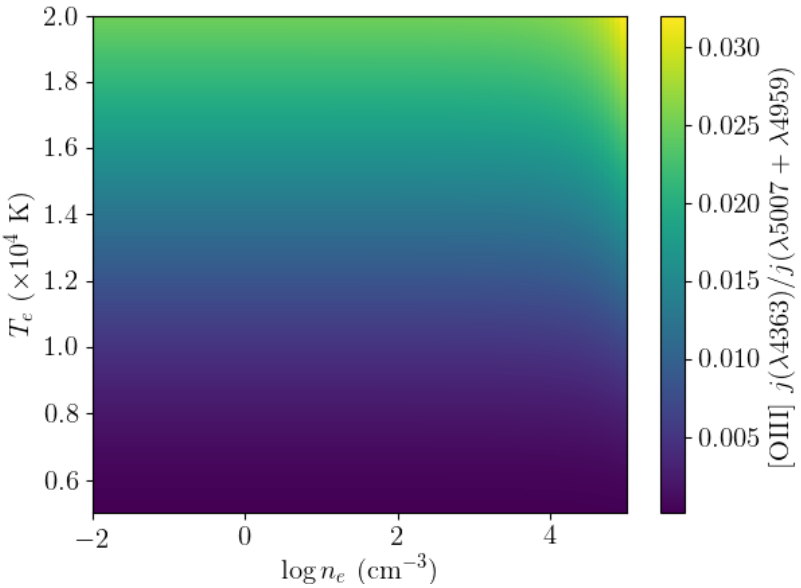

Figure 3.2: Colormap of [O III] volume emissivities ratio defined in Equation 3.8 of electron temperature vs density space. Obtained from PyNeb.

In Figure 3.2, it is clear that the ratio in Equation 3.8 does not depend on electron densities until $n_e = 10^5$ cm^{-3}, so it should be good enough to determine

the temperature in this situation, seemingly. It is wise to know though that using MB distribution for electron velocities has been debated: Nicholls et al. (2012, 2013) generalize this distribution to the so-called κ-distribution that satisfies the relation

$$\frac{q_{ij}(\mathrm{MB})}{q_{ij}(\kappa)} = \frac{\Gamma(\kappa+1)}{(\kappa-\frac{3}{2})^{3/2}\Gamma(\kappa-\frac{1}{2})}\left(1-\frac{3}{2\kappa}\right)\exp\left[\frac{\Delta E_{ij}}{k_B T_U}\right]\left(1+\frac{\Delta E_{ij}}{(\kappa-\frac{3}{2})k_B T_U}\right)^{-\kappa} \tag{3.9}$$

with $\Gamma(x)$ is the Gamma function, κ ranging typically from 2 to 100 (they report $\kappa \sim 20$ for H II regions and planetary nebulae) and T_U the kinetic (electron) temperature, defined as $U = 3k_B T_U/2$. The temperatures obtained by this formula show a considerable discrepance with those obtained by using MB depending on κ value, as we can see in Figure 3.3.

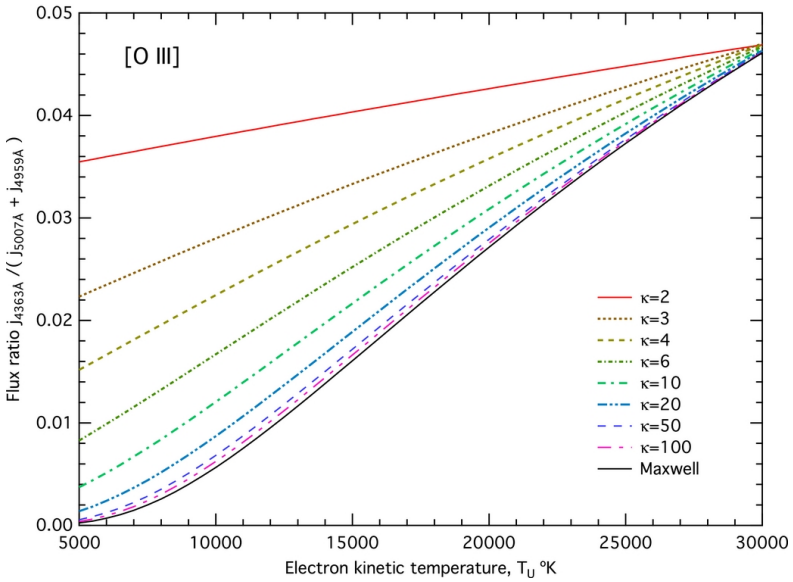

Figure 3.3: Flux ratio of [O III] forbidden lines ratio that usually are used to determine the electron temperature of a nebula. From Equation 3.5, at low values of n_e, it is obtained the curve labeled "Maxwell" while κ curves from Equation 3.9. Originally from Nicholls et al. (2013).

Nicholls et al. (2013) propose a density correction for different ions that determine the temperature, [O III], [S III] and [N II] to avoid these discrepances. Luckily, for the expected densities of the nebula associated to a supersoft X-rays source in LMC (i.e. CAL 83), $n_e \leq 10$ cm^{-3}, the contribution of the density correction can be

neglected as can be seen in Figure 3.4, where the real MB temperature ($T = 10^4$ K) is compared to temperatures obtained using the photoionization code MAPPINGS IV emission ratio in Equation 3.8. Also from the figure, it is evident that [O III] flux ratio is less affected at large densities in comparison with other sulphur and nitrogen forbidden lines.

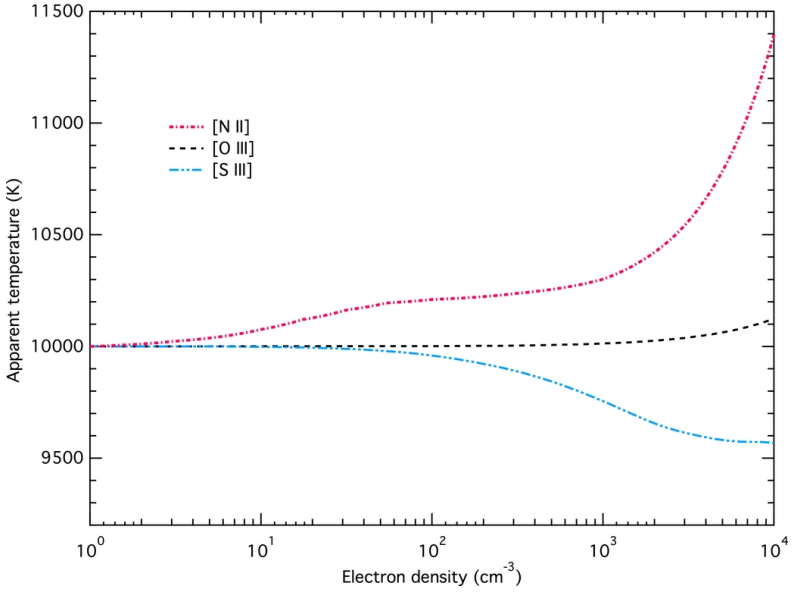

Figure 3.4: At fixed temperature $T = 10000$ K, it is shown the temperature deviations measured by [O III], [S III] and [N II] ions with respect to electron densities. It is clear that at low densities, the deviations are relatively small. Originally from Nicholls et al. (2013).

Retaking the properties of [O III]λ5007Å, a way to visualize the density and temperatures relation for this ion is using PyNeb[3] (Luridiana et al., 2015), a Python-based code that solves the equilibrium equations in a gaseous nebulae, namely Equation 3.2 for the level populations $i = 1..5$ in [O III] case (see Figure 3.1).

Basically, PyNeb calculates the emissivity of a certain level of a fixed ion given the physical conditions of the gas (namely, temperature and density). As a consequence, it may compute the critical density at which the deexcitation of $^1D_2 \rightarrow {}^3P$ becomes important (equation 3.6). Also, PyNeb contains the historical and updated database for collisional strenghts $\Omega(E)$ of [O III][4]. With the values of the collision strengths,

[3]http://www.iac.es/proyecto/PyNeb/

[4]The procedure to obtain Ω is not part of this thesis but at least we inform that it can be found a complete derivation in Brigg (2018), Ph.D Thesis, usually using the R-matrix approximation (Eissner et al., 1974).

and using the Equation 3.5, different papers, e.g Storey et al. (2014) and Palay et al. (2012), have obtained values of Υ in function of the energy/temperature, as seen in Figure 3.5.

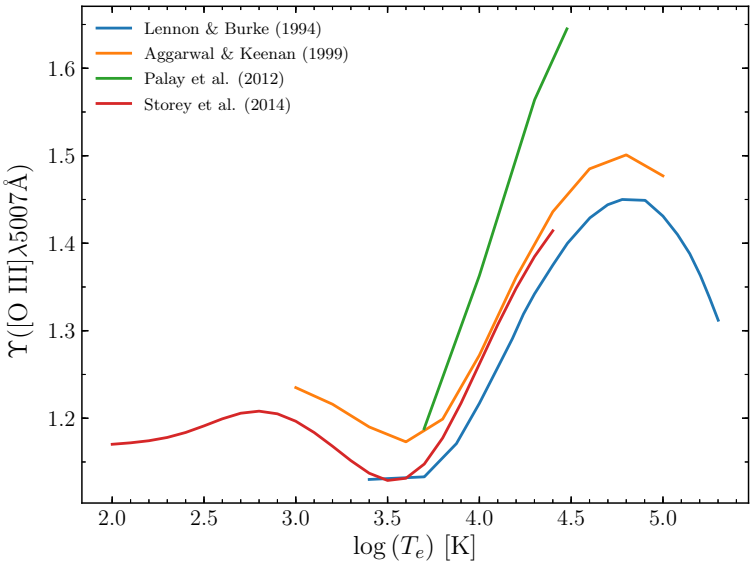

Figure 3.5: Effective collisional strengths Υ as a function of electron temperature for [O III]λ5007Å transition. From the database of PyNeb.

For typical nebular temperatures, $T \approx 10^4$ K, the critical density can be found using Equation 3.6, which leads to Figure 3.6. It is clear that the deexcitation starts to be important for $n_e \approx 10^5$ cm^{-3}, which is about four orders of magnitude larger than the typical values we expect of the density of a supersoft X-rays nebula.

A short and recent review of the physics in gaseous nebulae, specifically for planetary nebulae and H II regions, is given by Peimbert et al. (2017), with caution that the densities are much higher than the ones we expect to find. In this case, we expect densities in the range of $0.1 < n_{\rm H} < 10$ cm^{-3}, contrary to those of planetary nebulae, $n_{\rm H} \sim 10^5$ cm^{-3}, so deexcitations might be important. To model a static nebula, we have to "set up" its temperature T and to do this, it is needed to understand the heating and cooling mechanisms working in the nebula.

The most important heating source is the photoionization of hydrogen. Ionization equilibrium is simply described by the equilibrium between photoionization and recombination (Osterbrock & Ferland, 2006),

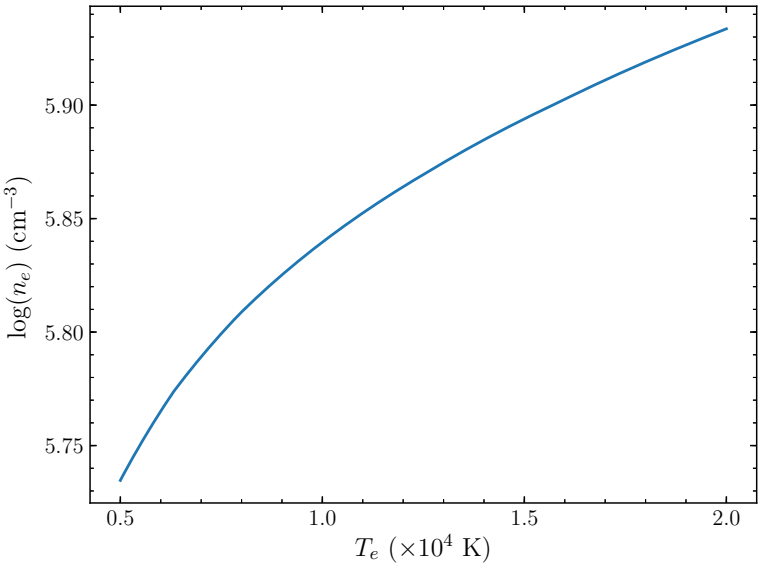

Figure 3.6: PyNeb output for critical density at typical nebular temperatures using Equation 3.6. A_{ij} values are taken from Storey & Zeippen (2000) and q_{ij} from Storey et al. (2014).

$$\underbrace{n_e n_p \alpha_A(\mathrm{H}^0, T_e)}_{\text{Recombination}} = \underbrace{n(\mathrm{H}^0) \int_{\nu_0}^{\infty} \frac{4\pi J_\nu}{h\nu} a_\nu(\mathrm{H}^0) d\nu}_{\text{Photoionization}} \tag{3.10}$$

where n_e, n_p, $n(\mathrm{H}^0)$ are the electron, proton and neutral hydrogen density respectively, $\alpha_A(\mathrm{H}^0, T_e)$ represents the recombination coefficient for H, $h\nu_0$, the energy to ionize H from the ground state (13.6 eV), J_ν the mean intensity of radiation, $a_\nu(\mathrm{H}^0)$ the ionization cross section for incoming photons. In photoionized nebulae, like the ones that are expected to be found in this work, the right term in Equation 3.10 dominates, so there is net heating in the form of many photoelectrons that, once thermalized, will collisionally excite the ions formed by the ionization front, such as O^{+2}.

Qualitatively, we can understand what happens just by looking at the photoionization cross sections of the lightest elements/ions, hydrogen, He and He^+ in Figure 3.7. From what we can see in this figure, the typical behaviour of a cross section

is having peaks at energies corresponding to the ionization potential of the ion of interest. At lower energies, obviously, we do not ionize, while at higher energies the cross section tends to reduce largely. From this crude analysis, we can expect, at least for these simple ions, that high-energetic photons, for example, with energies $E \geq 40$ eV (10^{-16} Hz), are more probable to not being absorbed by any H atom in the nebula.

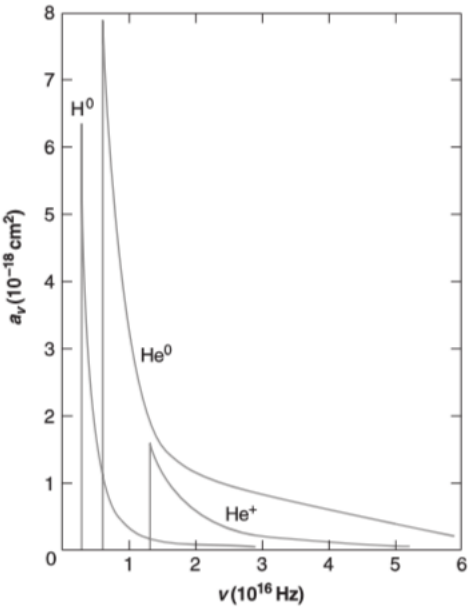

Figure 3.7: Photoionization cross sections of neutral hydrogen, helium and He^+ ion. From Osterbrock & Ferland (2006)

.

For heavier ions[5], the situation is not that simple because resonances are frequent (Covington et al., 2001), enlarging the cross sections as seen in Figure 3.8. Even with this complexity, the same argument should stand in the following sense: if a source can be approximated as a blackbody whose radiation peaks at ~ 50 Å (200 eV), photons with energies higher than the ionization potential of O^+, 35.12 eV (from NIST[6]), are able to travel longer distances than in H II regions or planerary nebulae due to its lower ISM density and low probability of being absorbed.

[5]For a full review on photoionization cross sections for oxygen ions, see Nahar (2004).
[6]https://physics.nist.gov/cgi-bin/ASD/ie.pl

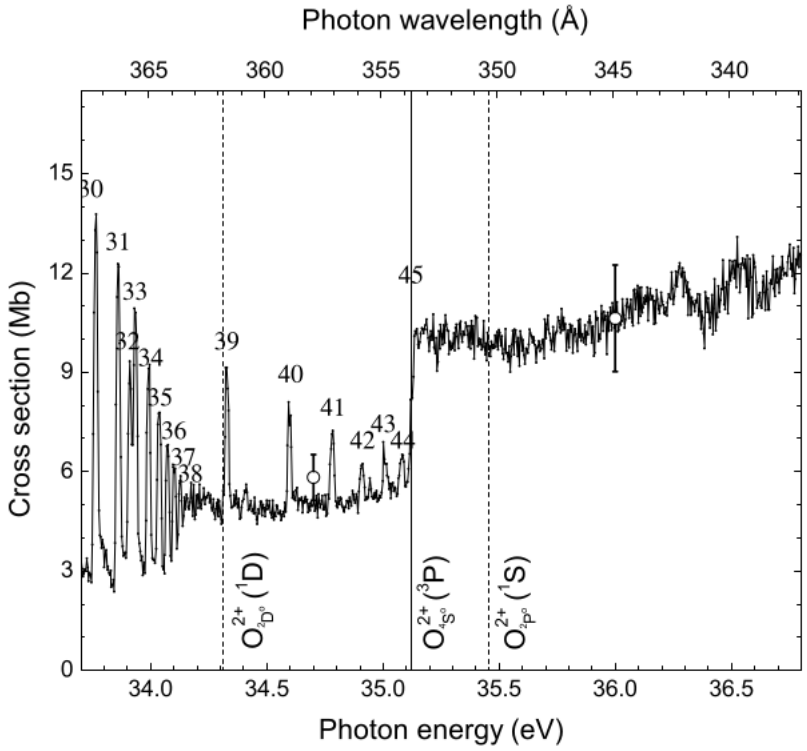

Figure 3.8: Photoionization cross section O^+ for energies in the range. At photon energies of 35.12 eV, we can see a huge break (label 45) which determines the ionization of O^+ from its ground state, $^4S^o$ (o for odd parity), to O^{+2} ground state, ^3P, in units of Mb $\equiv 10^{-18}$ cm^2. From Aguilar et al. (2003).

As already said, the heating of a photoionized nebula comes from photoelectrons, mainly for the ionization of H, which is the most abundant element present in place. Heating ($\Gamma_{\rm ion}$) is balanced by the action of different cooling mechanisms as stated by Osterbrock & Ferland (2006): first, the recombination of H and He (free-bound, Λ_R), ignoring the contribution of the heavier ions[7]. Second, the energy loss by free-free radiation or bremsstrahlung[8], Λ_{ff}, and third and most relevant in this thesis, energy loss from collisionally excited metal ions, Λ_{CE}. This mechanism yields to the emission of forbidden lines. In summary, the thermal equilibrium is reduced to (Peimbert et al., 2017)

[7]Because the luminosity from recombination is proportional to the density of the ion in the nebula, which is negligible in comparison with the lightest elements.

[8]Emission from decelerated -free- electrons by the action of the Coulomb force exerted by the protons of the nucleus.

$$\Gamma_{\rm ion} = \Lambda_{CE} + \Lambda_{ff} + \Lambda_R \tag{3.11}$$

It can be shown that while Γ decreases with temperature, the total cooling rate increases (Osterbrock & Ferland, 2006). This means that there is an equilibrium temperature T that satisfies the Equation 3.11. This is one of the main goals of a photoionization code such as CLOUDY[9] (Ferland et al., 2013): given an incident spectrum, initial gas density and composition, the code calculates the radiative transfer through the gas cloud, meaning that it obtains the ionization state, level populations, cloud spectrum and emitted spectrum at different distances from the source, called zones, by solving the equations of statistical and thermal equilibrium in 1-D (Woods et al., 2017).

3.1 Models from CLOUDY

Spectral synthesis code CLOUDY was used to obtain the volume emissivity $\epsilon(r)$ [**erg cm^{-3} s^{-1}**] of a nebula, with neutral hydrogen density ranging from $-1 \leq \log n \leq 1$, surrounding a blackbody source for a large range of luminosities $36 \leq \log L \leq 38$ and temperatures $2 \leq T \leq 7$ in units of cm^{-3}, erg s^{-1} and 10^5 K, respectively, corresponding to the upper and lower limits used by Woods & Gilfanov (2016). Also, we set up LMC abundances to be half the solar abundances, [Fe/H]~ -0.3 dex (Choudhury et al., 2016), and the geometry of the nebula to a sphere. Sphericity will be very important at the moment of the discussion of the results because there is no spherical symmetry in the (up to now) only known SSS nebula in the LMC, CAL 83 (Remillard et al., 1995). Finally, we used as a code-"stopping" condition the distance where the temperature of the nebula falls below 3000 K, according to the argument expressed by Woods & Gilfanov (2016): at these low nebular temperatures, the ionization fraction of hydrogen is below 10% meaning that the ionization front at that distance from the source is negligible. An example of a typical CLOUDY input script can be seen below.

[9] www.nublado.org

```
title typical input stream
blackbody 5e5 K                                                          #Temperature input linear
luminosity 38                                                            #log Luminosity input
hden 0.0 vary                                                            #Grid log hydrogen density input
grid from -1.0 to 1.0 in 1.0 dex steps
radius 17.0                                                              #Inner radius if geometry is not open
abundances GASS10                                                        #Solar abundances
metals 1.0                                                               #Scale solar abundances to LMC metallicity
sphere                                                                   #Geometry
stop temperature 3e3 K                                                   #Code stopping criteria
save lines, emissivity, "em.dat"                                         #Saving volume emissivity of lines per zone into em.dat
He 2 4686
O 3 5007
end of lines                                                             #Also needed file with lines of interest: "lines.dat"
save linelist, "lum.dat", "lines.dat", absolute, luminosity units erg    #save total lines luminosity into "lum.dat"
save radius "rad.dat"                                                    #Save distance from the source at each zone
save element oxygen "O.dat"                                              #Save neutral and ionic oxygens abundances per zone
save ionization rates oxygen "O_rate.dat"                                #save oxygen ionization rates per zone
```

It is known that in a SSS nebula, [O III] λ5007 Å is expected to be found, but there are more (forbidden and recombination) lines that would be useful to search a SSS nebula. Then, why surveys such as Remillard et al. (1995) are focused on detecting the [O III] λ5007 Å for searching supersoft nebulae? Rappaport et al. (1994), from photoionization models of the expected nebula around supersoft X-rays sources assuming fixed temperature (blackbody emission), luminosity from the source and metallicity, density from the nebula, plotted the integrated luminosity radial profiles for different lines, as we can see in Figure 3.9: [O III]λ5007 is the most prominent. The same can be said by looking at the surface brightness profiles for different lines in Woods & Gilfanov (2016) from CLOUDY models for three hydrogen densities.

A good exercise we can do is to take the two most prominent lines in Woods & Gilfanov (2016) and Rappaport et al. (1994) and try to obtain line behaviours similar to those papers, given that it is not straightforward to do this and it is helpful in the learning curve of the usage of CLOUDY.

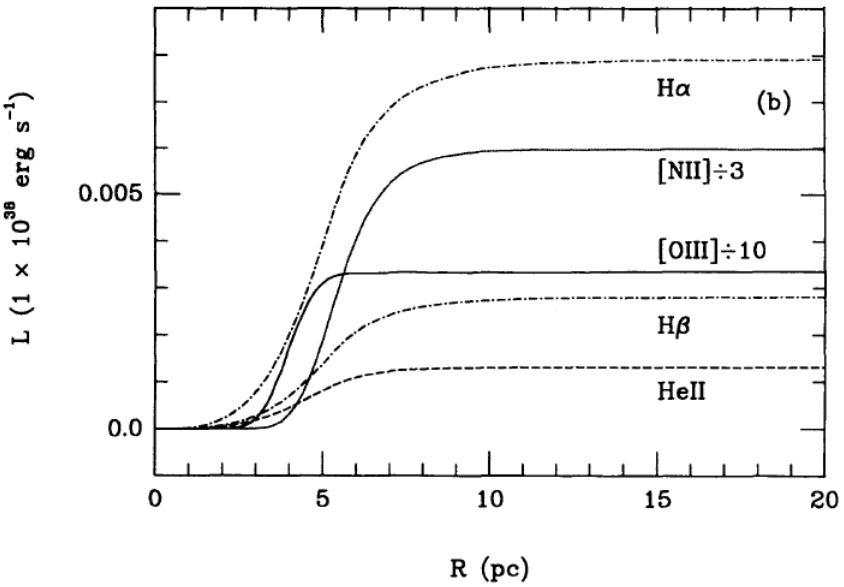

Figure 3.9: Luminosity profiles for different emission lines; [O III]λ5007, Hα, Hβ, [N II]λ6585 and He IIλ4686 in Å, of an ionization nebula surrounding a supersoft X-rays source, using the photoionization code from Rappaport et al. (1994) for a blackbody of $T = 4 \times 10^5$ K, $L = 10^{38}$ erg s^{-1} and $n = 10$ cm^{-3}.

3.2 Radial Profiles

What should we expect from models, at least for the only source we know it contains a nebula, CAL 83? One of the outputs of CLOUDY is the volume emissivity of line i with respect the distance to the source r, $\epsilon_i(r)$. In order to compare the possible results from this thesis with literature, e.g., Remillard et al. (1995), we need to find surface brightness, flux and luminosity profiles for each model. To do this, we integrate $\epsilon_i(r)$ along the line of sight (l.o.s) as we can see in Figure 3.10, leading us to equation A1 from Pellegrini et al. (2012):

$$S_i = \underbrace{\frac{1}{4\pi}\sum_k dl_k(x,y) \times \epsilon_i(x,y,z)}_{4\pi j_\nu = \epsilon_\nu} \times \underbrace{2.3504 \times 10^{-11}}_{\text{strad}^{-1}\rightarrow\text{arcsec}^{-2}} \text{erg s}^{-1}\text{cm}^{-2}\text{arcsec}^{-2} \qquad (3.12)$$

where S_i is the surface brightness in the ith emission line and j_i is basically the emissivity [**erg cm^{-3} s^{-1} strad^{-1}**]. In other words, we created a code that takes **z** axis to be parallel to the l.o.s. As we only implemented the spherical case, it is

evident that at each distance r to the source, the x and y projection onto the **x-y** plane are going to be determined by varying values $z_{\rm min}$ and $z_{\rm max}$ obtained such that x,y are exchangeable due to symmetry. For instance, we fix $l = \sqrt{x^2 + y^2}$ and:

$$z_{\rm min} = r_0$$
$$z_{\rm max} = \sqrt{r_{\rm max}^2 - l^2}$$

then we integrate over all $z \in \{z_{\rm min}, z_{\rm max}\}$ at a fixed $l(x, y)$. A good test of this method is to compare with the total luminosity output from CLOUDY, which are the ones used in Woods & Gilfanov (2016) in their Table 1.

Table 3.1: Derived Luminosity vs CLOUDY

Line [Å]	$n_{\rm H}$ [cm^{-3}]	$T_{\rm source} \times 10^5$ [K]	$\log L_{\rm source}$ [erg s^{-1}]	$L_{\rm CLOUDY}$ $\times 10^{35}$ [erg s^{-1}]	$L_{\rm CLOUDY}/\int_V \epsilon$	$L_{\rm CLOUDY}/L_{\epsilon \to S}$
	0.0	5.0	37.0	0.88	1.01	1.01
	0.0	5.0	37.5	4.40	1.01	1.01
	0.0	5.0	38.0	20.78	1.01	1.00
	-1.0	7.0	38.0	3.76	1.00	1.00
[O III]λ5007	0.0	7.0	38.0	10.13	1.01	1.01
	1.0	7.0	38.0	22.16	1.02	1.02
	0.0	4.0	37.5	6.75	1.01	1.01
	0.0	5.0	37.5	4.40	1.01	1.01
	0.0	6.0	37.5	2.92	1.01	1.01
	0.0	5.0	37.0	0.13	1.01	1.01
	0.0	5.0	37.5	0.48	1.01	1.01
	0.0	5.0	38.0	1.73	1.00	1.00
	-1.0	7.0	38.0	0.71	1.00	1.00
He IIλ4686	0.0	7.0	38.0	1.00	1.00	1.00
	1.0	7.0	38.0	1.32	1.02	1.02
	0.0	4.0	37.5	0.66	1.01	1.01
	0.0	5.0	37.5	0.48	1.01	1.01
	0.0	6.0	37.5	0.36	1.01	1.01
	0.0	5.0	37.0	0.70	1.01	1.01
	0.0	5.0	37.5	2.39	1.00	1.00
	0.0	5.0	38.0	7.95	1.00	1.00
	-1.0	7.0	38.0	5.11	1.00	1.00
O Iλ6300	0.0	7.0	38.0	7.08	1.00	1.00
	1.0	7.0	38.0	8.79	1.01	1.01
	0.0	4.0	37.5	2.47	1.00	1.00
	0.0	5.0	37.5	2.39	1.00	1.00
	0.0	6.0	37.5	2.18	1.00	1.00
	0.0	5.0	37.0	0.79	1.01	1.01
	0.0	5.0	37.5	2.79	1.01	1.01
	0.0	5.0	38.0	9.60	1.01	1.01
	-1.0	7.0	38.0	5.06	1.00	1.00
Hα	0.0	7.0	38.0	6.83	1.01	1.01
	1.0	7.0	38.0	8.61	1.02	1.02
	0.0	4.0	37.5	3.47	1.01	1.01
	0.0	5.0	37.5	2.79	1.01	1.01
	0.0	6.0	37.5	2.27	1.01	1.01

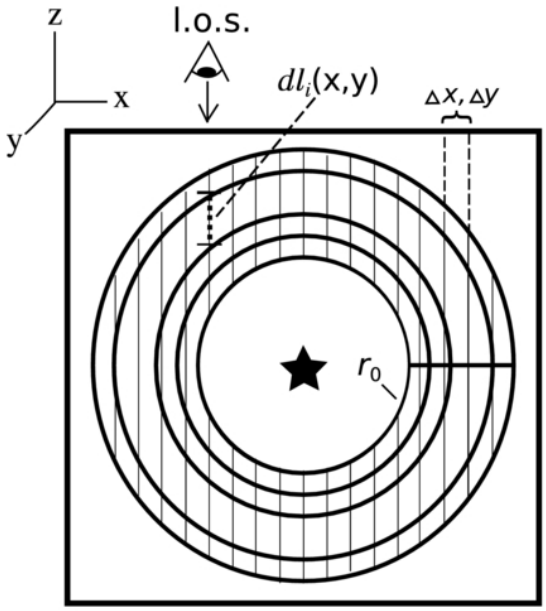

Figure 3.10: Scheme to perform the integration of the emissivity integration over l.o.s axis in order to obtain the surface brightness of an ionization nebula for line i. From Pellegrini et al. (2012).

It is evident that if the integration of the emissivity over a sphere is done, $\int_V \epsilon_i$ (column 5), and compare directly with the CLOUDY, the ratio is ≈ 1 (although it is expected exactly that value). Either way, if take a look at column (6), the ratio of the luminosities derived by the integration of ϵ over the line of sight (obtaining S_i) and then calculating the flux F[10], over CLOUDY luminosity, it is also practically one for all lines, which proves our correct usage of CLOUDY. Small differences between the outputs are probably due to the solving of the sum/integral in Equation 3.12. Even if there was a consistent difference between luminosities, in practice, qualitatively, the surface brightness profiles share the same shape and extension of the ones obtained by Woods & Gilfanov (2016), as seen in Figure 3.11 **a)** and **b)**.

Di Stefano et al. (1995) suggested that luminous X-rays nebulae might have luminosities in the [O III]λ5007 line similar to those asocciated with luminous planetary nebulae. In fact, it was stated that $\sim 1.5\%$ to $\sim 8.5\%$ of the total source luminosity

[10]Using the (squared) angular diameter to remove the dependency with arcsec^2, and finally multiplying by the factor $4\pi D^2$(Osterbrock & Ferland, 2006), with $\boldsymbol{D = 55\ \mathrm{kpc} \equiv 1.5 \times 10^{22}}$ **cm, the distance to the LMC**.

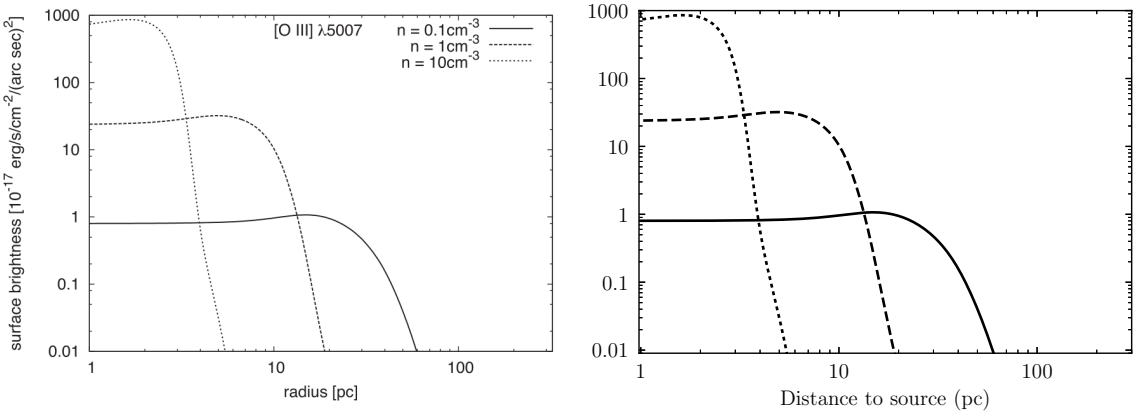

Figure 3.11: a) Surface brightness profiles of an ionization nebula surrounding by a SSS, from Woods & Gilfanov (2016), using CLOUDY for [O III]λ5007Å, assuming a source of $L = 10^{37.5}$ erg s^{-1}, $T = 5 \times 10^5$ K and three different densities: $n = \{0.1, 1, 10\}$ cm^{-3}. **b)** Same as **a)**, but obtained with this code. The results are essentially the same.

is reprocessed by the nebulae in form of [O III]λ5007 radiation, corresponding to a total [O III] luminosity in the range of $\sim 10^{36}$ erg s^{-1}, which is verified in Table 3.1. The main differences are the higher source temperatures of the supersoft nebula and its extent of parsecs. For example, the typical Strömgren radius of these objects is

$$R_S \approx 35\text{pc} \left(\frac{\dot{N}_{\text{ph}}}{10^{48} s^{-1}} \right)^{1/3} \left(\frac{n_{\text{ISM}}}{1\text{cm}^{-3}} \right)^{-2/3}$$

where $\dot{N}_{\text{ph}}$ is the ionizing photon luminosity of the source and n_{ISM} the density of the surrounding ISM (Woods & Gilfanov, 2016). For typical intercloud density values of the LMC, ($n_{\text{ISM}} \sim 0.1$ cm^{-3}), the Strömgren radius correponds to ~ 150 pc, which implies a very low surface brightness.

Finally, the ionization structure is extracted, i.e., the fractional abundance $f_{X^i} \equiv n_{X^i}/n_X$, from CLOUDY as a function of the distance to the source, and compare firstly, H^+, He^+ and He^{+2} structures to the ones obtained as temporal states of the ionization nebula surrounding a **turn-on** blackbody source of $T = 3 \times 10^5$ K, $L = 10^{38}$ erg s^{-1} and $n_{\text{H}} = 10$ cm^{-3}, using the time-dependant photoionization IONTIME, by Chiang & Rappaport (1996). As seen in Figure 3.12, the behaviour of all curves that lies at the right of the second dot-dashed curves in **a)**, representing the ionization

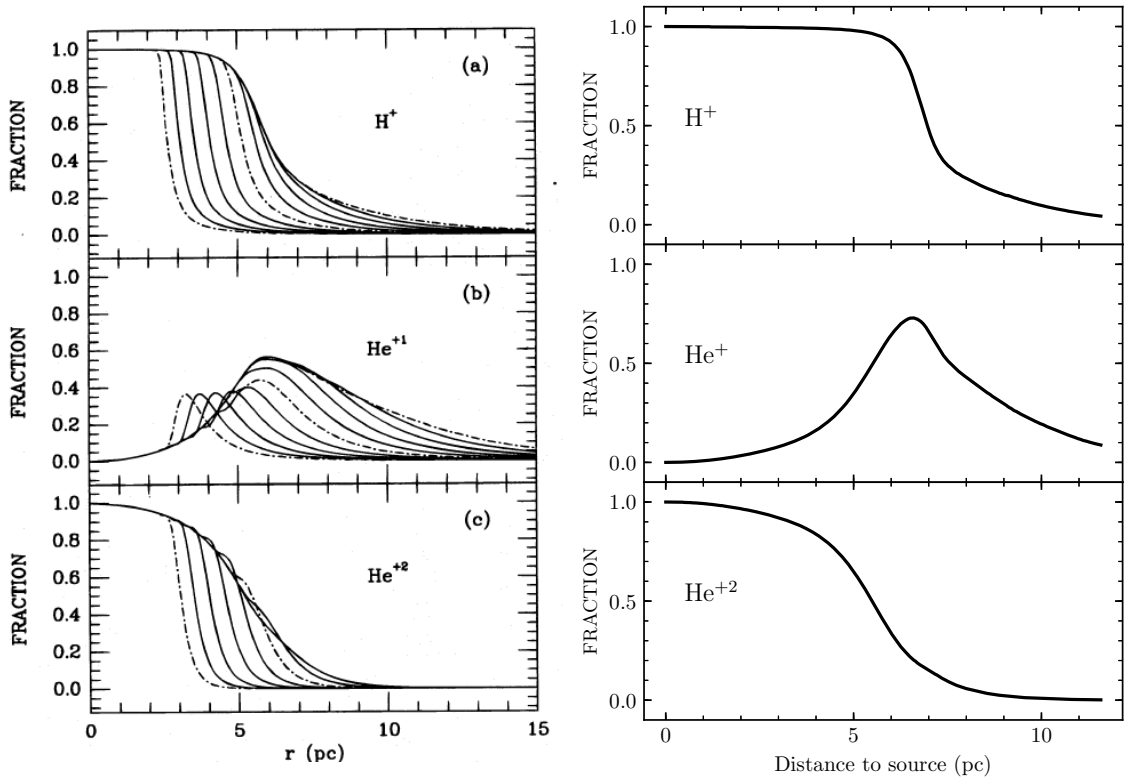

Figure 3.12: **a)** Ionization fraction of H^+, He^+ and He^{+2} of the "standard" model ($T = 3 \times 10^5$ K, $L = 10^{38}$ erg s^{-1} and $n_H = 10$ cm^{-3}) from Chiang & Rappaport (1996). **b)** The same "standard" model replicated in this thesis using CLOUDY .

fraction after $1.5\tau_R$[11], for each ion, and their corresponding three curves of **b)**, which represents a temporal evolution of $\approx 5\tau_R$[12], resemblances each other, which assures us that any conclusion made by Chiang & Rappaport (1996), in principle, can be used safely in this thesis.

Regarding this, the most important conclusions from the analysis are: 1) any dramatic and periodic **variability** of the source luminosity will not impact considerably the spatial structure of the SB (only the central regions might change), only briefly[13], for variability periods compared to the recombination timescale, and 2) the luminosity of the (recombination) lines will depend on the **time-averaged luminosity** of the central source for period variations below $\sim 0.1\times$ recombination timescale of the line. This means, in other words, that any luminosity variation of the source below that limit will correspond to a line luminosity produced by a source with a **constant lower luminosity**.

It is remarkable to see the behaviour of He^+ profiles at comparing with the similar H^+, He^{+2}. This is explained in Chiang & Rappaport (1996) and it is due to the necessity of the formation of the He^{+2} zone before than of He^+ near the source. In other words, there is an extended zone, about $r \leq 3$ pc, that ionizes less than 20% of the He^0 atoms and the ionization in this region raises only when photons with energies lower than 54.41 eV, but much higher than H ionization potential, 13.6 eV, [14] are able to escape. It is good to remember that, looking at Figure 1.6, for a typical assumption that SSS spectrum is a blackbody with $T \sim 5 \times 10^5$ K, the maximum intensity is reached for photon wavelengths of ~ 50 Å, which corresponds to energies of ~ 200 eV. Photons with larger energies, will escape from the innermost regions of the nebula and are absorbed much later, at larger distances from the source.

A nice way to observe that more energetic photons are the ones who might travel larger distances in SSS nebula is found in Figure 3.13, where it can be seen a model

[11] τ_R is the typical H recombination timescale at $T \approx 10^4$, $\sim 10^4$ yr.

[12] Considering that CLOUDY uses the fact that all the microscopic processes that enters to the equilibrium calculations must be **steady**, the longest timescale considered in the simulation is $\approx 5 \times 10^4$ years.

[13] About 1% the recombination time of the line.

[14] From Figure 3.7, the photoionization cross section a_ν of H is not negilible at frequencies where a_ν of He^0 have high values. This argument and the fact that H is the most abundant element in the medium, makes that He^+ fraction reaches only ≈ 0.6.

of a SSS spectrum near the source, in contrast to the spectrum at 20 pc from the source: the latter is composed by photons below H^0 edge, i.e., 13.6 eV (not ionizing!), almost no contribution from photons up to $\sim$ 100 eV some from the maximum of the emission, i.e, $\sim$ 150 eV (blackbody with $T = 4 \times 10^5$ K, the peak is reached at $\sim$ 70 Å), and a large contribution from the non-absorbed, high energetic photons, larger than $\sim$ 300 eV.

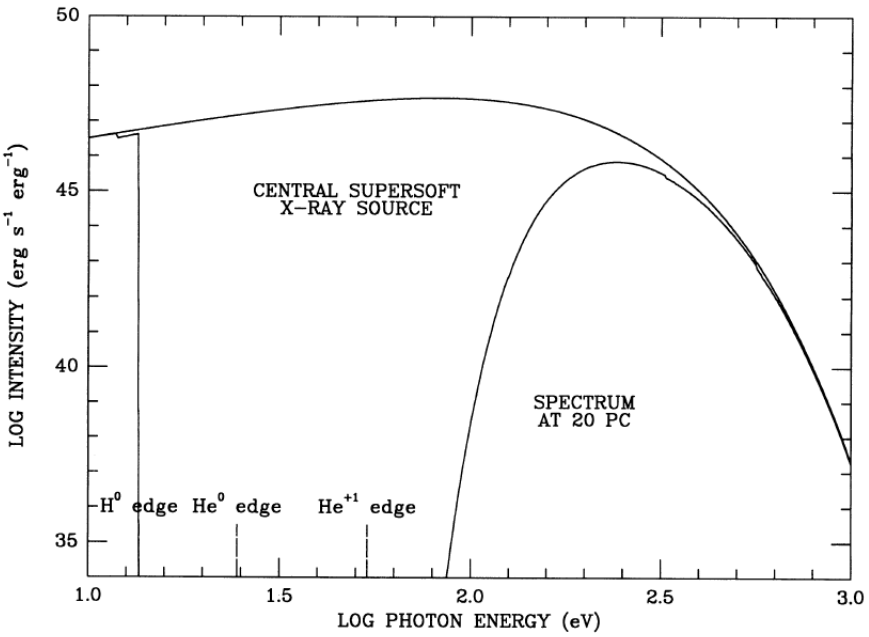

Figure 3.13: Spectrum of the central SSS with $T = 4 \times 10^5$ K, nearby and 20 pc far from the source. Also labelled, hydrogen and helium ionization edges energies. From Rappaport et al. (1994).

For the ionization fraction of O ions in Figure 3.14, it is seen that the large contribution to the innermost is given by the higher ionized oxygen atoms, which resembles the H^+ and He^{+2}. Now looking at the lower ionized regions separately, the curves look like more He^+, but far more complex to analize in terms of photoionization cross sections. This is due to CLOUDY solves the equilibrium equations for several elements and, as seen in Figure 3.8, the photoionization cross sections are far more complicated than the corresponding for H and He ions.

It is worth noting that **no temporal evolution studies** have been done for this kind of nebula since Chiang & Rappaport (1996), which did it only for recombination

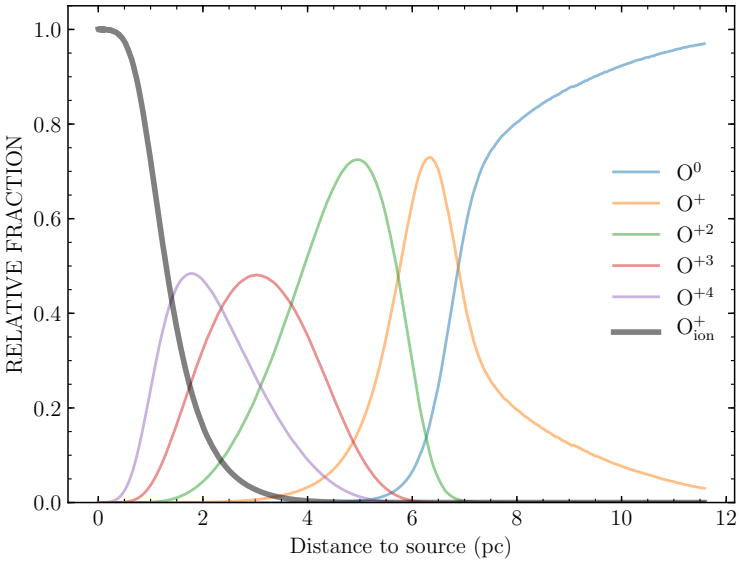

Figure 3.14: Ionization structure obtained with CLOUDY for O^0, O^+, O^{+2}, O^{+3}, O^{+4} and O_{ion^+}, which is the sum of O^{+5}, O^{+6}, O^{+7}, O^{+8} and O^{+9} contributions, for a blackbody source of $T = 5 \times 10^5$ K, $L = 10^{37.5}$ erg s^{-1}, $n_{\rm H} = 10$ cm^{-3} and LMC abundances ($\approx \frac{1}{2}$ solar abundances).

lines. In this sense, CLOUDY is powerful enough to replicate their results using, for instance, the command **stop time** and iterate over a large range of the years, at least for the **turn on** case[15], and could also be generalized to collisional excited lines, making it a huge improvement since the nineties. We must be aware that Chiang & Rappaport (1996) used as an argument to not solve the thermal equilibrium equation that the thermalization timescale for photoelectrons is about 0.01 yr ($<<$ τ_R), while the cooling timescale due to collisional line excitation from metals should not contribute to the ionization time evolution of the nebulae because it is much shorter than τ_R (about two orders of magnitude), so it is expected that the nebula has already reached a fixed temperature T for all their calculations, therefore, metals should not change the behaviour of the recombination lines in their paper.

[15]At first sight, the other three cases, namely, **turn off**, **variable** and **moving source** require more complex implementations.

Chapter 4

Physics Popurri

4.1 Electron Degeneracy

As seen in Chapter 2, the electrons, as all fermions, should follow the Pauli exclusion principle and have spin $s = \frac{1}{2}$. A system formed by many electrons, at conditions of low temperature (T) or high density (ρ), do not follow the classical Maxwell-Boltzmann statistics for distribution of energy states. In this case, the electrons cannot longer take any value in the momentum-position space (phase space), restricted by the Heisenberg Uncertainty Principle. Therefore, electrons follow the (quantum) Fermi-Dirac statistics

$$f_{\mathrm{FD}}(\epsilon) = \frac{1}{e^{(\epsilon-\mu)/kT}+1} \tag{4.1}$$

where μ is the total chemical potential (μ is a function of T), in order to obtain the number density of particles, $N/V = n$ (with N is the number of particles and V the volume that they could fill), respect to the state of energy ϵ. Starting from the Heisenberg uncertainty principle, the density of states, $g(p)$, of a gas of electrons, in a spatial volume V and with momenta $p \in [p, p+dp]$, is written as (Pols, 2012a),

$$g(p)dp = g_s \frac{V}{h^3} 4\pi p^2 dp$$

with $g_s = 2$ due to electron spin degeneracy. From this, using the Fermi-Dirac distribution to get $n_e(\epsilon)$ and assuming the non-relativistic limit[1], $\epsilon = p^2/2m$, then

$$\begin{aligned} n_e(\epsilon)d\epsilon &\equiv g(\epsilon) f_{\mathrm{FD}}(\epsilon) d\epsilon \\ &= \underbrace{\frac{\pi(2^{7/3}m)^{3/2}}{h^3}}_{A} \frac{\epsilon^{1/2}}{e^{(\epsilon-\mu)/kT}+1} d\epsilon \\ \rightarrow n_e &= A \int_0^\infty \frac{\epsilon^{1/2}}{e^{(\epsilon-\mu)/kT}+1} d\epsilon \end{aligned}$$

To evaluate the last integral, it is assumed that $T \rightarrow 0$, implying that if $\epsilon > \mu(0)$, the integral goes to zero and if $\epsilon < \mu(0)$, the integral goes to $\frac{2}{3}\tilde{\epsilon}^{3/2}$. It is usual to define $\tilde{\epsilon} = \mu(0) \equiv \epsilon_F$, the Fermi energy of the form

$$\epsilon_F = \frac{h^2}{2m}(3\pi^2 n)^{2/3} \tag{4.2}$$

The Fermi energy corresponds to the maximum energy that electrons in the gas will have if all the lower energy states are filled. The condition of degeneracy is that the average thermal energy ($\frac{3}{2}kT$) of electrons in the gas should be smaller than ϵ_F. In white dwarfs conditions, electrons are degenerated and have high momentum due to $\epsilon_F \gg kT$.

With the expressions of ϵ_F and $n(\epsilon)$, it is easy to derive the **electron degenerate pressure**, P_e, which is the responsible of maintaining the hydrostatic equilibrium in WDs, starting with the definition of pressure by a gas[2]. The final result, for a non-relativistic degenerate gas of electrons is (Carroll & Ostlie, 2007)

$$P_e{}^{NR} = \frac{(3\pi^2)^{2/3}}{5}\frac{\hbar^2}{m_e}\left[\left(\frac{Z}{A}\right)\frac{\rho}{m_H}\right]^{5/3} \tag{4.3}$$

[1]The equation of state changes in the relativistic case, but to derive it must follow the same argument.

[2]See the document http://home.strw.leidenuniv.nl/ nefs/FermionGas.pdf and references therein to see a nice derivation of P_e and discussion using the Fermi-Dirac integral.

where $\hbar$ is the reduced Planck constant, m_e the electron mass, ρ the density of the gas, Z the atomic number, A the mass number and m_H the hydrogen mass. Equation 4.3 corresponds to the polytropic equation of state ($P = K\rho^{\frac{n+1}{n}}$) with $n = 1.5$. The fact that P_e is an equation of state that does not depends on T, tell us that it is not needed an expansion of the star in order to attain hydrostatic equilibrium. For a relativistic degenerate gas of electrons, ${P_e}^{ER} \equiv P_e$ is also a polytrope with $n = 3$:

$$P_e = \frac{1}{8}\left(\frac{3}{\pi}\right)^{1/3} \frac{hc}{(\mu_e m_H)^{4/3}} \rho^{4/3} \tag{4.4}$$

where μ_e is the mean molecular weight per electron

$$\mu_e \approx \frac{2}{1+X}$$

with X the fraction of hydrogen in the star.

From the integration of one of the stellar structure equations, hydrostatic equilibrium,

$$\begin{cases} \frac{dP}{dr} = -\frac{GM(r)\rho}{r^2} \\ M(r) = \frac{4}{3}\pi\rho r^3 \end{cases} \tag{4.5}$$

$$\Rightarrow \frac{dP}{dr} = -\frac{4}{3}\pi G\rho^2 r \tag{4.6}$$

using the boundary $P(R) = 0$ (pressure at the surface) and $r = 0$ (the center of the star), the central pressure is approximately

$$P_c \approx \frac{2}{3}\pi G\rho^2 R^2 \tag{4.7}$$

Now, by comparing Equation 4.7 with ${P_e}^{NR}$ 4.3, the value of the radius of a white dwarf (R_{WD}) is found,

$$R_{\rm WD} \approx \frac{(18\pi)^{2/3}}{10} \frac{\hbar^2}{G m_e M_{\rm WD}^{1/3}} \left[\left(\frac{Z}{A} \right) \frac{1}{m_H} \right]^{5/3} \tag{4.8}$$

which is basically the well-known mass-volume $M_{\rm WD} V_{\rm WD} =$ constant relation. This means, the electrons must generate more (degeneracy) pressure via closer confinment while more massive is the white dwarf.

Comparing now the full relativistic Equation 4.4 to 4.7 it can be noticed that $M \propto$ constant. The exact value is given by Chandrasekhar (1983)

$$M_{\rm ch} = 5.76 \mu_e^{-2} M_\odot \tag{4.9}$$

Replacing

$$\mu_e \approx 2 \qquad (X \approx 0)$$

for a white dwarf (composed of carbon and oxygen mostly), $M_{\rm ch} = 1.44 M_\odot$ is obtained, which is the value that is identified as the maximum mass a white dwarf can support before collapsing under its own gravity or triggers a thermonuclear runaway.

4.1.1 The Virial Theorem

Following the Lecture Notes of Classical Mechanics from Rutgers University[3], it can be found a nice derivation of the Virial theorem. Consider a system of particles represented by momentum $\vec{p}_i$ (with mass m_i) and position $\vec{r}_i$, its kinetic energy T_i and F_i the corresponding force acting on particle i; the quantity G and its time derivative are defined as

[3]https://www.physics.rutgers.edu/ shapiro/507

$$
\begin{aligned}
G &= \sum_i \vec{p}_i \cdot \vec{r}_i \\
\rightarrow \frac{dG}{dt} &= \sum_i \left(\underbrace{\frac{d\vec{p}_i}{dt}}_{F_i} \cdot \vec{r}_i + \vec{p}_i \cdot \underbrace{\frac{d\vec{r}_i}{dt}}_{\vec{p}_i/m_i} \right)
\end{aligned} \tag{4.10}
$$

If the system is in thermal equilibrium[4], the average value of the temporal derivative of G in Equation 4.10 vanishes and

$$
\left\langle \frac{dG}{dt} \right\rangle = \left\langle \sum_i \vec{F}_i \cdot \vec{r}_i \right\rangle + \underbrace{2\langle T \rangle}_{\equiv \langle \sum \frac{\vec{p}\cdot\vec{p}}{m} \rangle} \equiv 0 \tag{4.11}
$$

Let be $U(\vec{r}_i, \vec{r}_j) = -\frac{K}{|\vec{r}_i - \vec{r}_j|} \equiv -\frac{K}{r}$ a gravitational-like potential of particles j and i (i.e. the energy required to assemble the star by bringing matter from infinity), its corresponding force is

$$
\begin{aligned}
F &\equiv -\frac{dU}{dr} = \frac{K}{r^2} \qquad \text{and} \\
\rightarrow &\left\langle \vec{F} \cdot \vec{r} \right\rangle = -\langle U \rangle \\
&\text{Using 4.11} \\
\Rightarrow &\langle T \rangle = -\frac{1}{2}\langle U \rangle
\end{aligned}
$$

This is one of the most important equations in physics and it is intrinsically related with stars in **hydrostatic equilibrium**: a more tightly bound star must be **hotter** and its **total energy** corresponds to half of its gravitational potential energy. An important timescale of stars is the time that it takes to react to a perturbation of the hydrostatic equilibrium, called **dynamical timescale**. For stars in the Main Sequence (MS), Tauris & van den Heuvel (2003) uses the following relations to express the stellar timescales in terms of $M_\odot$, $L_\odot$ and $R_\odot$ the mass, luminosity and

[4] Not easy to understand without a full refreshment of thermodynamics and Hamiltonian mechanics, see Chapters 2 to 7 in https://itp.uni-frankfurt.de/g̃ros/Vorlesungen/TD/.

radius of the Sun, respectively:

$$\tau_{\rm dyn} = \left(\frac{R^3}{GM}\right)^{1/2} \simeq 30 \text{ min} \left(\frac{R}{R_\odot}\right)^{3/2} \left(\frac{M}{M_\odot}\right)^{-1/2}$$

For the Sun is about of order of 30 minutes, so it is usually the shortest timescale in these objects.

Before the notion of nuclear reactions as the main mechanism of generation of energy in stars, it was believed that the luminosity (L) of the Sun was only due to its gravitational potential energy, so related to its contraction time in the absence of internal energy source, the so-called **thermal timescale**;

$$\tau_{\rm th} = \frac{GM^2}{RL} \simeq 10^7 \text{ yr} \left(\frac{M}{M_\odot}\right)^{-2}$$

For the Sun, this timescale is typically about 10^7 yr, so eleven orders of magnitude larger than the dynamical timescale.

Finally, the last timescale that it is going to be treated here is the **nuclear (evolutionary) timescale**: the time spent by a star while mostly burning hydrogen without evolving its structure significantly (in the main sequence, MS, which ultimately depends on the stellar mass). The energy source of nuclear fusion can be written as a certain fraction of the conversion of rest mass (Mc^2) available to a particular process, $K_{\rm nuc}$,

$$\tau_{\rm nuc} = \frac{K_{\rm nuc} Mc^2}{L}$$

For hydrogen fusion in the Sun, $K_{\rm nuc}$ is about 7×10^{-3}, so $\tau_{\rm nuc} \approx 10^{10}$ yrs, which is the longest timescale of stellar evolution.

4.2 Road to convection

One of the stellar structures equations specifies how the temperature (T) gradient behaves if the energy is being carried by photons, i.e., **radiative diffusion**:

$$\frac{dT}{dr} = -\frac{3\kappa_{\rm rad}\rho}{4acT^3}\underbrace{\frac{L(r)}{4\pi r^2}}_{F_{\rm rad}} \tag{4.12}$$

with $L(r)$ the luminosity at distance r from the center, c is the speed of light and $a = 7.6 \times 10^{-15}$erg cm^{-3} K^{-4} and κ is the so-called **opacity**. If the entire flow is carried by photons, the star is in **radiative equilibrium**. Stars with masses about of the Sun ($\sim 1.2M_\odot$) has radiative cores and convective envelopes, while stars with larger masses tend to have convective cores and radiative envelopes, determined mostly by the mass, therefore its core temperature, which can be expressed in terms of the mechanism of energy generation (Beccari & Carraro, 2015). This fact will be important later at defining the donor star in a binary system and its corresponding response to (its envelope) mass loss. Several sources of opacity are enlisted in Collins (1989) and Pols (2012a), like free-free, bound-free, negative H absorption and electron scattering.

Another mechanism of energy transport in stars are the collisions between electrons and ions called (collisional) **conduction**. Usually, stars like the Sun do not transport heat via this mechanism in its envelope nor its core because of the high conductive opacity

$$\kappa_{\rm cond} = \frac{4acT^3}{3\varkappa_{\rm cond}\rho} \tag{4.13}$$

with $\varkappa_{\rm cond}$, heat conduction coefficient, defined as

$$F_{\rm cond} = -\varkappa_{\rm cond}\nabla T \tag{4.14}$$

with F the energy (heat) flux transfered from hotter to colder zones, thus the minus sign. For the Sun, the conductivity fails to carry the solar luminosity by at least 5 orders of magnitude (Collins, 1989), while for white dwarfs, the ratio of heat

(thermal) conductivity $\varkappa_{\rm cond}$ and its simil $\varkappa_{\rm rad}$ for radiation is written as

$$\frac{\varkappa_{\rm rad}}{\varkappa_{\rm cond}} \approx \frac{T^4}{\rho^2} \times 10^{-21}$$

(Kothari, 1932), which means that "radiative" conduction is approximately 10^{10} lower than electron conductivity for $T = 10^6$ K and $\rho = 10^6$ g cm^{-3}, so the latter is the main mechanism of energy transport in the interior of WDs. This is crucial, because now it can be said that the degenerate stellar regions in these stars are nearly **isothermal**, i.e., the electrons can travel large distances at high velocities given that $\epsilon_F \gg kT$. Explicit forms of $\kappa_{\rm rad}$ and $\kappa_{\rm cond}$ can be found in Marshak (1940).

Even though it is already stated that conduction is the most important energy transport mechanism in WDs, in order to introduce the basic notions of SN Ia explosion, and also, to explain the behaviour of convective envelopes of donor stars, a refresh of **convection** is needed.

First, remember the concept **adiabatic process**: a thermodynamical process that does not exchange heat with its environment. The first and second thermodynamic laws relate the variations of internal energy (U) with changes in the volume (V) and entropy (S)[5], respectively. The heat content, δq, can be written as

$$\delta q = Tds = du + Pdv = du - \frac{P}{\rho^2} d\rho$$

where ρ is the density, $u = U/\rho$ is called **specific internal energy**, $s = S/\rho$ the **specific entropy** and $v = 1/\rho$ the volume of the unit mass, all defined **per unit mass**[6]. For an adiabatic process, $\delta q = 0$.

Now, stating that the general equation of state is of the form $P \propto \rho^{\chi_\rho} T^{\chi_T}$, where

[5] In theory it is incompleted due to the absence of the chemical potential.
[6] Pols (2012a), Chapter 3.

χ_ρ and χ_T[7] can be written as

$$\chi_T = \left(\frac{\partial \log P}{\partial \log T}\right)_{\rho,\mu} = \frac{T}{P}\left(\frac{\partial P}{\partial T}\right)_{\rho,\mu}$$
$$\chi_\rho = \left(\frac{\partial \log P}{\partial \log \rho}\right)_{T,\mu} = \frac{\rho}{P}\left(\frac{\partial P}{\partial \rho}\right)_{T,\mu}$$

The specific heats at constant volume c_V and at constant pressure c_P are defined as

$$c_V = \left(\frac{dq}{dT}\right)_v = \left(\frac{\partial u}{\partial T}\right)_v$$
$$c_P = \left(\frac{dq}{dT}\right)_P = \left(\frac{\partial u}{\partial T}\right)_P - \frac{P}{\rho^2}\left(\frac{\partial \rho}{\partial T}\right)_P$$
$$\Rightarrow \gamma \equiv 1 + \frac{P}{\rho T c_V}\frac{{\chi_T}^2}{\chi_\rho}$$

For an **adiabatic process**, denoted by the subscript "ad", e.g. γ_{ad}, the **adiabatic temperature gradient** is defined as

$$\gamma_{\text{ad}} = \left(\frac{\partial \log P}{\partial \log \rho}\right)_{\text{ad}}$$
$$\nabla_{\text{ad}} = \left(\frac{\partial \log T}{\partial \log P}\right)_{\text{ad}} \tag{4.15}$$

If γ_{ad} is constant, the equation of state$_{\text{ad}}$ takes the form of $P \propto \rho^{\gamma_{\text{ad}}}$, i.e., a **polytrope**.

Now, imagine an element of matter (like a bubble), at certain distance r from the center of a star, characterized by a temperature $T(r)^*$, density $\rho(r)^*$ and pressure $P(r)^*$, in pressure equilibrium with its surroundings (subscript "S"), $T_S(r) = T(r)^*$, $\rho_S = \rho(r)^*$ and $P_S(r) = P(r)^*$, suffers a small perturbation. Due to this perturbation, the bubble moves upwards some small displacement dr. In this moment, there is no longer pressure equilibrium with its environment, i.e., $P_S(r + dr) < P_S(r)$, $\rho_S(r +$

[7]For instant, the **chemical composition**, usually represented by the mean molecular weight, $\boldsymbol{\mu}$, **does not change**.

$dr) \neq \rho_S(r)$ and $T_S(r+dr) \neq T_S(r)$. As the time to restore mechanical equilibrium is much quicker than the time to exchange heat, the assumption of an adiabatic expansion is valid: the equality $P_S(r+dr) = P^*(r+dr)$ is easily reached, then ρ^* must change accordingly, $\rho^*(r+dr) \neq \rho_S(r+dr)$, in order to follow the adiabatic equation of state. Mathematically, Collins (1989) does a nice derivation of the latter statement starting with

$$
\begin{cases}
P \equiv P_S(r) & = P^*(r) = P(r) \\
\rho \equiv \rho_S(r) & = \rho^*(r) = \rho(r) \\
 & = \mathbb{A} P^{\frac{1}{\gamma_{\rm ad}}}
\end{cases}
$$

$$
\rightarrow
\begin{cases}
P(r+dr) & \equiv P_S(r+dr) = P^*(r+dr) \\
 & = P + \frac{dP}{dr} dr + \cdots \\
\rho_S(r+dr) & = \rho + \frac{d\rho}{dr} dr + \cdots \\
\rho^*(r+dr) & = \mathbb{A} P^{\frac{1}{\gamma_{\rm ad}}} (1 + \frac{1}{P} \frac{dP}{dr} dr + \cdots)^{\frac{1}{\gamma_{\rm ad}}} \\
 & = \rho (1 + \frac{1}{P} \frac{dP}{dr} dr + \cdots)^{\frac{1}{\gamma_{\rm ad}}} \\
 & \approx \rho (1 + \frac{1}{\gamma_{\rm ad} P} \frac{dP}{dr} dr + \cdots)
\end{cases}
\tag{4.16}
$$

with $P = \mathbb{A}\rho^{\gamma_{\rm ad}}$, $\mathbb{A}$ constant. Wheter the bubble rises or falls down can be determined: if $\rho^*(r+dr) < \rho_S(r+dr)$, the bubble will rise, effectively carrying heat by convection (usually called **unstable against convection**) and

$$
\text{by Equation 4.16} \quad \Rightarrow \frac{d \log \rho}{d \log P} < \frac{1}{\gamma_{\rm ad}} \tag{4.17}
$$

At contrary, if the density of the environment is lower than the density of the bubble at $r + \delta r$, the bubble will fall down, returning to its original position: being **stable against convection**. Taking the definition of the adiabatic temperature gradient given by Equation 4.15, and that all the energy is carried by radiation, $\nabla = \nabla_{\rm rad}$[8], Equation 4.17, for **stability**, is better known as **Schwarzschild criterion** [9]

[8] See Collins (1989), it is easy to obtain looking at $\nabla_{\rm ad}$.

[9] If you try to derive the stability criteria, remember the **signs** of dP/dr, $d\rho/dr$ and dT/dr.

$$\nabla < \nabla_{\rm ad}. \tag{4.18}$$

The last basic concept about convection is derived by the **mixing length theory (MLT)**, the **superadiabaticity** $\nabla - \nabla_{\rm ad}$, which is a measure of how much the temperature gradient ∇ exceeds the adiabatic value. Fully convective stars are well-approximated by polytropes of index $n = 1.5$ ($\gamma_{\rm ad} = 1 + 1/n$).

4.3 Main Sequence Evolution

It is known that a white dwarf is a star composed mainly by carbon and oxygen that prevents its collapse via degenerate pressure, and they have a maximum mass they can sustain before exploding as a SN Ia. Therefore, it is necessary to introduce the phases of stellar evolution that leads to a white dwarf for a single star. Even if the main focus of this thesis is the evolution of the binary system, the interaction of its component (e.g., mass transfer) is determined by the unperturbed evolutionary phases of low mass stars ($M \leq 11 M_\odot$).

Using the categories of Iliadis (2007), the stellar evolution can be separated in ranges of stellar masses, because mass at zero-age main sequence (ZAMS) determines the evolution of a star.

4.3.1 $0.4 M_\odot \leq M \leq 2 M_\odot$

Stars with masses below $\approx 1.5 M_\odot$ burn hydrogen in their core via the pp-chain, while more massive do it via CNO cycles. The main differences are the dependance with temperature of the energy generation (pp $\propto T^4$, CNO $\propto T^{17}$) and the transport of the energy in the core (pp is via radiation while CNO is via convection). In this work, the focus is only in low mass stars as donors in a binary system, so the stellar structure is a radiative core with a convective envelope.

Taking as an example the evolution of the Sun, Figure 4.1 shows the different stages on the evolution of a $\sim 1 M_\odot$ star:

1. The Sun borns and takes place in the **main sequence (MS)**, while burning

hydrogen in the core until it reaches the hottest point of the MS, called the turn-off.

2. After the exhaustation of hydrogen in the core, the Sun will start to burn hydrogen on a thick shell near the core, leaving the MS. The core will contract, increasing the temperature of the shell thus the energy generation as well. The Sun will develope a fully convective envelope. This stage is called **subgiant branch (SGB)**.

3. The extra energy from burning shell results in a surface expansion and the Sun starts ascending the **red giant branch (RGB)**, increasing the central temperature and density of the core by contraction. The core is so dense that the matter becomes electron degenerate; in a non-degenerate core, the star will start burning helium in the core, expanding due to the extra energy generation, decreasing its temperature and the nuclear burning rate in order to stabilize. But, in the Sun, the electron degeneracy pressure is independent of temperature; the temperature will increase until it lifts the electron degeneracy, igniting the helium in the core in a violent **helium flash (HeF)**.

4. HeF causes the star to expand, the hydrogen burning shell cools and generates less energy until it becomes a **horizontal branch (HB)** star, quietly burning helium in the core, producing a carbon-oxygen core.

5. The helium core is exhausted, contracts again, the temperature increases and ignites helium in a shell. There are two burning shells; hydrogen shell surrounding a shell of helium and the latter surrounding the carbon-oxygen core; this stage is called **asymptotic giant branch (E-AGB)**.

6. While the Sun ascends the E-AGB, the hydrogen and helium burning shell alternate as the major contributor of the overall luminosity, with the hydrogen shell providing the 90% of the nuclear energy. While hydrogen is burned, it adds mass to the helium shell to the point it results in a thermonuclear runaway similar to the helium flash, a **thermal pulse**, pushes out and cools the hydrogen burning shell until it ceases to burn; helium burning takes place as the only source of nuclear energy until the expansion stops the thermal pulse and the Sun contracts again, eventually igniting the hydrogen and making it the main contribution to the luminosity. This event may repeat many times,

which gives the name to this stage, **thermally pulsing asymptotic giant branch (TP-AGB)**.

7. Thermal pulses cease and the Sun losses mass via strong stellar winds, enriching the interstellar medium. This stage is usually called **postasymptotic giant branch (P-AGB)**. While the Sun losses its hydrogen envelopes, it undercovers hotter zones, thus moving to the left in the HR diagram; the intense ultraviolet radiation that comes from the surface ionizes the expanding ejecta, which appears to us as a **planetary nebula (PN)**.

8. The residual core is called **planetary nebula nucleus (PNN)**, formed by mostly carbon and oxygen. The hydrogen shell burning extinguishes so the luminosity decreases until it reaches the white dwarf zone of $\approx 0.5 M_\odot$.

4.3.2 $2M_\odot \leq M \leq 4M_\odot$

The evolution of the stars in this range is very similar to solar-like stars; the main difference is that they do not develop a helium degenerate core during the RGB stage, which means there is **no helium flash**. The condition to discriminate both cases is the so-called **Schöngber-Chandrasekhar limit**. After H exhaustation in the core, a He isothermal core is left while H is burning in a shell, adding more and more He to the core. There is a limit on how much mass an isothermal He core can support expressed by the mass fraction $q_{\rm SC}$ (Collins, 1989)

$$q_{\rm SC} = \left(\frac{\mu_{\rm env}}{\mu_{\rm ic}} \right)^2 \approx 0.1$$

with $\mu_{\rm env}$ and $\mu_{\rm ic}$ are the mean molecular weight of the envelope and the isothermal core, respectively. Stars of $M > 1.5 M_\odot$ cannot become degenerate, so they do not have another mechanism to push all the gravitational pull and end up contracting, generating a gradient in temperature, until the ignition of the He core. Stars of $M < 1.5 M_\odot$ are cool and dense enough that their electrons become degenerated, which will aid to support a little longer the inward pressure, until the thermonuclear He flash that lifts up the degeneracy, starting the α-process in the core.

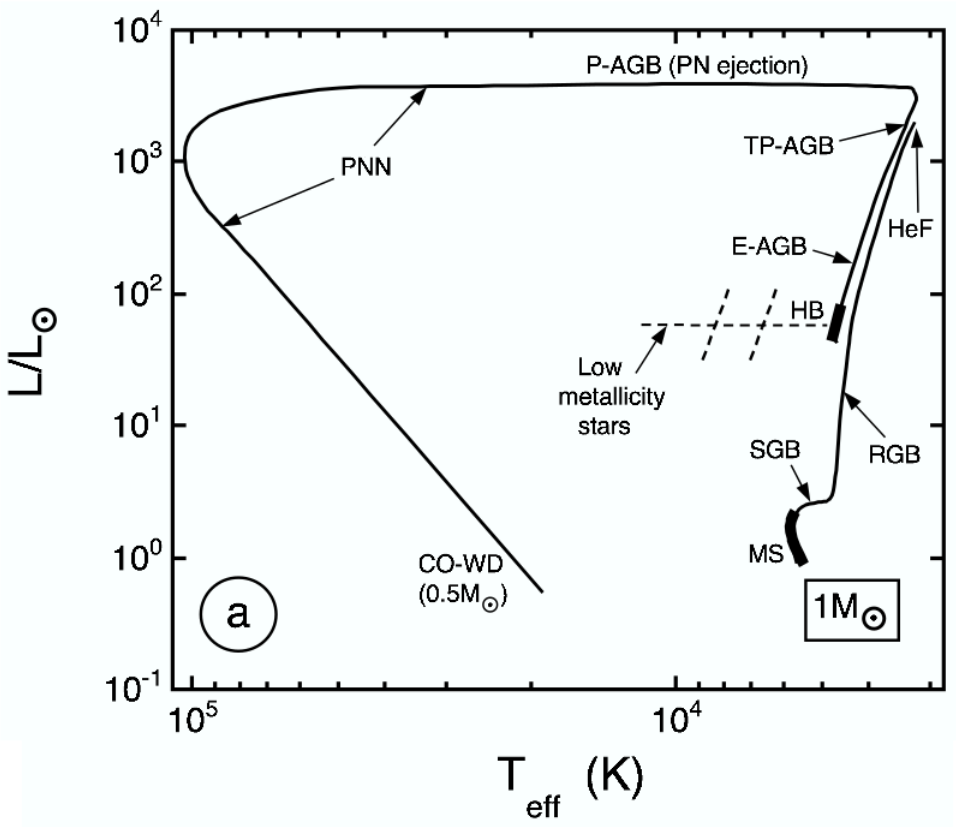

Figure 4.1: Stellar evolution of a 1 $M_\odot$ star from the MS to its WD phase. From Iliadis (2007)

.

4.3.3 $\sim 4M_\odot \leq M \leq 9M_\odot$

At the RGB phase occurs the first dredge-up event: the convective envelope is deep enough that dredges up the product of the hydrogen burning of the core to the surface. The main difference of this range of masses is that it is expected to occur a second dredge-up while reaching the E-AGB.

A full treatment of the physics through the beginning of stellar evolution, i.e., from the formation of a protostar and its establishment in the ZAMS, passing by the Hayashi and Henyey tracks and covering MS and post-MS evolution for a larger range of stellar masses, can be found in Chapter 5 of Collins (1989), while a brief

introduction is given by Beccari & Carraro (2015).

Finally, it is worth mentioning an empirical principle called the **Mirror principle**, which, basically, says that whenever there is shell-burning, the expansion and contraction behaviour of the shell translates to a contraction and expansion of the core, respectively. This principle can be explained in the following way: say that the total energy of the star, E, is a constant through the contraction-expansion of the envelope-core pair in a time less than $\tau_{\rm th}$, but longer than $\tau_{\rm dyn}$, therefore the Virial theorem holds. Both assumptions imply that the gravitational energy U must be a constant. For instance, in the case of contraction of a star with stellar and core radius R_* and R_c, respectively, the variation of both quantities can be written as

$$
\begin{aligned}
U \equiv \text{constant} = \frac{GM_c^2}{R_c} + \frac{G \overbrace{M_c M_{\rm env}}^{(M_c+M_{\rm env})M_{\rm env}\approx}}{R_*} \qquad & / \frac{d}{dR_*} \\
\Rightarrow \left(\frac{dR_c}{dR_*}\right) = -\left(\frac{M_c}{M_{\rm env}}\right)\left(\frac{R_c}{R_*}\right)^2 \ll -1 &
\end{aligned}
$$

if the masses of the core and envelope, M_c and $M_{\rm env}$, remains constant during the contraction. It is evident now, that when, e.g., the core contracts, the radius of the star grows given the negative slope of the last equation, ergo., the envelope must have expanded.

Chapter 5

Mass tranfser

5.1 Roche Lobe Overflow

In this section is determined what is a Roche lobe and how the mass transfer occurs in a binary system. Consider two stars in orbits around their center of mass in the $x - y$ plane with angular velocity ω, as seen in Figure 5.1.

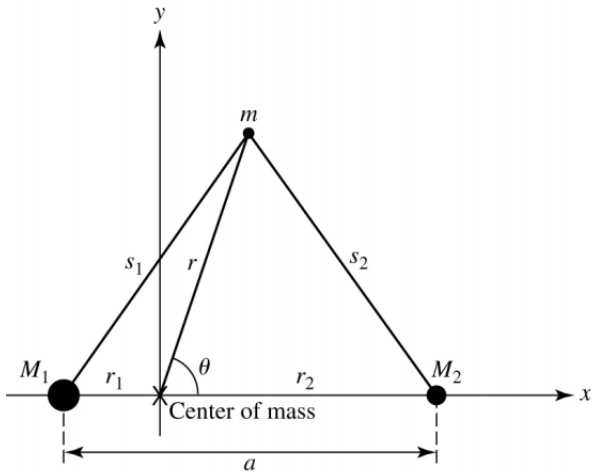

Figure 5.1: Corotating coordinates for a binary system. The binary system consists of two stars with masses $M_1 = 0.85M_\odot$, $M_2 = 0.17M_\odot$ and a separation $a = 0.718R_\odot$. Originally from Carroll & Ostlie (2007).

Considering the potential, $\Phi_i = \frac{GM_i}{r_i}$, in a generic point (x, y, z). We use the center of mass (CM) as the origin of the system. The coordinates of the CM, in terms of $q = \frac{M_2}{M_1}, \mu = \frac{q}{q+1}$ respecting to M_1, are

$$x_{\rm CM} = \frac{x_1 M_1 + x_2 M_2}{M_1 + M_2} = a\mu$$
$$y_{\rm CM} = 0.$$

Therefore, the potential exerted by M_1, located at $(x_1, y_1, z_1) = (-a\mu, 0, 0)]$ is written as

$$\Phi_1 = -\frac{GM_1}{[(x-x_1)^2 + (y-y_1)^2 + (z-z_1)^2]^{1/2}} = -\frac{GM_1}{((x+\mu a)^2 + y^2 + z^2)^{1/2}}$$

Analogously, for M_2, which coordinates are $(x, y, z) = (a(1-\mu), 0, 0)$ will be

$$\Phi_2 = -\frac{GM_2}{[(x-x_2)^2 + (y-y_2)^2 + (z-z_2)^2]^{1/2}} = -\frac{GM_2}{((x-a(1-\mu))^2 + y^2 + z^2)^{1/2}}$$

Now, the centrifugal force in the orbital plane (the plane where both masses and its CM of the system lie), that it is exerted to a test mass m with respect to the CM is $F = m\omega^2 r$, with the corresponding potential U:

$$F = -\frac{dU}{dr}$$
$$\rightarrow U = -\frac{m\omega^2 r^2}{2},$$

and in terms of x, y:

$$\Phi_c = -\frac{\omega^2 r^2}{2} = -\frac{[(x-x_{\rm CM})^2 + (y-y_{\rm CM})^2]^2 \omega^2}{2} = -\frac{\omega^2[x^2+y^2]}{2}.$$

Thus, the potential of the system is $\Phi = \Phi_1 + \Phi_2 + \Phi_c$ and using Kepler Third Law

$$\omega^2 = \left(\frac{2\pi}{P_{\rm orbital}}\right)^2 = \frac{G(M_1+M_2)}{a^3}$$

the potential is written as

$$\Phi = -\frac{GM_1}{[(x+a\mu)^2+y^2+z^2]} - \frac{GM_2}{[(x-a(1-\mu))^2+y^2+z^2]^{1/2}} - \frac{G(M_1+M_2)[x^2+y^2]}{2a^3}$$

From the definitions of q and μ, and noting that the above equations may be written in terms of normalized coordinates by the size scale of the orbit, i.e.,

$$\frac{x}{a} \to \hat{x} \qquad \frac{y}{a} \to \hat{y} \qquad \frac{z}{a} \to \hat{z}$$

the total potential becomes

$$\Phi(\hat{x},\hat{y},\hat{z}) = -\frac{G(M_1+M_2)}{2a} C(\hat{x},\hat{y},\hat{z})$$

where

$$C(\hat{x},\hat{y},\hat{z}) = \frac{2}{1+q}\frac{1}{[(\hat{x}+1)^2+\hat{y}^2+\hat{z}^2]^{1/2}} + \frac{2q}{1+q}\frac{1}{[(\hat{x}-1+\mu)^2+\hat{y}^2+\hat{z}^2]^{1/2}} + \hat{x}^2+\hat{y}^2 \tag{5.1}$$

For instance, if $\hat{y} = \hat{z} = 0$, it is readily that $dC(\hat{x})/d\hat{x} = 0$ is an equation of a polynomial of fifth order; the real roots are the so-called **Lagrangian points** and the minima between the two masses is the inner Lagrangian, or L_1, point. The equipotential surface that intersects L_1 and rounds the two masses corresponds to the **Roche Lobe**, as seen in Figure 5.2.

Physically, there is no net force in the Lagrangian points for the test mass m: the gravitational pull exerted on m by M_1 and M_2 is balanced by the centrifugal force of the rotating reference frame (Carroll & Ostlie, 2007).

Then, the question arises, when does mass transfer occur in a binary system? If the total energy per unit mass of a particle exceeds the value of Φ at L_1 (dashed line in Figure 5.3), then it can flow through the inner Lagrangian point between the two stars. There are three different cases for a binary system: if both stars do not fill their Roche Lobe it is usually called detached binary, when one has filled it is called semi-detached and if both stars have filled their Roche lobes it is called a contact

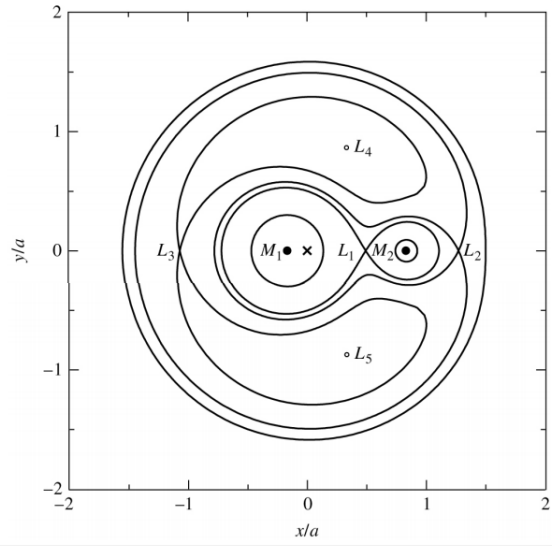

Figure 5.2: Roche equipotentials/lobes. The center of mass is marked with an ×. From Carroll & Ostlie (2007).

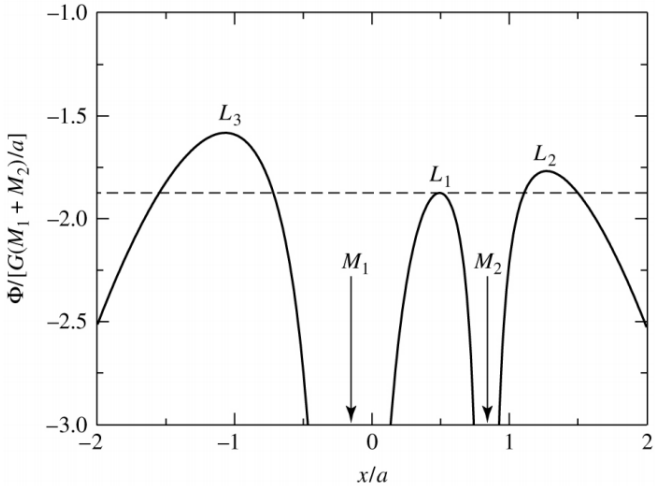

Figure 5.3: The value of the Roche potential Φ as a function of the distance along the x axis among the stars. From Carroll & Ostlie (2007).

system.

The study of close binary systems, their evolution and in particular, the mass transfer, started to develop computationally near the seventies: all the advances

in that matter until that point are summarized in Paczyński (1970). The first assumptions made to solve the problem of accretion were rather simple but needed in that moment: spherical symmetry for the components, the total mass and angular momentum of the system are conserved, circular orbit (and synchronous, see Pols, 2012b), the existence of a critical radius such that mass transfer takes place when the stellar radius exceeds it[1], that were approximated to the Roche lobe, hydrostatic equilibrium, among others, establishing the stable mass transfer. Not only that, Paczyński (1970) used all of the tools that had in hand and did a complete description of the three evolutionary phases where the star expands and may fill up the Roche Lobe in a binary system, **Case A, Case B and Case C** (definitions in the next Subsection and Figure 5.4) and stated concretely that the outcome of these systems may explain the behaviour of, e.g., cataclysmic variables.

Later, as expected, the problem became more complex as people was able to discard more assumptions: in order to explain the origin of novae and dwarf novae, Paczyński (1976) suggested that the progenitors of the their components, (short-period system composed of) a white dwarf and a main sequence companion, at one point through their binary stellar evolution, both filled their Roche Lobe (contact system), but they have expanded so much that exceeded the outer Lagrangian point L_2, leading to the so-called **common envelope** (CE) phase, which ends up reducing the orbital period sufficiently to match the observations of the possible progenitor system V 471 Tau. In this way, acreeting white dwarfs systems appeared as very interesting objects to study for the multiple and flexible configurations leading up to thermonuclear runaways in their surfaces (novae), and furthermore, with the right conditions, to SN Ia events.

The focus, then, was placed in two questions: how do these acreeting WD + companion systems are formed?, and once formed, what are the physical mechanisms that allow the WD grow in mass, in particular, what regulates the mass transfer from the companion?. Did not take long to realize that, related to the latter question, hydrogen or helium shell burning on the surface of the WD could only be thermally stable in a small range of mass transfer rates[2]; for example, Paczyński & Zytkow (1978),

[1]Not true in Paczyński (1970): the system could only be in contact if both stars filled their Roche Lobes, never surpass them.

[2]See Appendix of Sienkiewicz (1980) to view in full detail an "easy" derivation using small perturbations on how to test thermal stability.

in their study of hydrogen flashes of an accreting 0.8 $M_\odot$ WD, found that hydrogen stable burning would be produced at rates between $\approx 1.1 - 2.7 \times 10^{-7} M_\odot$ yr^{-1} (say $(dM/dt)_{R\mathrm{H}}$). For accretion rates above this range, the WD would expand its envelope to red-giant-like dimension following the degenerate core mass-luminosity relation for red giants (Paczyński, 1970), while below ($\approx 0.4(dM/dt)_{R\mathrm{H}}$), several cycles of flashes are expected. In this zone, the more rapid is the accretion rate, the weaker is the flash.

The last statement must be explained: following Starrfield, Iliadis & Hix (2016) work about thermonuclear runaways (TNR) in nova outbursts, they enumerate different variables that affect how a TNR is produced: the amount of material accreted to onto the WD depends on the WD mass, WD luminosity, composition of the accreted matter and the rate of mass accretion. If the latter is more *rapid*, the temperature of the hydrogen burning layers in the surface of the WD will increase rapidly via compresional heating, therefore, less material is accumulated in comparison to slower accretions, which implies that the flashes are weaker. In words of Sugimoto & Fujimoto (1978), the most important quantity that controls mass transfer rates (then, flashes) is the **response of the pressure to a perturbation of the entropy distribution**, in specific, the response of the donor at losing its envelope, and as a consequence, the response of adding mass with a specific entropy to the surface layer in the WD. So, the thermal properties of the envelope play a huge role in this and they vary depending on the configuration of the envelope, e.g., spherical or plane symmetry.

Regarding this, Sugimoto et al. (1979) used a spherical configuration for the helium burning-shell on the WD. In this case, as nuclear reaction starts, it adds specific entropy to the shell raising the temperature and, as a response, it expands, thus reducing the pressure in order to achieve equilibrium. Now, Sugimoto & Fujimoto (1978) considered a plane symmetry, where pressure only depends on the surface density[3]; as burning increases temperature, pressure remains constant, triggering a thermal instability that they called thermal pulse. From this, in terms of specific entropy, Nomoto et al. (1979) said that while more rapid is accretion, the hydrogen flashes are weaker because the **specific entropy of the accreted material** is almost constant, therefore, in order to ignite the burning, less pressure is

[3]Mass above this layer by unit area.

needed. In the case of slower accretion, there is enough time to radiate away the specific heat (entropy) in the process, so there is no much addition to the entropy in a plane-symmetry configuration. This is, of course, only an introduction to the concepts of stability of mass transfer and their consequences in the formation of supersoft sources. To a better understanding of these relations refer to Nomoto & Leung (2018), Lynden-Bell & Lynden-Bell (1977) and Thirring (1970).

5.2 Mass Transfer Stability

It is useful to know that, in general, whenever a star fills its Roche lobe, mass transfer occurs via L_1. What it is needed to point out is that in binary systems that will be encountered in next sections, given that SSSs should be seen at very narrow ranges of mass transfer rates, the stability of mass transfer plays a large role in the outcome of a hypothetical progenitor system. In this section we will not consider (explicitly) the presence of an accretion disk in the evolutionary stages to SSSs, but as it will be seen, these disks are pressumely responsible for the variability of these objects.

5.2.1 Types of mass transfer

Mass transfer (MT) will proceed in a stable or unstable manner depending on the response of the donor and its Roche lobe to the MT (Woods et al., 2012). By following the notation of Ivanova (2015), two processes occur simultaneously: first, mass loss implies changing in the radius of the donor star, typically written as $R_{\rm d} \propto M^{\zeta_*}$. This lost mass can be accreted directly to the mass gainer (and accumulated directly in the envelope or in a accretion disk) or lost from the system, always carrying angular momentum. Second, the Roche lobe's response to mass loss, written as $R_{\rm L} \propto M^{\zeta_{\rm L}}$, introducing the following exponents:

$$\zeta_{\{*,{\rm L}\}} \equiv \left(\frac{d \log R_{\{{\rm d,L}\}}}{d \log M} \right).$$

Mass loss in the donor will bring the star out of hydrostatic and thermal equilibrium. Then, the star, through expanding or contracting, will reestablish, first, the hydrostatic equilibrium and then thermal equilibrium (Woods et al., 2012). In order

to have stability in the mass transfer, the donor (ζ_*) must remain within its Roche lobe (ζ_L) during MT,

$$\zeta_* \geq \zeta_{\rm L},$$

otherwise there will be instability of Roche lobe overflow. The larger ζ_*, the more stable the mass transfer is. Unstable mass transfer could also be a result of the response of the mass gainer star against (too) fast accretion rates (Ivanova, 2015).

There are two different timescales that mass transfer will proceed; the dynamical timescale and the thermal timescale. Since the dynamical timescale is much shorter than the thermal timescale, the dynamical response to mass loss will be almost adiabatic. This is usually expressed with the adiabatic exponent $\zeta_{\rm ad}$. The criteria for dynamical stability of MT becomes $\zeta_{\rm ad} \geq \zeta_{\rm L}$; if it is fulfilled, the donor will shrink within its Roche lobe on a dynamical timescale and is able to recover hydrostatic equilibrium. Why does this happen?

To answer the latter question, we need to make a detour here and relate the intuitions from Chapter 4 with the historical mathematical approach, as Woods & Ivanova (2011) did. It has been stated that radiative and convective envelopes have different responses to mass loss, therefore, it is mandatory to define when this happens. In this context, there are three instances where a star, in their normal stellar evolution, could fill its Roche Lobe: cases A), B) and C) depending on how massive is the donor. As this work does not consider massive components in the binary system, a typical $5M_\odot$ star is useful to visualize when the envelope is radiative or convective as seen in Figure 5.4. First, each case represents the moment when the donor fills its Roche Lobe, so they are defined at a particular stellar evolutionary phases: **Case A)** corresponds to the hydrogen burning phase in the core (MS and subgiant branch), **Case B)** to the phase after exhaustion of hydrogen in the center of the donor (RGB and HB) and **Case C)** after the exhaustion of central helium burning (from EAGB). Green dashed lines in Figure 5.4 delimit each case, while the blue dotted line section indicates that the star has radiative envelope. The red solid line indicates a convective envelope. For a $5M_\odot$ star, this transition occurs when the donor is a red giant.

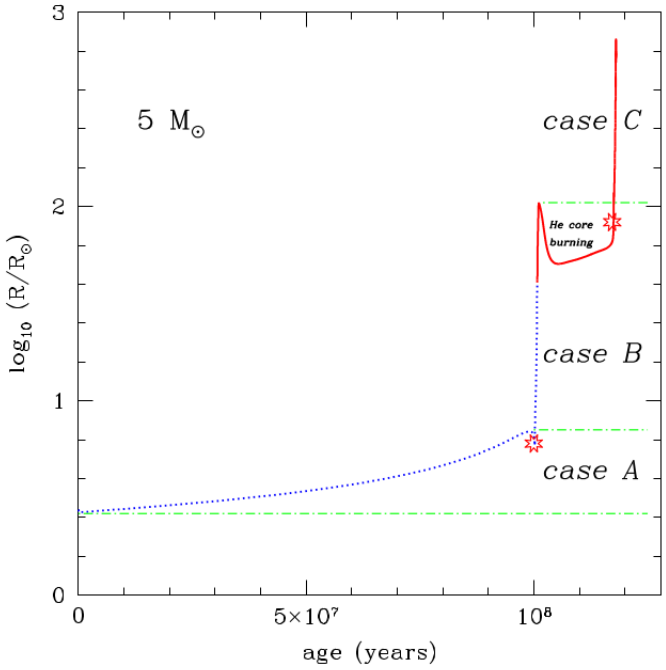

Figure 5.4: Evolution of the radius of a single star of $5M_{\odot}$ (metallicity $Z = 0.02$). Green dotted lines divide each one of the cases where MT may occur, while blue dashed line indicates the that the star has radiative envelope and red solid line indicates convective envelope. From Ivanova (2015).

Historically, mass transfer from not-so-evolved stars (MS and subgiant branch) to a WD is considered adiabatic, which leads to a mass transfer rate according to the thermal timescale of the donor, $\sim 10^{-7} M_{\odot} \mathrm{yr}^{-1}$ (van den Heuvel et al., 1992). Adiabatic means two things: the transfered matter conserves much of the entropy in the process of accretion, and in this context, the response of this kind of donor to perturbations of hydrostatic equilibrium will be much more rapid than the thermal timescale. This, however, is true for stars that have radiative envelopes. Commonly, from Equation 3.11, the specific entropy (Lagrangian coordinates) can be written in terms of the polytropic index n (and adiabatic index γ_{ad}) (Passy, Herwig & Paxton, 2012) as

$$s(m) = s_0 + (\underbrace{1 + 1/n}_{\gamma_{\mathrm{ad}}} - \gamma) c_{\mathrm{V}} \log \rho \tag{5.2}$$

If we take for instance an envelope with perfect monoatomic gas, $\gamma = 5/3$. From

stability criteria, it is "easy"[4] to note that, given Equation 4.18, a convective envelope, represented by a polytrope of $n = 1.5$, will lead to $ds/dm = 0$, a nearly constant specific entropy profile, which already says that $\zeta_{\rm ad} \leq 0$, or that these deep-convective envelope stars are kind-of-insensitive to mass loss. In practice, using the well-known mass-radius relation derived from the Lame-Emden equation for polytropes,

$$R \propto M^{\frac{1-n}{3-n}} \tag{5.3}$$

it can be seen that, for $n = 1.5$, $\zeta_{\rm ad} = -1/3$, convective stars will expand upon mass loss.

In contrast, a radiative envelope will have $\gamma > 1 + 1/n$ which implies that the (specific) entropy grows towards the surface. Then, mass loss will expose layers with lower specific entropy and, at restoring pressure equilibrium, the density of those layers has to increase, therefore, the donor will shrink (Ivanova, 2015) and $\zeta_{\rm ad} >> 0$.

If MT is dynamically stable, the thermal timescale becomes important: the thermal response of the donor is written as $\zeta_{\rm eq}$. If $\zeta_{\rm eq} \geq \zeta_{\rm L}$ and $\zeta_{\rm ad} \geq \zeta_{\rm L}$, stable mass transfer occurs on (usually) nuclear-evolution timescale (Woods & Ivanova, 2011). If $\zeta_{\rm ad} \geq \zeta_L > \zeta_{\rm eq}$, MT is dynamically stable and occurs at the donor thermal timescale, and in the case $\zeta_L > \zeta_{\rm ad}$, MT is dynamically unstable, which leads to a runaway situation, forming a common envelope (CE) (Paczyński, 1976). CE is a critical phase in the formation and evolution of close binaries (as the SSS case), where the components of the system are engulfed by this envelope. It often occurs to stars with, for example, deep convective layers, as response to mass loss, will expand and $\zeta_{\rm ad} \leq 0$, while, for conservative[5] mass transfer, $\zeta_{\rm L} > 0.46$ (Pols, 2012b), so MT will be poorly regulated and the accretor may end up filling its own Roche Lobe, forming a contact binary (Woods et al., 2012). Then, through L_2 Lagrangian point, a nebula surrounding both stars. In order to eject this CE, drag force must act and this will dramatically shrink the orbit Paczyński (1976).

[4]Do not forget the signs of the spatial derivatives at deriving this equation.
[5]Total mass and total orbital angular momentum of the binary are conserved.

This is, of course, idealistic, because evolved-stars, such a red giants, even with their deep convective envelopes, convection at the outermost layers ends up being inefficient, so in practice the energy is transported by both radiation and convection and $\nabla > \nabla_{\rm ad}$. The surface where this happens is called superadiabatic, and it has enormous consequences in the response of these stars to mass loss. On the contrary, stars in the MS are considered too stable to be influenced by this phenomenon, but it is important to indicate that there are cases in which these stars, with radiative envelopes (and convective cores), experience dynamical instability, such is the case for delayed dynamical instability (DDI) (Ivanova, 2015)[6].

Setting aside stars with radiative envelopes, the focus is on the superadiabaticity of convective stars. In simple words, this means that in these layers the local thermal timescale ($\tau_{\rm th,loc}$) is much shorter than the dynamical timescale ($\tau_{\rm dyn}$), so there is no hydrostatic equilibrium and the adiabatic assumption that had been stated in dynamically stable MT does not hold. In real giant stars (as red giants), the entropy profile will not remain constant in the outermost layers as expected, as seen in bottom panel of Figure 5.5, where there is a huge drop-off in those regions (ranges between outer 10% mass to surface) for $1M_\odot$ (black dashed), $5M_\odot$ (blue dotted) and $20M_\odot$ (red solid) giants. In the upper panel, with asterisks, there are the locations (to the right) where $\tau_{\rm th,loc} > \tau_{\rm dyn}$ for those three masses. For very massive stars, the superadiabatic layers almost contain 10% of the total mass, and for the low-mass stars, even if the superadiabatic layers are not seemingly deep, Woods & Ivanova (2011) found that, including those layers in their binary evolution calculations, a $5M_\odot$ giant suffering mass loss rates of $\dot{M} \sim 10^{-3}M_\odot$/yr does not expand upon mass loss but contracts, while for rates of $\dot{M} \sim 10M_\odot$/yr, these stars only expand about 0.15%, not even close to the supposed $\sim 30\%$ of previous studies. The conclusion about this is that understanding, qualitatively, these concepts, it is a good preparation to face the evolution of binary systems that lead to SN Ia, including the supersoft channel.

The **supersoft channel** that will be encountered in the next Section 5.3 will consist of the evolution of a white dwarf plus a companion star, in general not-evolved, involving MT on a thermal timescale of the donor, the more massive star in the system. Also, as one of the objects in this thesis is supposed to be a symbiotic system (RX J0550.0-7151), it is a necessity to introduce the channel white dwarf

[6]Although it is assumed to occur for the unlike-mass ratio above three.

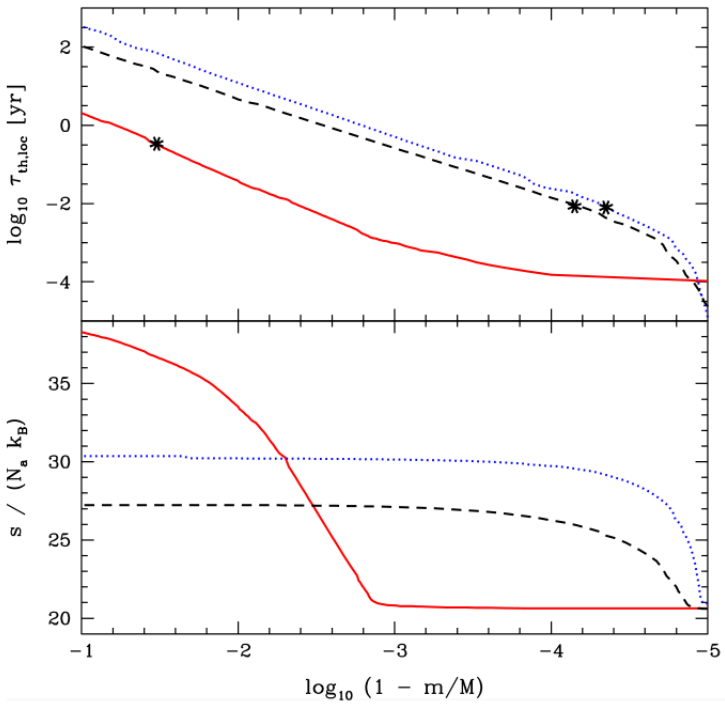

Figure 5.5: Local thermal timescale (upper) and entropy (lower) in the outer 10% mass of a $1M_{\odot}$ (black dashed), $5M_{\odot}$ (blue dotted) and $20M_{\odot}$ (red solid) giant. Note that to the right means to the surface. Asterisks indicate the locations of $\tau_{\rm th,loc} < \tau_{\rm dyn}$. From Woods & Ivanova (2011)

.

plus red giant star, the so-called **symbiotic channel**.

5.3 SN Type Ia

In the double-degenerate channel i.e., the merger of two WD dwarfs may produce a SN Ia, even if it is expected to undergo a supersoft X-rays stage, this would happen shortly before the SN Ia explosion and it is not a strong source of X-rays radiation (Hachisu et al., 2010). Also, Nielsen, Nelemans, Voss & Toonen (2014) conclude, by simulating a large number ($\sim 5 \times 10^5$) of binary systems from scratch, that the number of "SD-like" progenitors[7], should be about 2000, and practically $\sim 85\%$ of these binaries, in all accretion modes (see later, wind and RLOF), had its last MT

[7]DD progenitors, named in that way because they have to pass through a similar SSS SD phase in a point of their evolution.

event[8] at ≥ 400 Myr before the SN Ia explosion, so no SSS nebula should be visible from this channel.

There are other ideas for progenitors, such as the spin up/down models (Di Stefano, Voss & Claeys, 2011), in which MT spins up the WD to a critical rotational speed due to the angular momentum transfer, increasing the mass at explosion[9]. Once MT is low or has ceased, the WD spins down, exploding when the period reaches a critical value. However, this idea is even more unlikely because if this is the main contributor channel to SN Ia, an unseen large population or rapidly accreting WDs must exist.

Then, the focus will be set on the SD scenarios closer to the SSS. The main scenario is the WD + MS channel, or the supersoft channel, where a CO WD in a binary system accretes H-rich material from a MS or a slightly evolved subgiant star. Then H is burned into He and finally it becomes carbon and oxygen. Also enter in the discussion the WD + RG wide systems, in which the secondary star evolves to a RG, the so-called symbiotic channel.

The classical picture of the single degenerate Type Ia supernova consists of a white dwarf made of carbon and oxygen with a mass somewhat less than the Chandrasekhar limit, say $\sim 1.2 - 1.38 M_{\odot}$ and a companion, non-degenerate hydrogen or helium rich star, that is about to fill its Roche lobe and start transfering mass to the WD (Whelan & Iben, 1973). If the rate is too high, the system may enter into a common envelope (CE) phase i.e. mass transfer is dynamically unstable. If the rate is too low, the nuclear burning is unstable that leads to nova explosions in which all the accreted matter is ejected[10]. An essential assumption in single degenerate (SD) scenario is that optically thick winds must act on the unburned accreted-material in order to sustain the high accretion rate without forming a red giant-like envelope around the white dwarf (Meng & Podsiadlowski, 2017).

The action of the wind is reasonable in the sense that SSSs are thought to be

[8]Phase that should not be longer that $\leq 10^5$ yrs.

[9]For a solid rigid rotation, $M \approx 1.5 M_{\odot}$ (Uenishi et al., 2003).

[10] Although Idan, Shaviv & Shaviv (2013) proposed another scenario where at MT $\geq 10^{-6} M_{\odot}$ yr^{-1}, degenerate helium eruptions in the envelope blow all accumulated mass and at MT $\sim 10^{-7} M_{\odot}$ yr^{-1} there may be net accumulation but it is not enough to trigger a SN Ia.

systems which a WD and a not-so-evolved donor of higher mass with MT via RLOF (van den Heuvel et al., 1992). That condition generates very strong constraints on the secondary mass for (dynamical) stable MT: $1.16 \leq M \leq 3 - 4M_{\odot}$ for a typical WD mass ($\sim 1M_{\odot}$) (Kahabka & van den Heuvel, 1997). Any other configuration would lead to a dynamically instability (MT at dynamical timescale) which generates a CE. In order to widen the initial conditions of the binary system, Hachisu et al. (1996) introduced the action of a strong optically thick wind from the WD once MT reaches a critical value: this wind is able to stabilize the MT, avoiding the CE phase.

Taking as a reference the review from Wang & Han (2012) about progenitors of type Ia SNe, there are three main cases in the SD channel that leads to the CO + MS scenario. In Figure 5.6 from left (1) to right (3):

1. In this case, the initial system consists of two stars at zero age main sequence, the primary ($M_{1,i} \sim 4 - 7M_{\odot}$) and secondary star ($M_{2,i} \sim 1 - 2M_{\odot}$) with a period of $P^{i} \sim 5 - 30$ days. Basically, the primary star fills its Roche lobe at the sub-giant branch (Case B) and unstable Roche lobe overflow may form a common envelope (CE). After the ejection of the envelope, the primary evolves to a helium red giant star, a star with a helium envelope and a carbon oxygen (CO) core, and then stable Roche Lobe overflow occurs, where it losses its envelope and the CO WD + MS system is reached.

2. For this scenario, SN Ia explosions occur for the ranges $M_{1,i} \sim 2.5 - 6.5M_{\odot}$, $M_{2,i} \sim 1.5 - 3M_{\odot}$ and $P^{i} \sim 200 - 900$ days. What occurs here is that the primary star is in the EAGB; a common envelope phase is formed due to dynamically unstable Roche lobe overflow, and after its ejection it ends up being the same scenario as **1)**.

3. The primary star fills its Roche lobe at the TPAGB stage. A CE is formed due to the dynamically unstable mass transfer. After the CE ejection, the primary becomes a CO WD. For this scenario, SN Ia explosiones occur for the ranges $M_{1,i} \sim 4.5 - 6.5M_{\odot}$, $M_{2,1} \sim 1.5 - 3.5M_{\odot}$ and $P^{i} > 1000$ days.

As can be seen, having notions of MT is very useful to understand the evolutionary paths of binary stars. For WD + MS systems, the accretion timescale would be $\approx \tau_{\rm th} \approx 10^{6}$ yr (van den Heuvel et al., 1992). If the SN Ia explosion occurs in this phase, we expect to see a supersoft nebula surrounding the SSS, which will remain

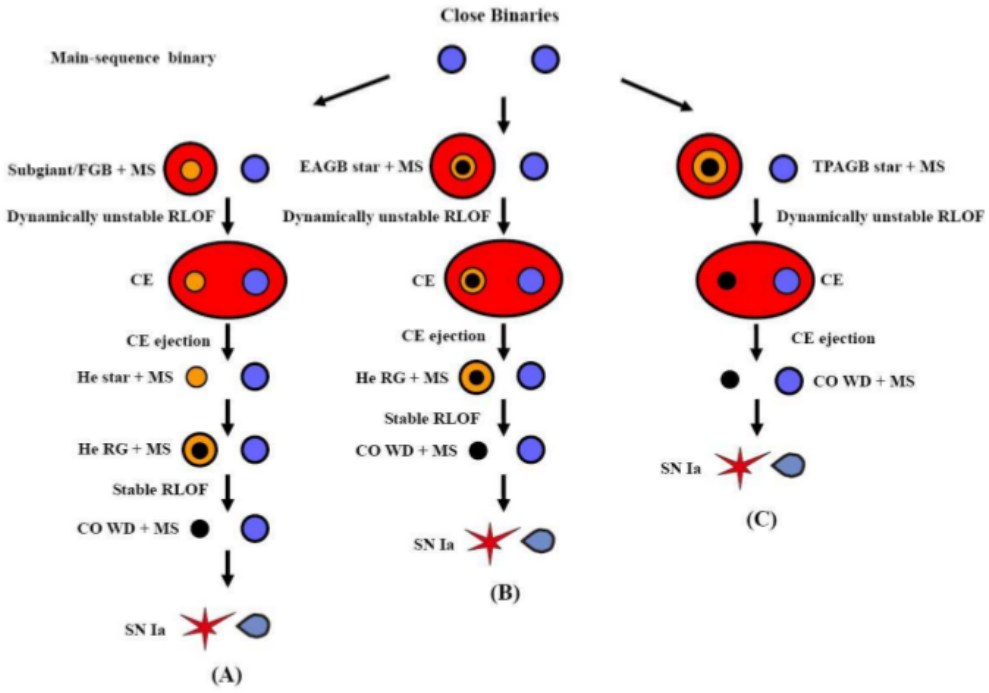

Figure 5.6: Binary evolutionary scenarios for WD + MS that yields to SN Ia. From Wang & Han (2012)

visible surrounding the SNR.

In the WD + RG case (Figure 5.7), the system consists in a red giant as a mass donor star, also called the symbiotic channel. Compared to the WD + MS channel, SN Ia in the WD + RG channel are from wider primordial binaries. The primary star fills its Roche lobe at the TPAGB stage, then a CE is formed due to the dynamically unstable mass-transfer during the Roche lobe overflow, which is eventually ejected and the primary becomes a CO WD while the MS companion becomes a red giant star. For this channel, SN Ia explosions occur for the ranges $M_{1,i} \sim 5 - 6M_{\odot}$, $M_{2,i} \sim 1 - 1.5M_{\odot}$ and $P^{i} > 1500$ days.

The main issue with this channel is that the appropriate initial parameter space for producing SN Ia is too small, meaning that the contribution of this channel will

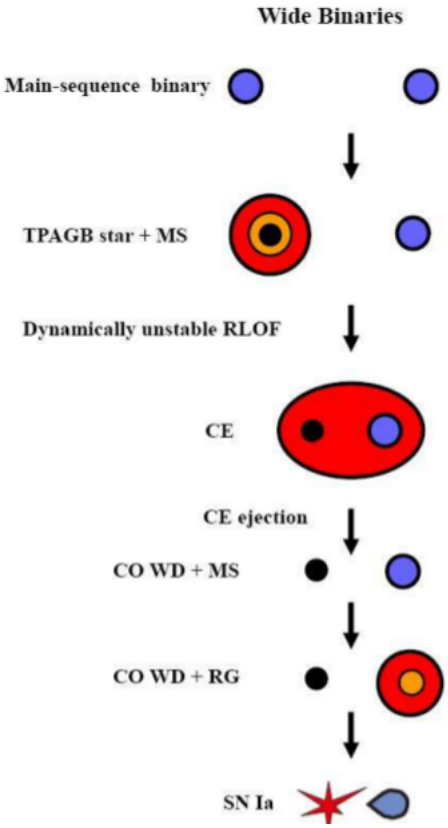

Figure 5.7: Binary evolutionary scenarios for WD + RG to SN Ia. From Wang & Han (2012)

be small compared to the WD + MS configuration (Wang & Han, 2012).

Truth to be told, throughout these years, people have put a lot of work on finding more ways to obtain SN Ia explosions. For that reason, new models of binary evolution, with variations in the (often same) parameters and classical recipes, show different results. These parameters are e.g., the amount of energy required to expell the CE, the accreted mass retentions, the metallicity of the WD/donor, if there is (or not) the action of a wind (from the WD or the donor), hydrogen and helium burning efficiencies (Bours et al., 2013), etc.

As the observations of SN Ia show the absence of hydrogen or helium in the spectrum (Filippenko, 1997), many potential progenitor systems, similar to the supersoft configuration, can be discarded. Suggestions such as a classical nova system loses a large amount of core material during the nova outburst which implies a decrease

in the WD dwarf mass, and the symbiotic novae, defined as a red giant-WD system where the red giant is too distant to fill its Roche lobe and mass loss occurs via stellar winds, could only produce sub-Chandrasekhar SN Ia events (Marietta et al., 2000). The last statement as been put on debate: as Hachisu et al. (1999a) proposed, given the correct ranges in the secondary masses and periods, the wide symbiotic channel systems are potential progenitors of SN Ia if the MT is mediated by a wind from the WD which strips mass from the secondary, avoiding then the typical CE phase that it is expected of a RLOF of stars with deep convective envelopes.

5.4 On the Hertzprung-Russell Diagram

SSSs are white dwarf accreting hydrogen from a donor star at a steady burning rate, so the problem turned into finding which rate makes this possible. From early works of Nomoto (1982), the range of steady-stable MTs to the WD[11] is tiny (see Figure 5.8), and that it is the reason of searching for mechanisms to stabilize the accretion and wide it up. These accreting WDs with different masses are located in the HR diagram as seen in Figure 5.9 depending on the mass transfer rate, where solid-lines represent the thermally stable models in Nomoto et al. (2007) (i.e., those that do not lead to thermonuclear runaways as novae), dotted-lines show the thermally unstable models (nova-like) and dashed-lines the part where an optically thick wind should rise and occult the supersoft X-rays radiation. Boxes constrain the location of some known supersoft sources.

The mass transfer ranges have been a hot-topic topic throughout the years because depending on the treatment of binary evolution and how to solve stellar structure equations (if done), the results vary: Starrfield (2004) made hydrodymical simulations of an evolving WD through a sucesion of nova cycles previous accretion from the donor and they found that the accretion ranges from 1.6×10^{-9} to $8.0 \times 10^{-7} M_{\odot}$ yr^{-1} led to thermally stable burning ("+" in Figure 5.9). In contrast, Nomoto et al. (2007) negates that statement by constructing steady state models for white dwarf accreting matter, saying that the ranges are much smaller for their thermally stable models. Their critical minimum value for steady stable accretion, $\dot{M}_{\rm stable}$, is

[11]Not considering an accretion disk yet, which is an accepted fact in these days.

$$\dot{M}_{\rm stable} = 3.066 \times 10^{-7} \left(\frac{M}{1M_{\odot}} - 0.5357 \right) M_{\odot} {\rm yr}^{-1}$$

while the maximum value, $\dot{M}_{\rm RG}$, is

$$\dot{M}_{\rm RG} = 6.682 \times 10^{-7} \left(\frac{M}{1M_{\odot}} - 0.4453 \right) M_{\odot}\ {\rm yr}^{-1}$$

It is expected that if $\dot{M} > \dot{M}_{\rm RG}$, the WD resembles a red giant due to the common envelope that has been formed. As a summary of what had been stated see Figure 5.8.

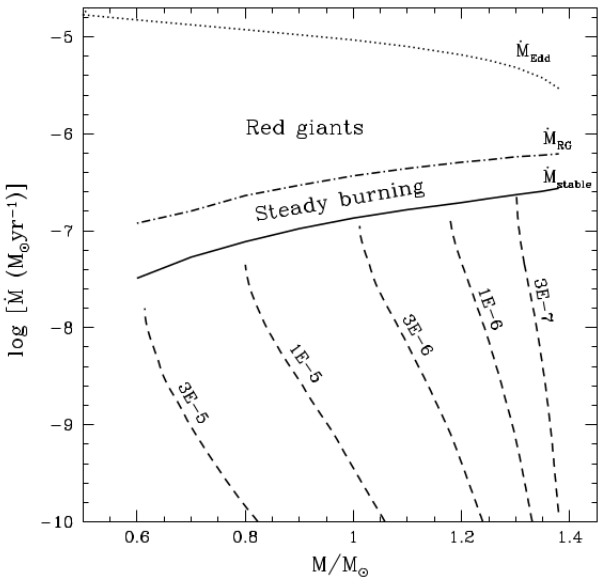

Figure 5.8: Properties of H-burning shells in accreting WDs, in a WD mass M vs accretion rate $\dot{M}$. Dashed lines trace the loci of envelope mass. From (Nomoto et al., 2007).

As a state-of-art study, Wolf, Bildsten, Brooks & Paxton (2013) does an extensive research about stability of accreting WDs, mostly focused on mass transfer below $\dot{M}_{\rm stable}$, and compares their results with previous studies such as Nomoto et al. (2007).

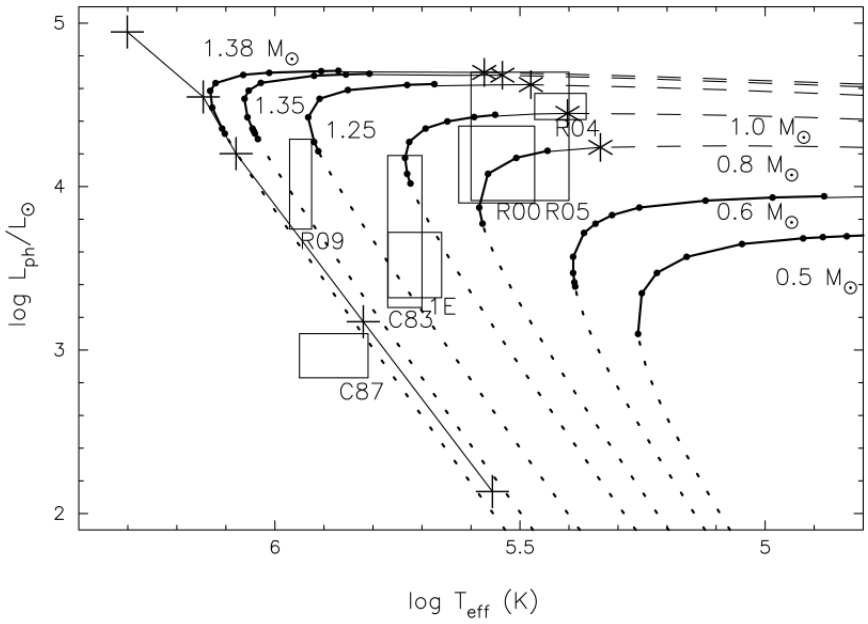

Figure 5.9: Loci of steady models in the HR diagram. Boxes represent the positions of several known-supersoft X-rays sources. From Nomoto et al. (2007).

5.5 Accretion Time

SSSs are thought to be one of the best candidates as the progenitors of the SN Ia in the SD model. One of the strong points of this proposal is that accreting WDs should spend a long period radiating X-rays. Using this fact, the SD model has been put in doubt recently. Gilfanov & Bogdán (2010) compared X-rays observations of Chandra of several early type galaxies with the predicted total luminosity in X-rays band of the population of nuclear-burning WDs (NBWDs) that explodes as SN Ia in those galaxies, assuming that they produce most of the seen X-rays radiation. For example, for M32 the observed luminosity is 1.5×10^{36} erg s^{-1} while their predicted value is 7.1×10^{37} erg s^{-1}. They concluded that no more than $\sim 5\%$ of Type Ia SN in early type galaxies can be produced by white dwarfs in accreting binary systems, practically discarding the SD model. Di Stefano (2010) claimed that the majority of the progenitors do not appear as SSS for long periods ($\sim 10^6$ yrs) based on the number of SSS observed in six nearby galaxies with respect to the expected number of NBWDs that becomes SNe Ia. For example, for M51, the number of SSSs is 15, while the expected number cannot be much smaller than several hundred, which clearly is against Gilfanov & Bogdán (2010).

Also, Hachisu et al. (2010) noticed that the results of Gilfanov & Bogdán (2010) assumed that all the accreting WDs are in the SSS phase which typically lasts $\sim 2 \times 10^6$ yrs before an SN Ia explosion (Meng & Yang, 2011). They found that progenitors of SN Ia spent most of the time in the wind phase rather than the supersoft phase (see Figure 5.10), which lasts $\approx 2.5 \times 10^5$ yr.

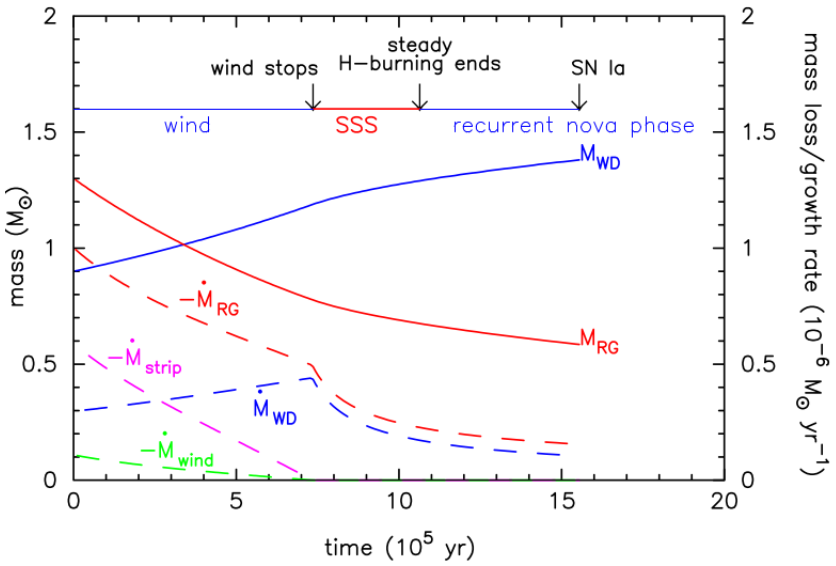

Figure 5.10: Time evolution of a WD + RG progenitor system for an elliptical galaxies. Dashed lines with different colors represent the contributions to the mass-loss/growth rate in a (Hachisu et al., 1999a)-like evolutionary model (wind, SSS and RN phases) and solid lines the WD and RG mass variations. From Hachisu et al. (2010).

Meanwhile, Meng & Yang (2011), by doing a binary population study, found that about 40% of the mass accreting CO white dwarfs that become SNe Ia spend less than 2% of their accretion time in the SSS phase (see Figure 5.11).

Therefore, the SD model cannot be excluded based only in the measurements of X-rays emission of (elliptical) galaxies because most of the NBWDs would not contribute to that radiation given that their SSS lifetimes are much shorter than claimed by Gilfanov & Bogdán (2010).

Many studies have been dedicated to the determination of the number of SSS throughout the years, which, as shown, should not be confused as the accreting time

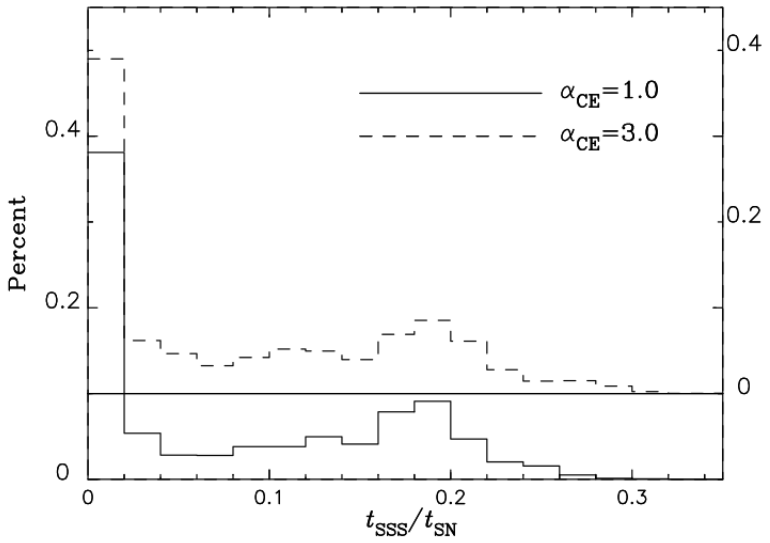

Figure 5.11: Distribution of the relative duration of SSS phase to the whole mass-increasing time until SN Ia explosion. Linestyles represent two different values of the CE ejection efficiency $\alpha_{\rm CE}$, which denotes the fraction of the released orbital energy used to eject the CE. From Meng & Yang (2011).

of NBWDs but they are intrinsically related. Kahabka & van den Heuvel (1997) did a great review about pioneer population synthesis studies that gives the hint that the predicted number of SSSs (more precisely, close-binary supersoft sources) was about 1000 in MW and M31, and of order of hundreds in the Magellanic Clouds. In practice, these numbers are strongly dependent of the binary evolution recipes that the authors used, like common-envelope treatment, the initial-mass-function (IMF), the type of star-formation-rate (SFR), etc. For example, Yungelson et al. (1996) found that for symbiotic stars and subgiant donor systems, the number of permanent SSSs in a flat distribution of zero-age MS binaries over the mass fraction, are about $\sim$ 400 in elliptical and spiral galaxies models, while Rappaport et al. (1994) found that in the MW should be around 1000 SSSs based in their BPS study, including magnetic-braking, common envelope phases and different IMFs.

5.6 Variability and duty cycle

It is good to know the historical background of the SSSs that will be used in this thesis: CAL 83, CAL 87 and RX J0513.9-6951. As explained in the next sections, the information about RX J0550.0-7151 is impresively almost nill because of the lack of X-rays detections. In the nineties, CAL 83 and CAL 87 were considered as prototypes of persistent SSS, while RX J0513.9-6951, since nearly the time of its discovery (Schaeidt et al., 1993), appeared as a X-rays transient[12].

The strangest object among the three SSS is CAL 87. CAL 87 is an eclipsing binary, with deep eclipses that were associated to high inclination $i \approx 77^{\circ}$ (Schandl, Meyer-Hofmeister & Meyer, 1997, see Figure 5.12b)[13]. By taking word-by-word the idea of van den Heuvel et al. (1992), it is expected that the mass ratio of the binary system component is $q = M_{\rm d}/M_{\rm WD} \geq 1$. However, by using radial velocities, Hutchings et al. (1998) determined a value of mass ratio $q \sim 0.25$, while Oliveira & Steiner (2007) confirmed this value using the wind-driven accretion model proposed by van Teeseling & King (1998) where MT (via RLOF) is driven by a strong wind from the irradiated secondary star triggered by e.g., a long phase of residual hydrogen burning after a shell flash (Ablimit et al., 2014). In van den Heuvel et al. (1992) hypothesis, the orbit of the system should shrink in a MT event (orbital period decreases over time, $\dot{P} < 0$), while in the van Teeseling & King (1998) counterpart, the period should increase with time ($\dot{P} > 0$). Oliveira & Steiner (2007) and Ribeiro, Lopes de Oliveira & Borges (2014) measured the temporal variations of CAL 87 period, based in optical and X-rays light curves respectively, obtaining $\dot{P}_{\rm orb} = 7.2(\pm1.3)\times10^{-10}$s s^{-1} and $\dot{P}_{\rm orb} = 6(\pm2)\times10^{-10}$s s^{-1}. The latter value changes when incorporating the optical data from Oliveira & Steiner (2007) (and shifting the reference ephemeris), yielding to a value of $\dot{P_{\rm orb}} = -2.2(\pm0.2) \times 10^{-10}$s s^{-1}. They concluded that there are cyclic orbital period changes induced by the interaction of the wind with strong magnetic fields. This hypothesis is neglected by Ablimit et al. (2014), proposing that it is more probable a shrinkage of the orbital separation due to large mass loss rates from the binary ($\geq 4 \times 10^{-8} M_{\odot}{\rm yr}^{-1}$) via Lagrangian point, L_3. With this background, even if it is known that there is agreement between

[12] About a factor of 20 difference between off/on states in the ROSAT counts rate.

[13] Given a model that contains contributions to the optical light from a hot spot spray connecting the donor to the hot WD via MT, an accretion disk surrounding the WD, and the irradiating secondary star, accounting for its evident asymmetry, as seen Figure 5.12a).

optical and X-rays light minimum in their light curves for this SSS (Ribeiro, Lopes de Oliveira & Borges, 2014), the original SSS hypothesis (in Figure 5.12b, Kahabka & van den Heuvel (1997) thought in a massive donor for CAL 87 system) has been put in doubt until these days and it is wise to avoid any conclusion about the nature of MT (therefore, variability) of this SSS.

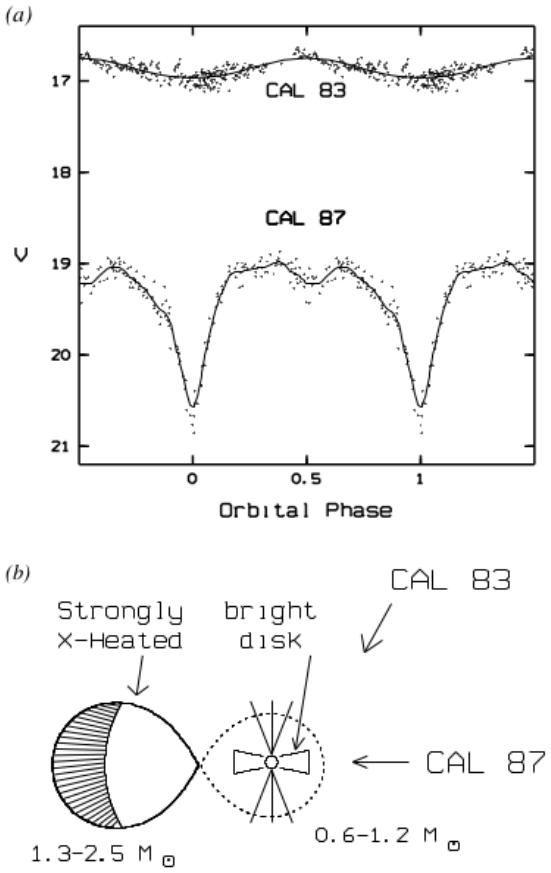

Figure 5.12: a) CAL 83 and CAL 87 optical light curves. b) Early diagram explaining the differences between CAL 83 and CAL 87 light curves because of the inclination angles. From Kahabka & van den Heuvel (1997).

The next case is the prototype CAL 83, which was thought to have stable burning in the WD surface, and that the classical picture of van den Heuvel et al. (1992) should hold. As can be seen in Figure 5.12, the optical variability has small amplitude in comparison to CAL 87, meaning that the inclination is very small. It did not take long, after the first X-rays detections of CAL 83, to find its X-rays off-states[14], so its behaviour is more difficult to explain than a persistent nuclear-burning WD.

[14]First offset (Kahabka & van den Heuvel, 1997), second (Greiner & Di Stefano, 2002), third

In fact, the variability of CAL 83 is similar to the one of the transient supersoft source RX J0513.9-6951. As seen in Figure 5.13, an anti-correlation between optical high/low and X-rays on/off states is evident, with a duration of optical low and high states of 200 and 250 days, respectively (with their according X-rays on/off states). The main difference with RX J0513.9-6951 is that the duration of the latter optical low/high states are much shorter than CAL 83 ones, ≈ 40 and $\approx 60 - 170$ days respectively, meaning that its mass accretion rate should be higher as well (see below), and the presence of a **bipolar outflow of** ~ 3800 **km/s** (Southwell, Livio, Charles, O'Donoghue & Sutherland, 1996) that suggests the action of mass-loss wind (Burwitz, Reinsch, Greiner, Meyer-Hofmeister, Meyer, Walter & Mennickent, 2008).

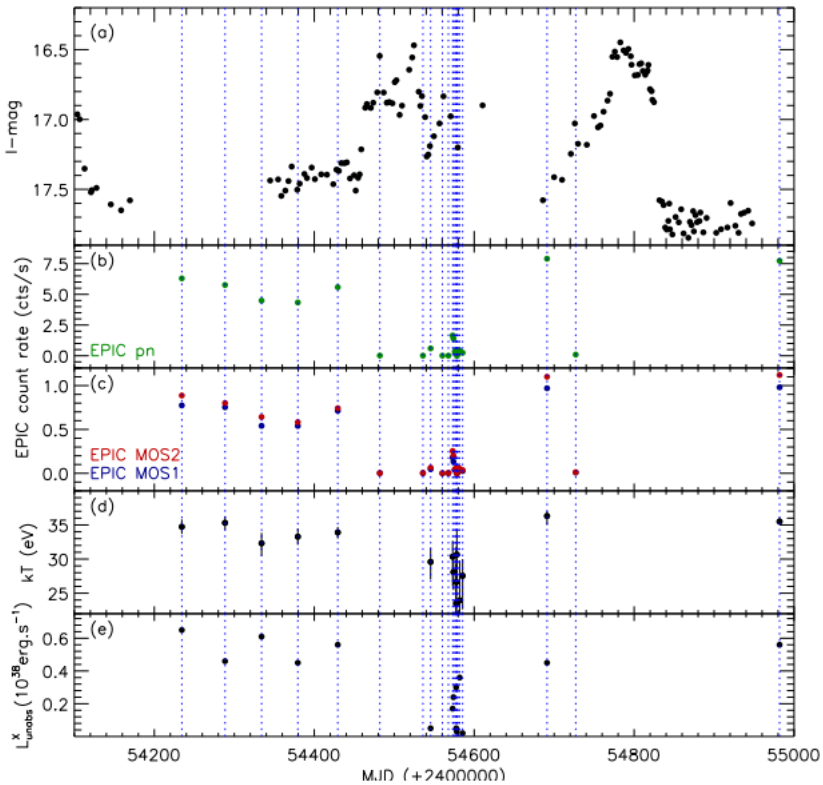

Figure 5.13: a) OGLE III, b) XMM-Newton/EPIC PN and c) MOS1 and MOS2 light curves of CAL 83. In panels d) and e) the temperature and luminosity evolution. From Rajoelimanana et al. (2013).

The last supersoft that will be treated is the recurrent RX J0513.9-6951. As

(Lanz, Telis, Audard, Paerels, Rasmussen & Hubeny, 2005) and recently, a total of eight X-rays off states has been reported since its discovery (Rajoelimanana et al., 2013), all during optical high states.

the variability is much shorter than CAL 83, there are more measurements about the anti-correlation between X-rays and optical light curves, as seen in Figure 5.14. In the van den Heuvel et al. (1992) picture, a **limit cycle** behaviour was expected if the accretion rates were close to the critical mass transfer rate ($\dot{M}_{\rm RG}$). In this scenario, on/off X-rays states should be presented due to the expansion of the WD envelope. This would quench the MT and therefore no nuclear-burning would occur until the envelope collapses again, re-starting the cycle. Taking this idea, Southwell, Livio, Charles, O'Donoghue & Sutherland (1996) and later Reinsch et al. (1996, 2000) proposed that the anti-correlation can be explained in terms of **changes in the photospheric** radius.

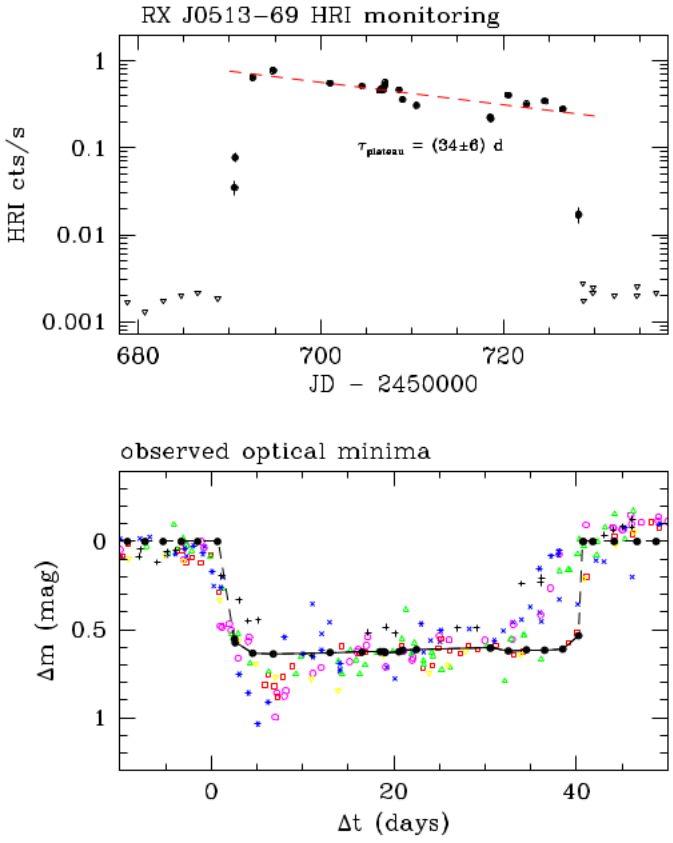

Figure 5.14: Upper panel: ROSAT detected (filled circles) and upper limits (triangles) of RX J0513.9-6951 in a complete outburst cycle. Bottom panel: MACHO light curves of different optical minima. Filled circles are predictions of optical light curve made by the X-ray data and a LTE WD model atmosphere spectra. From Reinsch et al. (2000).

Figure 5.16 shows a step-by-step diagram of the limit cycle behaviour that would explain changes in the photosphere of RX J0513.9-6951. First, the **optical luminosity** comes **mostly from the reprocessed X-ray radiation by the optically thick accretion disc** and the irradiation on the companion (similar to CAL 87 model), while the X-ray counterpart comes from the hot WD (nuclear burning on the surface). In Figure 5.15, the contributions of the WD, disc and companion to the absolute V magnitude are shown in terms of the photospheric radius. It is clear that the disc contribution dominates when the photospheric radius (namely R_1) is small while at larger values declines because the WD photosphere engulfs a section of the disc. As the envelope of the WD expands, its contribution to the optical flux arises. The contribution of the companion is rather constant in terms of changes in the photospheric radius.

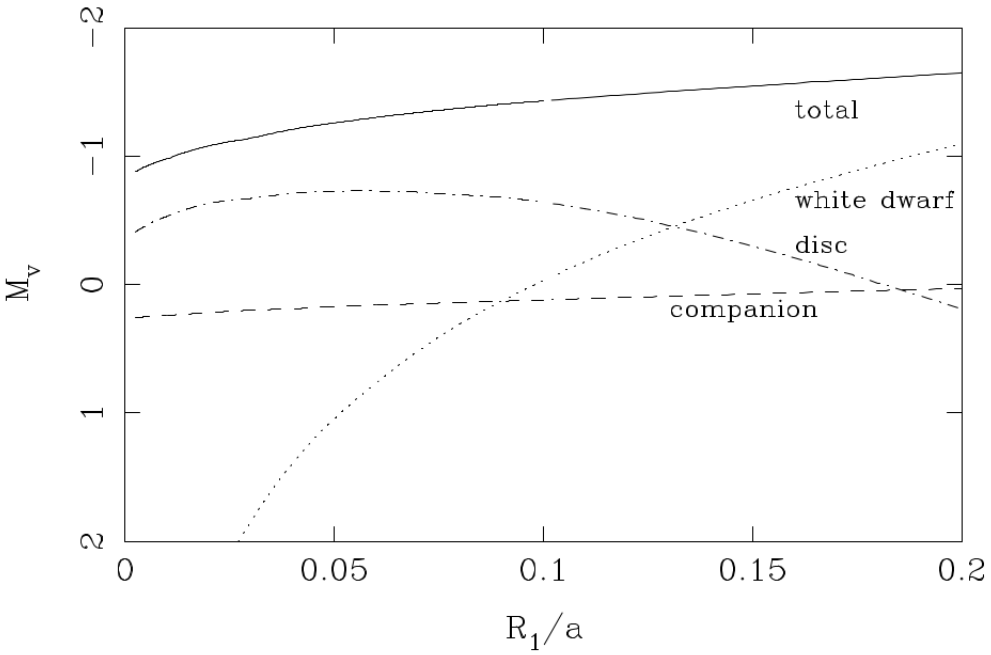

Figure 5.15: Magnitude variations versus (changes of) photospheric radius in the limit cycle model proposed by Southwell, Livio, Charles, O'Donoghue & Sutherland (1996). From Reinsch et al. (2000).

Changes in the photospheric radius are consequence of changes in the accretion rate onto the WD, which are controlled by changes in the viscosity of the disc. Say that the mass accretion increases somehow (see "final" step of the cycle), the pho-

tosphere of the WD will expand (d)→e) in Figure 5.16) as long the mass accretion onto the WD is above the critical value $\dot{M}_{\rm crit}$ for steady MT. How can this happen? The trick is that, throughout the WD expansion, the temperature of the disc, that has a dependency with the photospheric radius of the form $T_{\rm disc} \propto R_1$, increases the mass-flow rate in the disc[15], so the disc ends up being no longer in steady-state. While the mass-flow rate from the secondary to the disc is constant, the draining of matter onto the WD will occur at viscous timescale of ~ 130 days, emptying the disc, until the point that the accretion to the WD decreases below $\dot{M}_{\rm crit}$. At that moment, where the optical high state is fading, the WD begins its contraction and the disc cools down. The photosphere, in about ~ 5 days, reaches its minimum size, the low-density inner disk starts to fill in on viscous timescale (b)) during ~ 30 days while turning optically thick and increasing the accretion onto WD (c)); this is the X-rays on/optical low state phase with a duration of ~ 40 days. As accretion to the WD has been increasing due to the "new" viscosity of the filling-by-accretion disc at stage d), it reaches $\dot{M}_{\rm crit}$, completing the cycle (Reinsch et al., 2000).

As can be seen in Figure 5.14, the transitions between X-rays on/off appear to be really rapid ($\geq$ 2 days) and the expansion/contraction model of Reinsch et al. (2000) is only applied to the optical data (panel b), solid line). Including that the model is based on the expansion of the photosphere radius several times its original size(≤ 4), Hachisu & Kato (2003) argued that the contraction/expansion timescales are on the order of Kevin-Helmholtz timescales of the photosphere (much more than the observed X-ray transitions), which rules out the original idea of Reinsch et al. (1996) as the only reason of the anti-correlation.

In order to solve then the recurrency mystery of this supersoft[16], Hachisu & Kato (2003) proposed a model that does not use changes in the viscosity of the disc to explain the anti-correlation but it is based in the expansion of the accretion disc under the action of a strong optically-thick wind from the WD, which increases the optical radiation ($\sim$ 1 mag) while absorbing the supersoft X-ray emission (see Figure 5.17a). Going step-by-step, the first one is taken as the sine qua non condition that accretion onto the WD has to be rapid (Figure 5.18, A). In response to this

[15] The disc viscosity coefficient increases with $T_{\rm disc}$ through the dependency with the speed of sound in the medium.

[16] Also, applicable to the Galactic counterpart of RX J0513.9-6951, V Saggitae (Hachisu & Kato, 2003), although its optical light curve is CAL 87-like.

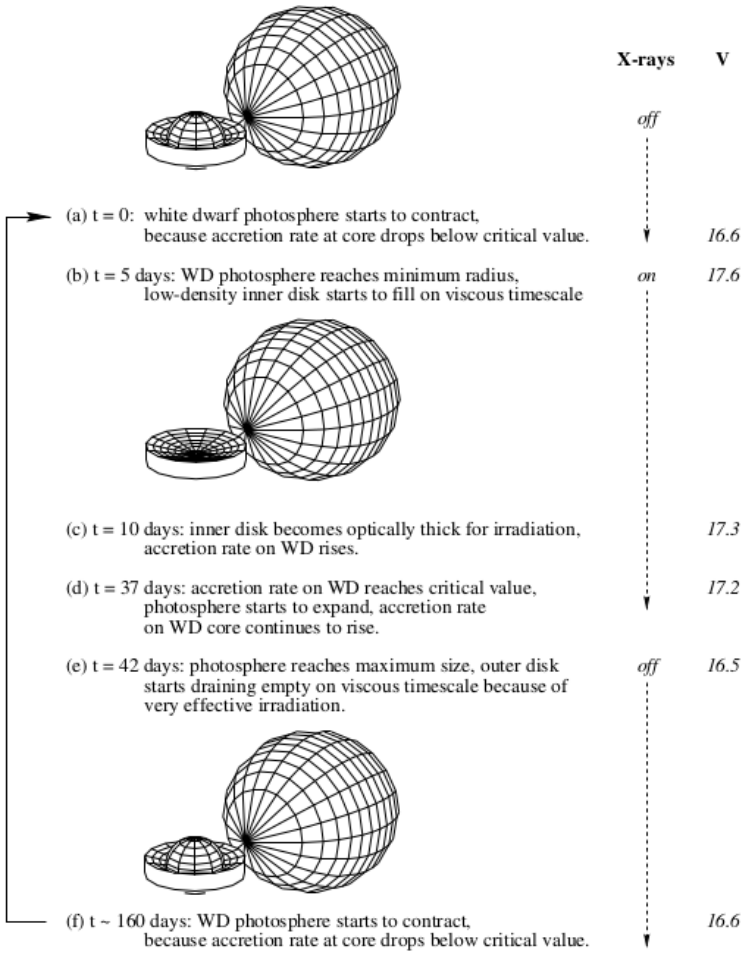

Figure 5.16: Photospheric radius adjustments to explain RX J0513-9-6951. From Reinsch et al. (2000).

rapid accretion, mass of the WD envelope rapidly increases and wind is accelerated deep inside the photosphere: an optically-thick wind. Strong winds makes the disc to expand several times (≈three times the Roche lobe radius in Hachisu & Kato (2003), Figure 5.17a) , which provokes a raise in the optical magnitude at Figure 5.18 B, as the disc is the main contributor in these wavelenghts. An optically-thick $\dot{M}_{\rm wind} \approx 10^{-8} M_{\odot} {\rm yr}^{-1}$ surely absorbes supersoft emission, causing the rapid drop in X-rays onto off states at high optical phase. In the same way that Reinsch et al. (1996) contraction, the photosphere of the WD keeps on expanding as long the accretion does not stop (Figure 5.18 B→C) while $\dot{M}_{\rm wind}$ keeps on increasing. The effect of the winds in the secondary is to strip off its surface layer, which is lost from the system ($\dot{M}_{\rm strip}$, proportional to $\dot{M}_{\rm wind}$). Once $\dot{M}_{\rm strip}$ is above the MT from the

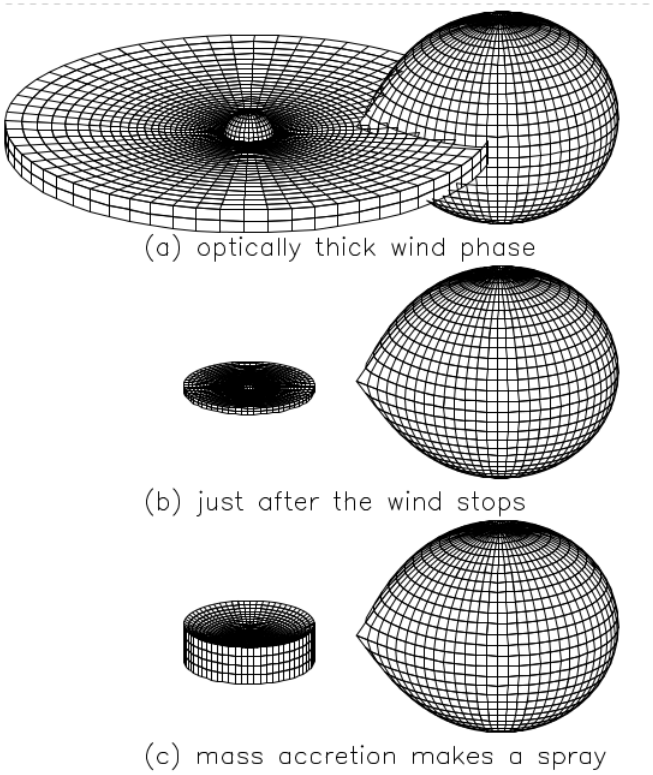

Figure 5.17: Step-by-step diagram of the action of an optically thick wind from the WD to explain RX J0513.9-6951 optical light curves. From Hachisu & Kato (2003).

secondary, the accretion onto the WD is still going on by draining the disc in the viscous timescale of the disc, $\sim$ 20 days (Figure 5.18 C$'$). After this, as accretion onto WD stops and the WD envelope has lost mass, the photosphere shrinks to its unexpanded size and the optical luminosity decreases until the wind stops (D at Figure 5.18). As the wind stops, also the disc returns rapidly to $\sim$ its unexpanded size (Figure 5.17b), decreasing even more the optical magnitude (D$\rightarrow$E in Figure 5.18) in several dynamical timescales i.e. orbital periods, while the supersoft X-ray emission is now visible (X-rays on state). Mass transfer from the secondary to the disc re-start at point E and the path E$\rightarrow$F is also done rapidly (few dynamical timescales). At F, the disc creates an spray (Figure 5.17c) surrounding the outer disc, which is approximately the start of the filling up of the disc on viscous timescales $\approx$ 20 days. After that time, the rapid accretion onto the WD begins and system returns to point A, which is the arbitrary starting point of this explanation.

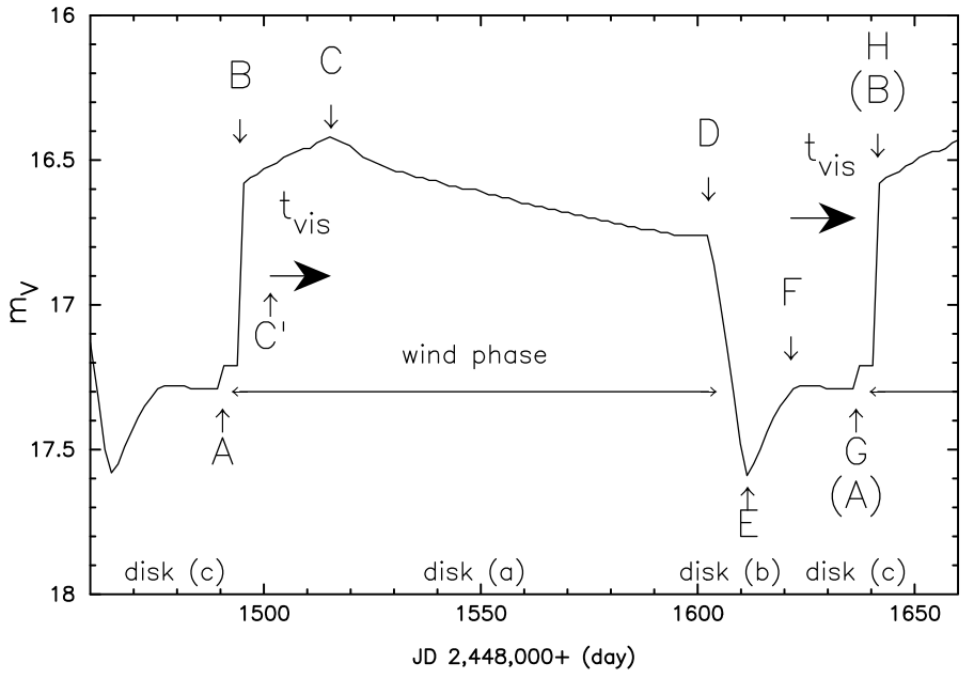

Figure 5.18: Magnitude variations in the limit cycle model proposed by Hachisu & Kato (2003) to explain RX J0513.9-6951 variability. From Hachisu & Kato (2003).

As seen, both ideas are quite complex to understand and great efforts have been made to confirm if they have some empirical grounds. McGowan, Charles, Blustin, Livio, O'Donoghue & Heathcote (2005) found that the expansion behaviour is most certainly true in RX J0513.9-6951 based in its UV and optical light curves: the raise in UV emission occurs before the raise in optical in low optical states, corresponding to a decrease in the X-rays in the light curve. In practice, this means that the evolution of the X-rays outburst leads to the peak in UV, which confirms an expansion of the photosphere or the disc. This, and the fact that winds of $\sim$ 4000 km/s have been found for this SSS are certainly in favour of Hachisu & Kato (2003) model.

Not everything are good news though: the Hachisu & Kato (2003) model could explain the differences in the duration of high optical states (ranges between 63 and 171 days from Burwitz, Reinsch, Greiner, Meyer-Hofmeister, Meyer, Walter & Mennickent, 2008) by changes in mass transfer rates from the secondary, while the duration of low optical rates is practically constant ($\sim$ 40 days) at those mass transfer

rates. Burwitz, Reinsch, Greiner, Meyer-Hofmeister, Meyer, Walter & Mennickent (2008), by taking account all of the optical data up-to-that-date, found that the expected correlation between short low optical states preceding long high optical states predicted by Hachisu & Kato (2003) model, was not seen in reality. Also, they claimed, based in a stability analysis of the model, that the mass accretion onto the WD can always adjust to the wind from the photosphere, therefore, there is no wind to stop the MT from the secondary, avoiding a limit-cycle model. As it is evident now, this thesis only shows the different hypothesis to explain the variability of SSSs, but it is wiser not to take any side in this still hot-modelling problem.

Chapter 6

Description

6.1 Fields

The Large Magellanic Cloud (LMC), an irregular barred galaxy with a mass of $\sim 10^{10} M_{\odot}$, is the largest satellite of the Milky Way. The hydrogen column densities along the line of sight of interstellar gas lies in a range of 5×10^{20} to 3×10^{21} cm^{-2} (see Kuuttila, Gilfanov, Seitenzahl, Woods & Vogt, 2019; Gänsicke, van Teeseling, Beuermann & de Martino, 1998) which implies that the absorption due to galactic gas principally affects those X-rays with energies less than 0.5 keV. The LMC was, in fact, the first external galaxy to be detected at X-ray energies (Mark et al., 1969) (see Figure 6.1).

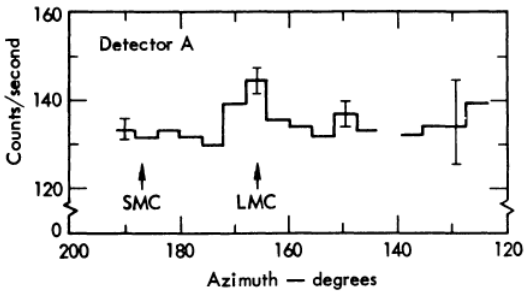

Figure 6.1: Count rate observed in the range 1.5-2.5 keV (X-rays) of the LMC. From Mark et al. (1969).

The following subsections deal with the objects of interest in this study: they are four SSSs; CAL 83, CAL 87, RX J0550.0-7151 and RX J0513.9-6951 plus three supernova remnants; SNR N103B, SNR 0519-69.0 and SNR 0509-67.5. As this study is focused mainly on SSSs, a brief description is given of what are supernova remnants (SNRs).

SNRs are a diffuse, expanding nebula that results from a supernova explosion: it consist of material ejected from the supernova explosion and interstellar material swept by the ejecta. Closer circumstellar matter ejected by the progenitor system before explosion may also be included. In the interaction zone between the ejecta and the circumstellar matter, strong forward and reverse shocks are formed. SNRs can have very soft X-rays spectra (Di Stefano et al., 2004). To illustrate the X-rays spectra of SNRs, the ASCA spectra obtained by Hughes et al. (1995) of all the SNRs in this study are shown in Figure 6.2. They are powerful X-rays and radio emitters due to the high temperatures of the plasma that is heated by the forward and reverse shocks; as the supernova ejecta that contains information about the SN progenitor and the explosion mechanisms is metal-rich matter, the spectra of SNRs contain prominent emission lines (Kosenko et al., 2010).

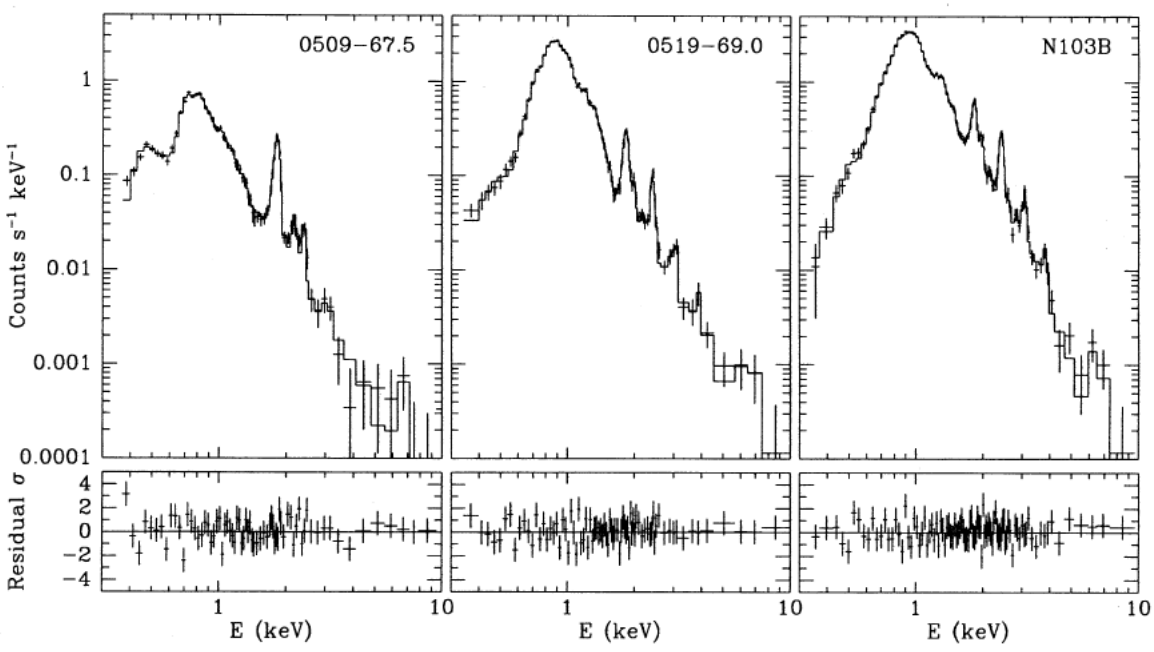

Figure 6.2: ASCA X-rays band spectra for the SNRs in this sample; SNR 0509-67.5, SNR 0519-69.0 and SNR N103B. From Hughes et al. (1995).

There is an ample concensus that the three SNRs in this sample are remnants of SNe Ia (see Badenes, Harris, Zaritsky & Prieto, 2009). If there are not high energy photons ahead the expanding shock that would increase the hypothetical nebular emission ([O III], debatable) from the pre-explosion nebulae, this unperturbed relic should put more evidence in favour of the SD channel, given that a supersoft phase throughout the mass transfer to the degenerate WD is expected. Now, if some nebular emission is detected from the images of regions where we know there are accreting WDs passing through a persistent supersoft phase, both roads connect to the conclusion that accreting WDs are the progenitors of at least some SN Ia, due to the absence of large supersoft emission from the DD channel.

With this in mind, the main goal of this thesis is clear: by taking images of known SNRs and SSS in a filter centered at [O III]λ5007Å and a broadband filter containing this line (e.g., Johnson V), the subtraction of these images will contain only the true emission of the line surrounding the object. In that case, physical fluxes can be obtained and compared to previous studies, in particular, for the unique CAL 83 nebula. If no emission is found, upper limits still may be put to the [O III] luminosity of these objects, thus directly connected to the density of the ISM, which could inform something about the evolutionary path of these objects.

6.2 Targets

6.2.1 CAL 83

CAL 83 was discovered in the original Einstein survey of the LMC (Long et al., 1981), identified as a 17^m variable blue stellar object; it is the prototype of the SSS class with orbital period of 1.04 days (Hasinger, 1994). Gruyters et al. (2012) estimated an average value for the electron density of $n \sim 10$ cm^{-3} which is consistent with the value of Remillard et al. (1995) using the ratio of sulphur [S II] λ6716/[S II] λ6731 at 7.5 pc from the source. The coordinates for this source obtained from SIMBAD[1] are: $\mathrm{RA}_{2000} : 5^{\mathrm{h}}43^{\mathrm{m}}34^{\mathrm{s}}.13$ and $\mathrm{DEC}_{2000} : -68°22'21''.89$.

[1] http://simbad.u-strasbg.fr/simbad/sim-id?Ident=CAL%2083

6.2.2 CAL 87

Also discovered in the first Einstein survey (Long et al., 1981), roughly a factor of four fainter than CAL83 (Hasinger, 1994), although it is and eclipsing binary with an eclipse depth of 2 mag, V mean magnitude $\sim 19^m$ and period of 10.6 hours (Cowley et al., 1990). From observations, it is suggested that we are seeing only the accretion disk and the WD must be more luminous (Starrfield, 2004). The celestial coordinates used in this thesis, from SIMBAD[2], are RA_{2000} : $5^h46^m46^s.54$ and DEC_{2000} : $-71°08'53''.9$.

6.2.3 RX J0513.9-6951

The X-ray variability of this source was discovered during the ROSAT All Sky Survey (Schaeidt et al., 1993). RX J0513-6951 is the most luminous of the known SSSs in the Milky Way or the Magellanic Clouds. The 0.76-day binary period is well-determined from optical light curves from the MACHO project (Hutchings et al., 2006). RX J0513-6951 displays some unusual characteristics such as repeated X-rays outbursts on timescales of years (Crampton et al., 1996). The celestial coordinates for this SSS are RA_{2000} : $5^h13^m50^s.8$ and DEC_{2000} : $-69°51'47''.0$ from SSSCAT[3].

6.2.4 RX J0550.0-7151

As this SSS is the less studied, we provide almost all of the information in the literature. RX J0550.0-7151 was not detected by *Einstein* but was discovered by Cowley et al. (1993)[4]: it lies $\sim 45'$ SW of CAL 87 at RA_{1950}: $5^h50^m2.^s6$ and DEC_{1950}:$-71°51'29.6''$. Its X-rays spectra is shown in Figure 6.3; see that the spectra of RX J0550.0-7151 is softer and brighter than CAL 87 (at the moment of discovery). Since its discovery, it has been mentioned in less than twenty references (by SIMBAD), and they mostly refer to the symbiotic nature of this object, which was first mentioned by Schmidtke & Cowley (1995)[5] due to the position being nearly coincident with a red star (V = 13.53, B-V = +1.45, U-B = +0.86) and verified by the presence of Balmer emission lines superposed on the spectrum of a cool star

[2]http://simbad.u-strasbg.fr/simbad/sim-id?Ident=CAL+87&submit=submit+id
[3]http://www.mpe.mpg.de/~jcg/sss/ssscat.html
[4]Though they have not provided much information about this SSS.
[5]With improved location, RA_{1950}: $5^h49^m46^s.7$, DEC_{1950}:$-71°49'38''$.

(Charles et al., 1996), which is a characteristic of symbiotic stars[6]. The coordinates of this object were transformed to RA_{2000} : $5^h50^m0^s.0$ and DEC_{2000} : $-71°52'9''.0$ from SSSCAT[7] and these were used in this thesis.

Since its characterization during the ROSAT All-Sky survey where this source presented its first (and unique) off-state (Reinsch et al., 1996), there have been no X-ray detections nor even a radio detection made by Fender et al. (1998) (also they do not obtained emission from CAL 83 and RX J0513.9-6951), who puts in doubt the nature of this object. The name used by this survey was RX J0550-71 which SIMBAD associated with RX J0550.0-7151. The mismatch between the names may be due to the 1950 vs J2000 coordinates, and it happens in several papers such as Reinsch et al. (1996)(RX J0549.9-7151) and Kahabka, Haberl, Pakull, Millar, White, Filipović & Payne (2008) (RX J0550.9-7151)[8]. Even if this mistake does not seem terrible, what is more sensitive is that these works used this SSS as a symbiotic system, even if Schmidtke et al. (1999) pointed out that the observation of RX J0050.0-7151 (another mismatch) was blended with RX J0549.8-7150 and that subsequent analysis (H. C. Thomas, 1996, private communication) resolved the two sources[9]. This source was observed again with Chandra ACIS-S (PI: Greiner), but it was not detected by Orio et al. (2007).

A brief summary from all the SSSs in the LMC of this work from Greiner (2000) is given below.

Table 6.1: Table of SSSs

Name	$L_{\rm bol}$ (10^{37}erg s^{-1})	$T_{\rm eff}$ (eV)
RX J0513.9-6951	$0.1-6$	$20-30$
RX J0550.0-7151	-	$25-40$
CAL 83	<2	$39-60$
CAL 87	$6-20$	$50-84$

[6]See Kenyon & Webbink (1984) for an excellent work addressing the spectral features of these objects, modeled by accounting the contributions of the ionized nebulae, a hot component, usually a WD surrounding by a accretion disk, and the cool giant.

[7]http://www.mpe.mpg.de/j̃cg/sss/ssscat.html

[8]They explicitly indicated that this SSS does not have optical counterpart.

[9]This remained a mystery because RX J0550.0-7151 faded below the detection level in the ROSAT All-Sky survey, 1995 data.

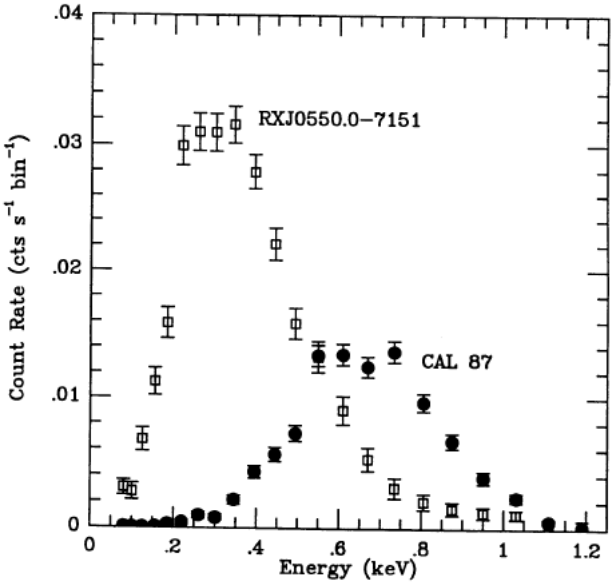

Figure 6.3: X-ray spectra of RX J0550.0-7151 and CAL 87 using ROSAT, count rate per bin vs energy. From Cowley et al. (1993).

6.2.5 SNR N103B

The young supernova remnant (SNR) N103B is the fourth brightest X-rays remnant in the Large Magellanic Cloud (van der Heyden et al., 2002). Its extent is about 3 pc radius, its X-rays luminosity in the $0.15 - 4.5$ keV band is 1.5×10^{37} (Hughes et al., 1995). By its light echoes, Rest et al. (2005) estimated the age of N103B to be 860 yr and it is confirmed a SN Ia remnant by light echo spectra although this is still debatable (see Someya et al., 2014)[10]. Optically, N103B consists of small bright knots which show the usual set of emission lines seen in most supernova remnant: [O III] λ5007, [S II]$\lambda\lambda$6716, 6731, Hα (Hughes et al., 1995). The equatorial coordinates used in this thesis are $\mathrm{RA}_{2000} : 5^{\mathrm{h}}08^{\mathrm{m}}59^{\mathrm{s}}.7$ and $\mathrm{DEC}_{2000} : -68°43'35''.5$ from Chandra SNR Catalog[11].

6.2.6 SNR 0519-69.0

Its radial size is 3.6 pc (Hughes et al., 1995). Its spectra is Balmer dominated indicating conditions of low excitation. Its age, from light echoes, is 600 ± 200 years

[10]Based on the study of the ISM surrounding SNR N103B, it was found that the progenitor of this remnant consisted of H-dominated plasma, in other words, it should have a Type II progenitor.

[11]https://hea-www.harvard.edu/ChandraSNR/SNRJ0509.0-6843/

(Rest et al., 2005).

The remnant was studied in X-rays by Hughes et al. (1995), the SNR is oxygen-poor and iron-rich and must be a remnant of a thermonuclear supernova (SN Ia) explosion (Kosenko et al., 2010). The celestial coordinates of this source are RA_{2000} : $5^h19^m35^s.14$ and DEC_{2000} : $-69°02'18''.05$ from SIMBAD[12].

6.2.7 SNR 0509-67.5

Of the four LMC SNRs that have been confirmed as a SN Ia remnant, the youngest and most symmetric of these is SNR 0509-67.5 (Edwards et al., 2012). Its size is about 3.3 pc (Hughes et al., 1995). By looking its light echoes, Rest et al. (2005) set an age of 400 ± 50 years. Its spectra is also Balmer dominated. No companion has been found near the centre of the SNR (Schaefer & Pagnotta, 2012); it was tentatively concluded that it is a result of a double degenerate channel. The equatorial coordinates were fixed at RA_{2000} : $5^h09^m31^s.0$ and DEC_{2000} : $-67°31'18''.0$ from SIMBAD[13].

6.2.8 RP 1406

Not much information we have about this planeraty nebulae; only the catalog where it was discovered and its actualization (Reid & Parker, 2006). In the following table the known physical parameters of this object are given:

Table 6.2: Table of RP-1406 data

Cat. Ref.	Other Cat. Ref.	RA J2000	DEC J2000	Dia (arsec)	Dia (pc)	V helio
RP1405	J35 LM2-18 SMP-54	05 22 42.93	-68 39 24.8	8.7	2.11	277.6

The diameters, column 5, including the extended halos have been measured on the Hα maps. Conversion of diameters to distances in parsec have been provided in column 6. These are based on an LMC distance of 50 kpc ±3 kpc (Reid & Parker, 2006).

[12]http://simbad.u-strasbg.fr/simbad/sim-id?Ident=SNR+0519-69.0&submit=submit+id
[13]http://simbad.u-strasbg.fr/simbad/sim-id?Ident=SNR+0509-67.5

6.3 Nebulae

For all of the objects in our sample, only CAL 83 has an ionization nebula (Remillard et al., 1995). One problem arises immediately when looking at its nebula in Figure 6.4; the observed nebula of CAL 83 is not homogeneous. This poses a problem, as already encountered by Gruyters et al. (2012), at computing line intensities from CLOUDY.

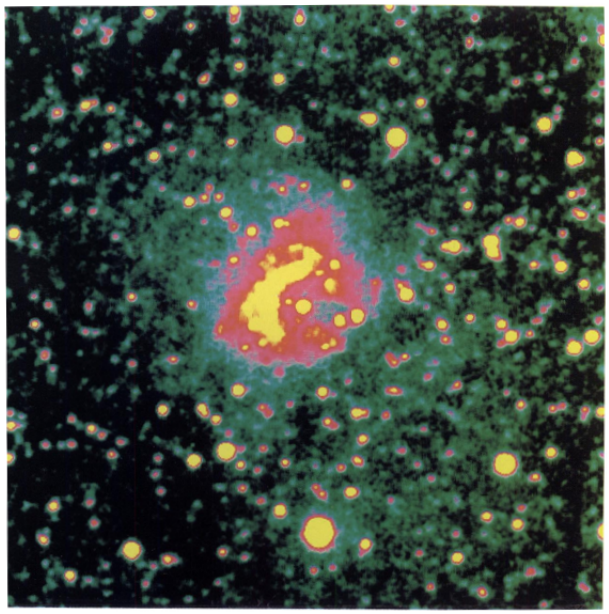

Figure 6.4: [O III] image containing CAL 83 nebula from Remillard et al. (1995).

For all of the other SSSs, Remillard et al. (1995) put an upper limit on the [O III] luminosities of $L \sim 10^{34.3}$ erg s^{-1} at 7.5 pc from the source, more than a factor ten below the value found for CAL 83 nebula. The main goal of this thesis is to detect emission, or obtain improved upper limits, around these SSSs plus three well known Magellanic SNRs. The limits obtained for those objects can be compared directly to measured values of the [O III] line from spectra at a different distances from the sources as presented by Kuuttila, Gilfanov, Seitenzahl, Woods & Vogt (2019).

6.4 Summary of the data

6.4.1 Data

Images at two epochs, December 12, 2015 and February 8, 2016, were taken with the Inamori Magellan Areal Camera and Spectrograph IMACS[14] of the Magellan Baade Telescope at LCO, using all-transmitting (all-spherical optics) f/4.3 long camera (known as f/4) for direct imaging. The f/4 camera, with the eight mosaics of $2k \times 4k$ (MOSAIC3), illuminates a 15.4×15.4 arcmin field, which corresponds to a pixel scale of 0.111 arcsec per pixel. Two different filters were used for each observation: Johnson-Cousins-Bessell V filter ($5200 - 7750$ Å) and a narrow filter centered at the observed wavelength of the [O III] 5007Å transition. The transmission curves, in comparison with Magellanic Clouds Emission Line Survey (MCELS) [O III]-filter and Magellanic Cloud Photometric System (MCPS) Johnson B and V filter, can be seen in Figure 6.5. To remove the instrumental signatures, bias and flat-field images were taken at each observing epoch. A log of the observations is given in Table 6.3.

Table 6.3: Summary of observations

Epoch	ID	central RA (h:m:s)	central DEC (d:m:s)	Exposure [O III] (sec)	Exposure V Bessell (sec)
12/12/2015	CAL 83	05:43:52.5	-68:20:17.3	~ 1200	~ 300
12/12/2015	CAL 87	05:46:23.9	-71:06:35.4	~ 1800	~ 600
12/12/2015	RP 1406	05:21:17.1	-68:37:27.2	~ 800	~ 270
12/12/2015	RX J0513.9-6951	05:13:23.8	-69:49:50.1	~ 1800	~ 600
12/12/2015	SNR 0509-67.5	05:09:08.3	-67:29:06.0	~ 1200	~ 210
12/12/2015	SNR 0519-69.0	05:19:10.1	-69:00:04.4	~ 1200	~ 300
12/12/2015	SNR N103B	05:08:31.8	-68:41:29.7	~ 1200	~ 280
08/02/2016	CAL 87	05:47:10.3	-71:06:48.5	~ 1800	~ 300
08/02/2016	RX J0550.0-7151	05:50:23.8	-71:49:59.3	~ 1800	~ 180

Unfortunately, both nights were non photometric, with low density clouds streaming through the sky. This prevented us from obtaining an absolute calibrated photometry and further complicated the analysis.

We notice that throughout this thesis we do not adopt the most appropriate distance to the LMC, $D_{\rm LMC}$ as 5×10^4 pc (Walker, 2012)[15] but, in order to compare

[14] http://www.lco.cl/telescopes-information/magellan/instruments/imacs/user-manual/the-imacs-user-manual

[15] This work is a recopilation of five different methods to measure distance and see how their consistency throughout the years.

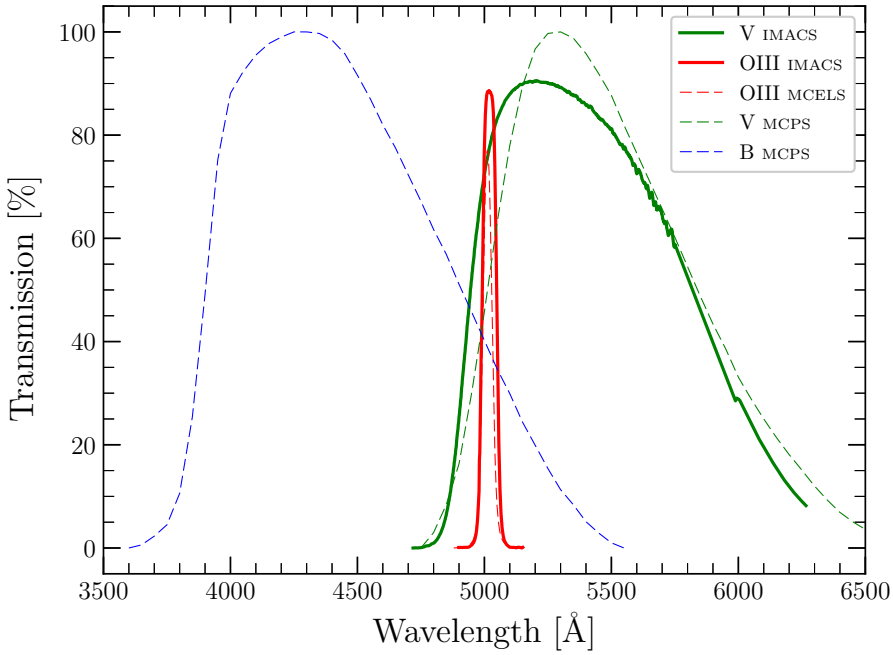

Figure 6.5: IMACS Bessell V and [O III], MCELS O III and MCPS Johnson V filters.

the results with e.g., Remillard et al. (1995), Rappaport et al. (1994), Gruyters et al. (2012), the distance is assumed to be 5.5×10^4 pc. With a pixel scale of $0.111''$, the projected distance in the LMC of one of our pixels is 0.029 pc.

Chapter 7

Method

The basic idea behind this work is that if we subtract from an [O III] narrow-filter image a V filter image conveniently scaled to match objects with no [O III] emission, the difference image should give us the emission in [O III] only. Any potential ionized nebula surrounding our objects of interest, e.g., SSS, PN, SNR or H II region, will thus be revealed.

In order to do this, we need to do bias and flat-fielding correction, then align the images at least in pixel-wise sense, match the shape of the PSFs, match the intensity scale of the pixels, and after that, do subtraction between the different filter images, hopefully stacked to increase the signal-to-noise ratio.

In principle, this did not seem a difficult task, as long as we used the right tools: to reduce the images we use an implementation of the typical astronomical software IRAF, PYRAF[1].

One collaborator, Armin Rest, suggested that the best way to align the images was using the SWARP code. His pipeline PHOTPIPE does difference imaging taking this route, SWARP + HOTPANTS. With the differenced images, we find the constant that transforms counts to energy. Lastly, we measure the flux radially, from the center of the objects to approximately 25 pc from the SSS or the SNR.

[1] https://github.com/spacetelescope/pyraf

7.1 Reduction and WCS

As we stated above, the first step is simple and straightforward: we take the IMACS chip where the object had been centered, with their respective calibration images, and reduced them. After that, we write in the header the WCS solution obtained by ASTROMETRY.NET.

7.1.1 PYRAF

Doing a PYTHON code in a ASTROCONDA[2] installation, we used the typical IRAF reduction package, CCDRED: ZEROCOMBINE creates a master bias frame (by coaddition of individual bias images), FLATCOMBINE creates a normalized master flat frame, and apply both corrections to all the science images with CCDPROC task. No anomaly was found in this process. Even though it may seem evident, bias and flat-fielding images were used for both filters.

7.1.2 ASTROMETRY.NET

In order to do a good image subtraction, the images must contain an accurate WCS. Headers of the images have WCS keywords that corresponds to a reference point in the sky and its projection in the pixel-space, and the transformation matrix world-to-pixel, but it was useless as we cannot reproduce the large field of view of IMACS using its WCS.

So in a sense, we needed to construct an appropriate WCS from scratch in order to optimize the time execution of the next code PHOTPIPE; we use the command-standalone version of ASTROMETRY.NET[3] (Lang et al., 2010). Basically, this code, after detecting the brightest stars in a query image, starts forming "quads" (set of four stars), spread in the whole image if possible, and keeps its geometrical shape in *hash codes*, as shown in Figure 7.1. The hash codes have the property to be invariant under translation, rotation and scaling of the star positions, so if we have a good map of the sky with its quads, it is easy to compare their hash codes.

With an all-sky database as USNO-B1 and 2MASS, people from ASTROMETRY.NET formed several sky-indexes containing the position of the stars in the catalogs, their quads and subsequently *hash codes*. Taking a certain portion of the sky (therefore,

[2]https://astroconda.readthedocs.io/en/latest/
[3]https://github.com/dstndstn/astrometry.net

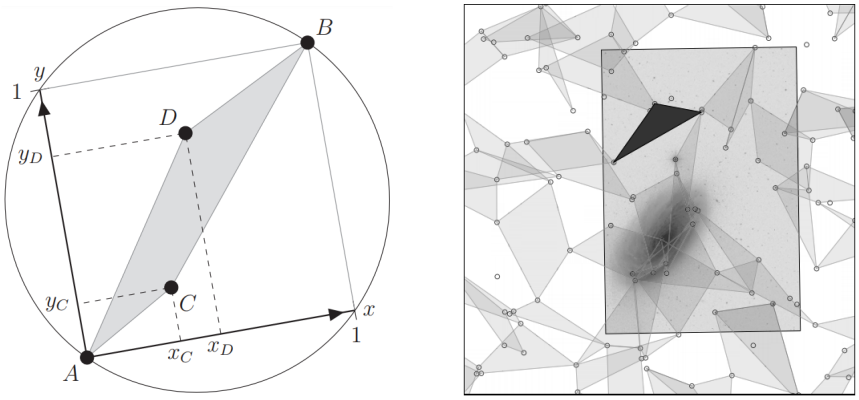

Figure 7.1: (Left) Representation of a ASTROMETRY.NET quad formed by {A, B, C,D} stars in the sky. The code saves the coordinates $\{x_C, y_C, x_D, y_D\}$ making a geometric *hash code*, which will be matched to the sky indexes database. (Right) The query image is plotted as a rectangle. One of the query quads matches one of the quads created in each of the cells, plotted as a shaded triangle.

indexes), hopefully by using user-input constraints, this region is gridded with cells about one third of the query image dimension, so each query image will have about one hundred query stars. For each cell, a fixed number of the (ordered by) bright stars (default at ten, in right Figure 7.1, five stars) are selected to create quads within an acceptable range of angular sizes and centers contained by. These quads are matched with the query quads via their respective *hash codes*, trying to find their potential rotation, scaling and position in the sky. The final result is an accurate solution of a WCS written in the header of the images, in SIP (Simple Image Polynomial) convention.

7.2 PHOTPIPE

PHOTPIPE is a pipeline created by Armin Rest and collaborators throughout decades of investigation and used in many successful time-domain surveys such as SuperMACHO, ESSENCE, PAN-STARRS1 (see Rest et al., 2014, and references therein). This system contains a lot of automatized tasks needed to, e.g., study transients on nightly basis. The implementation that we used in this thesis (under the permission of the author), is practically the same used in the last projects in which PHOTPIPE has been involved, e.g., Cowperthwaite et al. (2016), Rest et al. (2014). The whole code can be divided in different main sections: image calibration (e.g. bias and

flat-fielding), astrometric calibration, image coaddition and photometric calibration. Also, PHOTPIPE does difference photometry by using HOTPANTS and DoPHOT. Due to time constrain-learning phases, we used this system with images already reduced and with good-enough WCS (section above) saving us time and being less machine-demandant. In other words, we forced PHOTPIPE to coadd the images, do some "photometric calibration" and obtain differenced images. We expected that the final output, in the best case, subtract all the stars in our images and keep only the [O III]λ5007Å emission. By measuring its flux after finding the transformation between **counts-to-energy**, the results can be compared directly with CLOUDY models and values from Remillard et al. (1995) and Gruyters et al. (2012).

7.2.1 SWARP

From Bertin et al. (2002) and SWARP[4] Manual[5], there is not much to say about SWARP besides that it is a code created in order to align images with good WCS solution, which is this case. PHOTPIPE pipeline has a high dependence with SEXTRACTOR[6] tool, which is a very popular fast and automatized photometry code of the same creator of SWARP. To make easier and quicker the usage of this program, from all the science images of a certain field, PHOTPIPE, with its task **mkfieldfile4swarp.pl**, finds the center that all swarped images will be aligned to, which is passed onto SWARP manually. By forcing all the images to be centered at the same point, it is easy to coadd, if necessary, all the [O III] images into one stacked [O III] image (same for V images). This is done by the command **pipeloop.pl -red field chip -forcestage DOPHOTFIM-SWARPSTACK**. Until this point, PHOTPIPE has been doing its work flawlessly, as we can see in Figure 7.2, the stacked and astrometric aligned SNR 0509-67.5 science image.

It is worth noticing that, to get the best usage from SWARP and HOTPANTS, it is recommendable to create **mask** and **noise** images for each science one. In Figure 7.3, we can see the output from SWARP of the stacked noise and mask image: objects (usually stars), are masked given a certain threshold to a specific task of PHOTPIPE (MANA), while the generation of noise images are calculated as the shot noise & RON[7] of the science images. Also, we should be aware that SWARP creates catalogs of the

[4]https://www.astromatic.net/software/swarp
[5]https://www.astromatic.net/pubsvn/software/swarp/trunk/doc/swarp.pdf
[6]https://www.astromatic.net/software/sextractor
[7]https://www.eso.org/õhainaut/ccd/sn.html

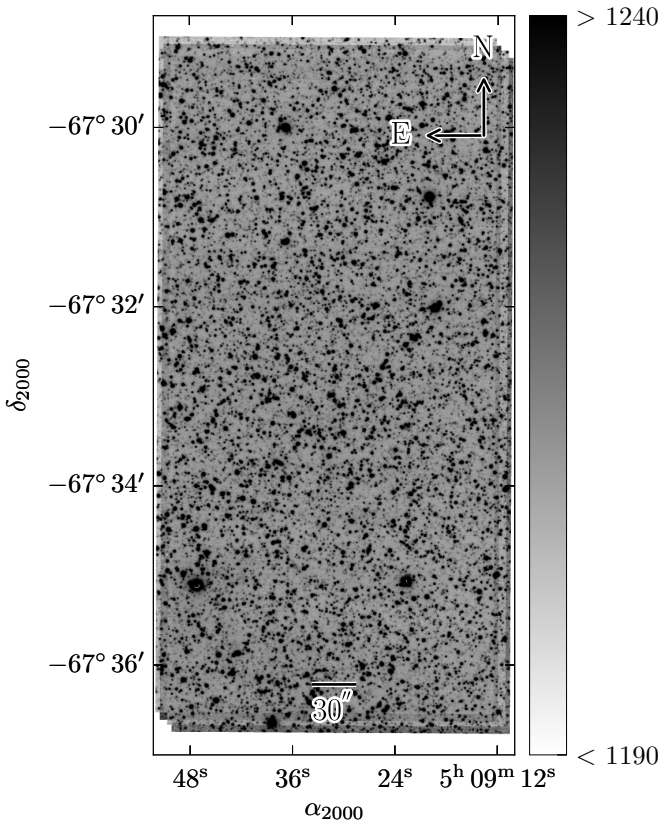

Figure 7.2: Science stacked image from SWARP of SNR 0509-67.5.

stars in the images of each field in almost every step, which are used in all following stages until the final results.

7.2.2 ABSPHOTOMETRY

Before differencing images, it is necessary to (PHOTPIPE) find a relation between the zeropoints of images from different filters. This is clearly related to one of the most important steps in the whole thesis that is to calibrate at least one of the images at the moment of counting the flux in a certain differenced area, thus, to find a *constant* to represent the transformation of counts to energy. The [O III] filter used to measure the emission in IMACS is not properly calibrated, then, we do not have any useful flux information from [O III] images besides counts. We have the information that IMACS V filter is a Bessell filter, so in theory, its zeropoint can be characterized approximating from, for example, the Johnson filters used in the Magellanic Cloud

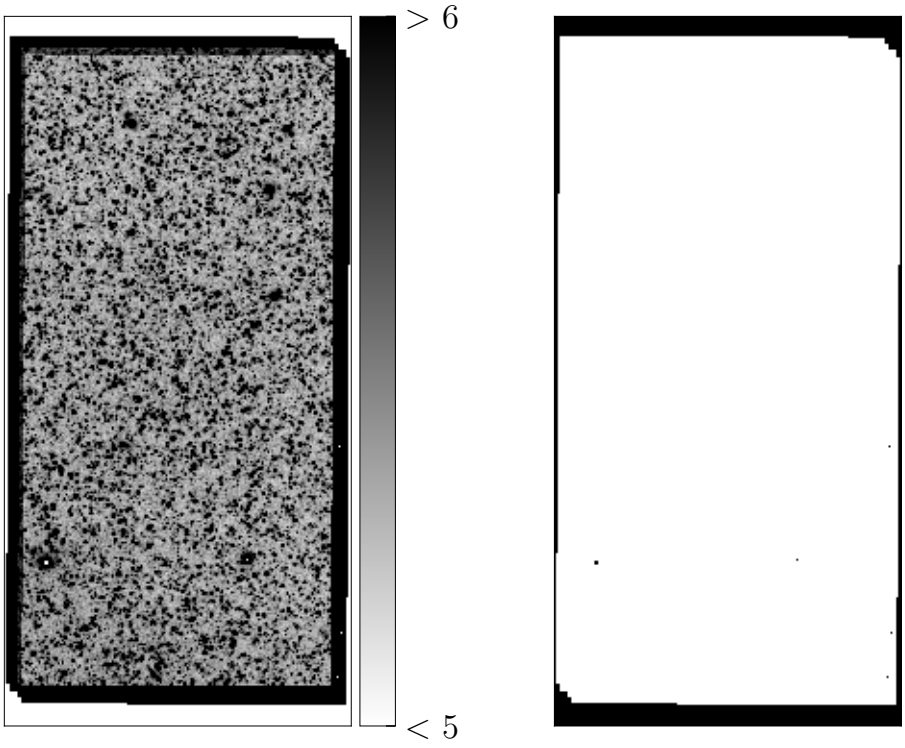

Figure 7.3: (Left) Noise stacked images from SWARP of SNR 0509-67.5. **(Right)** Mask image obtained by stacking the output images from SWARP of SNR 0509-67.5. White represents good pixels while black the masked pixels.

Photometric Survey (MCPS[8]) for the catalog of objects of the LMC (Zaritsky, Harris, Thompson & Grebel, 2004), with magnitudes placed in the Johnson-Kron-Cousins system (Landolt, 1992). In practice, this means that we also have Johnson U and B magnitudes.

As we have the transmission and the shape of the IMACS V and [O III] filters in Figure 6.5, and access to several flux-calibrated references stars from STScI[9] and ESO[10], we have, if we know (somehow or simply assume) the zeropoints ($Z_{\{O,V,B\}}$) of the filters and the spectra of some stars in these fields (or a relation between the

[8]http://svo2.cab.inta-csic.es/svo/theory/fps3/index.php?mode=browse&gname=Misc&gname2=MCPS
[9]http://www.stsci.edu/hst/observatory/crds/calspec.html
[10]https://www.eso.org/sci/observing/tools/standards/spectra.html

calibrated spectra and the unknown spectra), a rough calibration of the counts of the difference image can be made in the following way. Calling $\langle f_\lambda \rangle$ the mean flux of a star under a certain filter (centered in λ), we can write

$$\langle f_\lambda \rangle_{\text{FILTER}} = \frac{\int\limits_{\text{FILTER}} R(\lambda) f_\lambda(\lambda) d\lambda}{\int\limits_{\text{FILTER}} R(\lambda) d\lambda} \tag{7.1}$$

with $f_\lambda(\lambda)$ [erg s^{-1}cm^{-2}Å^{-1}] the calibrated flux of the reference star and $R(\lambda)$ a generalized filter function defined as the product of the atmospheric transmission, the mirror reflectivity, the optics transmission and the passband transmission (Bessell & Murphy, 2012). Assuming that the (unavailable) IMACS magnitudes of stars in our fields are equal to the MCPS counterpart, m_*, we obtain the corresponding flux $\langle f_* \rangle$ of each one of the stars MAGNITUDE EQUATION (Bohlin & Landolt, 2015) for IMACS/MCPS V FILTER and that the Vega magnitude is $m_{\text{VEGA}} \approx 0(0.03)$:

$$m_* - m_{\text{VEGA}} = -2.5 \log\langle f_* \rangle + 2.5 \log\langle f_{\text{VEGA}} \rangle \tag{7.2}$$

As a sanity test, let us do this: taking the Vega spectrum alpha_lyr_stis_005[11], we should find an good agreement between, e.g., the tabulated $Z^{\text{T}}_{\text{MCPS}_\text{V}}$ in MCPS filter description, 3.634×10^{-9}erg s^{-1}cm^{-2}Å^{-1}, and the (manually) derived using Equation 7.1 and the transmission curve for MCPS V filter ($Z^{\text{D}}_{\text{MCPS}_\text{V}}$). The ratio of both zeropoints is calculated as

$$\begin{aligned} \frac{Z^{\text{T}}_{\text{MCPS}_\text{V}}}{Z^{\text{D}}_{\text{MCPS}_\text{V}}} &= \frac{\int\limits_{\text{V}} R_\text{V} f_{\text{VEGA}} d\lambda \Big/ \int\limits_{\text{V}} R d\lambda}{3.634 \times 10^{-9}} \\ &= \frac{3.595 \times 10^{-9}}{3.634 \times 10^{-9}} \\ &\approx 0.99 \end{aligned}$$

which is close enough to the expected value of one. This fact assures us that using the derived fluxes owing the stellar spectra, the specific filters optics in Equation

[11] ftp://ftp.stsci.edu/cdbs/calspec/

7.2 and known m_{VEGA} for any filter, will lead us to a good-calibrated-magnitude in that filter. The same can be said in the other direction; with good-calibrated-magnitudes we will get $\langle f_* \rangle$. Thus, approximating IMACS to MCPS V-filters already gives us a rough calibration at dividing the real flux of the star by its instrumental flux (i.e. the counts), in the case of subtracting [O III] to V image and normalizing the difference counts by the latter. This is, for now, all the information we might get from the V magnitude of the MCPS catalog.

What about the [O III] magnitude? In practice, as we stated before, we only need to calibrate one filter in order to try to convert the difference counts to flux, and this treatment of V filter should be enough to do that in case we leave untouched the V image in the next stage[12], which, as a spoiler, was not the way we chose, as will be stated in Subsection 7.3.3. However, to make through the PHOTPIPE pipeline an [O III] catalog of the stars is a requirement. The only idea that appears naturally to us was using the MCELS [O III] magnitudes (with its corresponding calibration), assuming that there is a zeropoint shift, $\mathrm{C_O}$, between the instrumental magnitudes and MCELS ones in the form of

$$[\mathrm{O\ III}]_{\mathrm{MCELS}} - [\mathrm{O\ III}]_{\mathrm{IMACS}} = \mathrm{C_O} \tag{7.3}$$

which is reasonable because $\mathrm{C_O}$ should be close to zero[13]. This step is crucial because PHOTPIPE will not work correctly unless it has a stellar catalog of one of the images (see Subsection 7.2.3), in this case, [O III] image (for each field). It is good idea to use calibrated magnitudes (such as MCELS) rather than completely-artificial catalogs because, in principle, HOTPANTS will track the transformation between $\{Z_{\mathrm{O}}, Z_{\mathrm{V}}\}$ in the difference image O-V and this would give us more information about HOTPANTS subtraction.

As MCELS catalogs contains at most ≈ 6 stars per field (see up Figure 7.4 for CAL 83 field), it was easy for ABSPHOTOMETRY to fail when trying to find $\mathrm{Z_O}$ because of its strict constraints on position and magnitudes of the stars. So, in order to make through to HOTPANTS and try a calibration later (see Section 7.3), we decided to create a pseudo-artificial catalog with the PHOTPIPE task **cmp2cat.pl**; basically, this

[12]Do not forget the differences between the MCEPS and IMACS.

[13]In fact, the [O III] filter is more efficient than MCELS filter as seen in Figure 6.5 but not by much.

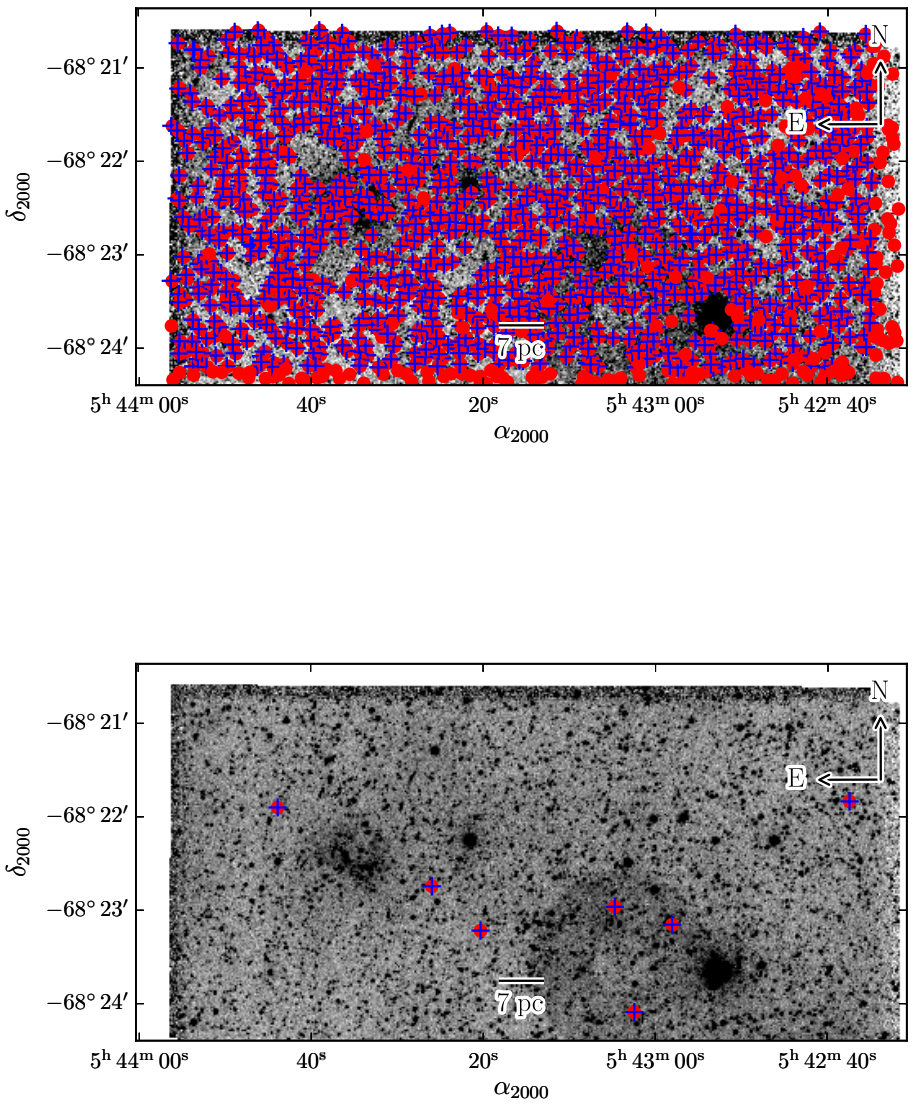

Figure 7.4: (Top) Red Points: stars whose magnitudes were calculated by adding Z_O to their instrumental magnitudes, collected in the DCMP Catalog. Blue cross represent ZAR stars that will be used to find the flux calibration in Section 7.3, for CAL 83 field. (Bottom) The same as the above plot, using instead of DCMP stars the seven real stars used to calculate Z_O.

task finds C_O from Equation 7.3 using the real MCELS magnitudes of the few stars in the fields (called REAL catalog) and the instrumental magnitude obtained directly by the measured flux (photometry) of those stars in SWARP catalog, and then apply it to all the stars of that catalog. In other words, we created a new big catalog with approximated real magnitudes that we called a DCMP catalog (see down Figure 7.4). Now, if we feed ABSPHOTOMETRY with the latter catalog[14], we will pass through it almost surely because it is more probable to find stars that satisfy the constraints.

7.2.3 HOTPANTS

Now we enter the last stage of PHOTPIPE: the usage of the image subtraction code High Order Transform of PSF and Template Subtraction, HOTPANTS[15] (Becker, 2015). HOTPANTS is designed to photometrically align one input image with a reference, after they have been astrometrically aligned, which is this case. This is an implementation-upgrade[16] of the well-known Alard algorithm ISIS (Alard & Lupton, 1999), also known as Optimal Image Subtraction (OIS) method, developed in Alard & Lupton (1998) and improved by using a spacial-varying kernel in (Alard, 2000).

HOTPANTS solves the main problem of difference imaging which is to find a convolution kernel (K) that matches the **Point Spread Functions** (PSFs) of two astronomical images, I, referred to the image, and T, the template. If we also can model the background difference between I and T using a 2D model, B, the difference image D can be written as the solution of the least-squares minimization

$$\sum_i D(x_i, y_i) = \min \left[\sum_i \left\{ \frac{[T(x_i, y_i) \circledast K(u, v)] - I(x_i, y_i) + B(x_i, y_i)}{\sigma(x_i, y_i)} \right\}^2 \right] \quad (7.4)$$

where (x_i, y_i) represents the position of pixel i, (u, v) are coordinates centred on the kernel, σ^2 is the pixel i variance and $\circledast$ is the symbol of convolution (Kerins et al., 2010). If we assume that the kernel can be decomposed into a linear combination of basis functions

[14] Usually called a dirty trick.
[15] https://github.com/acbecker/hotpants
[16] http://web.ipac.caltech.edu/staff/fmasci/home/astro_refs/HOTPANTSsw2011.pdf.

$$K(u,v) = \sum_{k=1}^{N_g} \sum_{p,q=0}^{p,p+q\leq M_k} a_{pq} u^p v^q e^{(u^2+v^2)/2{\sigma_k}^2}$$

where $a_{pq} \equiv a_{pq}(x,y)$ are coefficients that vary spatially (because the PSF varies across the image)[17]. Usually, the number of Gaussians components N_g, the gaussian widths σ_k, and the spatial order of the gaussians (confined in the maximum kernel size), M_k must be user-inputs. By default in HOTPANTS, $N = 3$, $M_k = \{6, 4, 2\}$ and $\sigma_k = \{0.7, 1.5, 3.0\}$, but it is highly recommended to find a $\sigma_{\rm MATCH}$ such that

$$\sigma_{\rm MATCH} = \frac{\sqrt{\left|{\rm FWHM_I}^2 - {\rm FWHM_T}^2\right|}}{2\sqrt{2\log 2}}$$

where $\rm FWHM_{I,T}$ is the average full width at half maximum of I and T in the whole image. Then, σ_k can be written as

$$\begin{aligned}
\sigma_1 &= 0.5\sigma_{\rm MATCH}; p+q \leq 6 \\
\sigma_2 &= 1.\sigma_{\rm MATCH}; p+q \leq 4 \\
\sigma_3 &= 2.\sigma_{\rm MATCH}; p+q \leq 2
\end{aligned}$$

while constrained by the size of the kernel, which is defined as $2\times\max\{\rm FWHM_I, FWHM_T\}$. Luckily, PHOTPIPE does several photometries at almost each one of the steps described here, so internally, it has implemented the determination of σ_k dynamically, adding, if necessary, more gaussians into the kernel. For the images of this thesis, PHOTPIPE uses $N = 4$ gaussian components, with $M_k = \{6, 4, 2, 2\}$ and $\sigma_k \approx \{1, 2.2, 4.5, 9\}$ and the spatial kernel size of ≈ 30 pixels, for IMACS chip 2 and 3. The same "decomposition" for a_{pq} can be made to $B(x,y)$

$$B(x,y) = \sum_{r,s=0}^{r,r+s\leq M_b} a_{rs} x^r y^s$$

[17]Eventually, a_{pq} are decomposed in terms of $\sum_{i,j} b_{ij} x^i y^j$ with b_{ij} constants to determine.

where a_{rs} are coefficients and M_b is the analogous of M_k, the degree of polynomial to model the background, in this case, $M_b = 1$. A complete and self-explanatory derivation of all the formulae can be found in Wozniak. (2008). The formal solution of the simplest problem, i.e., assuming a constant kernel across the image and no differential background, in order to find $\boldsymbol{a} = \{a_1, a_2...a_N\}$, can be written in matricial form (see Equation 7.4 and change $\sum_i \rightarrow \int dxdy$)

$$M\boldsymbol{a} = b$$

with

$$M_{ij} = \int \frac{C_i(x,y) \times C_j(x,y)dxdy}{\sigma(x,y)^2}, \quad b = \int \frac{I(x,y)C_i(x,y)dxdy}{\sigma(x,y)^2}$$

and

$$C_i = T \circledast K_i,$$

where the integral is over the whole image. All of the complex solutions, e.g., using space-varying kernel, $a \rightarrow a(x,y)$ and/or adding differential background, $B(x,y)$, can be expressed in terms of some C_i vectors. For example, if we add $B(x,y)$, the solution to this problem (Alard & Lupton, 1998), as a polymonial of degree one, i.e., $N_b = 3$, is

$$C_i(x,y) = \begin{cases} B_i \equiv x^{p_i} y^{q_i} & \text{if } i = 0..N_b \\ T \circledast K_i & \text{if } i = N_b..N_b + N_g \end{cases}$$

In practice, in order to find the best solution $D(x,y)$, i.e., $a_{pq}(x,y)$ coefficients of K, the program determines (or in this case, recieves a list of) objects to fill stamps in the image: one sub-stamp is centred in each object. If we assume that K is constant in each stamp, the procedure simplifies as

$$\int_\Omega dxdy \rightarrow \sum_k \int_{\Omega_k} dxdy$$

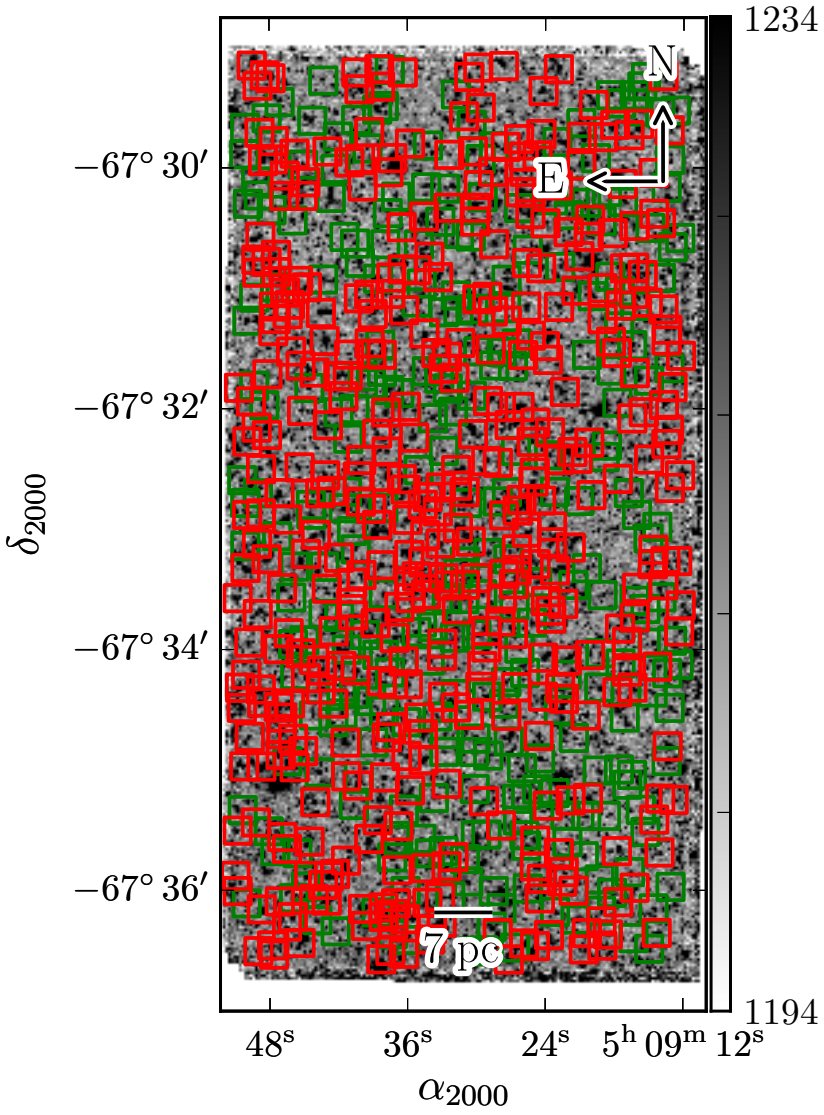

Figure 7.5: HOTPANTS output of the accepted (green) and rejected stamps (squares) in the determination of the kernel K to convolve for SNR 0509-67.5.

where Ω_k represents the stamp k. In a sense, what HOTPANTS does is calculate several local kernels, only to find the general solution for the image. In Zhao et al. (2012), we can find a very instructive pseudo-code sequence to find K in HOTPANTS and many spatial-varying kernels programs.

The number of stamps and the sub-stamps are fixed in this run to 30×60 and 7, respectively, for images of $2k \times 4k$ pixels^2. Not all of the stamps are going to

be useful to calculate the kernel. In fact, HOTPANTS defines a "good" stamp as a stamp that pass through rigorous constraints using different figures of merit such as the ratio of the empirical residual of a pixel value in differenced stamps versus the expected variance obtained by the convolution of the noise images. To reject a stamp is therefore necessary that it does not contain any good substamp that makes it pass the filters, so the code takes different sub-stamps in each iteration to make it valid.

As we can see in Figure 7.5, for SNR 0509-67.5, the number of red squares, i.e., rejected stamps, is far greater than the green squares, the accepted ones. This is expected though, because in principle HOTPANTS does not work for images in different filters, but as it is one of the most secure (and automated) way to find K and avoid to use brute machinery as in Graur & Woods (2019)[18], so we take the risk. One problem arises immediately; to create the noise images, it is necessary to have an accurate gain value of the instrument, which is not the case to the information given in the in the header of the images. In particular, the real instrumental gain is expected to be lower than the actual value therefore, the statistics, SWARP stacking and HOTPANTS subtraction should be affected.

How much does the gain affect the subtraction? First, we compare the difference image created by two consecutive [O III] images **(O-O)** and two consecutive V **(V-V)** images, exposure time of 300 and 70 seconds, respectively, of SNR 0509-67.5. The expected subtraction, in principle, should be really good and the statistics should show us that even if the gain is not well-known[19]. In Figure 7.7 we can see that the stamps to solve for K are well-distributed all over the image, which leads to a better subtraction, even if we are using a manual HOTPANTS configuration, i.e., not from PHOTPIPE. A priori, the useful statistics from HOTPANTS that we should use throughout this thesis are: **Final Figure of Merit of all the stamps** (**F.O.M**), which is defined as the ratio of the average variance of the subtraction versus the quadratic sum of the image and convolved noise images for GOOD stamps, and its corresponding standard deviation (**STD F.O.M**), the reduced $\boldsymbol{\chi_n^2}$ for the distribution of the differenced pixels with $\boldsymbol{n}$ the number of degrees (i.e. pixels), the global mean (**MEAN PIX**) and standard deviation of the pixels (**STD PIX**) used to determine the

[18]Their subtraction is simpler because they are using HST images, whose filters are already well-calibrated.

[19]$\mathrm{NOISE} = \left(\frac{\mathrm{COUNTS}}{\mathrm{GAIN}} + \mathrm{RON}^2\right)^{\frac{1}{2}}$, with RON the readout noise.

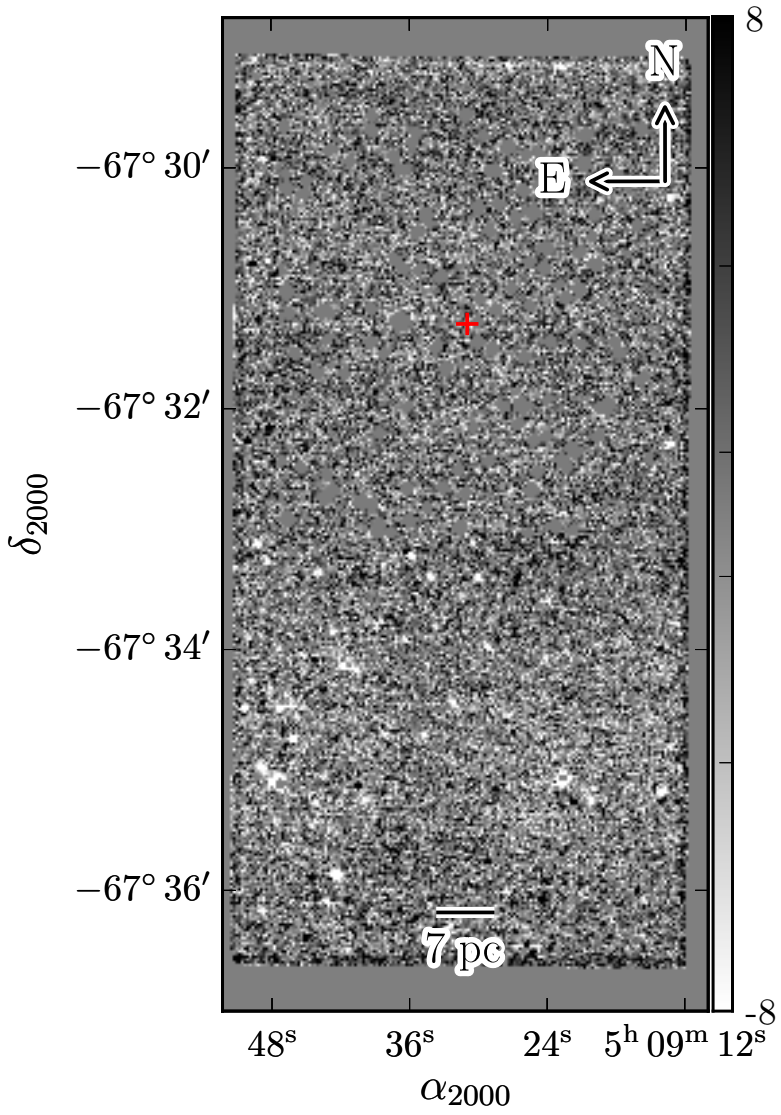

Figure 7.6: HOTPANTS difference image of SNR 0509-67.5 (red cross). At first sight, we cannot visualize any nebula-like structure in the whole image. It is not easy to see that for the area of interest, $\delta \approx 67^o30^{'} - 33^{'} \times 05^{\mathrm{h}}09^{\mathrm{m}}48^{\mathrm{s}} - 12^{\mathrm{s}}$, the residual stars are masked with zero value.

kernel K.

For both subtractions in Figure 7.7 and the one from Figure 7.6, we got Table 7.1, where we can see that the subtractions are statistically good if we take all the statistics (but reduced χ^2) made from the good stamps. These values are biased to-

wards better-than-realistic values, i.e., F.O.M is nearly one, which is the best expected value and MEAN PIX lies close to zero. On the contrary, the reduced χ^2 completely rejects the null hypothesis (i.e., how likely is to obtain D or any "extreme" difference image given T and I, in other words, how good was the fit of the kernel) for all the cases (p-values are zero). This is odd, because Alard (2000) should had found this issue in their goodness-of-fit tests. To explain this "bug", three possibilities have been thought: the degrees of freedom is way lower than the n (which does not make any sense), subtractions are very bad (which in cases O-O and V-V is clearly false), and/or the statistics, most notably, the expected noise which depends on the gain, are not reliable. So, as conclusion, we will show this information as a HOTPANTS result but we will take it with care, realizing that only MEAN PIX and STD PIX could be consider as "usable" as approximated estimates of the real values for the next stages.

Table 7.1: O-O, V-V and stacked O-V HOTPANTS subtraction statistics for SNR 0509-67.5: F.O.M, STD F.O.M, reduced ${\chi_n}^2$, n, MEAN PIX and STD PIX

	F.O.M	STD F.O.M	${\chi_n}^2/n$	n	MEAN PIX	STD PIX
V-V	1.018	0.062	1.160	8107445	0.878	13.038
O-O	0.909	0.049	1.261	7935096	-0.220	9.914
O-V	1.033	0.065	1.610	8439519	0.424	4.387

The last big question is: which image (V or [O III]) is the template?. In theory, the best subtraction is obtained by using the image with smaller FWHM as the template, so "blurring" the image with the best seeing. In practice, what we did was to **force [O III] image to be** I and normalize the differences by this image, while always convolving [O III] image because they "often" have smaller FWHM with respect to V counterparts[20].

7.3 Flux measurement

After obtaining the best PHOTPIPE difference images and their corresponding noise images for all the fields, we focus on how to obtain the surface brightness, flux and luminosity in order to compare with CLOUDY models described in section 3.1. This was done by creating a PYTHON code that takes as inputs the differenced science and

[20]Usually, the FWHM in both filters will be similar: the main differences are found in CAL 83, CAL 87 chip 3 and RP 1406.

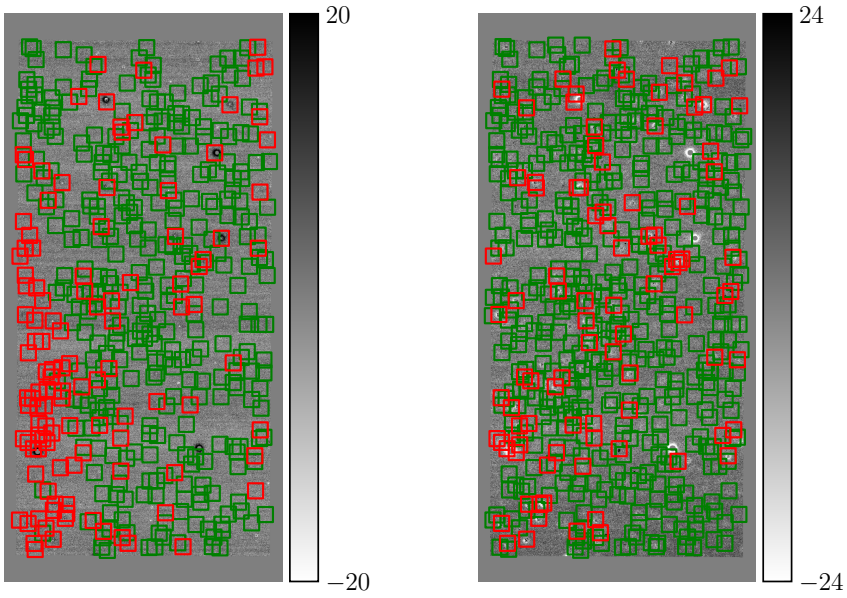

Figure 7.7: HOTPANTS difference image of (O-O) (left) and (V-V)(right) images of SNR 0509-67.5, along with their good (green) and bad (red) stamps. It is evident that the subtraction seems really good, as expected, the number of stamps increases in comparison to Figure 7.6 and their location is extended all over the image, near to the edges.

noise images, the SWARP V catalogs containing the photometry of V images and the [O III]DCMP catalogs[21].

7.3.1 Segmentation

The first step begins with the question: how do we discriminate what is emission from noise or residual flux from stars? As fair initial guess of an (emission) threshold would be **MEAN PIX** $\pm n$ **STD PIX** (with n a number) of the HOTPANTS output images. As explained before, PHOTPIPE has its unique peculiarities and methods, therefore we decided to (re)calculate the MEAN and STD directly from the difference image (and noise image when necessary), using safer constraints. We will not consider any pixel whose value is more extreme than ± 100 counts in any calculation. The idea is that we consider "emission" to the **filtered structures** (see next paragraph), negative or positive, that lie outside a certain pixel values range. After this first filter (± 100),

[21] As we will show, the differences on using REAL or DCMP catalogs are no more than 5% in radial profiles, which is reasonable.

we reconsider what is emission with respect of what is almost surely background: the second filter is that all the filtered structures whose values do not lie in the range $\pm$STD[22], will be called "emission". Any unfiltered pixel will be used to estimate a new background image.

To do the described procedure, we used the routine DETECT_SOURCES from PYTHON package PHOTUTILS DETECTION[23] to detect the emission. The inputs of this method are the data and its PHOTPIPE mask, the threshold, the **connectivity** and **npixels**. Connectivity (four or eigth) is the parameter that determines what is a neighbour/groups; four-connected pixels touch along their edges, eight-connected pixels touch their edges and corners, and npixels is the number of pixels (neighbours) above the threshold that make a zone of emission[24]. The output of this function is what we call a segmentation image.

For this thesis, we chose npixels= 20 and connectivity equals to four for all of the fields. The results do not depend much on the connectivity but do on npixels: in fact, an area of 20 pixels was chosen in order to avoid residual stars at looking the emission, whose peaks should be detected and their total areas are composed of about 20 pixels in the best cases based on a developed intuition and that the typical FWHM is more than 10 pixels. It would not be wise to set up a larger value of npixels, because we do not want to remove emission from the nebula itself. Many refinement could be done here with little effort, such as varying the npixels values. We did try some and found out that the main results and conclusions do not change.

As we stated, the main value of a segmentation image is to find an estimation of the background: we will show later that small deviations from zero of the mean of the background produce strong effects in the results that could be taken as signal. This makes it imperative, for instance, to verify if the background estimation done by HOTPANTS is good enough to avoid these spurious features. The idea, then, was to create linear and quadratic background images (i.e., adjusting functions of the form $Ax+By+C$ and $Dx^2+Ey^2+Fxy+Gx+Hy+J$ to the image pixels, respectively[25]) from the **unmasked pixels** using as a mask the inverse segmentation images, i.e., what should correspond to the background. Examples of the estimated background images are given in Figure 7.8, for the field CAL 83.

If the new background is accurate, we are ready to measure the flux after finding

[22]Assuming the MEAN is effectively zero for now.
[23]https://photutils.readthedocs.io/en/stable/detection.html
[24]Consider also the minus data case, i.e., below minus threshold.
[25]Based on this https://gist.github.com/amroamroamro/1db8d69b4b65e8bc66a6.

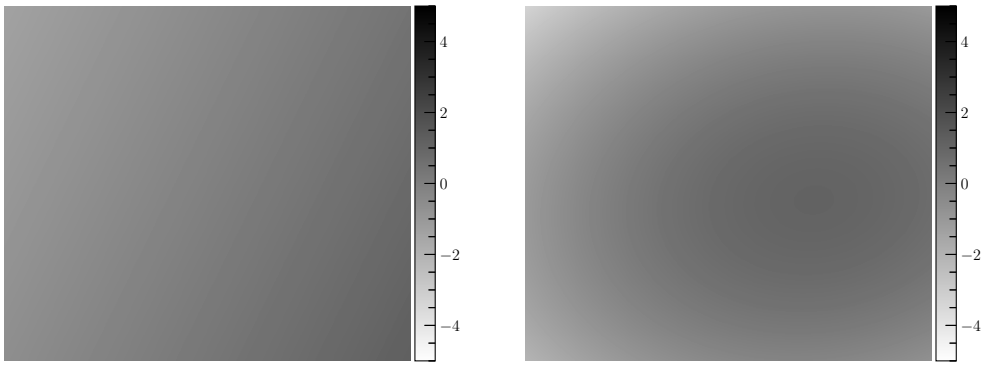

Figure 7.8: Background images created by masking the data image using as a threshold ±STD of the array to detect all but the background. (Left) Linear fit of the background, of the form $Ax + By + C$ with (x,y) the pixel position and A, B and C constants. The mean and standard deviation of the linear background is -0.052 and 0.573, respectively. (Right) Quadratic fit, $Dx^2 + Ey^2 + F^x y + Gx + Hy + J$, of the masked data. In this case, the mean is -0.008 and standard deviation 0.825.

the flux calibration. Our preferred background choice is linear. Assuming this case, we followed to set up a new threshold, stricter than the previous ones, because we want to find only the real emission, with the data already background subtracted. A good choice is then to chose the best hypothetical MEAN 0 ± 5 NEW STD, which is the STD of the new background subtracted data. With this, we run again the code DETECT_SOURCES and obtain the final segmentation images for each field. In case that the mask does not cover completely the flux residual object, we enlarged the mask of each source using the task DILATION from SCIPY[26]. In Figure 7.9, we see all the emission sources i.e., filtered objects in color and diluted mask in green, surrounding SSS CAL 83 source (Remillard et al., 1995), a zone-of-interest (about 50×40 pc^2) that clearly has a half-ring nebular-like structure, plus several stars that are brighter in O-V because the solution for K (kernel for convolution) did not fit well on those stars, or the difference in emission is indeed real.

CAL 83 is the best current example of a SSS nebula. What would we see in a field where no structures are detected? Figure 7.10, shows the final segmentation image of SNR 0509.67-5, where only some residual stars are seen. This behaviour will be typical for all our observed fields, with few exceptions.

[26]https://scipy-lectures.org/advanced/image_processing/index.html.

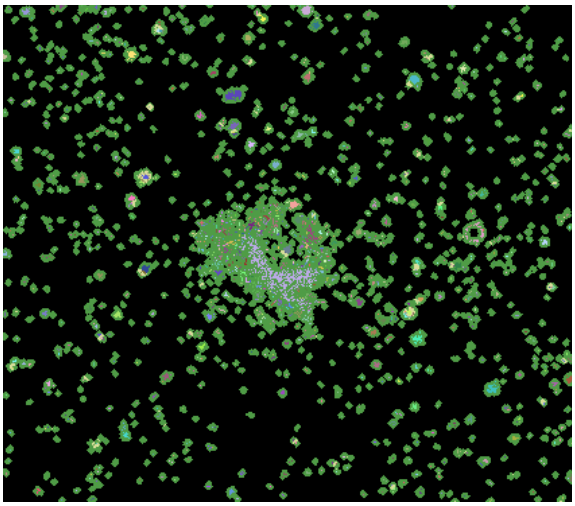

Figure 7.9: CAL 83 segmentation image obtained by the routine DETECT_SOURCES and DILATION in the background determination using npixels=20. Different colors represent all the detected sources while green represents the diluted mask for each one of these sources. The dimensions of the image are $\approx 50 \times 40$ pc^2, which is comparable to the radial distance of 25 pc used by Remillard et al. (1995). See the nebular-like structure at the center of the image, which corresponds to the only emission nebulae found in LMC associated with a SSS.

7.3.2 Flux Calibration

The next-to-last step is the most important one in the thesis, and as we stated before, the one that is most uncertain because of the lack of information we have in calibration. As said in subsection 7.2.2, the option to use V-filter image and magnitudes to find the calibration constant rather than the [O III] filter ones has to be discarded because we took [O III] images as the normalization reference. This choice is explained and justified in Subsection 7.3.3 from a mathematical point of view. Let us summarize the elements we have at our disposal: we have Johnson V-filter **MCPS** stellar catalog in the LMC[27], which we related to IMACS V-filter. Also, we have the measured flux byproduct of PHOTPIPE SWARP routine in the name of **DCMP** catalogs (IMACS [O III] catalog, uncalibrated), the original SWARPED science, mask and noise images, and their subsecuent PHOTPIPE HOTPANTS counterparts. The most sensible option would be to use the **MCELS calibration** (i.e., Z_O) to calculate directly $\langle f_* \rangle_O$

[27] Also Johnson U and B, provided by Zaritsky, Harris, Thompson & Grebel (2004), whose brightest stars are replaced by Massey (2002) catalog.

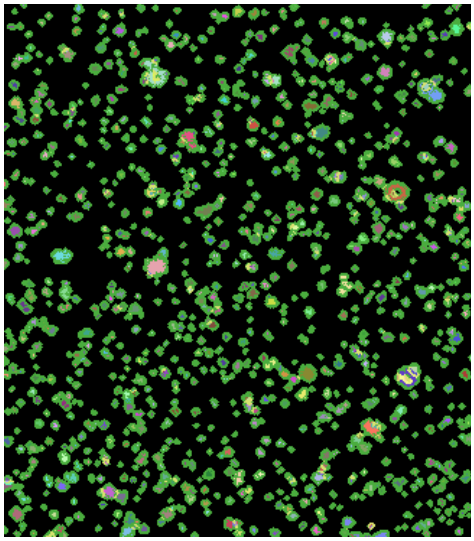

Figure 7.10: Same as 7.9 but for SNR 0509-67.5, but whose dimensions are 40×50 pc^2. See that there is no structure besides the residual of stars, not even from the supernova remnant itself at approximately the center of the image, although, as we will see, it is mostly masked.

using Equation 7.2. This, however, could not be done because MCELS survey does not have a proper calibration in our fields. The next best and almost unique option of calibration comes from the magnitude equation for a star in (Johnson-Kron-Cousins) B and V:

$$\mathrm{V}_* - \mathrm{V}_{\mathrm{VEGA}} = -2.5 \log \left(\frac{\langle f_* \rangle_{\mathrm{V}}}{\langle f_{\mathrm{VEGA}} \rangle_{\mathrm{V}}} \right) \tag{7.5}$$

$$\mathrm{B}_* - \mathrm{B}_{\mathrm{VEGA}} = -2.5 \log \left(\frac{\langle f_* \rangle_{\mathrm{B}}}{\langle f_{\mathrm{VEGA}} \rangle_{\mathrm{B}}} \right) \tag{7.6}$$

with $\langle f \rangle_{\mathrm{V}}$ defined in Equation 7.1, the VEGA counterpart, and V should be our V-band[28]. As we do not have any information about the spectra of any of the stars in the image, it is not straightforward to find the mean flux $\langle f_* \rangle$ in [O III] band.

Our plan is as follows: we have B and V magnitudes, calibrated: these two magnitudes will give us good estimations about $\langle f_* \rangle_{\mathrm{B}}$ and $\langle f_* \rangle_{\mathrm{V}}$, respectively. We might assume that any filter can be characterized by its effective wavelenght, λ_{eff},

[28]The ratio of zeropoints between MCPS and our filter is 1.034.

and effective width, $W_{\rm eff}$, defined as

$$\lambda_{\rm eff} = \frac{\int R f_* \lambda d\lambda}{\int R f_* d\lambda} \tag{7.7}$$

$$W_{\rm eff} = \frac{\int R d\lambda}{\rm MAX}(R) \tag{7.8}$$

with the caution that $\lambda_{\rm eff}$ is not perfect characterization of a filter because it depends on f_* (Bessell & Murphy, 2012). With these assumptions we may write the unknown $\langle f_* \rangle_{\rm O}$ as

$$\int_{\rm O} f_* R d\lambda \approx f_*(\lambda_{\rm O_{eff}}) \times W_{\rm O_{eff}} \tag{7.9}$$

this means, this integral can be thought as a **point in the spectra** of f_* at wavelength $\lambda_{\rm eff}$ times a filter-only dependent quantity, so $\langle f \rangle_{\rm O} \rightarrow f(\lambda_{\rm Oeff})$ given that the ratio $\int R d\lambda / W_{\rm eff}$ is close to one. The same applies to B and V filters so, using Equations 7.1 and 7.9, we obtain $f_*(\lambda_{\rm Beff})$ and $f_*(\lambda_{\rm Veff})$, **two known points** of the unknown stellar spectra from their respective magnitudes. This assumption can be tested using spectra and magnitudes of known stars. We did so using ≈ 270 stars mostly from the *Hubble Space Telescope* (HST) database CALSPEC, with accurate B and V magnitudes. Taking MCPS B and V filters to integrate, we see how good is the above approximation by comparing the calculated $f_*(\lambda_{\rm eff\{B,V\}})$ using Equations 7.9 and 7.2

$$f(\lambda_{\rm eff}) \simeq \langle f_{\rm VEGA} \rangle \times 10^{-(m_* - m_{\rm VEGA})/2.5} \tag{7.10}$$

with the flux evaluated at $\lambda_{\rm eff}$ directly from the spectra (usually interpolated at). The HST stellar spectra, in Figure 7.11, are obtained with the prescription that **B−V color** limits should enclose the $B - V$ values of the stars of this study, so its range corresponds to $-0.5 \leq B - V \leq 1.0$. Even if the range of magnitudes is large, the overall shape of the spectra at $\lambda \approx 5007$ Å is very close to a straight line. Therefore, by common sense, this method should be pretty accurate. A great revision about general absolute flux calibration, in particular for HST, can be found

in Bohlin, Gordon & Tremblay (2014).

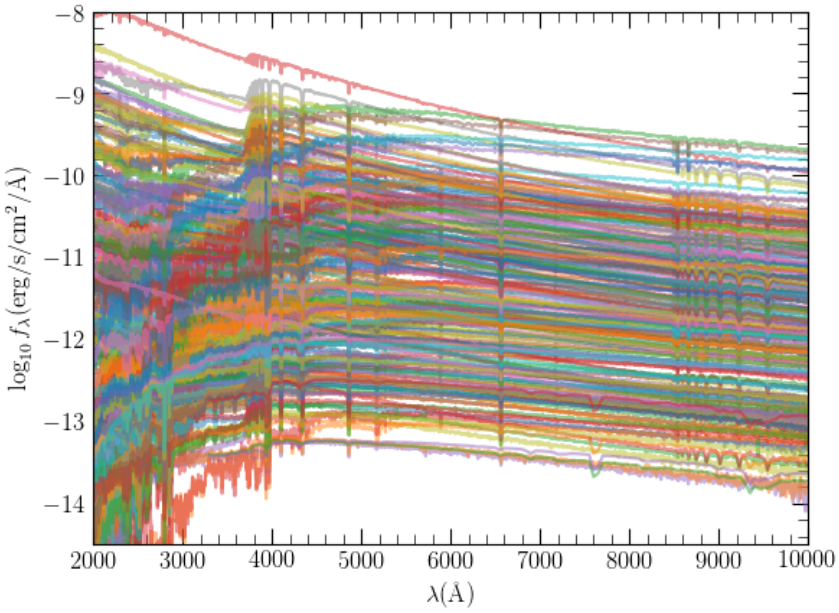

Figure 7.11: Spectra of ~ 270 stars from *Hubble Space Telescope* database CALSPEC, used to test the calibration method.

The idea is use Equation 7.10 as a replacement of the real flux in a certain λ. By taking all the available spectrum, we construct an histogram of different combinations of fluxes ($f = \{\mathrm{B,V}\}$): f_{eff}, the flux evaluated at λ_{eff} for each of the filters (B,V), $\langle f \rangle$, the mean flux under a filter, and f_{STD}, the flux derived directly from Equation 7.10 using only the magnitudes B,V since we have m_{VEGA} for both filters,

$$\Delta\{\mathrm{B,V}\}_{\mathrm{F}} = \frac{f_{\mathrm{eff}} - \langle f \rangle}{f_{\mathrm{eff}}} \tag{7.11}$$

$$\Delta\{\mathrm{B,V}\}_{\mathrm{STD}} = \frac{f_{\mathrm{eff}} - f_{\mathrm{STD}}}{f_{\mathrm{eff}}} \tag{7.12}$$

$$\Delta\{\mathrm{B,V}\}_{\mathrm{R}} = \frac{\langle f \rangle - f_{\mathrm{STD}}}{\langle f \rangle} \tag{7.13}$$

where subindex R stands for real, because it expresses the real approximation used in this thesis. The histogram and their respective statistics of all the flux differences can be seen in Figure 7.12 and Table 7.2.

To calculate the total sigma for the approximation $f_{\mathrm{eff}} \approx f_{\mathrm{STD}} \approx f_{\mathrm{R}}$, we take the

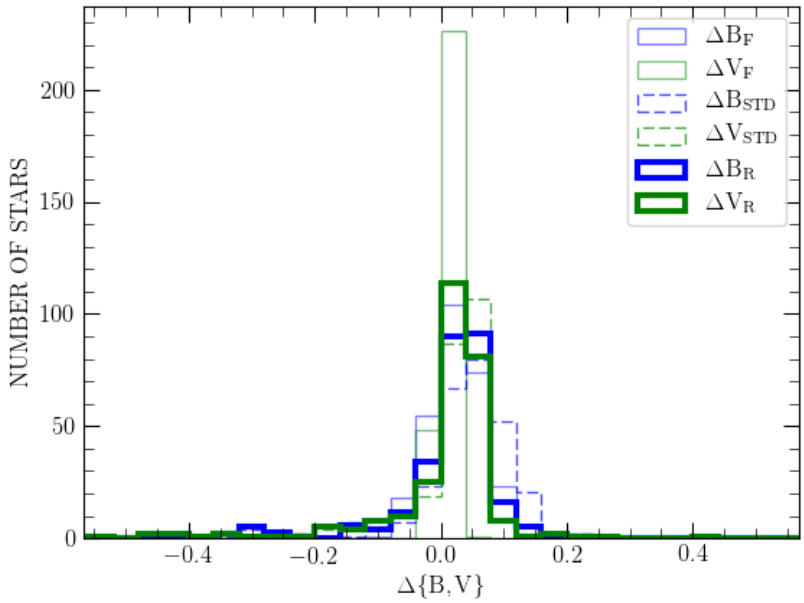

Figure 7.12: Histogram of the three defined {B,V} for the whole set of stellar spectrum, mostly from CALSPEC. It is readily that the statistics of Table 7.2 are accurate; the mean of the distributions is located at ≈ 0, while the standard deviation of $\{B,V\}_R$ is ≈ 0.1, which is really good given our assumption. The plot is limited to $5\sigma_{B_R}$, which covers almost all of the stars of the sample, as seen in column 5 of Table 7.2.

classical formula of propagation of errors (see Chapter 3 in Bevington & Robinson, 2003) for the sum of quantities $Q = M + N$ (ΔQ, ΔM and ΔN their respective errors)

$$\begin{aligned} Q &= M + N \\ \Delta Q &= \sqrt{\Delta M^2 + \Delta N^2} \end{aligned} \tag{7.14}$$

so, $\sigma_{\{B,V\}} = 0.17$. As there is an error associated with the method, the necessity to rely on spectra is vanished because we are going to use only the magnitude catalog and filter properties to obtain $f(\lambda_{\text{eff}} = \lambda_{O_{\text{eff}}})$. In order to do this, first, we derive three exact effective wavelenght for Johnson {B,V} and IMACS [O III] filters using Equation 7.7:

$$\lambda_{\mathrm{B_{eff}}} < \lambda_{\mathrm{O_{eff}}} < \lambda_{\mathrm{V_{eff}}}$$
$$\lambda_{\mathrm{B_{eff}}} = 4392.51\text{Å}$$
$$\lambda_{\mathrm{O_{eff}}} = 5019.37\text{Å}$$
$$\lambda_{\mathrm{V_{eff}}} = 5435.47\text{Å}$$

With these expressions, for each star "i" of the MCPS catalog that lies in a specific field, we think in a linear fit between $f_i(\lambda_{\mathrm{B_{eff}}})$ and $f_i(\lambda_{\mathrm{V_{eff}}})$, which, luckily (because it is an interpolation instead of an extrapolation), pass through $f_i(\lambda_{\mathrm{O_{eff}}})$. This can be seen in Figure 7.13, for CAL 83 field, which contains 769 stars of the MCPS catalog.

The FLUX ZEROPOINT is the constant that relates flux of spectra under [O III] filter and [O III] counts. The zeropoint, $\mathrm{Z_F}$, and its error, $\Delta\mathrm{Z_F}$, will be clearly biased towards lower energy-like values, due to the fact we have more fainter stars; this can be done more reliable if we apply some weights to the next calculations that have to be thought (it will not be done in this thesis). In order to fit simultanously all of the stars in the field, the used technique was SCIPY Orthogonal Distance Regression (ODR)[29] including the magnitude errors from the catalog.

For illustration purpose, we show in Figure 7.14 the flux contained in [O III] filter divided by the instrumental [O III] flux[30] for the 769 stars, versus wavelenght[31]. The gray shaded area represents $3\sigma_{\mathrm{FIT}}$, with $\sigma_{\mathrm{FIT}} = 3.049 \times 10^{-20}\mathrm{erg\ s^{-1}cm^{-2}\ COUNTS^{-1}}$. Therefore, for CAL 83, we obtain, using propagation of errors, $\mathrm{Z_F} = 2.02 \times 10^{-19}$ and $\Delta\mathrm{Z_F} = 4.59 \times 10^{-20}$, both in units of $\mathrm{erg\ s^{-1}cm^{-2}\ COUNTS^{-1}}$. This is independently done for all of the fields in this thesis, but their values are expected to be close.

7.3.3 Justification attempt

The calibration scheme we have converged to is not completely original. Similar ideas have been used to calibrate difference images from different pass-bands. Obtaining the value of $f(\lambda_{\mathrm{O_{eff}}})$ in units of erg/s/cm^2/Å from the $f(\lambda_{\mathrm{B_{eff}}})$ and $f(\lambda_{\mathrm{V_{eff}}})$ fluxes computed from the observed magnitudes via Equation 7.10 is a standard step of SED (spectral energy distribution) reconstruction. The SED method also assumes

[29] https://docs.scipy.org/doc/scipy/reference/odr.html.
[30] Strictly speaking, COUNTS, obtained from DCMP catalogs.
[31] Say, $f_\lambda \times \int_{\mathrm{O}} R d\lambda \times \mathrm{COUNTS_O}^{-1}$ versus λ.

Table 7.2: Statistics of $\Delta\{B,V\}$. Column 1 corresponds to the mean of each difference (μ), column 2 to the standard deviation of the histogram (σ), column 3 and 4 the maximum (MAX) and the minimum (MIN) of each of the differences respectively, and column 5 the fraction (FRAC) of the used stars with respect to the total in the calculations of columns {1,2,3,4} statistics.

	μ	σ	MIN	MAX	FRAC
ΔB_F	0.025	0.040	0.114	-0.084	1.00
ΔV_F	0.008	0.011	0.048	-0.027	1.00
ΔB_{STD}	0.035	0.114	0.764	-0.623	0.99
ΔV_{STD}	0.013	0.124	0.799	-0.666	0.99
ΔB_R	0.010	0.116	0.766	-0.690	0.99
ΔV_R	0.005	0.124	0.797	-0.684	0.99

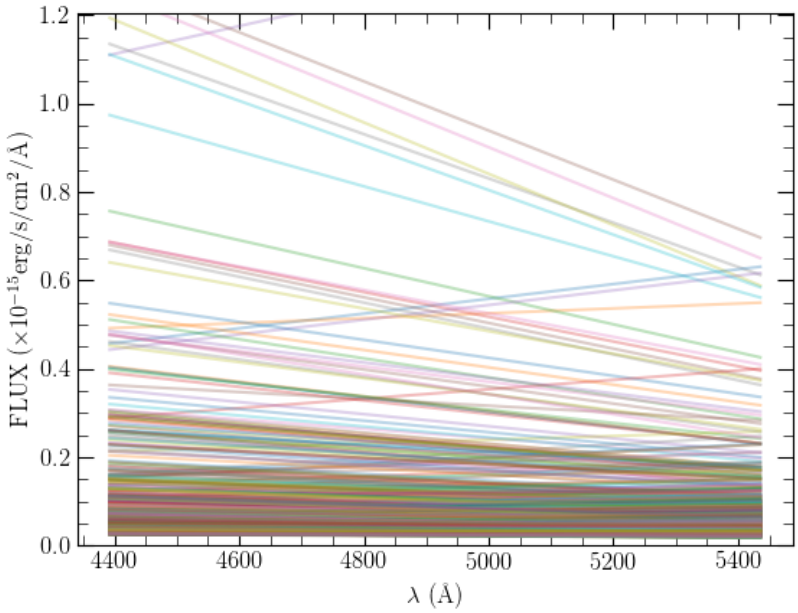

Figure 7.13: Relation between $\{\lambda_{B_{eff}}, f(\lambda_{B_{eff}})\}$ and $\{\lambda_{V_{eff}}, f(\lambda_{V_{eff}})\}$ pairs for 769 MCPS stars lying in the CAL 83 field. All the lines pass through, obviously, $\{\lambda_{O_{eff}}, f(\lambda_{O_{eff}})\}$, which corresponds to the value, in the assumption, times the integral over the filter, the flux of the star under that filter.

that the mean flux (defined in Equation 7.3) is a good representation of the spectra evaluated at the effective wavelength.

Figure 7.15 illustrates the SED method at work. The reconstructed spectra of Vega (left) and SN 1992A (right) are shown by linear segments connecting the dots, which are the magnitude-derived fluxes at filter-specific-wavelengths (Brown, Breeveld, Roming & Siegel, 2016). The top row shows the standard method of

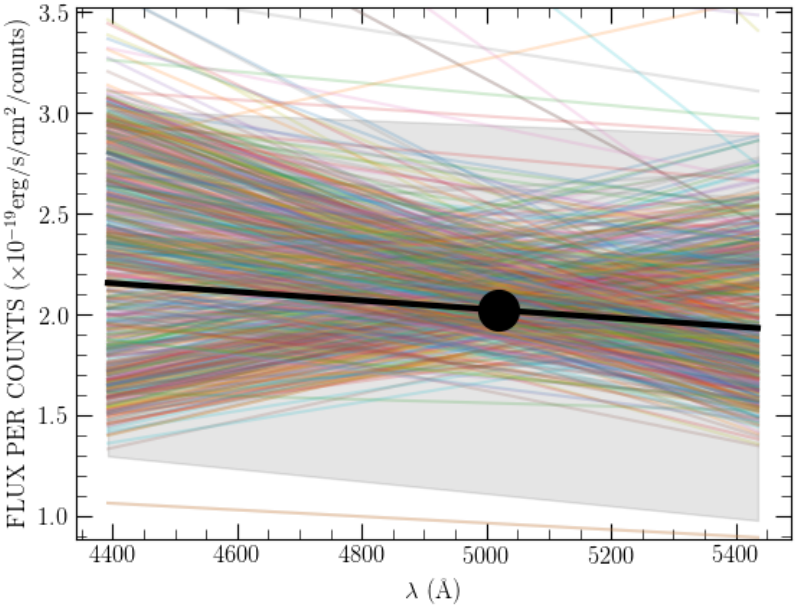

Figure 7.14: ODR fit to 759 ($\lambda_{\{B,V\}_{eff}}$) points corresponding to CAL 83 field stars, in units of $f_\lambda \times \int_O Rd\lambda \times \text{COUNTS}_O{}^{-1}$ versus wavelenght.

correcting for foreground reddening (fluxes are computed and then corrected by foreground reddening), and the bottom row shows the result of the "Floating SED" method (using the reddened fluxes to fit a reddened SED and then correct the reddened SED, Equation 7.10). The reconstructions in Fig. 7.15 use six passbands, but in our case we use just {B,V} because we care only about the flux at the [O III] line wavelength.

As we have two filters (B,V) we can only fit a linear segment and using as a criteria to choose the HST calibration stars having similar colors (see best-fit method in Brown, Breeveld, Roming & Siegel, 2016), the verification of Equation 7.10 stands firm. The flux at the effective wavelength is a reasonable representation of the mean flux in Equation 7.3, in a SED-wise sense, so it is also a reasonable approximation of the flux-integrated in the respective pass-band divided by the effective width (Vacca & Leibundgut, 1996).

The practice of subtracting an image taken with a broad band filter from another taken with a narrow band filter to subtract an underlying continuum from a narrow line emission arises in the 90s, addressed particularly at studying H II regions. Typically, a narrow band filter centered at approximately the Hα wavelength was used to capture the emission and a broadband filter like Johnson R was subtracted from to

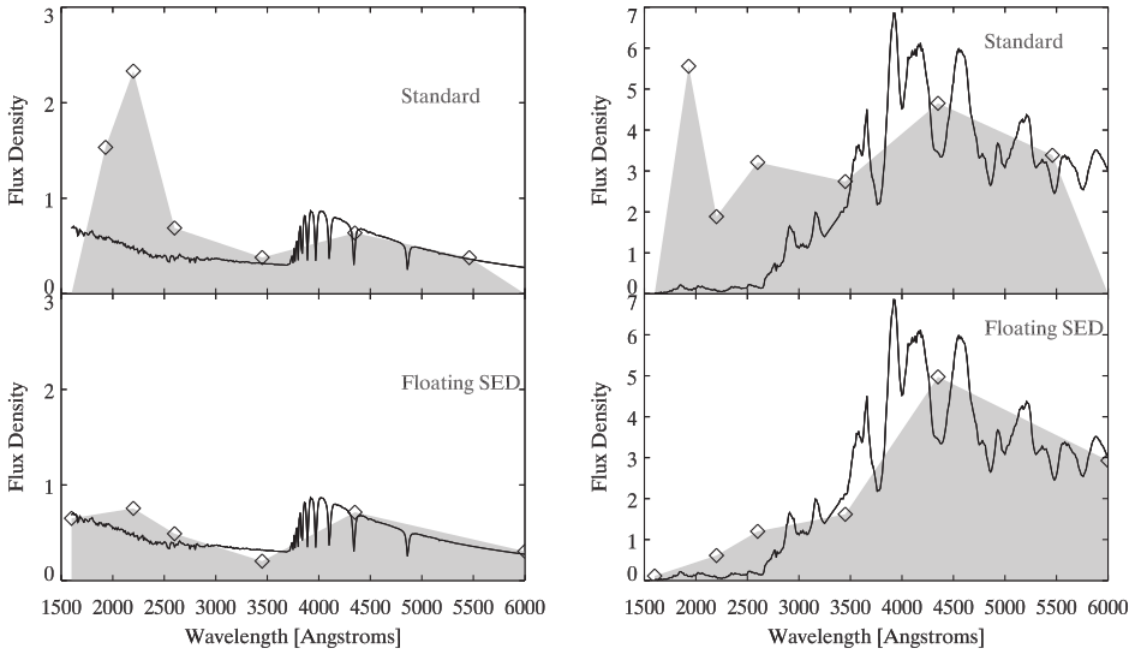

Figure 7.15: SED reconstructions of Vega (left) and SN 1992A (right) with their respective original spectrum: flux density, usually in units of erg/s/cm^2/Å, versus wavelenght, using two different methods: STANDARD corresponds to the magnitude-to-flux conversion and dereddening and then creating the SED, while FLOATING SED fits a SED to the reddened magnitudes and then corrects for extinction. From Brown, Breeveld, Roming & Siegel (2016).

those images. Waller (1990) is a classical example were the assumptions behind this technique are clearly detailed. A relevant assumption that is not well satisfied in our case is that the effective wavelengths of both filters should be close to the wavelength of the line of interest (our wavelength difference is ~ 400 Å). Remillard et al. (1995) alleviated this problem using a broadband image which was a combination of B and V images, whose effective wavelength lies much closer to the [O III] line. Cloudy weather prevented us from collecting the B images.

We follow the notation of Waller (1990) and Spector et al. (2012) to write the observed count rates in ADU s^{-1} for the wide and narrow filters, cps$_{\rm W}$ and cps$_{\rm N}$,

respectively, as

$$\mathrm{cps}_{\{\mathrm{N,W}\}} = \int_{\Delta_{\{\mathrm{N,W}\}}} f_\lambda \eta_{\{\mathrm{N,W}\}} d\lambda \tag{7.15}$$

$$\tag{7.16}$$

where $\eta_\mathrm{N} \equiv \eta_\mathrm{N}(\lambda), \eta_\mathrm{W} \equiv \eta_\mathrm{W}(\lambda)$ are the detector efficiency[32], Δ_N and Δ_W are the effective widths of the passbands in Angstroms, and f_λ the flux density in units of erg/s/cm^2/Å.

If the target line is the only significant spectral feature in the N and W bands (this is important as we will show later), $\mathrm{cps}_{\mathrm{N,W}}$ can be written as the sum of a line (L) and continuum (C) contributions,

$$\mathrm{cps}_{\{\mathrm{N,W}\}} = \mathrm{cps}_{\{\mathrm{N,W}\},\mathrm{C}} + \mathrm{cps}_{\{\mathrm{N,W}\},\mathrm{L}} \qquad \text{with e.g.} \tag{7.17}$$

$$\mathrm{cps}_{\{\mathrm{N,C}\}} = \int_{\Delta_\mathrm{N}} f_{\{\lambda,\mathrm{C}\}} \eta_\mathrm{N} d\lambda. \tag{7.18}$$

If we further assume that most of the stars do not emit in [O III], $\mathrm{cps}_\mathrm{N} = \mathrm{cps}_{\{\mathrm{N,C}\}}$, therefore the total flux under the filter N (in units of erg/s/cm^2) can be written in terms of the flux evaluated at λ_L, the wavelength of the line of interest, as

$$\mathrm{cps}_\mathrm{N} \equiv \mathrm{cps}_{\{\mathrm{N,C}\}} \approx f_{\{\lambda,\mathrm{C}\}}(\lambda_L)\Delta_\mathrm{N}\hat{\eta_\mathrm{N}}. \tag{7.19}$$

$\hat{\eta}_\mathrm{N}$, which is approximately constant in the narrow-band filter, is the same constant we mentioned in the previous section. In order to go on, we assume that $f_{\{\lambda,\mathrm{C}\}}$ is effectively $f(\lambda_{\mathrm{O}_\mathrm{eff}})$, so the count rates for [O III] emission from photometry correspond to cps_N. Since the effective width of the [O III] filter is known from Equation 7.8, all the elements to obtain $\eta_{\{\mathrm{N}\}}$ are in hand. Our preference to calibrate and normalize by [O III], although more cumbersome for the lack of calibrated stars in the field, follows the historical approach.

From the previous equation, we reach the main results of Waller (1990); the relation between the difference counts and f_line, the total flux of the line,

[32] $\eta_{\{\mathrm{W,N}\}}$ contains the transmittance of the filters, instrumental response, atmospheric transmittance, etc., and are typically given in units of ADU s^{-1}/erg/s/cm^2.

$$f_{\rm line} \approx \frac{\Delta{\rm cps}}{\hat{\eta}}$$

with Δcps the difference counts of a hypothetical nebula in the difference image. If V and [O III] filters are already calibrated, such as the case of Graur & Woods (2019) when using HST images of SN 2014J, then the last equation can be written as

$$f_{\rm line} \approx \Delta_{\rm N}(\langle f_{\rm N}\rangle - \langle f_{\rm B}\rangle).$$

In other words, the emission is obtained directly from the photometry. An extensive description of all this technique, and specifically, the more complex treatment of the continuum if more filters are used, and the corrections to apply when there are multiple lines falling in the narrow band filter and contaminating the narrowband flux, as Hα with [N II]$\lambda\lambda$6548,6584, or [O III]$\lambda\lambda$4959,5007 with Hβ can be found in Pascual, Gallego & Zamorano (2007). A prolific discussion is also been conducted on the usage of CLOUDY models with the results that are obtained by this procedure (see Erratum from Woods et al., 2018)[33]. We finally note that, in our case, the contribution from other lines, and especially from [O III]λ4959, are expected to be negligible.

7.3.4 Radial Measure

The last step to reach the goals of this thesis is to measure the flux in emission detected in the subtracted images. With the zeropoints and uncertainties calculated for each field, Z_F and ΔZ_F, the transformation to flux is accomplished by the multiplication of each pixel "i" counts, x_i by Z_F,

$$\hat{x}_i = Z_F x_i. \tag{7.20}$$

[33]https://academic.oup.com/mnras/advance-article/doi/10.1093/mnras/stz914/5421639

By propagation of errors of the multiplication the original uncertainty Δx_i at pixel "i", results into a new one, $\Delta \hat{x}_i$, given by

$$\Delta \hat{x}_i = \mathrm{Z_F} \sqrt{{x_i}^2 \left(\frac{\Delta \mathrm{Z_F}}{\mathrm{Z_F}} \right)^2 + {\Delta x_i}^2}. \tag{7.21}$$

The flux was measured in two different ways. In one of them we created our own routines from scratch, and in the other we used the PYTHON PHOTUTILS package to do it automatically.

Our own routines, that we call the BRUTE PYTHON method, take the masked image and create a set of annuli with uniform step, surrounding the source of interest. In each annulus, that we call **corona**, we keep track of on how good the background subtraction is by computing its mean and standard deviation from science and noise images, respectively. An example of a corona, at ≈ 500 pixels from the source, which is located at the center of the image, is shown in Figure 7.16.

The question arises naturally: What will happen if the background has not been correctly calculated by HOTPANTS or SEGMENTATION?. To study this we took the region of the SSS CAL 83, and computed the surface brightness (from now on, SB), which is the sum of pixel fluxes in each corona divided by its area, and the MEAN FLUX, which is the sum of all the pixels in all the corona at a certain distance from the source, divided by the total covering area. The results are shown in Figure 7.17.

The expected behaviour is that if there is no emission, MEAN FLUX and SB should be approximately zero. With this in mind, it seems that the BRUTE method on CAL 83 has worked correctly, given that the SB peak corresponds to the region where the dark structure is seen in Figure 7.16, and no apparent emission is found at large distances from the source. The fact that far away the SB reaches negative values will affect the FLUX profile in that region.

The behaviour of CAL 83 profile is different from those of the other sources. Figure 7.18 shows the SB and MEAN FLUX of the source RX J0550.0-7151, which lie near zero, in agreement with the overall MEAN value in Table 7.3. Importantly, there is no evidence of emission at any distance and the coronas at times reach negative values. The latter is somewhat worrisome, because one of the goals of this work is to put constraints on the luminosity at 7.5 pc from all the sources, and negative SB values may add up enough to derive a biased, even non-physical, luminosity.

Before doing any attempt to correct SB measurements we need to be sure that the

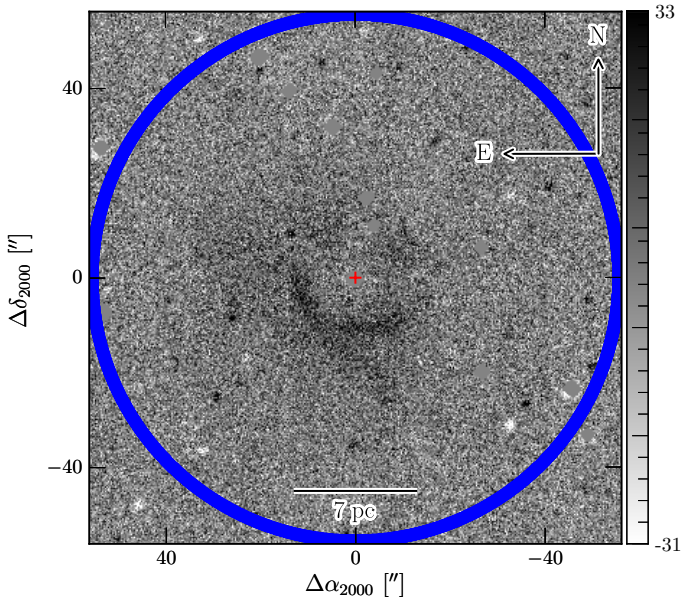

Figure 7.16: Corona at 500 pixels from the source, located at the centre of the image, with a width (step) of 10 pixels, for CAL 83 field. The nebula, black structure surrounding the centre of the image, is clearly seen.

BRUTE method is measuring correctly the flux of any hypothetical nebulae surrounding a source. This confirmation is also necessary to discard this putative large source of error when comparing with previous results, mostly on the CAL 83 nebula. The second method, APER, is a PYTHON script that relies heavily on different astronomical packages, most notably the PHOTUTILS aperture photometry tasks. Thanks to Graur & Woods (2019) work on [O III] measurements on a SSS nebulae surrounding SN 2014J, measuring surface brightness in practice is to do aperture photometry in coronas around the source, as written in this SB PYTHON code[34]. Therefore, if the centroid is placed in the object and then masked, we can create an array of different coronas, add the counts, and compare the statistics directly with those of BRUTE. The advantage of APER on BRUTE is that it is faster, analogous to the IRAF PHOT task used by Graur & Woods (2019) to determine the background and [O III] emission. Also, its astrometry is more accurate.

Having the two techniques to measure flux, we pay attention to Figures 7.17 and 7.18, noticing that the flux of some coronae fall to negative values, and so the question arises: How to work with SB profiles of, for example, RX J0550.0-7151 if, the

[34]https://github.com/fbuitrago/SB_profiles/blob/master/calculating_SB.py

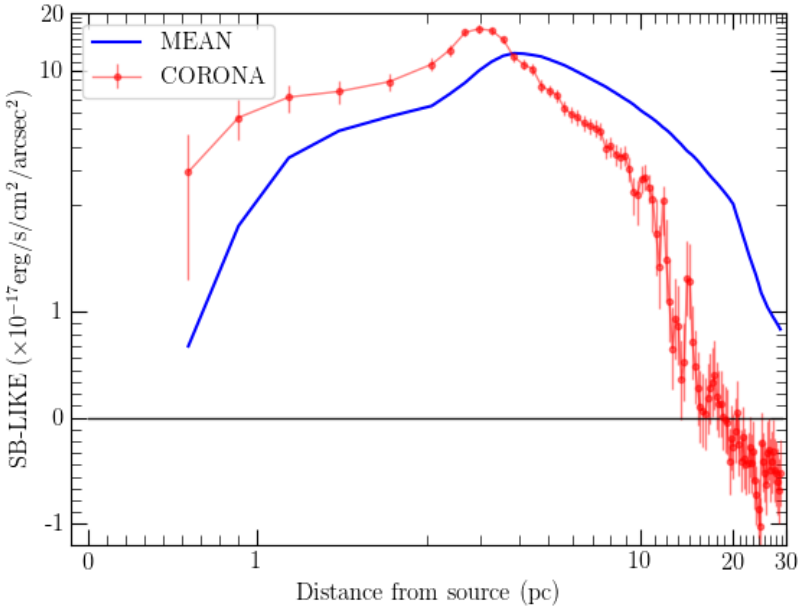

Figure 7.17: MEAN FLUX of the SSS CAL 83 (in blue line). This is the total sum of the COUNTS divided by the total area up to the given distance. The red line shows the SB of each corona, taken with a step of approximately 10 pixels. The errorbars correspond to 3σ. The emission of the nebula is clearly seen at < 5 pc while it slowly decreases at large distances from the center (note the logarithmic scale). The horizontal black line shows the SB$= 0$ level.

initial analysis reveals a systematic effect that may even result in a non physically estimate? Our hypothesis is that the negative values originate on a small error in the image matching that results in the subtraction of a background slightly larger than the right one. To illustrate this behavior we have computed the profiles expected for artificial images with a constant pixel value of ± 0.5 counts and another with pixels values following a Gaussian distribution with mean and standard deviation of 0.2 and 1.0 counts, respectively (see Figure 7.19). The SB profiles should be constant at ± 0.5 counts, for the constant images with those values, and nearly constant at ~ 0.2 counts for the image with a Gaussian distribution of pixel values. The FLUX profiles, however, where the counts are added within the given radii, are greatly affected by this non-zero backgrounds because the small difference add up. In fact, the effect of a slightly negative background is seen in the CAL 83 case. If the background were at the correct value, the counts will reach a maximum and then remain constant. The behavior observed beyond $\sim$ 15 pc matches that of a small, nearly-constant, negative background. A small deviation from zero of the SB of the coronas, will

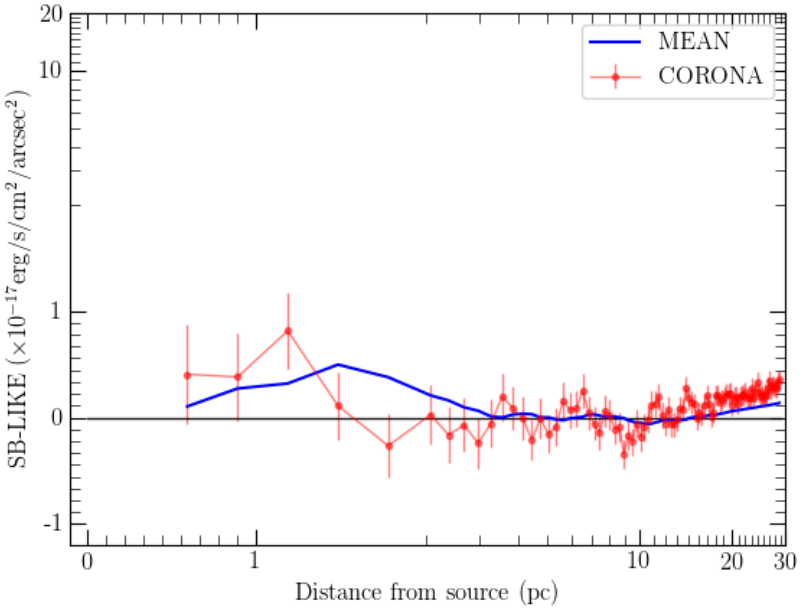

Figure 7.18: MEAN FLUX (blue) and SB of each of the coronas (red, 3σ errobar) for RX J0550.0-7151, with step of $\approx$ 10 pixels. In contrast to Figure 7.17, there is little-to-no emission in this field.

cause, as FLUX is proportional to the cumulative sum of the COUNTS inside the total area of the coronas, a luminosity below the real one.

A simple solution to compensate for this systematic effect is to estimate a pedestal to be added to the pixel counts to compensate from an overestimated subtracted background. And a simple estimation of this pedestal is the minimum value of SB, as seen in Figures 7.17 and 7.18. We named APER CORR the method that corrects the pixel values by this amount (it is just APER followed by the corona correction). A consequence of this is that the flux measurements obtained in this thesis will be, strictly speaking, lower limits to the real flux (the pedestal we subtract is just the minimum to take all coronae above zero).

Figure 7.20 displays the result of the three different methods applied to the region around CAL 83. It is remarkable how closely the uncorrected methods agree. The tiny differences in their error bars are possibly due to small differences in the position of the coronae. APER CORR profile is similar to the other profiles given that the value of the background correction, CAL 83 MIN in Table 7.3 is relatively small (≈ -0.5), closely matching the -0.5-background profile displayed in Figure 7.19. It is worth noting that the order of magnitude of SB is about 10^{-17} erg s^{-1} cm^{-2} arcsec^{-2}, which

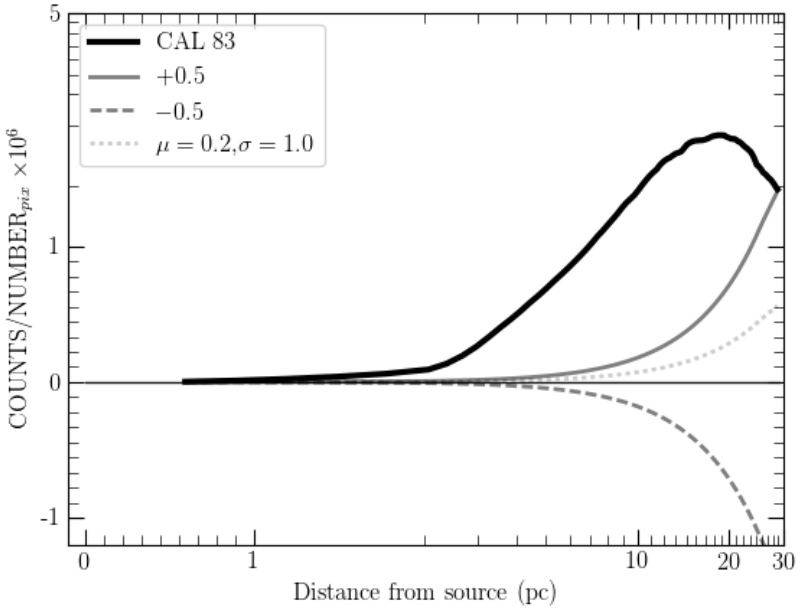

Figure 7.19: BRUTE FLUX profile of CAL 83 nebula, constant backgrounds ±0.5 and gaussian $\mu = 0.2$, $\sigma = 1.0$. As explained in the text, CAL 83 flux profile suffers a decay from $\approx$ 15 pc, which means the last coronas are summing up negative flux, that can be explained by a negative background not removed in both previous subtraction stages.

is in the range of the less denser CLOUDY SB profiles seen in Woods & Gilfanov (2016) and Figure 3.11.

Table 7.3: Corona statistics for all CAL 83 and RX J0550.0-7151 (REAL and DCMP catalogs): minimum MIN, maximum MAX, mean MEAN and standard deviation STD.

FIELD	MIN	MAX	MEAN	STD
RX J0550.0-7151 DCMP	-0.298	0.711	0.095	0.154
RX J0550.0-7151 REAL	-0.299	0.720	0.095	0.154
CAL 83 DCMP	-0.627	10.139	1.621	2.611
CAL 83 REAL	-0.630	10.137	1.613	2.613

The FLUX profiles for CAL 83 are shown in Figure 7.21. The blue line displays the results of the APER CORR method, where the effect the background correction is clearly seen. The tail of the profile at large distances from the source is lifted in comparison to both uncorrected profiles (BRUTE and APER). It is reassuring to confirm that our flux measurements for CAL 83 ($\sim 10^{-13}$ erg s^{-1} cm^{-2}) are consistent in order of magnitude with those of Remillard et al. (1995).

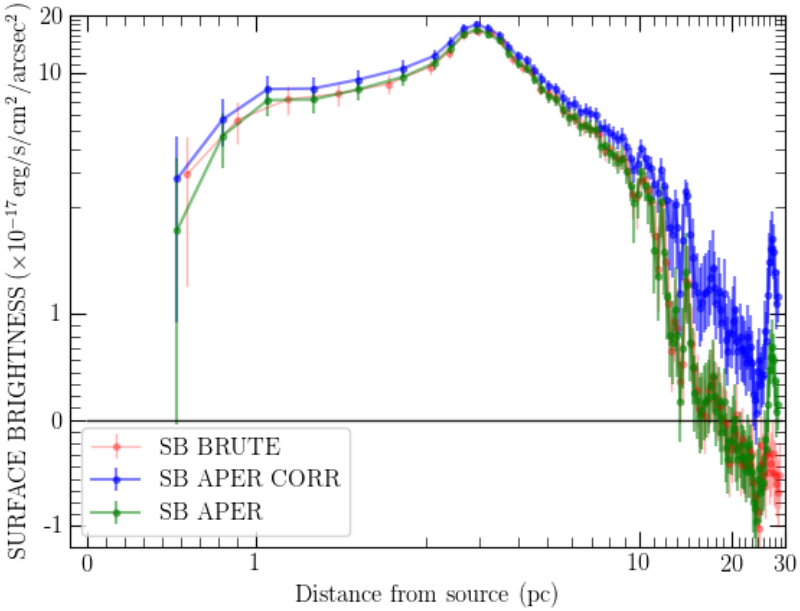

Figure 7.20: Empirical Surface Brightness profiles (and 3σ errorbars) of CAL 83 using three different estimates: APER CORR, a method corrected by a residual negative background in blue line, and two uncorrected estimates, APER, in green line, and BRUTE in red line (see text for their description). The differences are small between corrected and uncorrected methods (due to the small minimum value of the most negative coronae), while no apparent differences are seen between the uncorrected methods. Black line represents a SB = 0. These profiles are not corrected by foreground extinction.

The profile of CAL 83 is different from those of the other fields because it does correspond to an emission nebula. A main result of next chapter is that there are no emission nebulae surrounding the other objects of interest. Therefore, the profile corrections would be much more evident in them than in CAL 83. This is illustrated in Figures 7.22 and 7.23, where the SB and FLUX profiles of SSS RX J0550.0-7151 are shown. The negative contributions are more clearly seen than in CAL 83. SB APER profile contain several negative points, that correlate with negative variations in the FLUX. For example, at a distance of ≈ 10 pc, a negative luminosity is obtained from FLUX. This is non physical and indicate that we could not seriously constrain the progenitor properties using this result. However, the APER CORR profile appears clearly above FLUX$= 0$, and this translates into a better upper limit to the luminosity of the nebulae.

The APER CORR profiles can be directly compared with both CLOUDY models and the empirical values obtained by Gruyters et al. (2012) and Remillard et al. (1995)

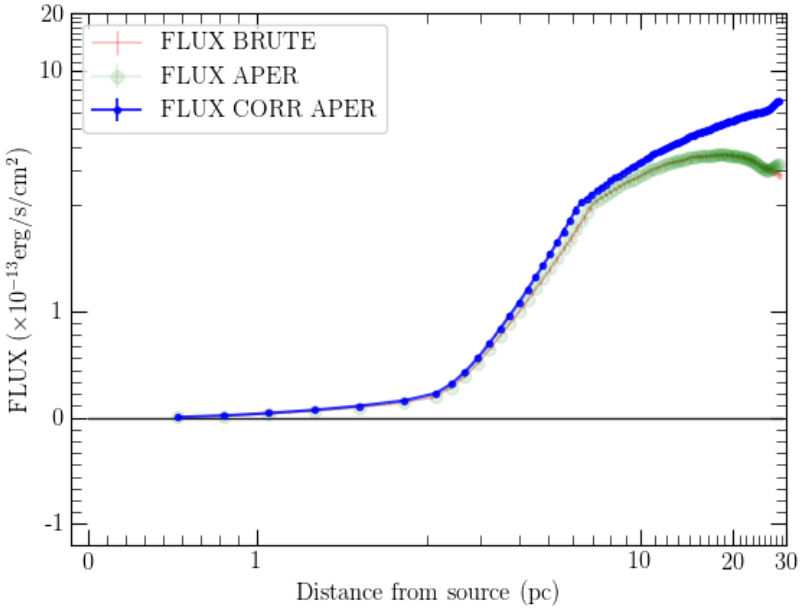

Figure 7.21: Empirical FLUX profiles (and 3σ errorbars) for CAL 83. The overall differences on error bars seen in Figure 7.20 are diminished due to scale effects. At large distances from the source the difference in FLUX between APER CORR and BRUTE/APER are apparent. The black horizontal line is FLUX= 0. These profiles are not corrected by extinction.

for CAL 83 nebula. In the case of the latter, the observable is an upper limit for the luminosity at 7.5 pc. Interestingly, as seen in the figures, the contribution of the pedestal at 7.5 pc is not so relevant. It is important to stress that very bright and negative sources within the area where we count the signal have been masked, above/below $\pm 5\sigma$ of the $\approx$ STD PIX of Table 7.1. This is important because the results would be systematically high if they were not masked. The difference, though, would not be larger than $\sim 20\%$, in zones where there is emission (see next section).

Finally, we checked the the ratio of the FLUX obtained by REAL and DCMP catalogs for the fields of SNR 0519-69.0 (chip 2), CAL 83 (chip 2) and RX J0550.0-7151 (chip 3). As seen, in Figure 7.24 the largest differences are $\sim 5\%$, consistently for all fields. In practice, DCMP FLUX catalogs and APER CORR profiles will provide the main empirical results of this work.

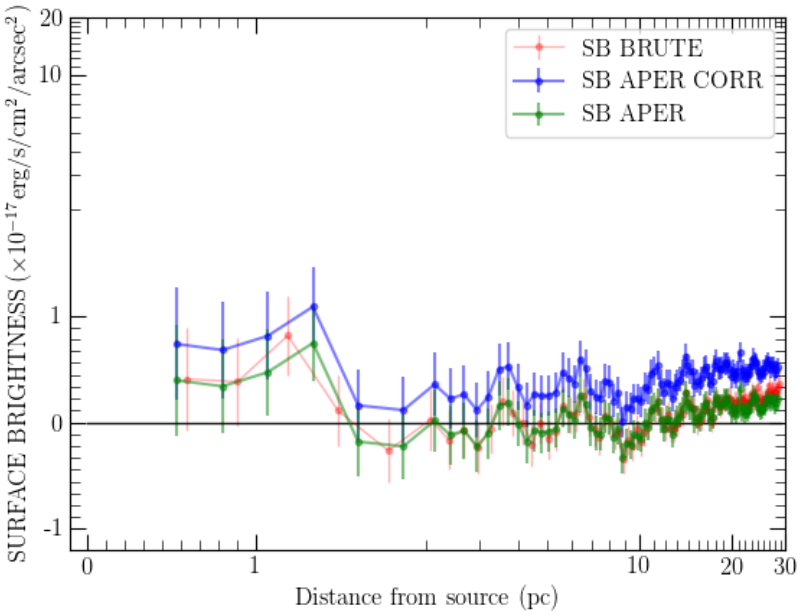

Figure 7.22: Emipirical Surface Brightness profiles (and 3σ errorbars) of RX J0550.0-7151, same as Figure 7.20 although the pedestal addition is evident to see at any distance. Black line represents SB= 0. Not corrected by extinction.

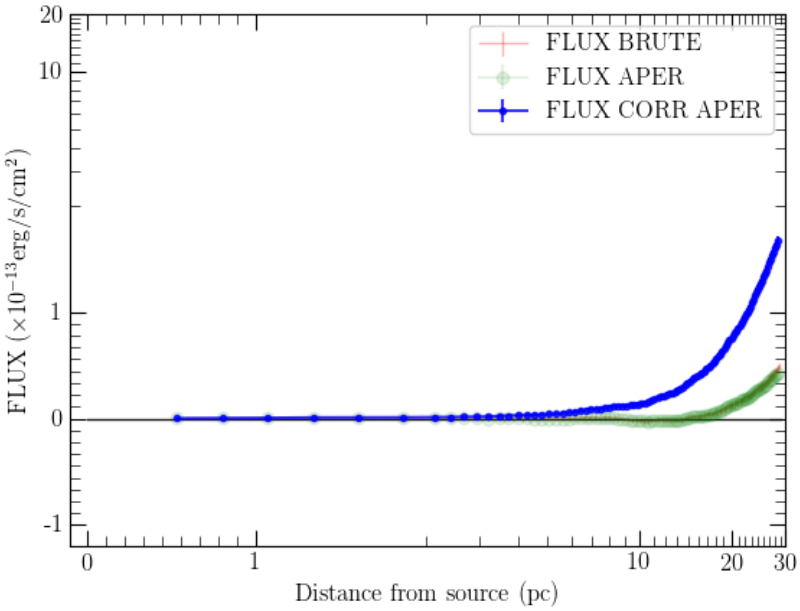

Figure 7.23: Empirical FLUX profiles (and 3σ errorbars) for RX J0550.0-7151, same as Figure 7.21. The addition of pedestal makes the FLUX, negative at one point, be positive at larger distances, for example, from 7 to 12 pc. Black line represents FLUX= 0. Not corrected by extinction.

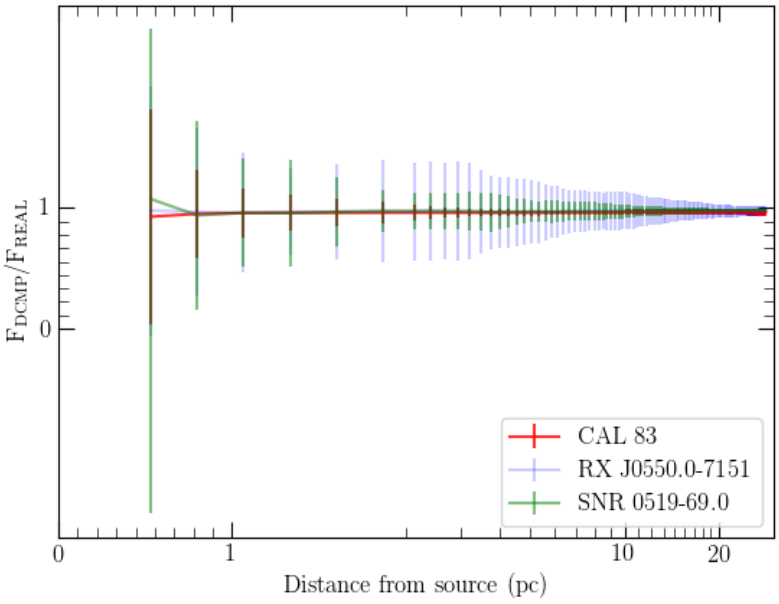

Figure 7.24: Ratio of the FLUX derived by using the DCMP and REAL catalogs to calibrate Z, ΔZ for three fields: CAL 83, SNR 0519-69.0 and RX J0550.0-7151. The values, for any distance from the source, of the three profiles differ from one by about 5%.

Chapter 8

Results

We will present our results in three stages. We will first analyze visually the subtracted images to establish if there are systematic defects attributable to the software used, or unusual features in the fields that could bias the radial profiles to be computed later. Secondly we will describe the radial profiles computed for the different sources and compare them with independent measurements when they are available in the literature. We will then present our theoretical models for the profiles based on CLOUDY (Ferland et al., 2013) and finalize the chapter with a discussion.

8.1 Visual Inspection of Subtractions

We base this section on the subtractions done with HOTPANTS. Table 8.1 presents some useful statistics provided directly by the code. As said before, the useful ones are MEAN PIX and STD PIX, which are inputs of the first masking stage at SEGMENTATION. We note that CAL 87 2 and CAL 87 3 are the two independent observations of this source taken at different epochs, which fell on chip 2 and 3.

We see in Table 8.1 that SNR 0519-69.0 MEAN PIX is higher than that of CAL 83, where we already know there is emission. This probably indicates that either the subtraction of this field was bad, with a large number of positive residuals of stars, or that there really has a large area of [O III] emission. The same can be said about SNR N103B and DEM L157[1]. No striking relevant information appears to be available in the table regarding the other fields.

[1]DEM L157 corresponds to a H II region in chip 1 of RP 1406 J35 field, which is a planetary nebula, both intereseting objects but not intrinsically related to the subject of this thesis.

Table 8.1: Subtraction statistics for all of the fields: F.O.M, STD F.O.M, reduced ${\chi_n}^2$, n, MEAN PIX and STD PIX

FIELD	F.O.M	STD F.O.M	${\chi_n}^2/n$	n	MEAN PIX	STD PIX
CAL 83	0.998	0.047	1.238	7113516	0.836	12.742
CAL 87 2	1.649	0.448	5.804	8255293	0.651	7.464
CAL 87 3	1.105	0.228	3.215	8120400	0.366	6.061
RX J0513.9-6951	1.128	0.082	2.486	8316259	1.822	12.047
RX J0550.0-7151	0.828	0.057	1.116	8263394	-0.171	4.958
SNR 0509-67.5	1.033	0.065	1.611	8439519	0.425	4.388
SNR 0519-69.0	1.544	0.287	5.735	8114530	3.734	11.596
SNR N103B	1.038	0.077	8.720	8280838	3.412	13.144
RP 1406 J35	1.276	0.243	3.639	8359651	0.364	5.420
DEM L157	1.065	0.144	2.606	8340510	2.343	5.407

8.1.1 SSSs and SNRs

We will start by inspecting the subtracted images of CAL 83, in particular the zoomed images shown in Figure 8.1 a) and b) which span a region of a $\approx 7.2 \times 7.2$ pc^2. This is an area of approximately $27'' \times 27''$ which corresponds closely to the image size discussed by Gruyters et al. (2012)[2]. These images are well suited to see how the masking of bright objects works. As the typical mask of DETECT_SOURCES task was smaller than required, i.e., some residuals of the stars, in the form of annulus, remained in the images. It was necessary then to enlarge those masks. We used the PYTHON BINARY DILATION[3], routines to do so for segmented objects. The dilation process depends mostly on the parameter ITERATION, which is number of times that the code recursively dilates the mask. It is a sort of dilemma: if ITERATION is too small it leaves bright rings centered on the masked objects. If it is too large (say, 30), the final shape of the masked objects ends up being rhomboidal and discards the flux of possible emission pixels. After some trial and error we converged to an ITERATION value of 10 as seen in b) in Figure 8.1. If we compare this image with panel a), it can be seen that the residual stars are completely masked. To remain consistent, we used this value in all of the other fields. The masked pixel values are set to the mean of the calculated background in SEGMENTATION, which is always ≈ 0.

The difference image of CAL 83 applying the masks described above is seen in Figure 8.13. This source is not embedded in a crowded field, which facilitates the subtraction and the masking. The nebula is located surrounding the source, as has

[2]Though there is a possible mistake in that work.

[3]https://docs.scipy.org/doc/scipy-0.14.0/reference/generated/scipy.ndimage.morphology.binary_dilation.html

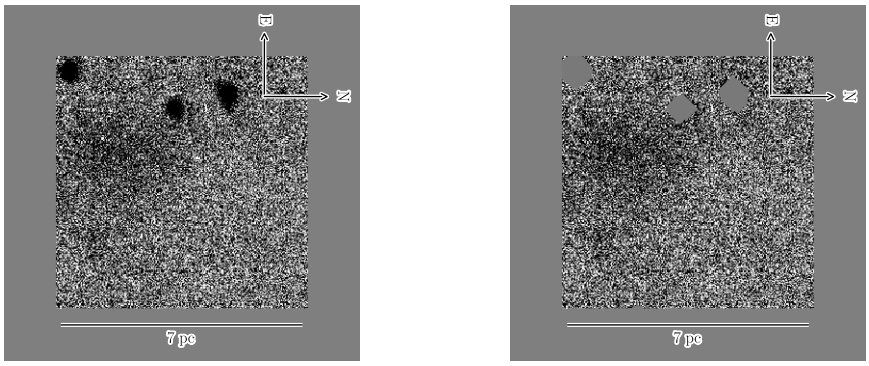

Figure 8.1: a) Before and **b)** after masking of CAL 83 images, in the SEGMENTATION stage. The pixel values of the mask are ≈ 0. It can be clearly seen in b) that all the the stars in a) are masked. Dimensions of the image are 7.2×7.2 pc^2.

been previously characterized by Remillard et al. (1995).

CAL 87 presents us with a different situation. We took two images of this source, epoch 1 on chip 2 (Figure 8.2) and epoch 2 on chip 3 (Figure 8.3). Neither of the difference images shows any kind of extended emission consistent with a nebula. The quality of the subtractions is not as good as that of CAL 83 because the field is more crowded. Small positive residual at the positions of stars are abundant. These residuals are not masked by SEGMENTATION because they do not match the criteria of being an object with 20 or more connected pixels above the threshold. The comparison of the two independent images of CAL 87 presents us with a good case to understand systematic effects associated with the subtraction technique that will, eventually, appear as differences in the SB/FLUX profiles (we note that there is a discrepancy in their zeropoints). The analysis of the radial profiles, to be done below, will clarify this. Even though the statistics shown in Table 8.1 are computed from the unmasked HOTPANTS images the results are consistent with the visual analysis. MEAN PIX is positive in both images, as could have been predicted just by looking at the prevalence of positive residuals of stars.

The difference image of RX J0550.0-7151, which was taken on epoch 2, is shown in Figure 8.4. It can be seen that it looks cleaner than those of CAL 87, with fewer masked objects. Again, no signal of extended emission surrounding the source, marked by a red cross, is seen. The MEAN PIX value negative, but also the closest to zero of all the fields. This is consistent with the absence of positive residuals of stars after masking.

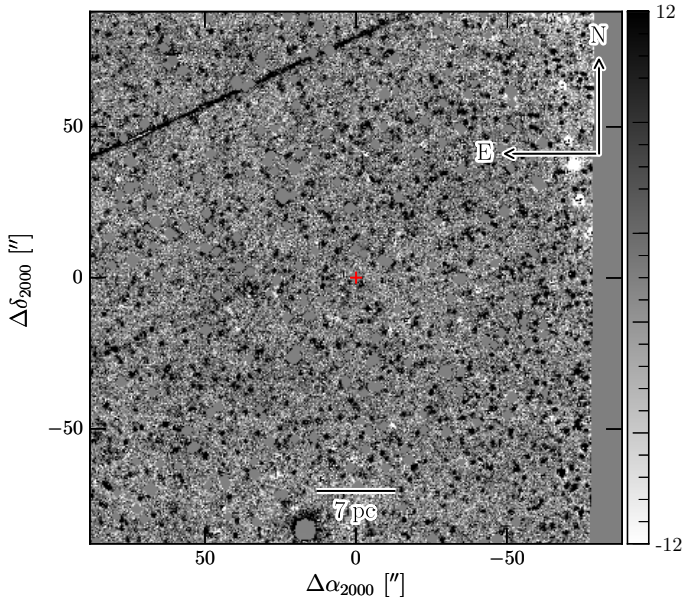

Figure 8.2: Masked HOTPANTS output of CAL 87 2, ready to be measured. There is no visible [O III] emission as CAL 83 nebula.

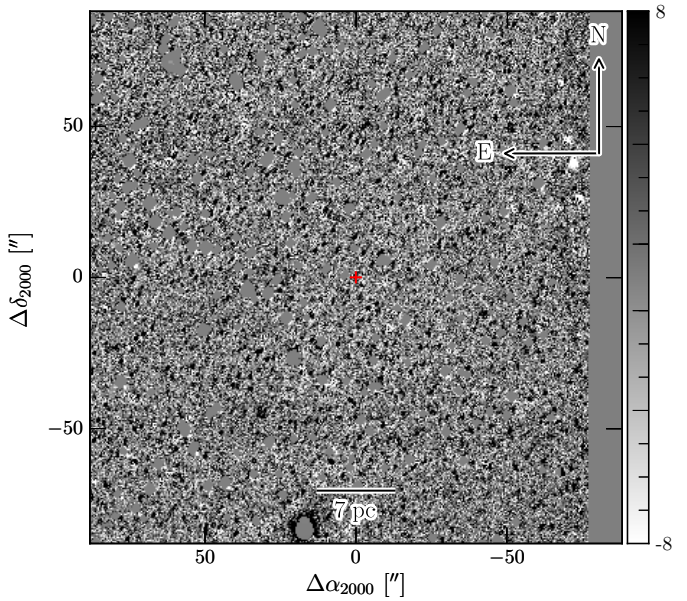

Figure 8.3: Same as Figure 8.2 but for CAL 87 chip 3. There is not much difference with its chip 2 counterpart. We expect that SB/FLUX profiles have similar shapes for this field, but different in scale due to the huge discrepancy in their corresponding Zs.

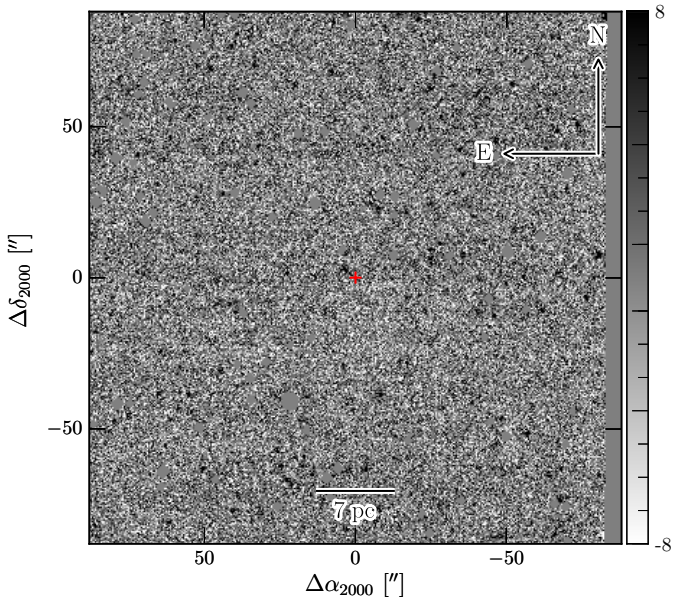

Figure 8.4: HOTPANTS RX J0550.0-7151 field image, after being mask in SEGMENTATION; visually, this subtraction looks cleaner than CAL 87, as there are not as many residuals, positive or negative, of stars, while the masked objects are few, such in the case of CAL 83.

The last of the SSSs is RX J0513.9-6951 in Figure 8.5. The difference image is similar to that of CAL 87, with many residuals of stars as black circles and several masked stars. This is, again, consistent with the large MEAN PIX values shown in Table 8.1 confirming the connection between them.

Overall, the visual inspection of the difference images corresponding to SSSs leads us to the same conclusion of Remillard et al. (1995): There are no [O III] emission nebulae surrounding them, with the only exception of CAL 83.

The three SNRs in the sample show the same kind of results. SNR 0509-67.5, shown in Figure 8.6, appears to be similar to CAL 87, both in the number of masked stars and the number and shape of the bad subtracted stars. This fact, plus the MEAN PIX value registered in Table 8.1, suggest no emission at all.

SNR 0519-69.0, shown in Figure 8.7, is interesting. The large MEAN PIX value in Table 8.1 suggest, as in the case of CAL 83, that either there is some sort of emission or the subtraction turned out really bad. Inspection of the difference image suggest that the latter is the most probable. There is a large emission like region in the left part of the image. What appears to be a circular object in the upper section is an instrumental artifact, probably related with a reflection in the [O III] filter that is not

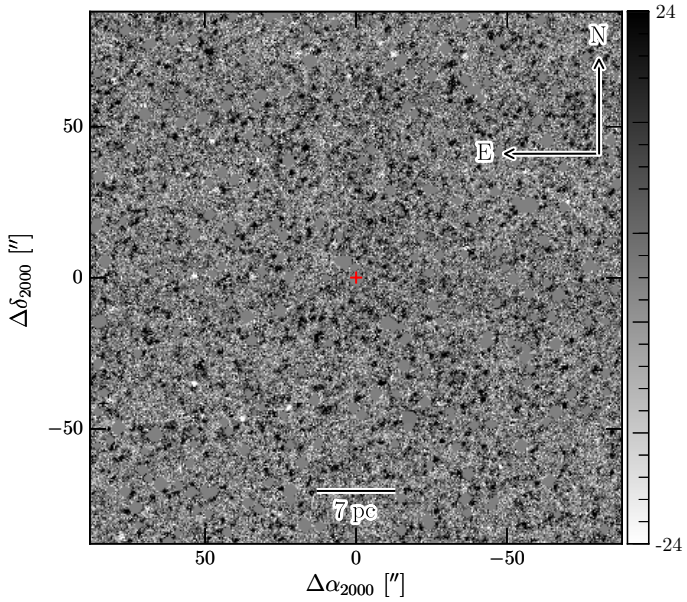

Figure 8.5: Same as previous difference images, for RX J0513.9-6951 field. It is remarkable the similitude between CAL 87 (Figures 8.2 and 8.3) and this image.

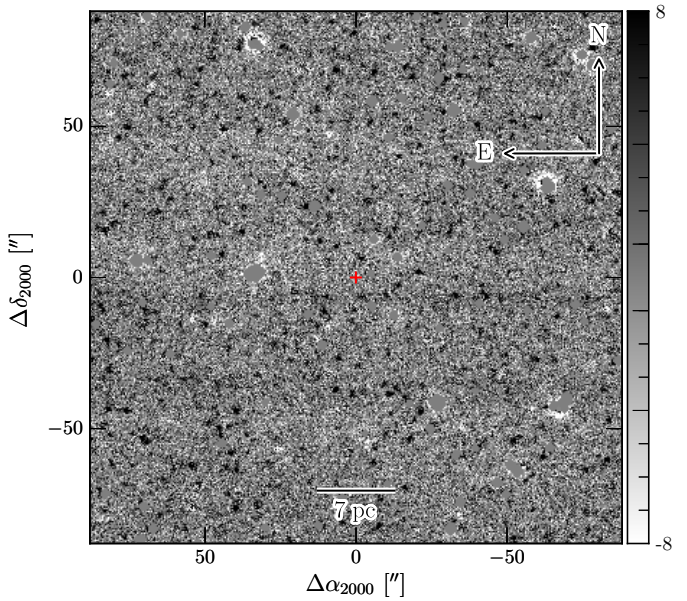

Figure 8.6: Difference image of SNR 0509-67.5; the resemblance with the (now prototype) CAL 87 counterpart is evident, which leads us to conclude that, at least visually, there is no [O III] emission from this field.

compensated by flat-fielding (it is seen in other chips of the CCD array in the some of the other field). These structures increase the value of MEAN PIX accordingly. As for the rest, there are only masked pixels and residual stars surrounding the source, and they which also contribute to the calculated mean of the image.

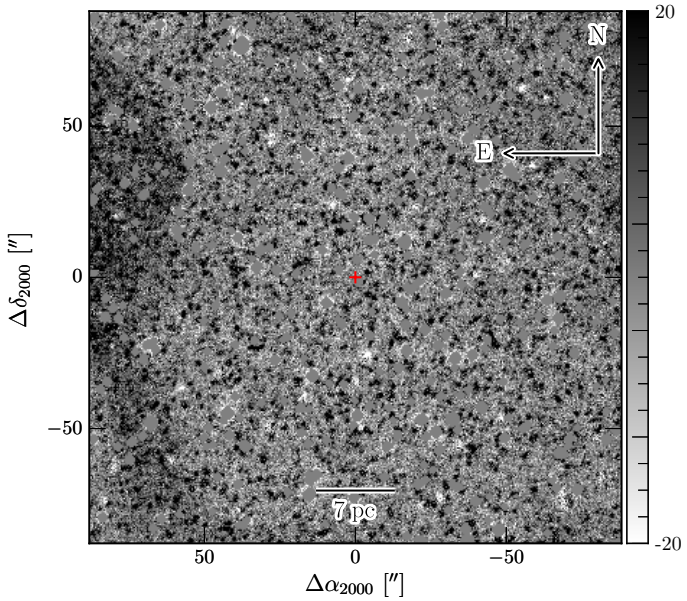

Figure 8.7: Difference image of SNR 0519-69.0 field. This is by far one of the most contaminated, mostly by a huge emission structure in the left side of the image. This structure, a half circle plus a tail, are thought to be artifacts of the [O III] filter

.

The last SNR of the set is SNR N103B, also known as SNR 0509-68.7, which is shown in Figure 8.8. This case shows a real detection of [O III] emission. First, the small-scale emission of the SNR itself is masked by the code, and only a small knot can be seen near the location of the source marked by a red cross, and surrounded by many negative residual of stars. It is known that SNR N103B is a very complex structure (see Li, et al., 2017, to appreciate all the physical structures of this SNR) but, overall the local emission is overshadowed by that from an extended object seen towards the Southwest, a superbubble surrounding the stellar cluster NGC 1850[4]. Its contribution will certainly be noticed at $\approx 50'' \sim 14$ pc from the source.

Figure 8.9 shows the unmasked version for this SNR to have a clear view of the small scale emission in [O III] by the knots surrounding the source. Williams, et

[4]http://simbad.u-strasbg.fr/simbad/sim-id?Ident=NGC+1850

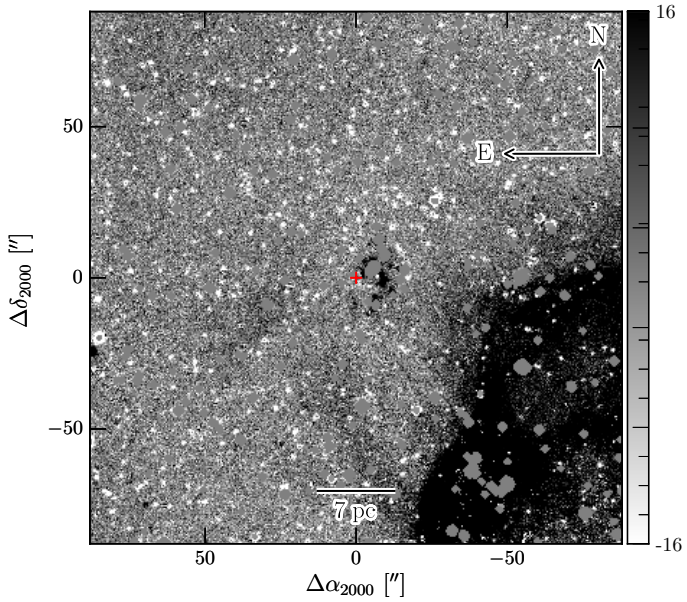

Figure 8.8: Difference image of SNR N103B. No emission could be obtained because the remnant is crowded with stars, while also there is a huge contribution of the superbubble surrounding NGC 1850 that we would include.

al. (2014) show that these knots match almost perfectly the corresponding X-rays emission in the 0.5-0.75 keV band. As any hypothetical SSS nebula should be formed from the location of these knots outwards, it was mandatory to mask them out when measuring the SB profile so as not to contaminate (even more) the results.

8.1.2 [O III] emission around other sources

In addition to the SSSs and SNRs we observed the planetary nebula RP 1406 J35 (Figure 8.10) in order to have an additional check of our system. The hot central stars of planetary nebulae are sources of X-rays, and, being the nebulae very dense, [O III] emission is expected. In practice, the emission is almost completely masked by our pipeline. As planetary nebulae are not as extended as supersoft nebulae, most of the emission is covered by the mask. The small unmasked region, though, will imply a peak of emission close to the source when computing the profile. Note that, a quarter of the circular artifact seen also in SNR 0519-69.0 appears here in the upper left area of the Figure.

Out of completness, we show the emission in [O III] of this planetary nebula without masking in Figure 8.11. The emission surrounding the central source is

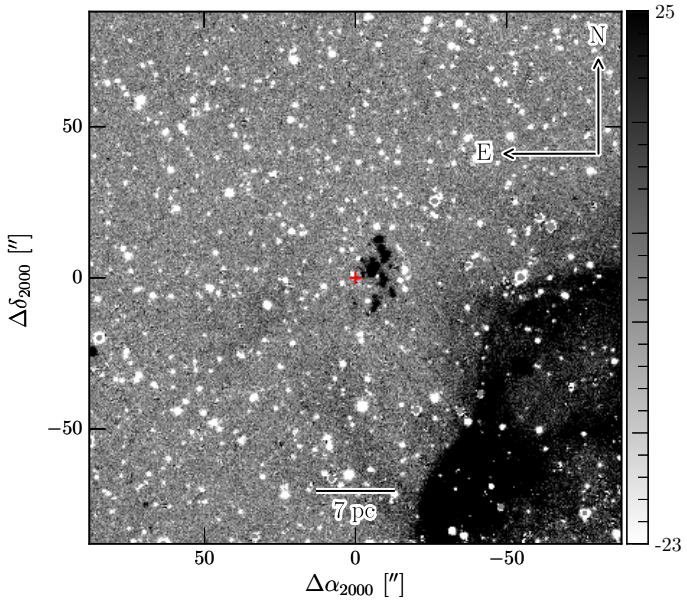

Figure 8.9: Difference image of the unmasked SNR N103B. In general, the subtraction is similar to Figure 8.8 (notice the difference in the scale), but here we clearly see the emission of [O III] knots (Li, et al., 2017).

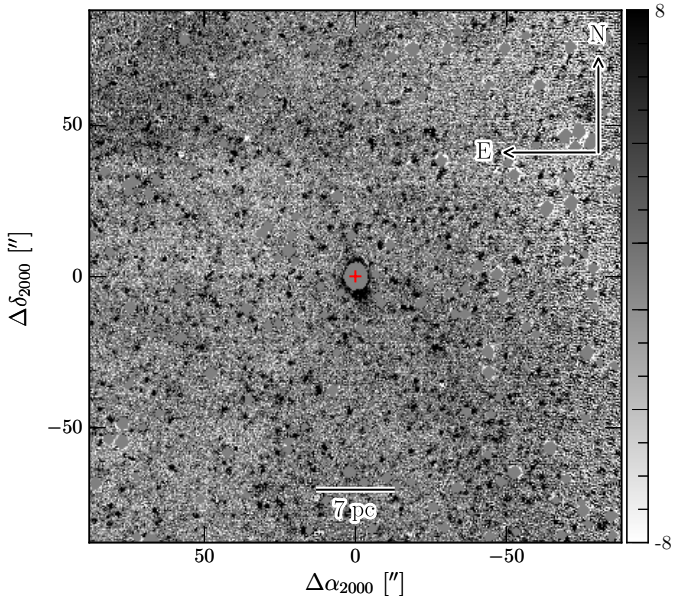

Figure 8.10: Difference image for planetary nebula RP 1406 J35. No emission is seen, but if we use more flexible constraints, we are able to see this object, which should not be a surprise.

apparent but, mostly due to higher densities of the nebula, the extension of the emission is far smaller than those expected for a hypothetical SSS nebula.

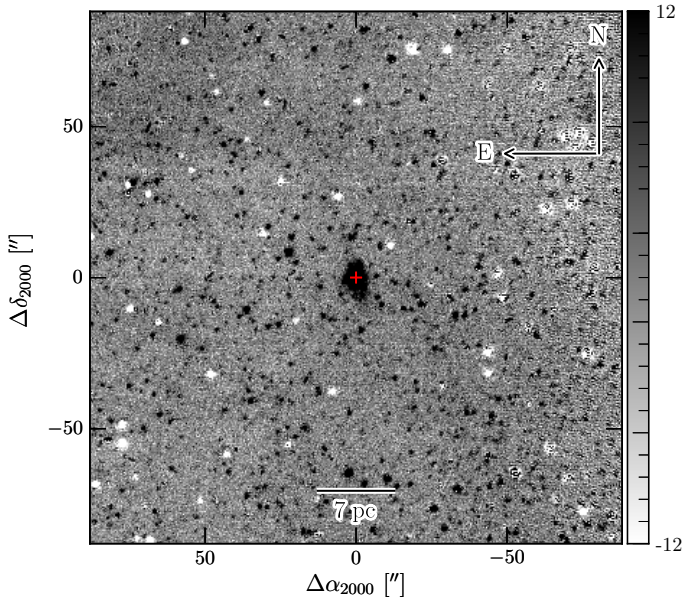

Figure 8.11: Difference image for unmasked planetary nebula RP 1406 J35. With this no-masking, it is appreciable the [O III] emission of this object. Notice the difference of the scale in the bar.

Serendipitously, we rediscovered the H II region catalogued by Pellegrini et al. (2012) as MCELS L203, also called DEM L157 (Davies et al., 1976), from the [O III] emission region formed by a dense CSM surrounding a hot OB central star. In this case, the nebula is clearly visible and extends ~ 3 times further than expected for a SSS nebula. Figure 8.12 shows that the emission reaches a distance of $\sim 50''$ from the center, even up to $\sim 80''$ in $\Delta\alpha$. This corresponds to a diameter of $100''$, which is smaller than the Hα extension of $\approx 3'$ measured by Davies et al. (1976). These estimates are reasonably consistent with our picture of CAL 83 where the associated Hα nebula is also larger than its [O III] counterpart. The reason behind this behavior is that hydrogen has a lower ionization potential than O^+. The axial symmetry of the emission suggests a bipolar geometry for the ejecta.

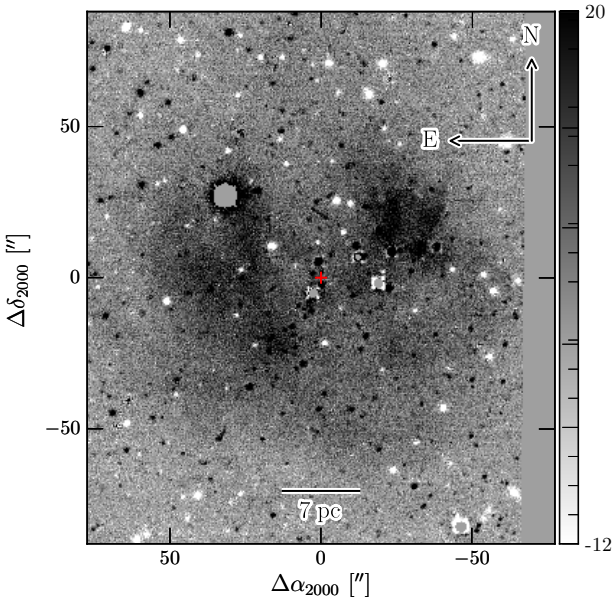

Figure 8.12: Difference image for DEM L157 field. An H II nebula found by Davies et al. (1976) doing a Hα mapping of the Magellanic Cloud. The [O III] emission is nearly symmetric, with an extension of $\approx 50''$ to $\approx 80''$.

8.2 Emission profiles

We present here our measurements of [O III] emission radial profiles to be compared later with theoretical models. We estimate the energy summing total counts and using the conversion factor Z_F calculated as explained in Section 7.3.2. The values of Z_F and its uncertainty ΔZ_F for each source are given in Table 8.2. When measuring radially over the nebula, or suspected nebula, we propagate the uncertainty ΔZ_F.

In addition to the counts, a relevant piece of information when computing the radial profiles is the distance from the source. The positions of CAL 83, CAL 87, SNR 0509-67.5, SNR N103B and SNR 0519-69.0 were obtained from SIMBAD ICRS coordinates[5], while those of RX J0550.0-7151 and RX J0513-6951 were obtained from the SSS LMC catalog SSSCAT[6]. Those of RP 1406 J35 and DEM L157 were obtained from Reid & Parker (2006) and Pellegrini et al. (2012), respectively. Extensive testing of the astrometry indicates that offsets of less than ten pixels are possible for the position of the sources in different versions of the same fields. Mismatches

[5]http://simbad.u-strasbg.fr/simbad. See additional references therein.
[6]http://www.mpe.mpg.de/$\tilde{\text{j}}$cg/sss/ssscat.html, and references provided there.

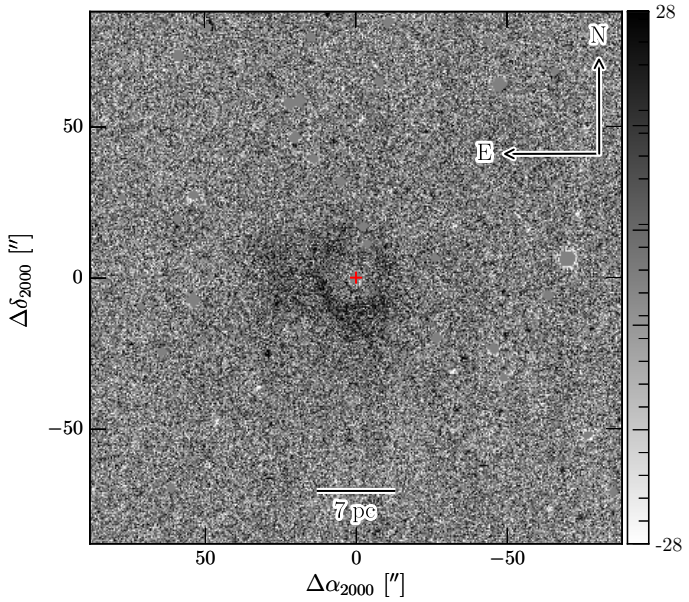

Figure 8.13: HOTPANTS CAL 83 output, the so called subtracted image, and input of radial measurement, i.e., after masking the objects in SEGMENTATION. The small red cross is the approximated position of the source. The image is 1600×1600 pixels^2, which corresponds to $\approx 178'' \times 178''$.

between coordinates from SSSCAT and SIMBAD originate in differences between the centroids of X-ray and optical images. In any case, the uncertainties implied by the offsets are irrelevant for the purposes of our study since we measure the relative distance between the source and circular coronae around them.

Table 8.2: Calculated Z_F and ΔZ_F in units of erg s^{-1} cm^{-2} COUNTS^{-1} .

FIELD	$Z_F \times 10^{19}$	$\Delta Z_F \times 10^{19}$	NUMBER OF STARS
CAL83	2.003	0.485	534
CAL 87 2	0.986	0.235	1102
CAL 87 3	1.516	0.354	1370
RX J0513.9-6951	0.748	0.180	1063
RX J0550.0-7151	1.412	0.376	452
SNR 0509-67.5	1.407	0.332	610
SNR 0519-69.0	1.214	0.273	1421
SNR N103B	2.573	0.518	1681
RP 1406 J35	2.405	0.534	885
DEM L157	2.202	0.452	1049

As explained in Chapter 7, a pedestal needs to be added to the base count value

of the difference image to avoid negative excursions of the [O III] FLUX, and therefore luminosity. In the absence of a better option we choose as pedestal the lowest mean value of the coronae. Table 8.3 provides the statistics for the coronae in all fields. MIN is the value of the pedestal added. Most of the pedestals are consistent with zero, the exceptions being RX J0513.9-6951 and SNR N103B. The latter is by far the largest departure from zero of the list, but this is not surprising because its difference image indicates a problem subtraction, with many negative residual on the stars surrounding the source, while the large emission region appears in the outskirts of the image. The pixels in this distant region add up to a larger positive value that compensates the negative isolated residuals, and therefore the field has a positive MEAN. Visual inspection clearly indicates the location of the MIN corona and strongly suggests why it is negative. But the difficulty of masking the small residuals leads us to prefer using the pedestal instead of excising the individual residuals for a cleaner background subtraction. Figures 8.14 up to 8.17 show different realizations of the SB profiles of our sources.

Table 8.3: Corona statistics for all of the fields: minimum MIN, maximum MAX, mean MEAN and standard deviation STD.

FIELD	MIN	MAX	MEAN	STD
CAL 83	-0.627	10.139	1.621	2.611
CAL 87 2	0.593	2.793	1.383	0.423
CAL 87 3	-0.662	1.318	0.629	0.300
RX J0513.9-6951	1.382	4.685	2.392	0.616
RX J0550.0-7151	-0.298	0.711	0.095	0.154
SNR 0509-67.5	-0.330	0.752	0.220	0.206
SNR 0519-69.0	0.068	5.037	2.368	1.339
SNR N103B	-2.458	7.197	2.696	2.839
RP 1406	-0.061	6.586	0.577	0.796
DEM L157	-0.610	11.414	4.567	3.554

Figure 8.14 displays the final SB profiles for those fields where we found [O III] emission. They generally confirm the conclusions of our initial inspections in the previous section: CAL 83, with a peak at ≈ 3 pc from the source, the superbubble in the field of SNR N103B which contributes effectively from ≈ 10 pc, the large H II region DEM L157, with an estimated radial extension of at least $\approx 50''$ (≈ 14 pc at the distance of the LMC) and the source RP 1406 J35, with a peak in emission close to the center (~ 1 pc), an evidence that the object was not entirely masked.

The rest of the sources, plotted in Figure 8.15, do not show clear signs of emission.

SNR 0519-69.0, the curious case that we named the worst subtraction of the list, shows an increment in the SB profile starting from ≈ 20 pc, which we associate with the instrumental artifacts discussed in the visual analysis. In any case, with the exception of CAL 83, neither of the SNRs or SSSs show signal of and emission nebula around the source. This is consistent with the conclusions of previous work (Remillard et al., 1995) for the objects in common.

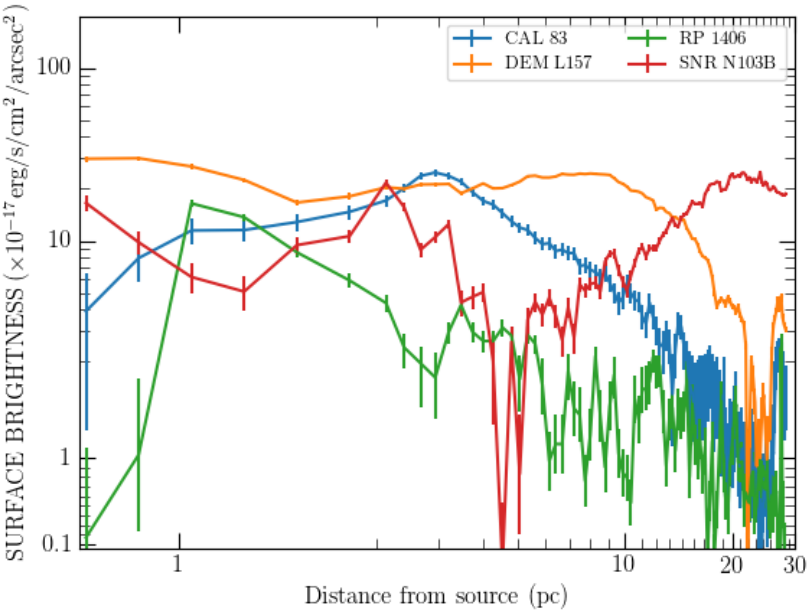

Figure 8.14: SB profiles of the fields that shows evident emission. Only four show clear traces of emission: CAL 83, H II region DEM L157 [O III] and RP 1406 J35 regions immediately surrounding the source, while SNR N103B rises up from ≈ 10 pc away to the source. This is not a surprise as those emission zones are readily seen in Figures 8.13, 8.8, 8.12 and 8.10

.

Our results on the CAL 83 SSS nebula can be compared with those of the two previous empirical works about it. Remillard et al. (1995) studied CAL 83, RX J0550.0-7151 and RX J0513.9-6951. For the former, they defined an inner region for the nebula extending up to 7.5 pc from the source and indicated that, within it, the emission reaches a maximum at ∼ 3.3 pc. They also commented that the region closer to 1 pc from the source represents a local minimum. Both of these observations are verified in this work, as seen in figure 8.13 and 8.14. It is necessary to say that one of the observations made by Remillard et al. (1995) is not found

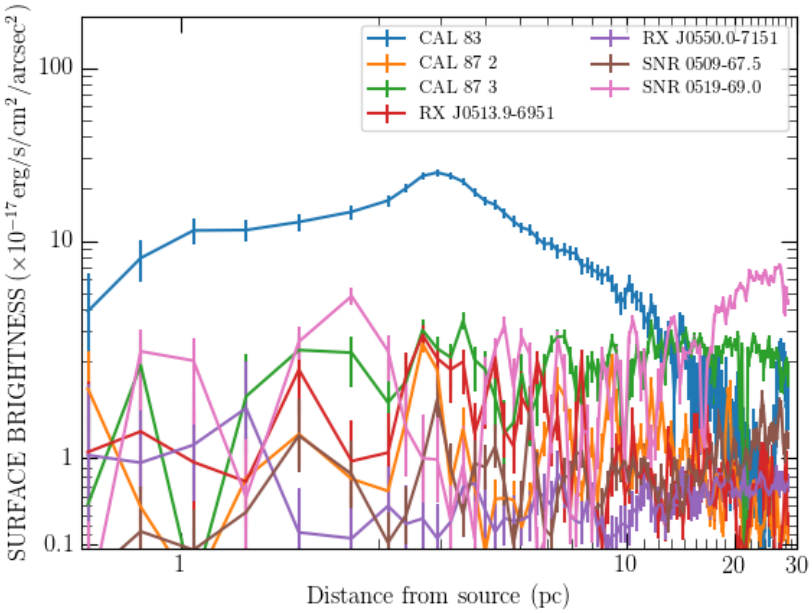

Figure 8.15: SB profiles of the fields that do not show apparent [O III] emission of our observations.

in our profiles: they stated that, even if there is a local minimum close to 1 pc, it should be no less than 50% of the intensity obtained at 3.3 pc, therefore, if there are discrepancies between the measurements, this must be reviewed. Remillard et al. (1995) also stated that the inner region contributes about 50% of the total flux measured up to 25 pc. This amounts to ~ 4 and 8.2 erg/s/cm^2 respectively, using a distance to the LMC of 55 Kpc and not considering the correction factor of 1.4 to account for Milky Way extinction (though they used it later to put upper limits in the luminosity of the sources).

Finally, they set an upper limit to the luminosity of all of the other sources at 7.5 pc, the count rate of those sources is more than a factor ten smaller than that of the CAL 83 inner nebula. They estimated that the total luminosity of CAL 83 at 25 pc was 4.1×10^{35} erg/s, corresponding to an upper limit of $\approx 10^{34.3}$ at 7.5 pc for the rest of the sources. Our own measurements for CAL 83 are 1.26×10^{35} erg/s and 3×10^{35} erg/s at 7.5 and 25 pc, respectively, using the same factor to correct for foreground extinction. This translates into upper limits of the luminosity $\approx 10^{34.1}$ erg/s at 7.5 pc.

We can also compare with the results of Gruyters et al. (2012) who provide

the only other published study of CAL 83 nebula. They study the flux emitted in about one quarter of the inner nebula using an IFU spectrum. A main conclusion of their work is that the total dereddened (reddened) [O III] flux in their quadrant is $\approx 9.7\times10^{-14}$ ($\approx 6.5\times10^{-14}$) erg/s/cm^2. They state that the quadrant has dimensions of $25.5'' \times 25.5''$, or equal to 7.5×7.5 pc^2 at a distance to LMC of 55 kpc[7]. Our measurement was done for an aperture of $27''\times27''$, centered to approximately match that of Gruyters et al. (2012), since they do not provide the center for the aligned images. Our result for this aperture is about $\approx 4 \times 10^{-14}$ erg/s/cm^2 for MASKED data, a value smaller than the reddened value of Gruyters et al. (2012) (about 65% of their flux). If we compute the profile without applying any mask to the data, other than the one corresponding to HOTPANTS, and do not do background subtraction, the change of the total flux is negligible. If we assume that the inner emission of CAL 83 nebula is symmetric, the reddened (dereddened) result of Gruyters et al. (2012) would be $\approx 2.6\times10^{-13}$($\approx 3.8\times10^{-13}$) erg/s/cm^2, $\sim$ 65% ($\sim$ 95%), of the one obtained by Remillard et al. (1995). Our measurement, hence, recovers just a fraction of the flux of either Remillard et al. (1995) at 7.5 pc or Gruyters et al. (2012) close to the source and appears to produce systematically low results.

How much different could the UNMASKED and MASKED SB profiles be, if the difference in a single quadrant are that small? To illustrate this, we plotted in Figure 8.17 (8.16) the UNMASKED data without background subtraction, and the usual MASKED data with the constraints already detailed, for two different fields, CAL 83 and SNR 0519-69.0 (CAL 87 3). It is reassuring to confirm that the overall shapes of CAL 83 and CAL 87 profiles do not significantly change, probably because these sources are located in relatively sparse stellar fields and, in consequence, their subtractions are good. On the contrary, the case of SNR 0519-69.0 (see Figure 8.7) does seem ill, with many stellar residuals that make clear the effect of the mask. For any field, masking translates into removal of peaks in the SB profiles, i.e. a smoothing of the curves.

8.3 Theoretical Modelling

We are ready now to compare the SB/FLUX radial profiles with CLOUDY theoretical models. To have a better feeling of the models it is important to understand the

[7]This cannot be correct: $25.5'' \times 25.5''$ corresponds to $\approx 6.8 \times 6.8$ pc^2, while their full FoV is $27'' \times 27''$ (7.2×7.2 pc^2).

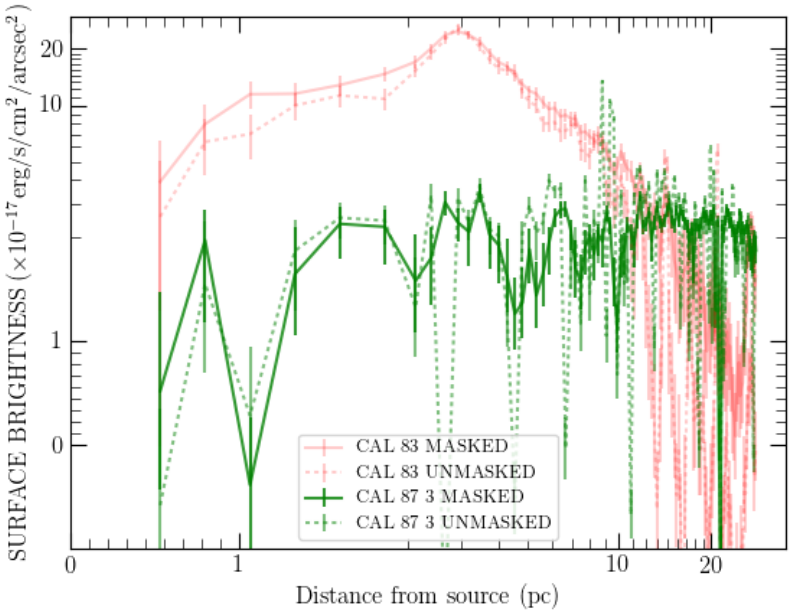

Figure 8.16: UNMASKED and MASKED SB profiles of CAL 83 and CAL 87. The meaning of UNMASKED is that de difference images of those fields are not corrected by any residual background and no mask is applied to the objects, while MASKED means the usual method explained in Chapter 7. It is easy to see that MASKED and UNMASKED resemble each other.

effect more critical free parameters (density of the ISM (n), temperature (T) and total luminosity (L) of the central source), on the SB profile and total luminosity of the nebula. Figure 8.18 shows the result of an illustrative study combining three ISM densities that span those expected for the LMC, with two radiation temperatures and two luminosities for the central source that span the characteristic range observed for SSSs. The chemical composition, other relevant parameter for CLOUDY models, was fixed at one half solar abundance (typical of the LMC) for all models in Fig. 8.18. Curves in the figure are labeled by the values of $\hat{n} = \log n$, with n in units of cm^{-3}, line-style coded according to the values of $\hat{L} = \log L$, with L in units of erg s^{-1}, and color coded according to the values of $T_5 = T \times 10^{-5}$, the radiation temperature of the source, with T in Kelvin. A note of caution should be given at this point. The CLOUDY models computed in this thesis are tuned to compare with SSSs and not with the planetary nebulae RP 1406 J35, or the H II region MCELS L203, since the central objects in these cases have different luminosity and radiation temperature.

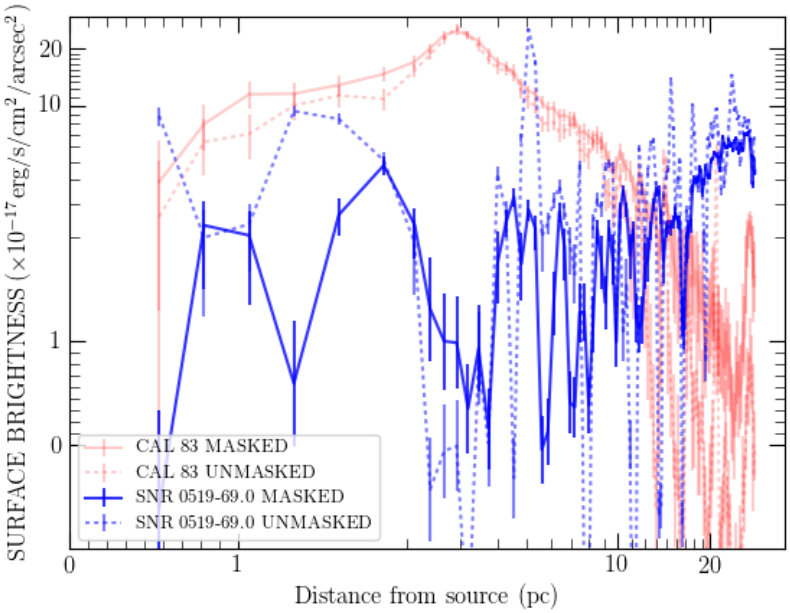

Figure 8.17: UNMASKED and MASKED SB profiles of CAL 83, and SNR 0519-69.0. The meaning of UNMASKED and MASKED are the same given in Figure 8.16. In this case, SB profiles of SNR 0519-69.0 is largely affected by the mask.

It is clear in Fig. 8.18 that the parameter that impact the most on the solution is the density of the ISM surrounding the source. Changing n by a factor of ten changes the central values of SB by a factor larger than 20 (as long as n is far from the critical density n_c). For L and T constants a denser medium implies that interactions that control [O III] emission, are bound to happen closer to the source trapping the sufficiently energetic photons nearby and preventing an extended emission zone. So, for L and T constant, the denser the medium the brightest and smallest the nebula.

The effect of L is also large but of a different signature. Changing L by a factor of 10 produces moderate changes in the inner values of SB (by factors of ~ 3) but makes for a more extended nebula (from two to five times bigger, approximately). So, for n and T constant, the more luminous sources provide for a slightly brighter but, especially, more extended nebulae.

The effect of the radiation temperature of the source is subtler but interesting. When n and L are kept constants, the profiles corresponding to the lower effective temperature (red lines in figure 8.18) are slightly brighter and more extended than those of the higher temperature. In other words, the cooler source produces a larger

and brighter [O III] region. This can be explained by second look at Figures 1.6 and 3.14. When the temperature is lower the peak of the black-body emission of the spectrum shifts to longer wavelengths. Thus, being still in the very hot interval $4-5\times10^5$ K, there are more photons that can ionize O^+ in the cooler source, which imply that more [O III] emission will take place in the inner regions in comparison with those of the higher radiation temperature. Also, as higher ionized oxygen abundance drops in regions closer to the source, more energetic photons are able to travel longer distances providing for more extended nebulae. Then, for n and L constant, the cooler central sources provide more slightly brighter and slightly more extended ionized nebulae.

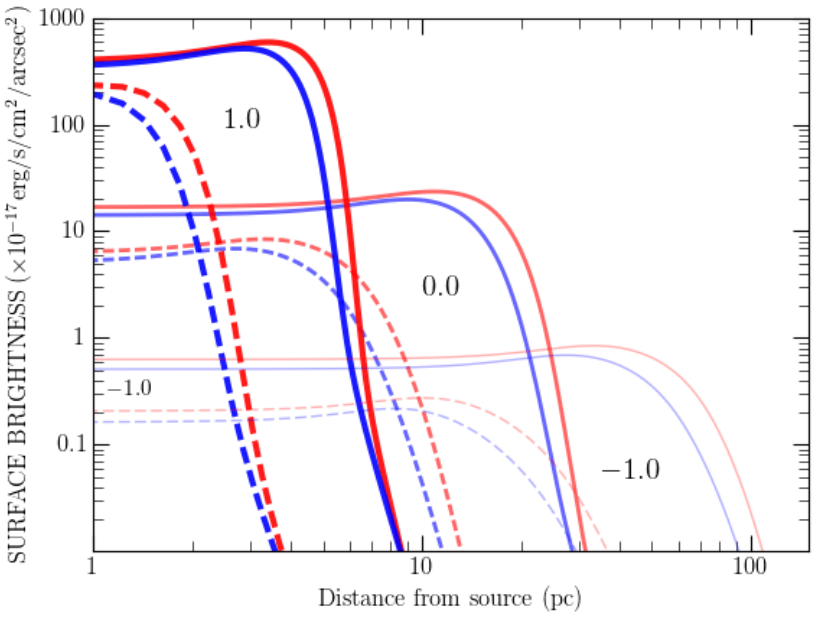

Figure 8.18: CLOUDY SB profiles for $\hat{n}\equiv\log_{10}n=\{-1,0,1\}$ (ISM density), $\hat{L}\equiv\log_{10}L=\{37,38\}$ (luminosity of the source in dashed and solid lines, respectively) and $T_5=T\times10^{-5}=\{4,5\}$ (temperature of the source in red and blue lines, respectively), with ranges of input parameters according to typical densities of ISM, and T, L of a SSS. These models were computed assuming LMC abundances (one half solar metallicity).

The understanding of CLOUDY models in terms of a simplified physics given by the previous paragraphs translates into strong constraints on n for the nebulae, or putative nebulae, studied here. We have plotted in Figure 8.19 all of the empirical SB profiles obtained in section 8.2, together with illustrative cloudy models computed for $\hat{L}=37.5$ and $T_5=5$. Most of the SB profiles are consistent with very low

values n, with no possibility of lying above $n = 1.0$ cm^{-3}, with many cases settling in the range $0.1 \lesssim n \lesssim 0.3$ cm^{-3}. As expected, the exceptions are the fields with prominent [O III] emission like CAL 83 and the particular case of SNR N103B where, at short distances, some emission from its unmasked knowts remains while, at larger distances, it is difficult to separate any emission from an hypothetical SSS fosil nebula, from the contribution of the superbubble surrounding NGC 1850.

Taking the offset in flux measurement that we found in section 8.2, between ≈ 1.2 and ≈ 2, at face value, we could increase all the profiles by a factor between 20% and 100%. We would find, then, that almost all the fields would still fall below $n = 1$ cm^{-3}. In the case of CAL 83, applying a factor two to the profile barely makes it reach the model with $\hat{n} = 0.5$ (it implies $n = 3.16$ cm^{-3} at 7.5 pc). This is marginally consistent with the lower bound of the interval $4 - 10$ cm^{-3} quoted by Remillard et al. (1995) and clearly smaller than the ≈ 10 cm^{-3} given by Gruyters et al. (2012).

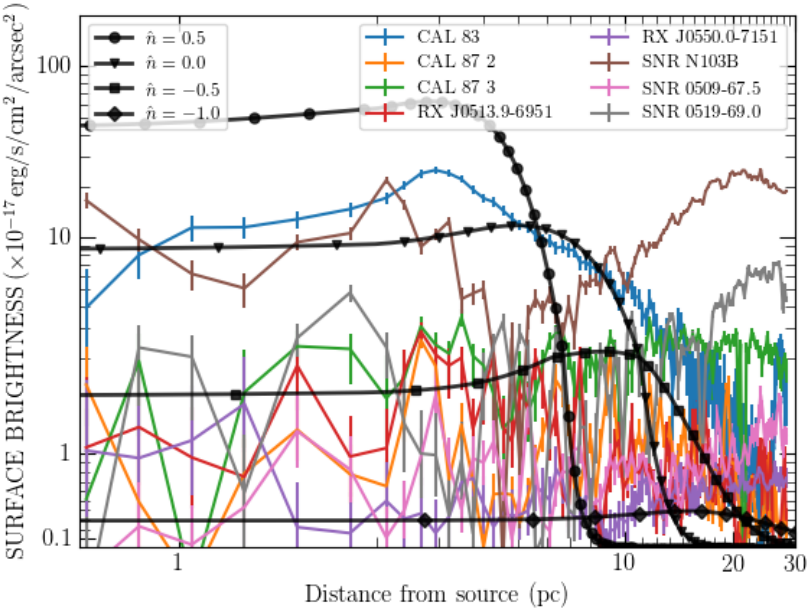

Figure 8.19: CLOUDY models for $\hat{n} = \{-1.0, -0.5, 0.0, 0.5\}$, $\hat{L} = 37.5$ and $T_5 = 5$, plotted alongside all the SB profiles of these fields. The fact that only one profile, CAL 83, lies for sure above $n = 1$ cm^{-3} at mostly any distance from the central source, suggest that in normal conditions, there is no nebular emission surrounding the other sources. Otherwise, it would required a really low ISM density to explain these SB profiles in the figure, or a bad subtraction and/or flux calibration.

As we saw when analyzing Figure 8.18, some degeneracy exists between the n, L,

and T input parameters. A higher luminosity model will be characterized by slightly more [O III] emission nearby the source and a generally more extended ionized region. In such a case, the CAL 83 profile is going to be represented by a model with lower density than the previously obtained ($1 \lesssim n \lesssim 3$ cm^{-3}), putting the CAL 83 nebula dangerously close, or even below, $n = 1$ cm^{-3}, a value inconsistent with the density of typical ISM in the LMC. The road to a source with higher luminosity seems to be closed, but that of lower luminosity sources appears to be possible. Decreasing the luminosity of the source and at the same time its radiation temperature, so as not to decrease the size of the ionized region, appears as an interesting option. In Figure 8.20 we show a study of this, where we compare the same profiles with models computed now with $T_5 = 4$ and $\hat{L} = 37$. As we can see, models with lower luminosity and temperature are qualitatively worse than the previous case. With $\hat{L} = 37$, even if the SB profiles of no-emission fields are better constrained by $n \approx 0.3$ cm^{-3} CLOUDY model (i.e. a model than behaved as an upper limit before provides now a better match), the shape of the densest profiles provide a poorer match to the CAL 83 SB profile. In Figure 8.19, the profile $n = 1$ cm^{-3} provided a good qualitative fit to the observed SB profile, and approximately matched the extension of the nebulae. In Figure 8.20, the $\hat{n} = 0.5$ profile drops sharply at ≈ 5 pc, and even worse, the $n = 1$ cm^{-3} does not extend past ≈ 10 pc. We can therefore conclude that $\hat{L} \approx 37.5$ is a better value for the luminosity of a typical source, at least for a nebula like CAL 83.

Figure 8.21 presents a study of the FLUX enclosed in growing apertures for CAL 83 compared with both CLOUDY models and the values 8.2×10^{-13} erg/s/cm^2 and $\approx 4 \times 10^{-13}$ erg/s/cm^2, which are the measurements provided by Remillard et al. (1995) for the flux enclosed at 25 and 7.5 pc, respectively. The CLOUDY models of this figure were computed for a temperature $T_5 = 5$, luminosity $\hat{L} = 37.5$, and five different densities $\hat{n} = \{-1.0, -0.5, 0.0, 0.5, 1.0\}$. It is clear in the figure that $n = 1$ cm^{-3} provides the profile that better matches the observations, but that a value slightly larger would provide an even better match. On the other hand, the differences in shape between the empirical and model profiles probably indicate that the nebula does not have a constant density.

Figure 8.21 sheds some different light into the mismatch reported in section 8.2 between the inner estimate of Remillard et al. (1995), consistent with that of Gruyters

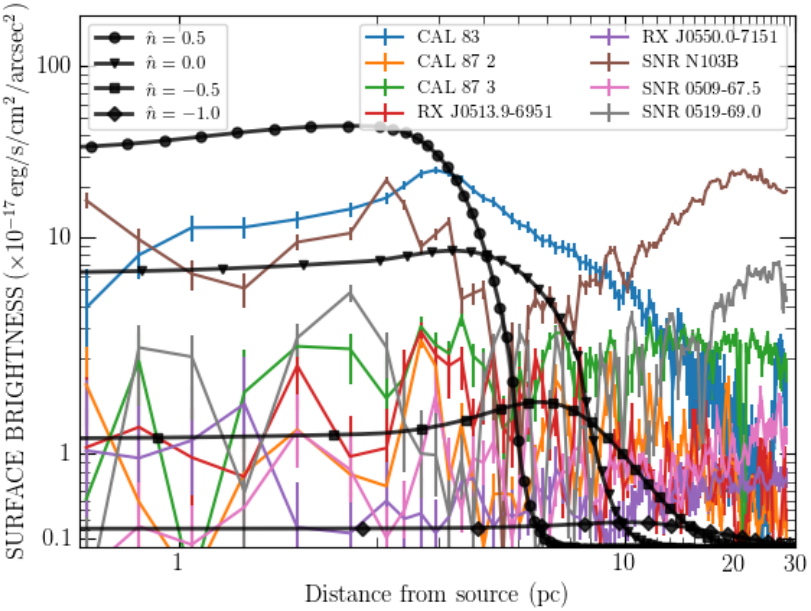

Figure 8.20: Same as Figure 8.19, but models calculated for fixed values $\hat{L} = 37$ and $T_5 = 4$. Qualitatively, these models are worse than the previously presented due to a severe mismatch between the shape of the densest models ($\hat{n} = \{0.0, 0.5\}$) and CAL 83 profile.

et al. (2012), and our own measurement. They reach the 50% value given by the lower horizontal line at 7.5 pc and we do at $\sim$ 12 pc. At 7.5 pc we are about 35% shy of the their estimate. Our measurement, however, is below theirs by 25% at 25 pc. We are aware that the more precise flux in Remillard et al. (1995) is enclosed within the 25 pc aperture than the one within the 7.5 pc aperture[8] (Figure 8.21), we take the more conservative value at 7.5 pc, meaning that our calibration is underestimated by $\sim$35%. The differences, however, are within 2 σ of the uncertainty in our zero-point for this field (c.f. 8.2), as the 1 σ and 2 σ "worms" plotted in the figure indicate. Gruyters et al. (2012) studied one quadrant of the CAL 83 nebula and provide a total [O III] flux of 6.52×10^{-13} erg s^{-1}, within 7.5 pc of the central source. We have plotted this measurement as well in Figure 8.21, assuming that the emission is spherically symmetric (which is clear that not the case for CAL 83).

Our measurements, then, are consistent within the uncertainties with those of previous work. Since our relative flux calibration is more precise than our absolute flux calibration, the different discrepancies with Remillard et al. (1995) at different

[8]They write "The brighter inner nebula of CAL 83, which we measure by integrating the surface brightness out to a radius of 7.5 pc from the central object, contributes $\sim$50% of the total flux."

distances from the source indicate something more complex than just a difference of $\sim 30\%$ in the zeropoints.

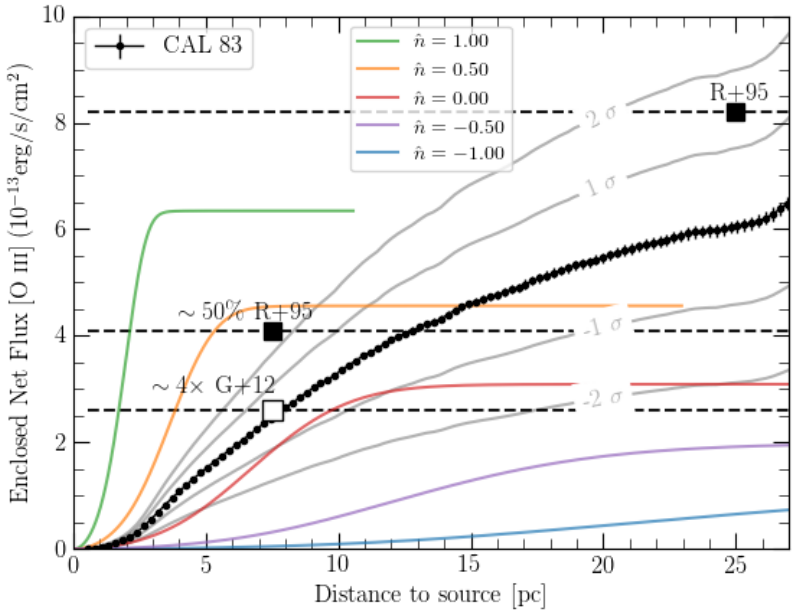

Figure 8.21: CAL 83 FLUX profile compared with the measurements of Remillard et al. (1995) & Gruyters et al. (2012) flux values at 7.5 and 25 pc from the source, and CLOUDY FLUX profiles, for $\hat{n} = \{-1.0, -0.5, 0.0, 0.5, 1.0\}$, $T_5 = 5$ and $\hat{L} = 37.5$. Our flux measurements are below those of Remillard et al. (1995) by $\sim 35\%$ at 7.5 pc and $\sim 25\%$ at 25 pc. The mismatch, though, is within 2 σ of our uncertainty in the calibration for this field (c.f. 8.2). At 7.5 pc our value is about the same as that of Gruyters et al. (2012) (under the assumption of spherically symmetric emission).

Keeping in mind a possible uncertainty in flux calibration between our work and the previously reported measurements, and assuming that our zeropoints are consistent in all of our fields, we will measure the [O III] luminosity at 7.5 pc ($L_{\mathrm{OIII},7.5}$), or their upper limit, for all our SSSs and SNRs and compare them with those resulting from CLOUDY models integrated to the same radius. We will use the previously determined FLUX values and scale them to a 7.5 pc aperture to obtain upper limits on the luminosity. CAL 83 will be our test bench case. Figure 8.22 presents the results of this exercise. In order to simplify the analysis, and due to its smaller impact on the results, we use only one radiation temperature for the central source, $T_5 = 5$. We will allow four values for the luminosity, $\hat{L} = 36.5$, 37.0, 37.5, and 38.0, which correspond to $\log(L/L_\odot) = 2.92$, 3.42, 3.92, and 4.42, and allow the more

critical parameter, the density of the nebula, to run between 0.1 and 10 cm^{-3}.

We note that Woods & Gilfanov (2016) studied some of the LMC fields included here and claimed that the upper limit the luminosity for those with no emission is $L = 10^{34.6}$ erg/s. This upper limit is wrong, since they took the values that Remillard et al. (1995) compute for an aperture of 25 pc and attributed them to the smaller aperture of 7.5 pc. As mentioned before, the real limit should be about a factor of 2 smaller, i.e. $L \approx 10^{34.3}$ erg/s, which is the value we have plotted in figure 8.22 with the dashed black line labeled R+95 upper limit.

A look at the Figure confirms that our measurements of CAL 83 agree with those of previous studies. Our CLOUDY limits for central source luminosity $37.0 \lesssim \hat{L} \lesssim 37.5$ ($3.42 \lesssim \log L/L_{\odot} \lesssim 3.92$), which comfortably fall within the luminosity of the central source plotted in Figure 5.9, leave a range of possible ISM densities for the nebula ($1.8 \lesssim n \lesssim 10$ cm^{-3}), which is consistent with the range quoted by Remillard et al. (1995) and Gruyters et al. (2012) for their measurements a 7.5 pc ($1.0 \lesssim n \lesssim 10$ cm^{-3}). For SNR N103B we do measure some emission, but we have already analyzed the case and concluded that it is not emission associated with the kind of [O III] ionized region we are after. For all of the other fields our study sets constraints more stringent than those of Remillard et al. (1995). As a result, only the assumption of extremely subluminous central sources, with $\hat{L} = 36.5$ or less, allows for densities of the surrounding nebulae comparable to that of CAL 83. For a more reasonable luminosity of the central source, like $\hat{L} > 37$, the required nebular densities are uncomfortably low compared with the expected density of the LMC ISM. Factoring in the $\sim$30% difference with the flux of Remillard et al. (1995) does not substantially change the previous conclusion, since it would amount to raising all of our horizontal lines ~ 1.5 small vertical divisions of the figure. They will still be more stringent limits than those of Remillard et al. (1995).

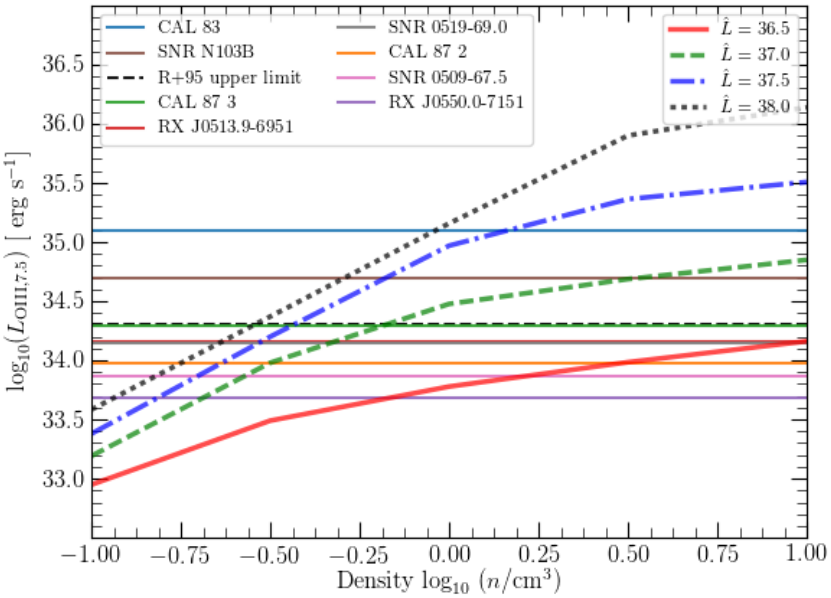

Figure 8.22: Logarithm of the [O III] luminosity, or its upper limit, enclosed within 7.5 pc of the central source ($L_{\mathrm{OIII},7.5}$) for all the fields, together with the luminosity predicted by four CLOUDY models with $T_5 = 5$, four luminosities for the central source $\hat{L} = \{36.5, 37.0, 37.5, 38.0\}$ (corresponding to $\log(L/L_\odot) = 2.92$, 3.42, 3.92, and 4.42), and nebular densities in the range of $-1.0 \leq \hat{n} \leq 1.0$. The upper limit to the luminosity of the nebulae undetected by Remillard et al. (1995), $\hat{L}_{\mathrm{O}} = 34.3$, is also plotted.

Table 8.4: [O III] luminosity at 7.5 pc

Object	$L_{\mathrm{OIII},7.5}$[1]	Remarks
CAL 83	35.10	real nebula
SNR N103B	34.70	not a nebula
R+95 upper limit	< 34.3	upper limit
CAL 87 3	34.29	upper limit
RX J0513.9-6951	34.16	upper limit
SNR 0519-69.0	34.15	upper limit
CAL 87 2	33.98	upper limit
SNR 0509-67.5	33.86	upper limit
RX J0550.0-7151	33.68	upper limit

[1] Logarithm of the luminosity at 7.5 pc, in erg s^{-1}

Chapter 9

Discussion and Conclusions

9.1 Discussion

The results presented above are consistent with the earlier work of Remillard et al. (1995). The only [O III] emission nebula around a SSS is CAL 83. Although we manage to establish more sensitive upper limits, no [O III] ionized regions are detected around the other SSSs o SNRs. The exception, where some emission is measured, is SNR N103B. But as it has stated before, the signal in this case does not correspond to an [O III] ionized nebula associated with the central source but to compact emission knots and a nearby superbubble.

If we insist that there must be [O III] emission nebulae surrounding SSSs, not finding them around SNRs is a problem for the validity of the supersoft channel as a source of Type Ia SN progenitors. The different models of "duty cycles" described in section 5.6 were seen as a possible solution to the absence of [O III] ionized regions. However, any luminosity variability, for example the period of on/off states of the source, that is shorter than a tenth of recombination timescale of [O III], approximately 10^5 yr according to Pequignot et al. (1991), should not strongly affect the ionization nebula SB profiles. For example, since the on-states (whether optically high/low) of CAL 83 and RX J0513.9-6951 are of order of hundred of years (Rajoelimanana et al., 2013), then, the ionization nebulae should be visible around them, which is the case for CAL 83, only. In general, the time-average luminosities for all these SSSs are large enough to show an ionized nebula, as concluded by Chiang & Rappaport (1996). Hence, variability of the sources does not appear as a valid reason to alter the SB profile over long timescales.

We are led to conclude that either the ISM densities surrounding CAL 87, RX J0513.9-6951 and RX J0550.0-7151 are about ~ 0.1 cm^{-3}, or less, much lower than that of CAL 83, or that there is something that obscures the soft X-ray emission of the sources and prevents the formation of the nebulae. There are several ways to make this happen (Kuuttila, Gilfanov, Seitenzahl, Woods & Vogt, 2019). One possibility is the action of an optically thick wind reacting to accretion rates above the stable-burning region (Hachisu et al., 1999a). Another are strong changes in the irradiation behaviour of the source. The latter would imply an alternative scenario to that proposed by Chiang & Rappaport (1996), one where the on/off states would make a larger impact in the structure of the ionization nebula.

The idea that the detection of ionized nebulae would help us to find obscured SSS that cannot be detected via X-rays (Remillard et al., 1995), does not consider the possibility that the ionizing radiation could not reach the ISM around the source. The issue has been considered in studies trying to understand the discrepancy between the observed and expected number of SSSs in galaxies. We note Gilfanov & Bogdán (2010), who focus on elliptical galaxies, and Di Stefano (2010), who focus on spiral ones. Nielsen, Dominik, Nelemans & Voss (2013) proposed that the circumbinary stellar medium (CSM) surrounding a SSS should be able to obscure most of the radiation by the action of large mass loss from the system via a dense wind. This idea was rejected by Nielsen & Gilfanov (2015), who used CLOUDY to prove that these hypothetical nebulae would look very different from the expected SSS nebulae (Rappaport et al., 1994), with higher He II/Hβ and lower [O III]/Hβ ratios, while requiring mass loss rates comparable to the stable-burning accretion rate ($\sim 10^{-7} - 10^{-6} M_\odot$) for a typical SSS system[1]. The amounts of CSM material implied by this scenario would imprint features in the early spectrum of a SN Ia, which are very seldom seen (see Patat, et al., 2007, for the case of SN 2006X). These kind of objects are yet to be discovered.

With respect to the SNRs, our results are consistent with those of Kuuttila, Gilfanov, Seitenzahl, Woods & Vogt (2019), although they use a different approach. They measured the surface brightness upper limits from the spectrum of the three SNRs, SNR 0509-67.5, SNR 0519-69.0 and SNR 0509-68.7, using the He II 4686 Å emission line from spectra taken at $\sim 4-5$ pc from the central sources. They did not find emission in any of the SNRs, and from the upper limit of He II emission of SNR

[1] $kT_{\rm eff} = 50$eV, $L_{\rm bol} = 10^{38}$ erg/s, inner/outer radial distances to the compact source $r_{\rm inn} = 1$ AU, $r_{\rm out} = 10$ AU, and wind speed $u_{\rm w} = 10$ km/s.

0519-69.0, and the constraints on the companion luminosity given by Edwards et al. (2012), they ruled out any possibility of a single degenerate progenitor, including SS X-rays sources.

Regarding SNR 0509-67.5, we also agree with Woods et al. (2018) who have already discarded the possibility of SS binary sources as a progenitor given the high content of neutral hydrogen in the close environment. The last statement requires some further elaboration. SNR 0509-67.5 is one of those remnants where Hβ is detected with both narrow and broad components. In an ISM with $T \sim 10^4$ K, ionized and neutral elements are affected differently by the interaction with the forward shock. While the neutrals are practically unaffected by the compression, some are collisionally excited before being ionized and the decays give rise to the narrow component of Hβ because the preshock temperature is low. In contrast, the charged particles are heavily compressed and strongly heated, producing fast protons. The collisional ionization and charge exchange between these and the neutral particles produce fast neutrals. The radiative decay from those is the source of the broad component of Hβ (Vink, 2012). Hence, an Hβ line with both narrow and broad components indicates a SNR surrounded by mostly neutral ISM, which practically rules out progenitors that are sources of high energy photons during the last $\sim 10^5$ yr before explosion, such as SSS. They confirm, as well, that SN Ia are not a powerful source of ionizing photons (Cumming et al., 1996).

The possibility exists of setting upper limits to the [O III] emission from the [O III]λ5007 line visible in the spectrum of Kuuttila, Gilfanov, Seitenzahl, Woods & Vogt (2019, see their Figure 2). However, the forward shock itself would contribute some UV-soft and X-ray radiation (Woods, private communication), and this makes it necessary to model the whole SNR spectrum in order to separate a hypothetical relic nebulae from the diffuse emission resulting from the ejecta. If this were done, the results would be easily comparable to ours, as long as we measure the emission ahead of the forward shock ($\sim$ 5 pc from the central source). This will be an additional probe on the systematic effects involved in our subtraction and calibration stages.

We stress, finally, that we would seem to face a two binary scenario. If it is true that there are much more SSSs than those that are detected through their hard radiation (Di Stefano, 2010; Nielsen & Gilfanov, 2015; Chen, Woods, Yungelson, Gilfanov & Han, 2015), then we either do not see them or, when we do detect the sources, they do not carry a [O III] emission region around. So, whatever the reason, the usual case appears to be that SSSs do not carry [O III] ionized regions around

them. Not finding [O III] emission inside recent SNRs, then, is not a problem for the supersoft X-Ray sources as progenitors of Type Ia SNe. It is just the expected result. If this is the case, [O III] emission is just not an appropriate way to establish the connection between these putative progenitors and the SNe.

9.2 Further work and improvements?

One of the aspects of our work that could be easily improved is technical. Part of our the uncertainty in flux calibration probably results from the fact that our narrow [O III] passband falls on the side of the broadband V passband, where there is a steep slope. Subtraction of the continuum and calibration of the difference will be facilitated by following the prescription by Waller (1990), of using an [O III] filter, calibrated independently, and a broadband filter whose effective wavelength is close to that of the [O III] line. We should not blame ourselves too hard regarding this infelicity, as this field seems to be well populated by colleagues still on the learning curve: at trying to understand the calibration of our fluxes I (D.F.) found some inconsistencies in Graur & Woods (2019), who motivated a conscientious exchange of emails, and, finally, a very serious errata[2], although my role in uncovering their mistake was not acknowledge.

Another dimension for improvement is the spectrum we used as a source of radiation to model the nebulae in CLOUDY. One could consider that, even in the case of non-stable burning on the WD, the source will still emit UV and soft X-rays originated directly in the accretion process. By the virial theorem, only half of the potential energy contributes to the kinetic energy of the system (in stars and protostars raising the temperature), while the other half is radiated away. It is assumed usually that this gravitational energy is emitted by a disk. If we have the spectrum of a disk model, it can be used as an input of CLOUDY providing for improved nebular models (e.g. Woods et al., 2017, 2018; Graur & Woods, 2019). These models can in turn be used to set upper limits of the accretion rate for these typical WD with slightly evolved companion stars, therefore constraining, for example, the mass transfer rate of an optically thick wind from the WD (Hachisu et al., 1996) or mass loss from the system (Hachisu & Kato, 2003).

A simple piece of further work, on which we are already working, are mode

[2]https://academic.oup.com/mnrasl/article/486/1/L89/5489660

elaborated models for the CAL 83 nebula. The profile we show in Figure 8.21 will be the first one published and deserves further attention.

9.3 Conclusions

Although we are within 2σ of the results in the literature, the uncertainty in flux calibration prevents us from stating too hard conclusions regarding flux or luminosity of the undetected nebulae. Rather than blaming our particular set of observations, the fact that we subtracted V passband images instead of $B + V$, or the lack of absolute calibration in photometry because we did not get photometric nights, the uncertainty appears to be intrinsic to the method. It is practically impossible to warrant that background determination used in image subtraction is done to within a fraction of an ADU across the whole field of view, and the difference between our measurements and those of Remillard et al. (1995) amounts to just 0.4 ADU per pixel. We are still concerned about the statistics provided by HOTPANTS when subtracting images taken with different filters, since even in the optimal cases we tried, such as the subtraction between V-V and O-O filters of consecutive images, the results were puzzling to us.

In qualitative terms, though, our results are fully aligned with those of the previous work. Neither the SSSs nor the SNRs display signals of [O III] ionized nebulae. We have managed, in addition to obtain some interesting results:

1. We have presented SB profiles around several hard energy sources in the LMC. Seven of them were presented here, including four SSSs and three SNRs. In spite of having been studied since 1995, curiously, our SB profile of CAL 83 will be the first published.

2. The [O III] flux measurement of CAL 83 nebula at 7.5 and 25 pc are broadly consistent with those in the literature, but the slope we measure is steeper than that measured by Remillard et al. (1995). They reported a 50% increase in luminosity between 7.5 and 25 pc and we measure a 60% increase, approximately, between the same radii.

3. The shape of the [O III] SB profile is not consistent with those provided by CLOUDY models, a probably indication that the matter density in the nebula is not constant, as the typical CLOUDY models of SSSs nebulae assume.

4. The [O III] luminosities for almost all the fields at 7.5 pc lies below $10^{34.3}$ erg/s, which is about 15% our measurement of the luminosity of CAL 83 nebula, therefore, according to the CLOUDY models their densities should be $\lesssim 0.5$ cm^{-3}.

5. The negative detections would require either a very rarefied ISM or a very unstable accretion time on the SSSs, with unrealistically low average accretion rates. This is consistent as well with other observations, like the absence of emission surrounding SN 2014J (Graur & Woods, 2019). These results might indicate that SN Ia do not explode as SSS objects but, for example, in the dwarf nova phase of the binary evolution (Meng & Yang, 2010a).

6. The density of the ISM for CAL 83 at 7.5 pc has to be ≥ 1 cm^{-3} if we assume a blackbody temperature $T = 5 \times 10^5$ K and $L \leq 10^{37.5}$ of the source, which lies in the same order of magnitude with the calculations made by Gruyters et al. (2012)(≈ 10 cm^{-3}) using sulphur lines ratios (analog to the Equation 3.8 but for densities) and $T_e = 10000$ K, and Remillard et al. (1995) ($4-10$ cm^{-3}) using photoionized models by Rappaport et al. (1994). If the luminosity of CAL 83 were about $L = 10^{38}$ erg/s, by the CLOUDY models, it would translate to a ISM density surrounding CAL 83 of ≤ 1 cm^{-3} which would not be consistent with the physics of this LMC region.

Bibliography

Ablimit, I., Xu, X.-j., & Li, X.-D. 2014, ApJ, 780, 80

Aguilar, A., Covington, A. M., Hinojosa, G., et al. 2003, ApJS, 146, 467

Alard, C., & Lupton, R. 1999, Astrophysics Source Code Library, ascl:9909.003

Alard, C., & Lupton, R. H. 1998, ApJ, 503, 325

Alard, C. 2000, A&AS, 144, 363

Badenes C., Harris J., Zaritsky D., Prieto J. L., 2009, ApJ, 700, 727

Beccari, G., & Carraro, G. 2015, Ecology of Blue Straggler Stars, 1

Becker, A. 2015, Astrophysics Source Code Library, ascl:1504.004

Bertin, E., Mellier, Y., Radovich, M., et al. 2002, Astronomical Data Analysis Software and Systems XI, 281, 228

Bessell, M. 2000, in Encyclopedia of Astronomy and Astrophysics(IOP Publishing Ltd and Nature Publishing Group), 1638

Bessell M., & Murphy S., 2012, PASP, 124, 140

Bevington P. R., Robinson D. K., 2003, drea.book

Bohlin R. C., Gordon K. D., Tremblay P.-E., 2014, PASP, 126, 711

Bohlin R. C., Landolt A. U., 2015, AJ, 149, 122

Bours, M. C. P., Toonen, S., & Nelemans, G. 2013, A&A, 552, A24

Branch, D., Livio, M., Yungelson, L. R., Boffi, F. R., & Baron, E. 1995, PASP, 107, 717

Brown P. J., Breeveld A., Roming P. W. A., Siegel M., 2016, AJ, 152, 102

Burwitz V., Reinsch K., Greiner J., Meyer-Hofmeister E., Meyer F., Walter F. M., Mennickent R. E., 2008, A&A, 481, 193

Callanan, P. J., Machin, G., Naylor, T. & Charles, P. A. 1989, MNRAS, 241, 27p.

Carroll, B. W. & Ostlie, D. A. 2007, An Introduction to Modern Astrophysics, 2nd Ed., Pearson Eduction, Inc.

Charles, P. A., Southwell, K. A., & O'Donoghue, D. 1996, IAU Circ, 6305, 2

Chandrasekhar S. 1983, On Stars, their Evolution and their stability, Nobel Prize lecture

Chen, H.-L., Woods, T. E., Yungelson, L. R., Gilfanov, M., & Han, Z. 2014, MNRAS, 445, 1912

Chen H.-L., Woods T. E., Yungelson L. R., Gilfanov M., Han Z., 2015, MNRAS, 453, 3024

Chevalier, R. A., Kirshner, R. P., & Raymond, J. C. 1980, ApJ, 235, 186

Chiang, E. & Rappaport, S. 1996, ApJ, 469, 255

Choudhury, S., Subramaniam, A., & Cole, A. A. 2016, MNRAS, 455, 1855

Collins, G. W. 1989, New York, W. H. Freeman and Co., 1989, 512 p.

Cowperthwaite, P. S., Berger, E., Soares-Santos, M., et al. 2016, ApJ, 826, L29

Covington, A. et al., 2001, Phys. Rev. Lett. 87, 243002

Cowley, A. P., Schmidtke, P. C., Crampton, D., & Hutchings, J. B. 1990, ApJ, 350, 288

Cowley, A. P., Schmidtke, P. C., Hutchings, J. B., Crampton, D., & McGrath, T. K. 1993, ApJ, 418, L63

Crampton, D., Hutchings, J. B., Cowley, A. P., et al. 1996, ApJ, 456, 320

Cumming, R. J., Lundqvist, P., Smith, L. J., Pettini, M., & King, D. L. 1996, MNRAS, 283, 1355

Davies, R. D., Elliott, K. H., & Meaburn, J. 1976, MEMRAS, 81, 89

Di Stefano, R., & Rappaport, S. 1994, ApJ, 437, 733

Di Stefano, R., Paerels, F, & Rappaport, S. 1995, ApJ, 450, 705

Di Stefano, R., Kong, A. K. H., Greiner, J., et al. 2004, ApJ, 610, 247

Di Stefano, R. 2010, ApJ, 712, 728

Di Stefano R., Voss R., Claeys J. S. W., 2011, ApJ, 738, L1

Edwards, Z. I., Pagnotta, A., & Schaefer, B. E. 2012, ApJ, 747, L19

Eissner W., Jones M., Nussbaumer H., 1974, Comput. Phys. Commun., 8,270

Fender, R. P., Southwell, K., & Tzioumis, A. K. 1998, MNRAS, 298, 692

Ferland, G. J., Porter, R. L., van Hoof, P. A. M., et al. 2013, RMxAA, 49, 137

Filippenko, A. V. 1997, ARA&A , 35, 309

Fitzpatrick, R. 2015, Quantum Mechanics, by Richard Fitzpatrick. ISBN 978-981-4689-94-6. Published by World Scientific, 2015

Gabriel, M., Noels, A., Montalbán, J., & Miglio, A. 2014, A&A, 569, A63

Gänsicke B., van Teeseling A., Beuermann K., de Martino D., 1998, uabi.conf, 411, ESASP.413

Gilfanov, M., & Bogdán, Á. 2010, Nature, 463, 924

Graur, O., Maoz, D., & Shara, M. M. 2014, MNRAS, 442, L28

Graur O., Woods T. E., 2019, MNRAS, 484, L79

Greiner, J. 2000, New Astronomy, 5, 137

Greiner, J., & Di Stefano, R. 2002, A&A, 387, 944

Groth, E. J. 1986, AJ, 91, 1244

Gruyters, P., Exter, K., Roberts, T. P., & Rappaport, S. 2012, A&A, 544, A86

Hachisu, I., Kato, M., & Nomoto, K. 1996, ApJL, 470, L97

Hachisu, I, Kato, M. & Nomoto, K. 1999b, ApJ, 522, 487

Hachisu, I., Kato, M., Nomoto, K., & Umeda, H. 1999, ApJ, 519, 314

Hachisu I., Kato M., 2003, ApJ, 590, 445

Hachisu I., Kato M., 2003, ApJ, 598, 527

Hachisu, I., Kato, M., & Nomoto, K. 2008, ApJ, 679, 1390

Hachisu, I., Kato, M., & Nomoto, K. 2008, ApJ, 683, L127

Hachisu, I., Kato, M., & Nomoto, K. 2010, ApJ, 724, L212

Hamuy, M., Phillips, M. M., Suntzeff, N. B., et al. 2003, Nature, 424, 651

Han, Z., & Podsiadlowski, P. 2004, MNRAS, 350, 1301

Han, Z., & Podsiadlowski, P. 2006, MNRAS, 368, 1095

Hansen, B. 2004, Physics Reports, 399, 1

Hasinger, G. 1994, Reviews in Modern Astronomy, 7, 129

Heise J., van Teeseling A., Kahabka P., 1994, A&A, 288, L45

Hillebrandt, W., & Niemeyer, J. C. 2000, ARA&A, 38, 191

Howell, D. A., Sullivan, M., Nugent, P. E., et al. 2006, Nature, 443, 308

Hughes, J. P., Hayashi, I., Helfand, D., et al. 1995, ApJ, 444, L81

Hutchings, J. B., Crampton, D., Cowley, A. P., & Schmidtke, P. C. 1998, ApJ, 502, 408

Hutchings, J. B., Cowley, A. P., Mann, R., Schmidtke, P. C., & Crampton, D. 2006, Astrophysics in the Far Ultraviolet: Five Years of Discovery with FUSE, 348, 260

Idan I., Shaviv N. J., Shaviv G., 2013, MNRAS, 433, 2884

Iliadis, C. 2007, Nuclear Physics of Stars, by Christian Iliadis. ISBN 978-3-527-40602-9. Published by Wiley-VCH Verlag, Wenheim, Germany, 2007

Ivanova, N. 2015, Ecology of Blue Straggler Stars, 179

Kahabka, P., Pietsch, W., & Hasinger, G. 1994, A&A, 288, 538

Kahabka, P., & van den Heuvel, E. P. J. 1997, ARA&A, 35, 69

Kahabka P., Haberl F., Pakull M., Millar W. C., White G. L., Filipović M. D., Payne J. L., 2008, A&A, 482, 237

Kenyon, S. J., & Webbink, R. F. 1984, ApJ, 279, 252

Kerins, E., Darnley, M. J., Duke, J. P., et al. 2010, MNRAS, 409, 247

Kerzendorf, W. E., Schmidt, B. P., Asplund, M., et al. 2009, ApJ, 701, 1665

Kosenko, D., Helder, E. A., & Vink, J. 2010, A&A, 519, A11

Kothari, D. S. 1932, MNRAS, 93, 61

Kuuttila J., Gilfanov M., Seitenzahl I. R., Woods T. E., Vogt F. P. A., 2019, MNRAS, 484, 1317

Landolt, A. U. 1992, AJ, 104, 340

Lang, D., Hogg, D. W., Mierle, K., Blanton, M., & Roweis, S. 2010, AJ, 139, 1782

Langer, N., Deutschmann, A., Wellstein, S., & Höflich, P. 2000, A&A, 362, 1046

Lanz T., Telis G. A., Audard M., Paerels F., Rasmussen A. P., Hubeny I., 2005, ApJ, 619, 517

Li, W., Bloom, J. S., Podsiadlowski, P., et al. 2011, Nature, 480, 348

Li C.-J., et al., 2017, ApJ, 836, 85

Livio, M., & Mazzali, P. 2018, Physics Reports, 736, 1

Livne, E., & Arnett, D. 1995, ApJ, 452, 62

Long, K. S., Helfand, D. J., & Grabelsky, D. A. 1981, ApJ, 248, 925

Luridiana, V., Morisset, C., & Shaw, R. A. 2015, A&A, 573, A42

Lynden-Bell D., Lynden-Bell R. M., 1977, MNRAS, 181, 405

McGowan K. E., Charles P. A., Blustin A. J., Livio M., O'Donoghue D., Heathcote B., 2005, MNRAS, 364, 462

Maoz, D., Mannucci, F., & Nelemans, G. 2014, ARA&A, 52, 107

Mark, H., Price, R., Rodrigues, R., Seward, F. D., & Swift, C. D. 1969, ApJ, 155, L143

Marietta, E., Burrows, A., & Fryxell, B. 2000, ApJS, 128, 615

Marshak, R. E. 1940, ApJ, 92, 321

Massey, P. 2002, ApJS, 141, 81

Meng, X., & Podsiadlowski, P. 2017, MNRAS, 469, 4763

Meng, X., & Yang, W. 2010, ApJ, 710, 1310

Meng, X.-C., & Yang, W.-M. 2011, Research in Astronomy and Astrophysics, 11, 965

Nahar, S. N. 2004, Phys. Rev. A, 69, 042714

Nicholls, D. C., Dopita, M. A., & Sutherland, R. S. 2012, ApJ, 752, 148

Nicholls, D. C., Dopita, M. A., Sutherland, R. S., Kewley, L. J., & Palay, E. 2013, ApJ, 207, 21

Nielsen M. T. B., Dominik C., Nelemans G., Voss R., 2013, A&A, 549, A32

Nielsen M. T. B., Nelemans G., Voss R., Toonen S., 2014, A&A, 563, A16

Nielsen M. T. B., Gilfanov M., 2015, MNRAS, 453, 2927

Nomoto, K., Nariai, K., & Sugimoto, D. 1979, PASJ, 31, 287

Nomoto, K. 1982, ApJ, 253, 798

Nomoto, K., Saio, H., Kato, M., & Hachisu, I. 2007, ApJ, 663, 1269

Nomoto K., Leung S.-C., 2018, SSRv, 214, 67

Nugent, P., Phillips, M., Baron, E., Branch, D., & Hauschildt, P. 1995, ApJ, 455, L147

Nugent, P. E., Sullivan, M., Cenko, S. B., et al. 2011, Nature, 480, 344

Oliveira A. S., Steiner J. E., 2007, A&A, 472, L21

Orio, M., Zezas, A., Munari, U., Siviero, A., & Tepedelenlioglu, E. 2007, ApJ, 661, 1105

Orio, M., Nelson, T., Bianchini, A., Di Mille, F., & Harbeck, D. 2010, ApJ, 717, 739

Osterbrock, D. E., & Ferland, G. J. 2006, Astrophysics of gaseous nebulae and active galactic nuclei, 2nd. ed. by D.E. Osterbrock and G.J. Ferland. Sausalito, CA: University Science Books, 2006

Paczyński, B. 1970, A&A, 20, 47

Paczyński, B. 1976, Structure and Evolution of Close Binary Systems, 73, 75

Paczyński, B., & Zytkow, A. N. 1978, ApJ, 222, 604

Palay, E., Nahar, S. N., Pradhan, A. K., & Eissner, W. 2012, MNRAS, 423, L35

Pakull, M. W., & Motch, C. 1989, European Southern Observatory Conference and Workshop Proceedings, 32, 285

Pascual S., Gallego J., Zamorano J., 2007, PASP, 119, 30

Passy J.-C., Herwig F., Paxton B., 2012, ApJ, 760, 90

Patat F., et al., 2007, Sci, 317, 924

Peimbert, M., Peimbert, A., & Delgado-Inglada, G. 2017, PASP, 129, 082001

Pellegrini, E. W., Oey, M. S., Winkler, P. F., et al. 2012, ApJ, 755, 40

Pequignot, D., Petitjean, P., & Boisson, C. 1991, A&A, 251, 680

Pols, O. 2012, Lectures of Binary Stars

Pols, O. 2012, Lectures of Stellar structure and evolution

Pringle, J. E. & Wade, R. A. 1985, Interacting binary stars

Rajoelimanana, A. F., Charles, P. A., Meintjes, P. J., Odendaal, A., & Udalski, A. 2013, MNRAS, 432, 2886

Rappaport, S., Chiang, E., Kallman, T., & Malina, R. 1994, ApJ, 431, 237

Rappaport, S., Di Stefano, R., & Smith, J. D. 1994, ApJ, 426, 692

Reid, W. A., & Parker, Q. A. 2006, MNRAS, 373, 521

Reinsch, K., van Teeseling, A., Beuermann, K., & Thomas, H.-C. 1996, Roentgenstrahlung from the Universe, 183

Reinsch, K., van Teeseling, A., Beuermann, K., & Abbott, T. M. C. 1996, A&A, 309, L11

Reinsch, K., van Teeseling, A., King, A. R., & Beuermann, K. 2000, A&A, 354, L37

Remillard, R. A., Rappaport, S., & Macri, L. M. 1995, ApJ, 439, 646

Rest, A., Suntzeff, N. B., Olsen, K., et al. 2005, Nature, 438, 1132

Rest, A., Scolnic, D., Foley, R. J., et al. 2014, ApJ, 795, 44

Ribeiro T., Lopes de Oliveira R., Borges B. W., 2014, ApJ, 792, 20

Ruiz-Lapuente, P., Comeron, F., Méndez, J., et al. 2004, Nature, 431, 1069

Schaeidt, S., Hasinger, G., & Trümper, J. 1993, A&A, 270, L9

Schaefer, B. E., & Pagnotta, A. 2012, Nature, 481, 164

Schandl S., Meyer-Hofmeister E., Meyer F., 1997, A&A, 318, 73

Schmidt, B. P., Suntzeff, N. B., Phillips, M. M., et al. 1998, ApJ, 507, 46

Schmidtke P. C., Cowley A. P., 1995, IAU Circ. , 6278

Schmidtke, P. C., Cowley, A. P., Crane, J. D., et al. 1999, AJ, 117, 927

Sienkiewicz, R. 1980, A&A, 85, 295

Soberman, G. E., Phinney, E. S., & van den Heuvel, E. P. J. 1997, A&A, 327, 620

Someya, K., Bamba, A., & Ishida, M. 2014, PASJ, 66, 26

Southwell K. A., Livio M., Charles P. A., O'Donoghue D., Sutherland W. J., 1996, ApJ, 470, 1065

Spector, O., Finkelman, I., & Brosch, N. 2012, MNRAS, 419, 2156

Starrfield, S., Timmes, F. X., Hix, W. R., et al. 2004, ApJ, 612, L53

Starrfield S., Iliadis C., Hix W. R., 2016, PASP, 128, 51001

Sugimoto, D., & Fujimoto, M. Y. 1978, PASJ, 30, 467

Sugimoto, D., Fujimoto, M. Y., Nariai, K., & Nomoto, K. 1979, IAU Colloq. 53: White Dwarfs and Variable Degenerate Stars, 280

Storey, P. J., & Zeippen, C. J. 2000, MNRAS, 312, 813

Storey, P. J., Sochi, T., & Badnell, N. R. 2014, MNRAS, 441, 3028

Tauris, T. M., & van den Heuvel, E. P. J. 2006, Compact stellar X-ray sources, 39, 623

Thirring W., 1970, ZPhy, 235, 339

Toonen, S., Claeys, J. S. W., Mennekens, N., et al. 2014, A&A, 562, A14.

Turatto, M., Benetti, S., Cappellaro, E., et al. 1996, MNRAS, 283, 1

Uenishi, T., Nomoto, K., & Hachisu, I. 2003, Apj, 595, 1094

Vacca W. D., Leibundgut B., 1996, ApJ, 471, L37

van den Heuvel, E. P. J., Bhattacharya, D., Nomoto, K., & Rappaport, S. A. 1992, A&A, 262, 97

van der Heyden, K. J., Behar, E., Vink, J., et al. 2002, A&A, 392, 955

van der Sluys, M., 2013, Binary evolution in a nutshell

van Teeseling, A., & King, A. R. 1998, A&A, 338, 957

Vink J., 2012, A&ARv, 20, 49

Walker, A. R. 2012, Ap&SS, 341, 43

Waller, W. H. 1990, PASP, 102, 1217

Wang B., Han Z., 2012, NewAR, 56, 122

Wang, L., Baade, D., & Patat, F. 2007, Science, 315, 212

Wei, Z. 1988, Astrophysical Letters and Communications, 27, 275

Wheeler, J. C., & Benetti, S. 2002, Allen's Astrophysical Quantities, 451

Whelan, J., & Iben, I., Jr. 1973, ApJ, 186, 1007

Williams B. J., et al., 2014, ApJ, 790, 139

Wolf W. M., Bildsten L., Brooks J., Paxton B., 2013, ApJ, 777, 136

Woods T. E., Ivanova N., 2011, ApJ, 739, L48

Woods, T. E., Ivanova, N., van der Sluys, M. V., & Chaichenets, S. 2012, ApJ, 744, 12

Woods, T. E., & Gilfanov, M. 2016, MNRAS, 455, 1770

Woods, T. E., Ghavamian, P., Badenes, C., & Gilfanov, M. 2017, Nature Astronomy, 1, 800

Woods, T. E., Ghavamian, P., Badenes, C., & Gilfanov, M. 2018, ApJ, 863, 120

Woosley, S. E., & Weaver, T. A. 1994, ApJ, 423, 371

Wozniak, P. 2008, Manchester Microlensing Conference, 3

Yan Zhao, Qiong Luo, Senhong Wang, Chao Wu, "Accelerating Astronomical Image Subtraction on Heterogeneous Processors", eScience (eScience) 2013 IEEE 9th International Conference on, pp. 70-77, 2013.

Yoon, S.-C., & Langer, N. 2005, A&A, 435, 967

Yungelson, L., Livio, M., Truran, J. W., Tutukov, A., & Fedorova, A. 1996, ApJ, 466, 890

Yungelson L. R., 2010, AstL, 36, 780

Zaritsky, D., Harris, J., & Thompson, I. 1997, AJ, 114, 1002

Zaritsky D., Harris J., Thompson I. B., Grebel E. K., 2004, AJ, 128, 1606